INTERFACIAL CHEMICAL BEHAVIORS AND SYNERGISTIC EFFECTS OF POTASSIUM HYDROXIDE AND UREA-MODIFIED SEWAGE SLUDGE BIOCHAR ON PHORATE REMOVAL FROM WATER

A THESIS SUBMITTED TO
THE GRADUATE SCHOOL OF NATURAL AND APPLIED SCIENCES
OF
MIDDLE EAST TECHNICAL UNIVERSITY

BY

BEGÜM BAŞER

IN PARTIAL FULFILLMENT OF THE REQUIREMENTS
FOR
THE DEGREE OF MASTER OF SCIENCE
IN
ENVIRONMENTAL ENGINEERING

SEPTEMBER 2021

Approval of the thesis:

INTERFACIAL CHEMICAL BEHAVIORS AND SYNERGISTIC EFFECTS OF POTASSIUM HYDROXIDE AND UREA-MODIFIED SEWAGE SLUDGE BIOCHAR ON PHORATE REMOVAL FROM WATER

submitted by **BEGÜM BAŞER** in partial fulfillment of the requirements for the degree of **Master of Science** in **Environmental Engineering, Middle East Technical University** by,

Prof. Dr. Halil Kalıpçılar
Dean, Graduate School of **Natural and Applied Sciences**   _____

Prof. Dr. Bülent İçgen
Head of the Department, **Environmental Engineering**   _____

Prof. Dr. Ülkü Yetiş
Supervisor, **Environmental Engineering, METU**   _____

Dr. Balal Yousaf
Co-Supervisor, **Environmental Engineering, METU**   _____

Examining Committee Members:

Prof. Dr. Bülent İçgen
Environmental Engineering, METU   _____

Prof. Dr. Ülkü Yetiş
Environmental Engineering, METU   _____

Dr. Balal Yousaf
Environmental Engineering, METU   _____

Assist. Prof. Dr. Sema Sevinç Şengör
Environmental Engineering, METU   _____

Prof. Dr. Erkan Şahinkaya
Bioengineering, Istanbul Medeniyet University   _____

Date: 10.09.2021

I hereby declare that all information in this document has been obtained and presented in accordance with academic rules and ethical conduct. I also declare that, as required by these rules and conduct, I have fully cited and referenced all material and results that are not original to this work.

Name, Last Name: Begüm Başer

Signature:

ABSTRACT

INTERFACIAL CHEMICAL BEHAVIORS AND SYNERGISTIC EFFECTS OF POTASSIUM HYDROXIDE AND UREA-MODIFIED SEWAGE SLUDGE BIOCHAR ON PHORATE REMOVAL FROM WATER

Başer, Begüm
Master of Science, Environmental Engineering
Supervisor: Prof. Dr. Ülkü Yetiş
Co-Supervisor: Dr. Balal Yousaf

September 2021, 213 pages

Phorate is one of the widely used organophosphorus pesticides (OPPs) having detrimental impacts on living creatures and the environment. As such, biochar is a low-cost and environment-friendly material that can be used as a catalyst to develop the strategic tools that reduce and overcome the challenges caused by their rising concentration. Herein, phorate removal strength of potassium hydroxide and urea-modified sewage sludge-derived biochars were described for the most goal-oriented technique. The advanced characterization techniques form an essential basis for the knowledge of surface functionalities and physicochemical properties of produced biochars. The results of multiple characterization techniques revealed that the generated biochars have a high specific surface area, porous surface, equally distributed elemental composition, miscellaneous mineral content, diversified surface functional groups and a high-level of thermochemical stability, which encourage the removal mechanism of phorate. The batch removal experiments affirmed that biochars pyrolyzed under 700°C, treated under hydrothermal conditions and modified with the combination of potassium hydroxide (KOH) and urea chemicals showed the best phorate removal efficiencies. These selective samples were further chosen for the 2nd batch removal experiments with changing

temperature, biochar dose and pH variables. As a result of 2nd stage batch experiments, three selected biochars shows enhanced Phorate removal efficiencies at lower batch temperatures (25°C), higher biochar doses (5 and 15 g/L) and pH within 6 – 7. Moreover, three biochar samples were reused four times and they showed higher than 85% removal at the 5th experiment. GC-MS analysis was performed to comprehend the intermediate degradation products (i.e., 2, 4-Di-tert-butylphenol, [1,1'-Biphenyl]-2,3'-diol, 3,4',5,6'-tetrakis(1,1-dimethylethyl)) of phorate.

Keywords: Biochar, Physicochemical Modifications, Phorate Removal, Characterization Techniques

ÖZ

POTASYUM HİDROKSİT VE ÜRE İLE MODİFİYE EDİLMİŞ KANALİZASYON ÇAMURU ESASLI BİYOKÖMÜRÜNÜN ARAYÜZEYSEL KİMYASAL DAVRANIŞLARI VE SUDAN FORAT GİDERİMİ ÜZERİNDEKİ SİNERJİK ETKİLERİ

Başer, Begüm
Yüksek Lisans, Çevre Mühendisliği
Tez Yöneticisi: Prof. Dr. Ülkü Yetiş
Ortak Tez Yöneticisi: Dr. Balal Yousaf

Eylül 2021, 213 sayfa

Forat, canlılar ve çevre üzerinde zararlı etkileri olan, yaygın olarak kullanılan organofosforlu pestisitlerin bir çeşididir. Biyokömür, foratın artan konsantrasyon değerlerinin neden olduğu zorlukları azaltan çevre dostu ve düşük maliyetli katalizör olarak dikkatleri üzerine çekmektedir. Bu çalışmada, potasyum hidroksit ve üre ile modifiye edilmiş kanalizasyon çamuru esaslı biyokömürlerin forat giderimi üzerinde gösterdikleri sinerjik etkiler vurgulanarak açıklanmaktadır. Başvurulan gelişmiş karakterizasyon teknikleri, üretilen biyokömürün yüzey işlevleri ve fizikokimyasal özellikleri hakkında bir temel oluşturmaktadır. Karakterizasyon teknikleri sonucunda, üretilen biyokömürlerin foratın uzaklaştırma mekanizmasını teşvik eden yüksek bir spesifik yüzey alanına, gözenekli yüzeye, eşit olarak dağıtılmış element bileşimine, çeşitli mineral içeriğine, çeşitlendirilmiş yüzey fonksiyonel gruplarına ve yüksek düzeyde termokimyasal dayanıklılığa sahip olduğu ortaya konmuştur. Kesikli sorpsiyon deneyleri, hidrotermal ön işleme tabi tutulmuş, 700 °C sıcaklıkta piroliz işlemi görmüş, KOH ve üre kimyasalları ile kombine şekilde modifiye edilmiş biyokömürlerin %100 forat uzaklaştırarak en yüksek verimi gösterdiğini

ortaya koymuştur. Bu üç numune üzerinde değişen sıcaklık, biyokömür dozu ve pH değişkenleri ile ikinci aşama giderme deneyleri uygulanmıştır ve sonucunda daha düşük yığın sıcaklıklarında (25 °C), daha yüksek biyokömür dozlarında (5 ve 15 g/L) ve 6 – 7 pH da gelişmiş forat giderimi verimlilikleri göze çarpmıştır. Ayrıca, üç biyokömür numunesi dört kez yeniden kullanılmış ve 5. deneyde %85in üzerinde Forat giderimi göstermiştir. GC-MS analizi ^{18}C kolonunda foratın serbest radikal aracılı ara bozunma ürünlerini (örn., 2, 4-Di-tert-butylphenol, [1,1'-Biphenyl]-2,3'-diol, 3,4',5,6'-tetrakis(1,1-dimethylethyl)) araştırmak amacıyla yürütülmüştür.

Anahtar Kelimeler: Biyokömür, Fiziko-kimyasal Modifiye, Forat Giderimi, Karakterizasyon Teknikleri

To my family

ACKNOWLEDGMENTS

I would like to express my sincere appreciation and gratitude to my supervisor Prof. Dr. Ülkü Yetiş and my co-supervisor Dr. Balal Yousaf, for their endless support in all aspects during my graduate career, interest and great supervision. I am feeling thankful for their guide with kindness and deepest knowledge on this thesis. Prof. Dr. Ülkü Yetiş inspired me to have a long and active academic career in environmental engineering, and I tried to acknowledge her extensive experience. Dr. Balal Yousaf encouraged me with his guidance, advice, criticism, insight, and curiosity throughout the research. He extended my vision more into environmental science and chemistry. Considering their personal unspeakably attitudes, I grant myself lucky for meeting advisors like them. They do not refrain from supporting me, and I am thankful for their trust.

I wholeheartedly thank my mother for her confidence and strong standing beside me whenever I felt tired. I owe my deepest gratitude to my father since he was always showing me his endless support and sincere emotions.

I also wish to thank to my friends Cansu Özcan, Selin Yanar, İrem İnce, Aslı Gül Gün, Özgür Yazıcı, Bilgesu Şen, Sara Jeffar, Matilda Hague for their sincere support and neigbour-laboratory friends Işkın Engin, Berivan Tunca, Mert Şanlı, Yasin Odabaş, Ece Kutlar, Amin Ghaderi Kia for keeping the energy up in the department.

Finally, I would like to express my sincerest thank to Aykut Kaş for his patience, encouragement and support in every moment. He was always physically and mentally there, providing two more hands throughout this period.

TABLE OF CONTENTS

xiv

LIST OF TABLES

LIST OF FIGURES

FIGURES

LIST OF ABBREVIATIONS

ABBREVIATIONS

AChE	Acetylcholinesterase enzyme
AOP	Advanced oxidation processes
ATR	Attenuated Total Reflectance
BET	Brunauer–Emmett–Teller
BJH	Barrett-Joyner-Halenda
BTEX	Benzene, Toluene, Ethylbenzene, Xylene
CAS	Chemical Abstracts Service
CEC	Cation exchange capacity
COD	Chemical oxygen demand
DBP	Disinfection by-product
DMPO	5,5-dimethyl-1-pyrrolin–N-oxide
DWLOC	Drinking Water Level of Comparison
EBC	European Biochar Certificate
EBDS	Electron Backscatter Diffraction Spectroscopy
EC	Emerging contaminant
EC	Electrical conductivity
EDX	Energy Dispersive X-ray Spectroscopy
EOC	Emerging organic contaminant
EPA	Environmental Protection Agency
EPR	Electron Paramagnetic Resonance Spectroscopy
ESR	Electron Spin Resonance Spectroscopy
EU	European Union
FTIR	Fourier Transformed Infrared Spectroscopy
GC-MS	Gas Chromatography-Mass Spectrometry
h-BN	Graphitic boron nitride
HK	Horvath-Kawazoe

HPLC	High Performance Liquid Chromatography
HT	Hydrothermal temperature
ICP-MS	Inductively Coupled Plasma-Mass Spectroscopy
IR	Infrared Radiation
MAF	Ministry of Agriculture and Forest
MBR	Membrane Bioreactor System
MOF	Metal-organic framework
NEXAFS	Near-edge X-ray Absorption Fine Structure Spectroscopy
NLDFT	Non-local Density Functional Theory
nZVI	Nano Zerovalent Iron
OCP	Organochlorine pesticides
OPP	Organophosphorus pesticide
PAH	Polycyclic Aromatic Hydrocarbon
PCB	Polychlorinared Biphenyl
PCP	Personal care products
PDS	Peroxodisulfate ($^-O_3SO–OSO_3^-$)
PMS	Peroxymonosulfate ($HO–OSO_3^-$)
P$_{octanol/water}$	Octanol-water partition coefficient
POP	Persistent organic pollutant
SEM	Scanning Electron Microscopy
SS	Sewage sludge
TGA	Thermogravimetric Analyzer
UPW	Ultrapure water
UV	Ultra-violet
WFD	Water Framework Directive
WHO	World Health Organization
WW	Wastewater
WWTP	Wastewater treatment plant
XPS	X-ray Photoelectron Spectroscopy
XRD	X-ray Diffraction Spectroscopy

CHAPTER 1

INTRODUCTION

1.1   General

The use of pesticides has always remained controversial. While the benefits it adds to agricultural activities are indisputable facts; the risk it carries for the environment and living beings has brought it to this level. They act as a medicine for plants in order to protect from diseases, pests or weeds. Pesticides are a highly preferred group of chemicals in order to enhance agricultural activities by saving from unwanted conditions on crops and vegetables (European Commission, 2020). It has been determined that one-third of the worldwide agricultural production is carried out using pesticides. Without the application of pesticides, agricultural yield decreased significantly, i.e., fruits, vegetables and cereals production fell 78%, 54% and 32%, respectively (W. Zhang, 2018). Annual pesticide use of the world was recorded nearly 2 million tons, where the primary role belongs to China, followed by the U.S.A. and Argentina in the second and third place. By 2020, the global record has been added up to 3.5 million tons. The trend continues to rise with a constant increase (Sharma et al., 2019). In Turkey, total pesticide usage was recorded as 60 thousand tons in 2018 with 340 different active compounds. This number showed 7 times increase compared to the use in 1979, even though 3% decrease in the agricultural sites between 2014 and 2018 (MAF, 2019).

The term "biocides" is general and its sub-categories are as follows: insecticides, herbicides, fungicides, rodenticides, fumigants, algaecides, miticides, acaricides, nematicides, molluscicides, growth regulators, repellents and pesticide. Among these, pesticides can also be categorized concerning their active compounds such as carbamates, organophosphates, organochlorine, acetanilides, pyrethroids (WHO, 2008). They are named under the persistent organic pollutants (POPs), which can

stay for long periods of time in the environment, accumulate on sediments or fatty tissues of living beings, be deposited at far distances, or show toxic effects to the non-targeted bodies, including environment, humans and biota (Malakootian et al., 2020). Dichlorodiphenyltrichloroethane (DDT), toxaphene, chlordane, aldrin, dieldrin, endrin, mirex, heptachlor and hexachlorobenzene are the POP pesticides having high priority in the Stockholm Convention list. They were banned concerning their harm and toxicity and required to take measures to eliminate or reduce the release of POPs in the environment (European Parliament, 2019).

Water is one of the heavily pesticide-contaminated matrixes. In the year of 2000, the European Commission published the Water Framework Directive (WFD, 2000/60/EC) and listed priority substances in Annex X. The WFD requires the elimination of pollution of surface water by the priority substances, which have a considerable risk for aqueous mediums due to wide range utilization (European Commission, 2000). There is a close relationship between the adverse impact of pesticides on hydrological systems and human health, aquatic life and food chains.

The most widespread type of pesticides is the organophosphorus pesticides (OPPs) which are released from agro-industrial practices. Sales of OPPs account for 34% of the global sales (Khedr et al., 2019). These chemicals are structured as human-made esters of phosphoric acid. They are readily degradable, insoluble in water, and hydrophobic by nature, allowing them to dissolve easily in organic solvents and fats (Tankiewicz et al., 2010). Environmental influences and microorganisms are capable of quick decomposition of OPPs. Thus, they become rated under non-persistent pesticides. Yet, continuous exposure to those chemicals results in accumulation in humans even under reduced grades. Certain types of illnesses and damaged muscles have been shown as consequences of continuous exposure (Jaipieam et al., 2009). Extensive usage and unconscious dumping of these pesticides also harm the environment and cause long-lasting remains, contamination in the aqueous, gaseous and solid mediums. OPPs enter into the food chain via the consumption of food products or these contaminated mediums (X. Lin et al., 2021). Chlorpyrifos,

malathion, parathion, diazinon, glyphosate, dichlorvos and phorate are the commonly applied OPPs.

Phorate (O, O-Diethyl S-[(ethylsulfanyl)methyl] phosphorodithioate) is an organophosphate insecticide that was registered by the US Environmental Protection Agency (EPA). It is applied onto potatoes, corn, peanuts, cotton, sugarcane, wheat, soybeans, beans, sugar beets, lilies and no record for the residential application. The US EPA published that approximately 1.5 thousand tons of phorate production is achieved annually and it accounts for 10 billion m^2 per year 2.5 million acres. It is found as risky for non-targeted organisms such as birds, mammals, aquatic species and endangered species. Phorate eliminates corn rootworm, white grubs, seedcorn beetles, leafhoppers, black cutworms, nematodes, wireworms and grasshoppers. It is mainly implemented as a granular form.

EPA has been determined that phorate can warn the human's nervous system resulting in nausea, dizziness, confusion. Moreover, respiratory stroke and fatality cases have been observed at very high exposure levels (e.g., accidents or major spills). Although residues on food alone are not a major level of the EPA's concern, the maximum detected concentrations of phorate and its intermediates (sulfoxide and sulfone) in the groundwater show a little higher grades than the EPA's Drinking Water Level of Comparison (DWLOC) for chronic drinking water exposure (EPA, 2001).

Advanced oxidation processes (AOPs) are recently one of the outstanding methods for pesticide removal from aqueous media. Various technologies are used within AOPs, showing high performance in water and wastewater remediation. For the organic's removal, the processes are based on the generation of radical groups (e.g., $H\bullet$, $O_2^-\bullet$, $O_3^-\bullet$, $OH\bullet$) which degrade or mineralize the targeted pollutant by oxidizing into CO_2, H_2O and inorganics. Besides radical based degradation, some of the other AOPs (i.e., electrochemical, UV/H_2O_2 photolysis, Fenton-like, plasma, gamma irradiation, sulfate-based catalyst, sonolysis and ozonation technology) are also referred methods for the OPPs removal (Malakootian et al., 2020). Recently, biochar

application in the AOPs gained attention in connection with its tendency to be modified and ability to take part in both adsorption and catalytic degradation. Biochar has a versatile structure and stable carbonaceous composition, which enable easily adjustable physicochemical properties. Its benefits are exploited for the removal of emerging contaminants (ECs) from water and wastewater. It is commonly produced by the pyrolysis method, which promotes greater conductivity, larger surface area, various active functionalities and better porous structure in the catalytic mechanisms. Some factors, such as pyrolysis temperature, feed material, pyrolysis atmosphere, reaction pressure, residence time and pre-post treatments, have an impact on the formation of biochar and its efficiency on the targeted pollutant. Biochar can be generated from various biomass such as sewage sludge, manure, algae, wood, peanut shell, etc. (Nidheesh et al., 2021). Phorate, as one of the widely used OPPs, were degraded with the use of multiple advanced oxidation techniques. TiO_2/UV photocatalysis (Malakootian et al., 2020), photolytic ozonation (Ku et al., 2007), persulfate activation (P. Zhang et al., 2021), UV/Fenton system (Gandhi et al., 2016) are the foundings of phorate removal by the advanced oxidation techniques in the literature.

Sewage sludge management in wastewater treatment plants is a worldwide problem; therefore, the valorization of this excessive and nourishing source becomes a crucial innovation in pollutant remediation strategies. Sewage sludge-derived biochar showed superior physicochemical properties, rich in nutrients and active functional groups, ability to attract both organic and inorganic compounds, proven performance towards ECs (e.g., heavy metals, pesticides, polycyclic aromatic compounds, polychlorinated biphenyls (PCBs), pharmaceutical products, etc.). Sewage sludge biomass is rich in content with cellulose, lignin, minerals, and N, P, S, O elements (Singh et al., 2020). Particularly, nitrogen load strengthens the organic contaminant penetration ability onto the facial part of biochar. Nitrogen can be either found originally in the feed material or doped externally. Urea and melamine are the most commonly preferred external nitrogen-rich components (Zhonghao Wan et al., 2020a).

In the literature, although there are many studies focused on OPPs removal by the application of biochar (Baharum et al., 2020; Isakovski et al., 2020; Khalid et al., 2020; Varjani et al., 2019; Zhen et al., 2018), little attention was explicitly given to phorate pesticide removal with photocatalytic degradation (R. J. Wu et al., 2010), adsorption (J. P. Chen et al., 2004), bioremediation (Jariyal et al., 2018) and coagulation (Venkatachalapathy et al., 2020). Moreover, no study is available on the subject of phorate removal from aqueous media by using modified biochar materials. Thus, the present study designates to fill this gap in the literature by presenting specific modification techniques on biochar to remove the phorate pesticide from water effectively.

1.2 Aim and Scope of the Study

The aim of the present study is to investigate the efficiency of potassium hydroxide and urea-modified sewage sludge-derived biochar on the removal of phorate as an organophosphorus pesticide from water. Two objectives were determined in this study; the first objective is using potassium hydroxide (KOH) and urea on production characteristics of produced biochar and examining the interfacial chemical behavior towards the organic contaminant. In line with this objective, multiple advanced analytical techniques (i.e., Elemental Analysis, BET analysis, SEM analysis, XPS, XRD spectroscopy, FTIR spectroscopy, TGA, EPR spectroscopy) were used in order to provide an essential basis for the knowledge of surface functionalities and physicochemical properties of produced biochars. The second objective is to determine the effect of reaction parameters on enhanced phorate removal from water using produced sewage sludge biochar-based catalysts. In line with this objective, two stages of batch experiments have been carried out throughout the experimental framework. 1st stage batch removal experiments were based on the standard conditions (i.e., 1 g/L biochar dose in 1 ppm phorate solution under 25 °C) with the use of the raw sewage sludge (Raw SS) and 34 biochars. 2nd stage batch removal experiments were continued with the selective biochars having 100% phorate

removal efficiencies in the 1st stage batch experiments. In the 2nd stage, phorate removal performances were conducted by various temperatures (25, 30, 35 and 40 °C), pH (3, 5, 7, 9 and 11) and biochar doses (0.2, 1, 5 and 15 g/L). In addition to these two stages, reusability experiments were conducted in order to test the stability of the material. Moreover, real wastewater has been utilized in the batch experiment to compare the phorate removal efficiency of biochars with the deionized water. The concentration measurements of batch experiments were analyzed in the High-Performance Liquid Chromatography (HPLC) with the specific method for phorate pesticide. Gas Chromatography-Mass Spectroscopy was performed in order to detect the phorate biochar-based degradation intermediates.

CHAPTER 2

LITERATURE REVIEW

2.1 Overview of emerging organic contaminants

2.1.1 Main types of emerging organic contaminants and their usage

Emerging organic contaminants (EOCs) are compositions that are out of the scope of current regulations. The phrase "emerging" indicates the increasing abundance in the environment. The center of attraction has recently evolved towards EOCs, leaving conventional priority pollutants behind (Dhangar & Kumar, 2020). In aquatic/terrestrial environments, EOCs have mainly anthropogenic origins and release from pharmaceuticals, plasticizers, personal care products (PCPs), endocrine disruptors, pesticides, surfactants, flame retardants, and industrial additives. These synthetic constituents are produced in a vast amount in order to raise preserved food fabrication, sustain the efficient industrial progression, achieve human and animal wellness (García et al., 2020). The agenda of EOCs is updated and expanded over the years. For example, nanocomponents are a notable category for the expanding EOC list (Cebrián, 2010).

2.1.2 Sources and fate of EOCs in the environment

EOCs have been known for their adverse environmental effects and their long period of residence times. Besides the long residence time, they are also investigated considering their human toxicity, bioaccumulation in humans and the environment, eco-toxicity and long-distance transportation (García et al., 2020). The concentration levels of EOCs in aquatic and terrestrial environments continue to increase exponentially. Their detrimental impacts on the environment have inspired

researchers to develop sophisticated tools that reduce and overcome the challenges caused by the rising concentration of EOCs. The interest was shaped around the sources of EOCs in the terrene and marine environment, their fate and likely toxicity on humans and ecology (Dhangar & Kumar, 2020). These compounds' access to the environmental media compose of sewage sludge or wastewater discharges from treatment plants, quiescent vessels, wastes from medical fields, farming enterprises such as manure use, underground domestic and industrial refuse deposition (Lapworth et al., 2012).

EOCs present in aquatic media has been well-contextualized such as surface waters and wastewaters. The wastewaters cause the principal portion of EOCs and so surface waters carry the biggest amount of those constituents. When the variety of EOCs present in the aquatic media is compared, groundwater has a narrower range upon surface and wastewaters. In the groundwater, 10^2 - 10^4 ng/L of ECs were detected containing a substantial amount of endocrine disrupters such as pesticides, pharmaceuticals, caffeine, nicotine, cosmetics, industrial supplements and by-products, food supplements, disinfection by-products, flame retardants, surfactants, hormones and sterols which are all in the EOCs list (Lapworth et al., 2012).

Soil is another major sink of chemicals after they are fully utilized. Those chemical constituents have higher persistence usually become eventually in the soil or sewage sludge or sediment after the passage of the water treatment plant. The EOCs found in the soil environment can be exemplified as BTEX compounds, fuel oil, Polycyclic Aromatic Hydrocarbons (PAHs), nitro-aromatic compounds and Polychlorinated Biphenyls (PCBs). Organic pollution in soil media eventually diminishes biological variety and damaged orderliness belong to soil fauna (Vicent et al., 2013).

In order to debate the fate of EOCs, different environmental sections are examined, such as bulk water, suspended solids, pore water and sediments. Since there is a interaction between environmental media and their quality parameters, assessing fate in aquatic and solid media becomes complicated. However, there is a vast amount of

research study on the fate and transport of EOCs in aquatic ecosystems, sediments and groundwater in the literature (X. Tong et al., 2021).

2.2 Organophosphorus Pesticides as EOCs

2.2.1 Physicochemical properties and uses of OPPs

Artificial organophosphorus constituents can be benefitted as pesticides, plasticizers or air-fuel additives. Pesticides generally occur from artificial sources and the grouping of organic constituents can be classified in four categories: (a) organochlorines, (b) organophosphates, (c) carbamates and pyrethrins, and (d) pyrethroids. OPPs are non-polar, fat-soluble and have a relatively low vapor pressure. By the consideration of the leaving groups, they can be grouped in three divisions: (a) aliphatic, (b) phenyl, and (c) heterocyclic (Gao & Zhu, 2000). Since OPPs have a lower accumulation and retention rate in the environment compared to organochlorine pesticides (OCPs), 38% of overall global pesticides application is composed of OPPs for domestic and industrial pest management. However, OPPs are not being utilized purposive since they barely diminish the intended pests (~0.1%). Therefore, the released portion of applied pesticides creates an enormous range of environmental and health problems. For example, it was approved OPPs create acute poisoning in humans, which results in at least three million instances and almost 200,000 deaths recorded each year (Sarlak et al., 2021).

OPPs are originated from phosphoric, phosphonic, phosphinic or phosphoramidic acids. The chemical composition contains aryl and/or alkyl classes as active parts linked to the phosphorus atom which is in the center. The active sites are bonded by both directly or oxygen or sulfur atom. Aryl group is generally linked to the central phosphorus atom, while the alkyl group is associated with oxygen or sulfur atom. These active sites can be separated via hydrolysis from the central atom (Sarlak et al., 2021). Most of these pesticides are found in liquid form in nature. However, the

solid granule addition is also performed in agricultural activities (Kaushal et al., 2021).

2.2.2 Phorate pesticide

In this study, phorate pesticide was selected as one of the widely used OPPs on crops such as corn, sugar, beets, cotton, brassicas and coffee (Raaij et al., 2003). In the U.S.A., phorate pesticide is under "restricted use" as a use classification with respect to its acute dermal and oral toxicity. Phorate can damage the nervous system resulting in nausea, dizziness, confusion, and high exposures (e.g., accidents or major spills) can lead the respiratory paralysis and death. Acute and chronic dietary risks from phorate leftovers on crops are lower than the US EPA's concern. However, phorate and its metabolites (sulfoxide and sulfone) found in groundwater and surface waters are higher to a degree than the concern level of US EPA. In addition to anthropogenic toxicity, environments are also affected by the use of these chemicals. Phorate use was found as risky to birds, fish, and mammals at high levels. For example, the utilization in the fall period creates a distinct degree of risk since the degradation and downward motion are slow during the winter. Hereby, concentrations of phorate and its metabolites reach a very toxic level in aquatic and soil media in the spring. In aqueous sites, marine livings are affected acutely and chronically due to leaching from land to rivers, streams and coastal areas. Mammals and honey bees are also affected by farming activities (US EPA, 2006). Detailed properties of phorate pesticide are given in Table 2.1.

Table 2.1 Physicochemical properties of phorate pesticide (US EPA, 2006)

Property	Explanation
Common name	Phorate
Chemical name	O, O-diethyl S- (ethylthio)methyl phosphorodithioate
Chemical family	Organophosphate

Table 2.1 (continued)	
Molecular formula	$C_7H_{17}O_2PS_3$
CAS number	298-02-2
Molecular weight	260.38
Boiling point	At 0.1 kPa: 118-120 °C
Melting point	-43.7 °C
Vapor pressure	At 25 °C: 0.09 Pa
Solubility in water	Slightly soluble (at 25 °C: 5 mg/100 mL)
Log $P_{octanol/water}$	3.92
Appearance	Clear, pale yellow mobile liquid
pH range (stabilized)	5<pH<7 (2 years)
pH range (hydrolyzed)	pH<2 or pH>9
Inhalation LC_{50} - Rat	0.06 mg/L (F) 0.011 mg/L
Oral LD_{50} - Rat	3.7 mg/kg (M) 1.4 mg/kg (F)
Dermal LD_{50} - Rat	9.3 mg/kg (M) 3.9 mg/kg (F)
Use	Insecticide, acaricide, nematocide

2.2.3 Pollution status of phorate in the environment

In general, OPPs are supporter auxiliaries in the agricultural need of a continuously growing population. However, the number of OPPs is outrageous and they carry their toxicity to humans and the environment. Their toxicity can diverge to a broad extent with regards to the phosphorus charge and sulfur atom present. Different compositions of OPPs induce various biochemical, physiological actions. The entrance of phorate leftovers is proved via water, soil or air into the human food

chain resulting in fetal abnormalities and deterioration of nerve agents (Q. Chen et al., 2021; Kaushal et al., 2021). The most prominent toxicological action of phorate is the irreversible restriction of the acetylcholinesterase (AChE) enzyme progression, which is well-known as a signal transmission agent in the nerve system. In addition to the pesticide properties, phorate can also be utilized as an herbicide. In the environment, these hazardous compounds are encountered in groundwater channels by leaking into undergrounds, rivers from the outflow of agricultural sites, air by the emission of crop sprays. This situation shows how mobile these pesticides and to what extent humans and the environment are exposed in all peripheral compartments (Kaushal et al., 2021).

2.3   Remediation processes of OPPs/phorate removal

Promising approaches have been evolved in order to ameliorate the organic pollution in environmental compartments. Efficient and fast methods are in concern on the subject of organophosphorus pesticides removal (Vlyssides et al., 2004). In this regard, abiotic and biotic degradation mechanisms are studied for OPPs.

The basic strategy for the removal of OPPs is based on the conversion into non-hazardous forms. It can be performed chemically or mechanically as an abiotic driving force. The logic behind the abiotic degradation is the disruption of the chemical formation of pesticide by the use of abiotic factors, which can be typically found in the environment or an adsorbing material draw out the pesticide on itself (Janos et al., 2014). Many chemicals are available and checked, such as oxidizing agents (i.e. ferrate (VI) and manganese dioxide). Also, catalytic hydrolysis can be performed with the use of metals such as silver. Further, Gama radiation can directly strike the OPPs (Kaushal et al., 2021). Activated carbon application stands as a straightforward and efficient abiotic technique for the removal of OPPs from water. In the study of Banerjee & Kumar (2002), the adsorption of acephate by the addition of optimum 85 g/L granular activated carbon (GAC) at initial pesticide concentration of 2.9 mg/L and almost 100% removal of acephate was achieved. Another OPP

12

removal experiment was conducted by W. Ling et al. (2011) on omethoate pesticide by 20 mg/L Fe(III)-loaded activated carbon catalyst and pristine iron loaded AC could only remove pesticide by 10%. However, chlorination significantly enhanced the removal efficiency by promoting the •OH radical generation up to 82.4%. In the study of Beckinghausen et al. (2020), sewage sludge-derived biochar ammonia adsorption performance were compared with the performance of activated carbon. It has been mentioned that sewage sludge-derived biochar had shown comparable theoretical ammonia adsorption capacities with the regular activated carbon, but experimentally it was at a lower state. In the case of phorate removal, Venkatachalapathy et al. (2020) investigated different clarifiers such as AC, gelatin, casein, bentonite and chitosan in 0.05% concentration for 1, 2 and 4 h periods. As a result of this study, AC and chitosan have been shown the best removal efficiencies for 200 μg/kg pesticide and they were increasing with the residence time. While the AC showed 52% removal from the initial pesticide concentration, chitosan removed 63% of phorate.

Applied pesticides on crops can leak and compile in the farming land. The soil bacterial community and their generated enzymes can be a promising way of degrading the OPPs (Abraham et al., 2014). In the biotic degradation experiments, the application of multiple bacterial communities into multiple OPPs contaminated sites unveiled that multiple functioning biodegradation processes can result in the generation of organic acids such as formic acid or acetic acid, which is a valuable product for other operations (Kaushal et al., 2021). Metal-organic frameworks (MOFs), which are compositions including metal ions or clusters linked to organic ligands, can also be an auxiliary since they form crystalline non-porous compounds for adsorption. Microbial performance in soils has been approved as the most efficient and important reason for OPPs degradation (Kaushal et al., 2021; Pailan et al., 2015). Microbial decontamination becomes as an emerging biotic degradation experiment on OPPs regarding to its efficiency, safety, cost and ecological approach. Bioremediation is a prominent biotechnological technique for the decontamination of polluted environments and biostimulation, biosparging, bioaugmentation are the

examples applied in the bioremediation studies. As an example, degradation capability of probiotic microorganisms, which are categorized under safe microorganisms, has been declared as well linked with the pesticides. Variety in responsiveness to stimuli of different OPPs against probiotic microorganisms can be arisen from various physicochemical properties such as structure, insolubility in water, volatility of and environmental properties such as moisture, temperature, pH, light and type of medium (Sarlak et al., 2021). In the case of phorate pesticide, *L. plantarum strains* (Changkun Li et al., 2018), *S. thermophilus* and *L. helveticus* (Zhao et al., 2012) showed an observable degradation as probiotic microorganisms. Phosphodithioate sulfoxide and phosphodithioate sulfone are the resulted biodegradation products of phorate. However, they can diverge both with the nature of microflora as well as environmental conditions and end up with various degradation products (Henderson et al., 2004; Szeto et al., 1990).

2.4   Biochar as an emerging catalyst to remove OPPs/phorate

Recently, bio-wastes generated from residential, gardening or agricultural activities have become the most prominent waste production capacity worldwide. In 2017, it was stated that the European Union (EU) produced 144 kilotons of oil-based bio-waste with various contributors. More than 60% of produced bio-waste was incinerated and approximately 10% was used in the bio-gas generation. Bio-diesel was another output of this valorization methodology by 12%, contributing to 76% bio-diesel, 17% bio-ethanol, 7% other bio-gas types. The rest of the biological waste (<10%) was sent to landfilling or composting sites (Flach et al., 2019).

Wastes from agricultural activities are mostly composted or incinerated in open fields, which release greenhouse gases to the atmosphere (i.e., CO_2, CH_4, and N_2O) and gases hazardous for the atmosphere (i.e., H_2S, SO_2, and NH_3). Moreover, these techniques lessen the waste quality, which can be used for further applications. Biochar material is one of these bio-waste valorization applications which is generated by various thermochemical operations resulting in a large amount of

production, applicability in a broad range and obtainment from a wide variety of feedstock (Dunnigan et al., 2018; Xiao Yang et al., 2018). Biochar applications can vary from wastewater and soil remediation to agricultural fertilizer by keeping nutrients on hold or support a circular economy. It is also a beneficial contributor for the climate change mitigation activities by carbon sequestration and carbon emission decrease (Y. Zhou et al., 2021).

2.4.1   Biochar production mechanisms

Thermochemical techniques are commonly applied in biochar production. They consist of pyrolysis, hydrothermal carbonization, gasification and torrefaction (Y. Lin et al., 2016). The type of feedstock and thermochemical operational parameters can be adjusted for desired quality and yield of application. These operational factors can be exemplified as temperature, heating rate, and residence time, along with reaction pressure, gas atmosphere and flow rate (Yaashikaa et al., 2020). Among them, the temperature is the most influential operating parameter affecting the pyrolysis yield. In common sense, the amount of generated biochar reduces and syngas formation enhances by the rise in pyrolysis temperature (Wei et al., 2019).

Pyrolysis is performed under oxygen-free ambient at a broad range of temperature values (200-900 °C). At the end of pyrolysis operation, valuable by-products are obtained as biochar, bio-oil and syngas. Syngas is comprised of CO_2, CO, and H_2. Pyrolysis is carried out in the reactors such as split-type tube furnace, fixed-bed reactors, fluidized-bed reactors, auger-screw reactors, and indirect-fired rotatory kilns. There are fast and slow pyrolysis characterization with respect to pyrolysis temperature, heating rate, residence time and pressure. While the fast pyrolysis is performed under a high heating rate (>100 °C/min), low residence time (0.5-2 s), and high temperature (400-600 °C), resulting in high quality and yield of bio-oil; slow pyrolysis is carried out under low heating rate (5-7 °C/min), high residence time (>1 h) and low temperature (200-400 °C) generating a high biochar yield (Yaashikaa et al., 2020).

Hydrothermal carbonization is a comparatively cheap operation since the temperature needs to reach to 180−250 °C (J. Lee et al., 2018). Differently from biochar, the output is named hydrothermally treated biochar due to its production conditions (Fang et al., 2018). The feed material is mixed with water before the carbonization experiment and the time interval can be longer than pyrolysis by rising the temperature slowly in order to keep the stability. Diversified outputs can be obtained under various temperatures: hydrothermally treated biochar produced at lower than 250 °C is known as hydrothermal carbonization, bio-oil generated at 250-400 °C is called hydrothermal liquefaction and syngas formed at higher temperatures (>400 °C) is noted as hydrothermal gasification (Safaei Khorram et al., 2016). Condensation, polymerization and dehydration inside the molecule are carried out in the production of hydrothermally treated biochar (Yaashikaa et al., 2020).

Gasification is the thermochemical conversion of carbonaceous bio-wastes into gaseous outputs such as syngas. It can be grouped in two stages: (a) drying and (b) oxidation/combustion. Syngas generation is highly dependent on the gasification temperature. For example, when the operating temperature rises, CO and H_2 release enhance. However, CH_4, CO_2, and hydrocarbons were observed to be declined (Prabakar et al., 2018).

Torrefaction/hydrothermal treatment is a relatively recent technique among other biochar production mechanisms. It is performed under a low heating rate (<50°C/min) and oxygen-free environment at moderate temperatures (200-300 °C). There are various torrefaction operations such as steam torrefaction, wet torrefaction and oxidative torrefaction. It can be stated as incompleted pyrolysis since its residence time takes approximately 30 min. Different stages are included in the torrefaction process, such as pre- and post-heating, drying, torrefaction and cooling (Yaashikaa et al., 2020).

2.4.2 Biochar modifications

Regular biochar materials have outstanding efficient characteristics, but physical and chemical modification techniques enhance their features adjusted to be used in particular applications (Zhuang et al., 2021). The examples for modification techniques can be given as alkaline execution, acid execution, sulfur or nitrogen addition and physical activities. Among them, alkalinity and polarity improvement has been observed with the nitrogen addition; surface area and porosity enlargement have been seen with the physical modification methods. These enhanced characteristics lead to be an advanced soil compost, electrochemical compound, catalyst and adsorbent (Y. Zhou et al., 2021).

Modification strategies are applied to biochar materials in order to upgrade the performance in certain practices. Physical modification activities performed by steam, thermal, or plasma increase the biochar's specific surface area and pore volume while removing volatile organic compounds and inserting new functionalities (Sajjadi et al., 2019). Acid application performed both as pre- & post-qualification by the use of H_3PO_4, HCl in order to contribute oxygen-based functionalities into biochar. The acid application also enhances the surface area and pore structure while removing the impurities and forming carboxylic forms (Sizmur et al., 2017). Alkaline modification is performed both as pre- & post-qualification by the use of KOH, NaOH in order to contribute oxygen-based functionalities into biochar. The alkaline application produces hydroxyl forms to biochar surface while lessening the polarity due to positively charged compositions (Xue Yang et al., 2019). On the other side, nitrogenation escalates the alkalinity and polarity while adding nitrogen-based functionalities onto biochar. Various types of nitrogen sources can be utilized, such as ammonia, urea, melamine. In the nitrogenation experiments, it was observed that ammonia modification adds amine groups, urea modification adds pyridinic groups and melamine adds graphitic groups (Zhonghao Wan et al., 2020a). Sulfuration was performed both as pre- & post-qualification by the use of H_2S, fuming H_2SO_4 in order to contribute sulfur-based functionalities into

biochar (Sajjadi et al., 2019). Compositing is another common method in chemical modifications, which is performed both as pre- & post-qualification by the use of metal salts, Fe^{3+}/Fe^{2+}, functional materials in order to produce biochar composites. This technique adds metal oxides, magnetic iron oxides, nZVI by supporting its magnetic properties (W. H. Huang et al., 2021).

2.4.3 Biochar characteristics

Various operating conditions create an alteration in the physicochemical characteristics of biochar (Y. Zhou et al., 2021). In this section, the physical and chemical characteristics of biochar are explained and the effects of feed material or operational conditions on these physicochemical properties are discussed.

Physical characteristics have sub-divisions as density and porosity, specific surface area, pore size and volume distribution, mechanical stability. Density and porosity are highly linked with the feedstock material, applied pre-modification method and operational conditions. Thus, if the desire is to have a greater density and porosity in the biochar, the type of feed material, operational conditions and pre- & post-modification techniques must be adjusted according to that. For example, chemical activation is highly preferred due to its promising results and H_3PO_4 treatment created comparatively improved micro porosity than the conventional biochar. The adsorption efficiency of biochar mostly counts on the active functional groups on the surface and porosity (X. J. Lee et al., 2017; Y. Zhou et al., 2021). Another important physical characteristic of biochar is the surface area and biochar material is rich in specific surface area. Determination is commonly done by the analysis of Brunauer–Emmett–Teller (BET). In common sense, the specific surface area develops with the increasing carbonization temperature and the application of CO_2 further enhances the surface area formation. Biochar with a high specific surface area and pore volume applied in soil improves its water holding capacity and nutrient penetration (Shareef & Zhao, 2017). The leading characteristic of holding water and gases is the biochar pore size and pore volume distribution, even if they are rich in specific surface area.

Pore sizes differ in three options: micropores (0.0001-0.05 μm), moderate-sized pores (0.002-0.05 μm) and macro pores (0.05-1000 μm). The sum of pore volumes in biochar rises with the increasing carbonization temperature. Treated biochars have a quite high amount of micropores (>80%) compared to conventional biochar (<10%) (Weber & Quicker, 2018). Density is the base for mechanical stability. Dominant lignin composition and dense feed materials are the factors of forming a stabilized biochar. The decline in the hydrophilic oxygen-containing functional groups, oxygen-carbon (O/C) and hydrogen-carbon (H/C) ratios in biochar are highly influential for the stability as the heating temperature increases (Weber & Quicker, 2018; Y. Zhou et al., 2021).

Chemical characteristics have sub-divisions as elemental composition, pH and electrical conductivity (EC), cation exchange capacity (CEC). The elemental composition of biochar is comprised of volatile (i.e., aliphatic) and non-volatile (i.e., aromatic) parts. The carbon atom in the biochar is high, while the oxygen atom is low. Amount of carbon atom increments and OH^- declines through the carbonization operation. The most prominent alteration in the elemental composition appears between 200-400 °C. Carbon and oxygen capacity at great temperatures rise up to >95% and <5%, respectively. While the hydrogen capacity is between 5-7%, during the carbonization (>700 °C), it decreases even lower than 2% (Y. Zhou et al., 2021). Mostly pH of biological feed materials is between 5-7. Carbonization operation can diminish the acidic surface-active classes (i.e., carbonyl, hydroxyl, carboxyl) due to their weaker linkages and result in an alkaline pH. Temperature becomes a prominent factor in the pH adjustment (S. Li et al., 2018). The alkalinity of pH grows into a very beneficial factor in the acidic soil because of the heavy use of nitrogen-based fertilizers in agriculture. In this case, the biochar application stabilizes and buffers the soil pH, while decreasing CO_2 and N_2O release from acidified soils. Electrical conductivity (EC) escalates by the rise in heating temperature since the volatile contents in the biochar are destroyed, cation exchange capacity (CEC) boosts by the replaceable ions and rise in nutrient content (D. Wu et al., 2018). The surface of biochar is mostly negatively charged, which has a high tendency through cations.

Biochar is rich in minerals such as K, Ca, Na, and Mg and this eases up the CEC. A low level of CEC leads to acidic soil pH (Teutscherova et al., 2017; Y. Zhou et al., 2021).

2.4.4   Role of biochar surface functionalities in remediation

Biochar has fundamental surface functionalities, such as carboxyl (−COOH), phenol (−OH), pyridine and amine. Feedstock type and heating temperature are the major parameters in the formation and alteration of surface functionalities. The change in surface-active groups are not predictable because the surface functionalities can decrease while pH, specific surface area and porosity increment. The surface-active forms are characterized by various advanced types of equipment such as Fourier Transformed Infrared Spectroscopy (FTIR), X-ray Photoelectron Spectroscopy (XPS), and Near-edge X-ray Absorption Fine Structure Spectroscopy (NEXAFS) (Yaashikaa et al., 2020). Selected feed material, applied pre- & post-modification techniques, carried out operational carbonization conditions acquire diversified surface-active forms which have a high impact on biochar's adsorption performance. The categorization of biochar surface functional groups with respect to their major central atom can be done in three ways: oxygen-, nitrogen-, and sulfur-based forms. Among them, oxygen-based forms are the most prevailing groups of biochar surface functionalities. The oxidative modification is stated as a remarkable adsorption ability developing technique (Xueyang Zhang et al., 2019). On the other hand, nitrogen-based functionalities are a great cause for the increase in surface polarity. This creates a well-behaved link in the cooperation of contaminants and polar biochar. Besides, sulfur-based functionalities affect the biochar's surface area and porosity which are linked with the adsorption efficiency. The composition, polarity and hydrophilicity/hydrophobicity of biochar materials are significant factors in the remediation processes. Structural and chemical composition of surface functional groups reveal that present positive and negative surface charges are used as a signal

to predict the electron-donating and accepting capacity of biochar. Further, the quantity of charges strengthens the electrostatic synergies (X. F. Tan et al., 2021).

2.5   Biochar-mediated nitrogen functionalities

2.5.1   Types of nitrogen functional groups in biochar

Nitrogen is found as linked to oxygen or carbon atoms in biochar. Since carbon and nitrogen are placed juxtaposed to each other in the periodic table, they demonstrate complementary characteristics and can collaborate without difficulty. Nitrogen addition to the carbonic structure still provides an abundant carbon complex but also distinct nitrogen active parts (Saha & Kienbaum, 2019). As a result of the single and multiple bonding configurations between C and N atoms, 5- and 6-numbered rings are created as heterochains. Organic and inorganic nitrogen-containing components are two kinds of nitrogen classes in biochar. Inorganic nitrogen compositions are made up of ammonium (NH_4-N), nitrite (NO_2-N), and nitrate (NO_3-N) (Leng et al., 2019). The aforementioned forms can be promoted by organic species in the environment or they can be often transformed into several heterochains. Organic N-functional groups, generated from protein structure or from the relation of biomass or external nitrogen-rich compounds, are already in the shape of multiple heterocyclic rings. They undergo various interactions such as straight cycling and duplication reagents or removal of water, hydrogen or amine groups (Leng et al., 2019). Subsequent to the pyrolysis process, quaternary, pyridinic oxide, pyrrolic and pyridinic types of nitrogen primarily remain due to their higher persistency among other organic nitrogen active forms (W. Chen et al., 2017; Leng et al., 2019a). Nitrogenous components addition into biochar can be classified under two main methods; intrinsic nitrogen source from the feedstock and extrinsic nitrogen source due to the contributors and ammonia degreasing activities (Zhonghao Wan et al., 2020a).

2.5.2   Formation mechanism of nitrogen functional groups in biochar

The formation mechanism of nitrogen-containing surface-active groups in biochar materials can be achieved by intrinsic, extrinsic or co-doping methods, which are further discussed in this chapter. Since biochar production is based on the thermochemical conversion of feed materials, this conversion becomes a driving force to generate the nitrogen surface active components. Formations of various N-functional groups in biochar during the thermochemical conversion process are shown in Figure 2.1.
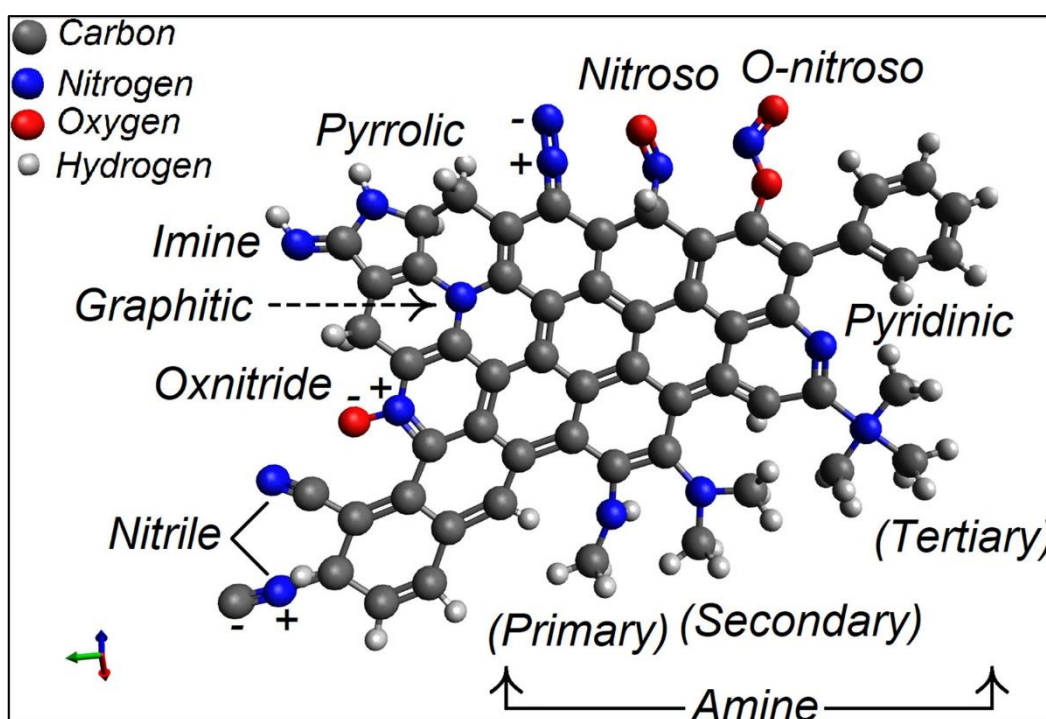
Figure 2.1. Formation of N-functional groups in biochar during the thermochemical conversion process (Başer et al., 2021)

2.5.2.1   Intrinsic N-doping from biomass feedstock

Type of feedstock and the nitrogen content in this raw material gain importance for the internal nitrogen doping technique. As such, biomass such as algae (especially cyanobacteria), microorganisms, and animal tissues assures a high nitrogen load

level transferred into biochar (Zhonghao Wan et al., 2020a). It can be deduced that the choice of biomass becomes as a decisive tool for the maintenance of nitrogen content in biochar and its catalytic activity. Among N-functional groups, it is suggested that the planar pyridinic-N and pyrrolic-N content courage the catalytic performance (X. Zhou et al., 2021).

2.5.2.2   Extrinsic N-doping from the contributors

The external N-dopants can be selected from the inorganic nitrogen origins such as NH_3, NH_4^+ salts, NHO_3 and organic nitrogen origins such as urea (CH_4N_2O), aniline ($C_6H_5NH_2$), and melamine ($C_3H_6N_6$). The addition of nitrogen from an external source requires forming a suitable artificial medium (Z. Lin et al., 2012; Zhu et al., 2018). Various molecular structures and chemical textures cause a distinction among the final biochar conformation when they are coupled with different operating parameters. Present oxygen functional groups level in the feedstock firmly relates to the amount of nitrogen in biochar since the oxygen functionality supports the bond formation with N-initiators under thermal conditions (Duan et al., 2018; Zhonghao Wan et al., 2020a).

Degreasing ammonia is one of the N-doping methods by supplying NH_3 for the reaction with the carbonaceous structures in biochar under high-temperature conditions. However, the introduction of ammonia mainly drives partial N-doping such as the existence of aminated components. Mian et al. (2020) and Chen et al. (2016) describe the potential N-doping mechanisms. In, present –OH plays a critical role in the formation of amino components (R-NH_2) under elevated temperatures. Imported amino components react with –OH for the purpose of producing –C=N functionality in Equation 2-2. The reaction of NH3 and carbonyl (X-C=O) parts by the Maillard cooperation producing hydrogen monohydride (H_2) is illustrated in Equation 2-3.

$$R - OH + NH_3 \rightarrow R - NH_2 + H_2O \qquad\qquad \text{Equation 2-1}$$

$$R - NH_2 + R - OH \rightarrow R - N = R + H_2O \qquad\qquad \text{Equation 2-2}$$

$$(C)biomass + NH_3 \rightarrow C - NH_2 + C - NH + H_2 \qquad\qquad \text{Equation 2-3}$$
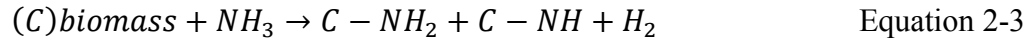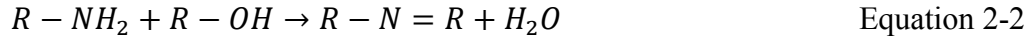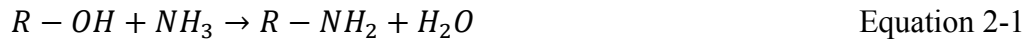
Carboxyl groups on biochar are advantageous for creating a hydrogen bond with NH_3, which supports transformation toward the pyridinic and graphitic type of nitrogen. Hence, the contributory impact of ammonia degreasing associated with oxygen functional group consumption is to enhance the microporous nature of biochar (Zhonghao Wan et al., 2020a; W. Yu et al., 2018).

Ammonium salts are a more cost-efficient source of external nitrogen, which gains importance in the gas degreasing process and feedstock solid-gas interface. In the study of Zhu et al. (2018), a herb in a marshland as a feedstock and an external nitrogen supply (ammonium nitrate) are carried through the solvent evaporation in order to obtain homogenously dispersed N-source on biomass. The acquired composite is strengthened under a temperature of 900 °C to form a nitrogen-loaded carbon-based composite having a notable graphitic-N portion (67 at. % of all nitrogen amounts). NH_4NO_3 (ammonium nitrate) is noted as an executive function to enhance the porous structure and reducing N-doping medium concurrently emits NH_3, N_2, or N_2O in the thermal decomposition process. The nitrogen-doping method with ammonia degreasing activity under various temperature stages during pyrolysis is presented in Figure 2.2.
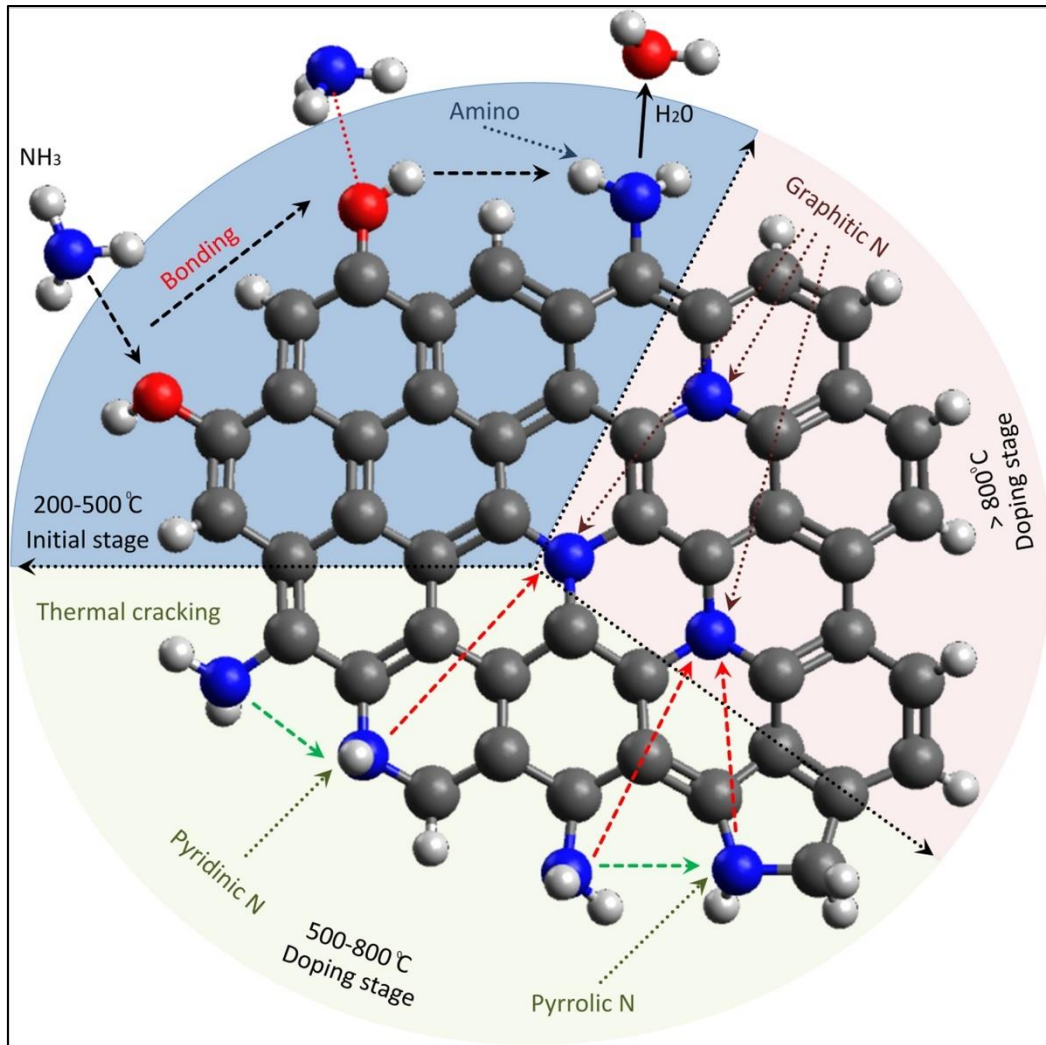
Figure 2.2. Nitrogen-doping method with ammonia degreasing activity under various temperature stages during pyrolysis (Başer et al., 2021)

Nitrogenous organic additives are the most frequently used precursors to dope biochar with nitrogen because of their ease of operation. Urea stands as a pervasive matrix with the presence of both nitrogen and carbon elements among the nitrogenous organic additives. The homogeneity of resultant N-doped biochar can also be achieved by the penetration of dissolved urea into raw feedstock (Zhonghao Wan et al., 2020a). Oh et al. (2018) investigated the interaction of lignocellulosic wasted coffee sediments with urea for the purpose of forming N-doped biochar

throughout the mixing and pyrolysis (1000°C) processes. The mass ratio of feedstock to urea was recorded as 1:5. Ding et al. (2020) selected 2 g of rice hay and 0.75 g dissolved urea in 80 mL water to be carried out in 1000 °C pyrolysis. The mass ratio of feedstock to urea was noted as 2:0.75. However, the reaction temperature becomes a critical and sensitive parameter when the matter is organic ingredients because organic nitrogenous compounds such as urea, aniline or melamine can be transformed into various intermediate molecules under specific temperatures (Zhonghao Wan et al., 2020a). It is stated that urea can break down into intermediate molecules through poly-condensation steps such as cyanuric acid and melamine. Carbon nitride is one of the potential formations at the initial state of pyrolysis at 300 °C with different aminated components on biochar structure such as $-NH_2$, $N - H$, $C - N$. These aminated components are broken and fused into carbonized biomass lattice creating further N-based compositions at elevated temperatures above 400 °C such as pyrolytic, pyridinic, and graphitic types of nitrogen. When the provided heat is brought higher than 700 °C, some portion of graphitic type of nitrogen is able to survive (Oh et al., 2018). On the other hand, melamine follows different steps forming different intermediate molecules (Y. Wang et al., 2019). Indeed, organic additives demand various temperatures to break down, nitrogen sources perform in a characteristic range. For example, pyridinic and pyrrolic types of nitrogen prevail when the heat is lower (<700 °C) and graphitic nitrogen outcompetes by temperatures more than 800 °C. The Source of nitrogen is one of the factors that govern the total nitrogen level in the resultant biochar. Besides, the retention time slightly impacts on the N-bond configuration and this feature differs from NH_3 degreasing activity or NH_4^+ salts energizing. The operational parameters would facilitate the organic supplements to fuse nitrogen functionality into the carbon complex with poly-condensation and co-polymerization processes (Oh et al., 2018; Zhonghao Wan et al., 2020a).

2.5.2.3   Co-doping methods

Duan et al.(2015) suggested that doping a heteroatom such as S, B, P or I inside of the carbonaceous material is a barren technique for carbon-based catalysis (Duan et al., 2015). However, researchers pay particular attention to the co-doping methods with a heteroatom to adjust the physicochemical characteristics of nitrogen-enriched biochar due to its enhanced reactiveness to influence bond compositions positively.

Alternating electrochemical properties of different heteroatoms (i.e., atomic radius, orbitals, electronegativity, electron density) can govern the nature of N-doped biochar and its application areas (Zhonghao Wan et al., 2020a). To set an example, single nitrogen doping to biochar can hold onto defective parts and oxygen functional groups, and the logic it brings is advanced porosity, high alkalinity, high electron density, disturbed electron circulation for the generation of a dipole moment, battle to oxidize and medium without metal atoms. Single N-doped biochar is feasible in adsorption, oxygen oxidation mechanism, activation of PMS/PDS, and electrochemical degradation activities (Ho et al., 2019; Oh et al., 2018; Zaeni et al., 2020).

Doping nitrogen with a heteroatom of boron is another technique which links only the defective parts on biochar. Chen et al. (2019) achieved co-doping of boron with nitrogen on graphene with the purpose of producing a very efficient catalyst and the addition of boron brought high reactivity of boron-carbon-nitrogen attachment composition and developed graphitization level, also restrained oxidative corrosion. The importance of B-C-N attachment composition arises from the tendency of boron to readily counterbalance the singular electrons of nitrogen additives, forming a deficiency in electron configuration. While the most active configuration of B-C-N attachment is when the boron is positioned as meta with nitrogen, hexagonal boron nitride (h-BN; *graphitic boron nitride*), which is the most stable crystalline version, is stated as chemically inactive and inhibitory for the carbo-catalysis (X. K. Ma et al., 2011). However, Wan et al.(2020) mentioned that there is a need for further study on biochar in the field of adding N and B for a potential application.

Co-doping nitrogen with sulfur (S) can associate via defective parts and oxygen functional groups similar with single N-doping. Ma et al. (2019) stated that a small amount of co-doping S (1.04 at. %) with nitrogen derived from human hair significantly impacted the electrochemical carbo-catalysis of biochar. Almost similar electronegativity of carbon (χ_s = 2.58) and sulfur (χ_c = 2.55) atoms creates an apparent spin-based activity instead of a charge-based movement that is in the single N-doping (Ortiz-Medina et al., 2019). Yet, Ding et al. (2020) argued the negative impact of S-doping on the catalytic activity of nitrogen biochar functionality, asserting current researches about the heteroatom injection technology onto biochar stands at an insufficient level and demands more legibility.

The addition of metal atoms with high electron densities in co-doping method is joined with the oxygen functional groups. In this regard, a stable metallic state has to be managed with Metal-N-C or Metal-O-C bond compositions in order to enhance the electrochemical state in the active medium (Zhonghao Wan et al., 2020a).

2.5.3 Factors affecting the formation of nitrogen functionalities

2.5.3.1 Feedstock materials

A raw biomass feedstock is a critical parameter affecting the physical/chemical characteristics of biochar in terms of its functionality. There is a direct relationship between the nitrogen content of feed material and the functional characteristics of biochar (Leng et al., 2019a). Pyrolysis temperature and type of feed material are two major parameters having an impact on the surface area, surface-active groups, hydrophilicity, stable nature, zeta potential and pH of biochar. Optimization studies are achieved with the arrangement of these factors to select the most goal-oriented technique (Hassan et al., 2020). It is possible to generate biochar by using diversified sources, including crop and forest residues, wood chip, algae, sewage sludge manures, organic municipal solid wastes (Xiang et al., 2020). However, not the entire nitrogenous feed sources show the same capacity to generate the biochar nitrogen.

The selection of feed material becomes crucial for the intrinsic nitrogen addition into biochar which has been discussed previously. Protein nitrogen, such as amide (R1NR2)- group-containing amino acid arginine, can featly generate NH3 and other gases during pyrolysis (Leng et al., 2019a). Among the sources, microalgae are approved to have a high amount of nitrogen content and thus, the biochar produced from microalgae gets a greater nitrogen load compared to other feedstock types. Microalgae contain a significant amount of pyrrolic and pyridinic types of nitrogen (13.94%), also these functional groups are converted into C–N–C, pyrroline, pyridine, quaternary nitrogen (6.57-12.93%) found in biochar (Leng et al., 2019). Sewage sludge and animal manure are other types of biomass having a high nitrogen content due to their polyacrylamide content and therefore promote a more interactive region for electrostatic cooperation (Zhonghao Wan et al., 2020a).

2.5.3.2   Carbonization processes

Slow and fast pyrolysis are conventionally performed techniques in biochar production and are affected by a heating rate, residence time, and temperature. Besides, flash carbonization and gasification are certain thermochemical operations referred to as pyrolysis alternatives. Biochar can be classified as a co-product in these processes, along with biofuel. Biochar quality and functionality are highly contingent on the noted carbonization process in line with its operating parameters (Manyà, 2012). While slow pyrolysis treated biomass favors the solid (biochar) portion by 35 wt. % and fast pyrolysis employed biomass forms 70 wt. % of the liquid (biofuel) portion, gasification yields 85 wt. % of gaseous (biogas) fraction (Mohan et al., 2014). Electrical and microwave-assisted heating pyrolyses are also carried out for carbonization purposes. Conventional electric heating decelerates the heating rate, which provides an effective means for the thermal gradient in a raw (biomass) feedstock. The importance of controlling the thermal gradient arises from the release of pyrolysis gases creating irregular microstructure and off-grade product quality. In general, the thermochemical process decreases the nitrogen functionalities

content in biochar. While higher temperatures (≥600 °C) courage greater pH, stable nature, recalcitrance and heating value of biochar; biochars generated under low temperatures (≤400 °C) yield larger mass, energy production, volatile matter and diversified surface functional groups. Therefore, it can be said that slow pyrolysis provides more biochar yield, which is rich in surface functional groups compared to fast pyrolysis and gasification (Ghodake et al., 2021). On the other hand, microwave heating is a promising alternative to conventional electric heating because it supports chemical reactions by providing heat for the reactants, strong vibration and breakup of chemical bonds, and improving thermo-chemical processes, which positively affect the structural deficiency in biochar. Indeed, there is a demerit in terms of mass production of biochar through microwave-assisted pyrolysis of biomass. Nonetheless, the microwave heating method currently gains more consideration for porous carbon development, such as activated carbon (Zeqing Wan & Li, 2018). Synthesize of N/O-enriched microwave heated porous carbon is experienced by Wan and Li (2018) and it is claimed that; i) it has more C/O deficiency, which positively influences the active sites for N/O introduction, ii) microwave heating based porous carbon has more potential to simultaneously introduce N/O components by electrophilic aromatic substitutions simultaneously.

2.5.3.3   Operating parameters

In the carbonization process, certain factors influence the quality and yield of biochar that include: temperature, heating rate, and residence time (that are readily regulated operating parameters), along with reaction pressure, gas atmosphere and flow rate (Xuanmin Yang et al., 2020).

As the heat of the carbonization process increases, the ash content also simultaneously increases, followed by a decrease in the N-load in biochar due to the loss of some portion of nitrogen. It is reported that pyrolysis of *chlorella* algae feedstock at 600 and 900 °C corresponds to 12.93 and 6.57% nitrogen content, respectively, indicating the loss of N at a higher temperature. Carbonization

temperature also impacts the N-functional group formation because it causes the breakage of chemical bonds and their impacts on biochar functionality. Higher temperatures derived biochar tends to be more stable despite the existing unstable components. Apart from that, double bonds are converted into single bonds or rings and create more stable complexities (Leng et al., 2019a).

In general, CO_2 and N_2 atmospheres are applied for thermochemical conversion of bio-feedstock to produce biochar. The doping method with nitrogen-containing compounds such as NH_3 is referred to create N-functionality on the biochar surface. Excluding NH_3, provided gas atmosphere slightly impacts the amount and kind of nitrogen functional groups of biochar at higher temperatures (800 °C). Nevertheless, at lower carbonization temperatures, less than 400 °C, the carbonization process contributes a diversified range of N-functional groups and nitrogen content. The inorganic type of nitrogen, such as NH_4-N, is more efficient for doping purposes under the CO_2 atmosphere instead of N_2 air at lower temperatures (Leng et al., 2019a; Yuan et al., 2018). The nitrogen content under NH_3 atmosphere and different temperatures are monitored by Zhang et al. (2014) and Lian et al. (2016); it is demonstrated the nitrogen content becomes more than that in CO_2 and N_2 supplied air. Yet, the CO_2 atmosphere also provides beneficial effects for the generation of N-functional on biochar. The formation of amino acids-N (amide-N) is achieved by the relation of CO_2 for the primary (R-NH_2), secondary (2R–NH) and tertiary amines (3R–N) (Leng et al., 2019a).

Pyrolysis pressure has a negligible impact on the nitrogen content of biochar. In reference to carbonization temperature, the trend of nitrogenous species formation remains almost stable, showing a slight increasing and then decreasing trend. Pressure indicates an influential property on the forms of nitrogen functionalities. More significant amounts of exogenous nitrogen bring along the polymerization and ring condensation of nitrogen functionalities to evolve more stable nitrogenous parts. High pressures combined with the high temperatures improve the conversion of pyrrolic-N structure to pyridinic-N and quaternary-N structures (Leng et al., 2019a; Maliutina et al., 2018b). However, an excessive amount of pressure supply causes

the gasification of some nitrogen groups, yielding HCN and NH_3 and thus decreasing the N amount in biochar composition (Leng et al., 2019a; J. Yu et al., 2018). Nonetheless, pyrolysis of biomass under a pressurized condition is beneficial to collect the combustible gases (syngas) in that transporting syngas required a pressurized vessel.

When the impact of the rise in the residence pyrolysis time coincides with the high carbonization temperature, this favors the decomposition and loss of nitrogen species. On the contrary, lower carbonization temperatures increase biochar N-load with the rise of the exposure time period. It is noted that the level of breakdown of inorganic nitrogen-containing parts (ammonia-N and nitrates-N/nitrites-N) proceed under 200 °C, nitriles under 250 °C, amides under 400 °C, pyrrolic and pyridinic type of nitrogen under 500 °C temperature (W. Chen et al., 2017; Leng et al., 2019a). The logic behind the decrease in nitrogenous species in biochar due to thermal conversion relies on the fact that the breakdown of nitrogen functionalities and the deficit of unstable (volatile) constituents. The impact of residence time on the nitrogen functional groups can fluctuate with different temperatures. This issue has been explored by Chellappan et al. (2018), by preparing biochar at a carbonization temperature of 400 °C. When the time of exposure was increased from 1 h to 4 h, the nitrogen content increased from 0.56 to 0.64%. On the contrary, at the carbonization temperature at 600 °C, when the identical conditions were maintained, the nitrogen content decreased from 0.71 to 0.65% (Chellappan et al., 2018).

Other parameters can be exemplified as heating and air supply rates, which influence the amount of nitrogen in the biochar. It is investigated that the rise in heating rate from 1 to 10 °C min^{-1} favors the biochar nitrogen load, increasing from 0.41 to 0.57%, respectively. The increase in the air supply rate from 0.0012 to 0.012 m^3 h^{-1} influences the nitrogenous components, first positively from 0.57 to 0.89% and then negatively to 0.66% (Abbas et al., 2018; Leng et al., 2019a).

2.5.3.4   Influence of pre- & post- treatments

Pre-treated feedstock materials and post-treated biochar are strongly interlinked with the physicochemical characteristics of biochar. Applied pre-/post-modification methods can be altered concerning the type of feed source and the intentional application area. The pre-treatments can be grouped into three physical, chemical, and biological methods. Crumbling and washing/drying processes have pre-physical induced effects on biochar's properties; external functionality enrichment operations change biochar composition chemically, while the application of microorganisms encounters biological pre-treatment through nitrification. On the other hand, post-treatment applications are covered mainly by physical and chemical alteration operations. Magnetizing and removing causticity are some examples of post-application (Xiang et al., 2020). Heteroatom (i.e., nitrogen) doping techniques in order to create N-enrichment in the biochar can be achieved by *in-situ* addition and post-addition after the pyrolysis process. The diversity within the doping techniques arises from the time of introduction, which is basically the nitrogen source interference with biomass feedstock and biochar (Zhonghao Wan et al., 2020a). Various modification techniques create a diversified range and forms of active functionalities that are responsible for the physicochemical alterations in the biochar interface (Chacón et al., 2020). For example, (Güzel et al., 2017) post-treated the weed derived biochar by oxidizing with nitric acid with the purpose of remediating the methylene blue contaminant from aqueous solution and the obtained carbonaceous composition displayed the following alterations: minimized BET interface area and pore volume, enhanced oxygen and nitrogen active forms, and rise in the biochar's acidity. The methylene blue penetration ability of modified biochar ultimately showed remarkable progress from 39.68 to 161.29 mg g^{-1}.

Post-pyrolysis treatment is an effective strategy for the optimization of biochar structure and surface properties in the purpose of enhancing its clarification efficiency and environmental advantages. Acid/based treatment, HNO3 oxidation and magnetic modification are commonly referred examples of these post-treatment

techniques. Applicability and accomplishment of treatments are well-linked with the pollutant type such as organic/inorganic, cationic/anionic, hydrophilic/hydrophobic, polar/non-polar, ambient properties, and targeted remediation. Therefore, it is stated that post-pyrolysis treatments need to be optimized for various applications and feedstocks (Yan et al., 2018). Biochars after post-pyrolysis treatment possess high specific surface area, hierarchical pore structure, hydrophilic surface functional groups and excellent electrical conductivity (Chenglong Li et al., 2018). These references from the literature can be referred as effective studies which use the post-treatment as a modification technique: (Van Vinh et al., 2015), (X. fei Tan et al., 2016), (Dai et al., 2017). Thus, both the pre- and post-treatment methods have their individual performance enhancements in the certain applications with a common advantage of improved physicochemical properties of biochars. Interaction between biochar-based nitrogen functionalities and OPPs/phorate

2.5.4 Reaction mechanisms between biochar-based nitrogen functionalities and OPPs/phorate

The interaction of the N-doped biochar with contaminants is dependent on the type of nitrogen functional groups. In general, it is mentioned that the increase in the overall nitrogen content and density of influential nitrogen functional groups in biochar is favorable for an efficient contaminant removal activity (Leng et al., 2019a).

The removal efficiency of the OPPs such as Malathion, Parathion, Diazinon, Tribufos is also associated with the amount of nitrogen-containing components in biochar (Shen & Fan, 2013; F. Yang et al., 2017). Since organic compounds are more exposed to nucleophilic composition arising from their electron-rich macromolecular nature, adsorption of organic contaminants is carried out from the present $\pi-\pi$ attraction and Lewis acid-base interaction by nitrogen sources on biochar. Electron diffusion with the polarization of carbon π networks and the formation of positive electron gaps are also the result of an addition of nitrogen

34

precursors. These evolutions demonstrate a powerful inclination for binding the electron-rich aromatic ring structures such as organic pollutants. The researchers stated that there exists a beneficial trend in between the graphitic-N content and adsorption action (Zhonghao Wan et al., 2020b; L. Wang et al., 2018).

AOPs perform the mineralization of organophosphates with the help of incentive and oxidizing instruments (peroxides and ozone). Complex composition (highly amorphous character) and non-stoichiometric character (secondary loading ability and powerless electro-catalysis ability) of biochar and alike materials prohibited the consideration of these materials as AOP activators (Zhonghao Wan et al., 2020b). Pyridinic-N and graphitic-N contents in biochar correlate well with the improved catalytic reactions (Y. Xie et al., 2020). Unpaired electrons brought by pyridinic-N provide enclosed radicals in order to hold the H_2O_2 compounds with their high-level electro-demanding properties (Duan et al., 2018). Differently, graphitic-N placed into a pristine hexagonal unit in biochar gradually transmits the total interaction of local carbon approaching electron-acceptor oxyanions ($A_xO_z^{-y}$) (Zaeni et al., 2020). The presence of N and C atoms creates an electronegativity divergence. This allows the adsorption of peroxide molecules on positively charged neighbor C atoms following an acceptance of donor electron from N. Cooperation of adsorption and activation processes carries the potential of decreasing the surface charge of the peroxide O-O cooperation needed to be broken down (Duan et al., 2018; Zhonghao Wan et al., 2020b). The first developed graphitic N-doped biochar (at 900 ℃) was found to have a highly stable carbon structure with its high-level conductivity for the electrochemical interaction both towards peroxydisulfate (PDS) activation and adsorption of organic contaminants (Zhu et al., 2018). This remarkable electrochemical potential of N-containing biochar provokes an integral $^1O_2$ and electron transmission in order to degrade organic contaminants through a non-radical pathway (Oh et al., 2018). Greater peroxide O-O bond length in PMS (HO–OSO$_3^-$) molecules and their unsteady asymmetric composition when it is compared with the symmetric PDS ($^-O_3SO–OSO_3^-$) molecules enables them more prone to electrophilic attack (D. Wu et al., 2020). The relationship between nitrogen species composition

and catalytic stability of biochar gains more attention. The graphitic type exhibits better catalysis potential and resistance than the pyridinic and pyrrolic forms of nitrogen (Zhonghao Wan et al., 2020b).

2.5.5   Factors affecting removal of OPPs/phorate

The effectivity of biochar for the adsorption or degradation of organophosphates is affected by some critical factors. Physicochemical properties of biochar, including pore structure, pH and surface charge, modification of biochar, and hydrophobicity/hydrophilicity properties, are considered as important factors controlling its performance to remediate the environmental contaminants (Y. Yang et al., 2020).

2.5.5.1   Pore structure

Interface extent, porous structure and diameter of these pores are parameters of biochar pore structure and are regarded as dominant physical factors affecting interactions with organic contaminants (Suliman et al., 2016). The extent of interface and pore distribution is highly correlated with carbonization temperature. Seeking an optimum heat level is critical to understand the connection between carbonization temperature and the physical characteristics of biochar. A suitable pore structure enables the immobilization of contaminants in the medium. In general, an increase in carbonization throughout biochar production leads to enhanced performance due to upgraded pore structure and surface area (Y. Yang et al., 2020). Another parameter influencing the pore structure is the type of feedstock. Organic and inorganic components found in a raw feedstock influence the physical characteristics of biochar and its remediation capability. Among the feedstock types, microalgae are proven to have a high amount of nitrogen content. Thus, nitrogen load in microalgae-derived carbonaceous adsorbent becomes more significant than the other types (Maliutina et al., 2018a). Pore structure modification with an activating agent is an

accepted technique to modify biochar for enhanced removal/adsorption capability. Pore modification develops the meso- and micro-pore formations and also maintains better adsorption for organic contaminants. While the micro-pore entities are favorable for the phorate penetration, meso- and macro-pores promote the penetration of phorate by creating pathways. Zhenhao Li et al. (2020) prepared a nitrogen-enriched carbonaceous material with urea precursor and activated it by $KHNO_3$. The framework, as observed using the scanning electron microscopy (SEM) showed that nitrogen-loaded biochar had a more condensed porous interface compared to pristine biochar, which carried broader and untied composition. The reason for the improvement was explained by a fast reaction with urea as an N-precursor and $KHNO_3$ as an activating agent. Contrarily, nitrogen overload (>10% w/w) into biochar displayed inhibiting properties for the pore generation (Zhenhao Li et al., 2020). Pore volume is a factor affecting the absorbance performance of biochar and certain physical and chemical techniques are being promoted to enhance its presence. The temperature, holding period, gas flowrate and chemical additives (KOH, NaOH, etc.) are used as pore volume modification techniques (W. H. Chen et al., 2021). It is reported that the SEM analyses display tinier biochar sizes with the accelerating pyrolysis temperature, which supports the idea of increasing surface area and creating more of crevices or pores. Development in the water holding capacity is one of the results of increased porosity. Increased pore volume is an encouraging parameter in the biochar adsorption activities by serving a large available capacity for contaminants (C. Yang et al., 2021).

2.5.5.2 Surface functional groups

Surface functional groups are the active spots on the interface of biochar that arrange the characteristics and catalytic activities. Biochar is acknowledged as a complex heterogeneous structure loaded by various functionalities (e.g., carbonyls, hydroxyls, phenols, carboxyl, nitriles, peptides, quinones, lactones, pyrones, and free radicals, etc.). Comprehensive information on the surface functional groups facilitates the

selection of goal-oriented AOP. Pyrolysis temperature and time, type of feedstock, pretreatment and modification methods are controlling factors for the formation of functional groups. Currently, the connection between the active sites and interaction mechanisms with contaminants take most of the attention, leaving the inherent physicochemical properties behind. Among heteroatoms doped, nitrogen shows a remarkable trend. It is stated that planar graphitic-N and pyridinic-N are favorable types of nitrogen functionalities for electrocatalytic activities. Current research on functional groups pays attention to evaluating auxiliary parameters in AOPs such as O-containing functionalities, free radicals, metals content, and added heteroatoms (X. Zhou et al., 2021). These active sites provide advanced surface properties, including hydrophilicity, surface charges and ion exchange features, while the high surface area and greater porosity support the adsorption performance. Biochar functional groups give an outstanding capability in the environmental remediation applications of contaminated soils (C. Xu et al., 2021).

2.5.5.3   pH and surface charge

Nitrogen enrichment into biochar adds alkaline characteristic, which contributes radicals to hold positively charged metal(loid)s on the carbonaceous interface. As such, the highest level of adsorption efficiency of nitrogenous biochar occurs at lower pH conditions (pH<7) (Zhonghao Wan et al., 2020b). At very low pH values (pH<3), the removal ability of biochar becomes lesser due to the competitive anionic metals or metalloids by loading of H^+ ions into the nitrogen source. Therefore, the continuous rising of pH value from very acidic conditions to moderately acidic conditions progressively enhances the formation of active functional groups and captures the effectivity of the sorbent for phorate. The zeta potential of biochar is a representative component of remediation activity with respect to pH impact. If the zeta potential value is positive, the biochar interface holds mostly cations. In consideration of the charge state of the contaminant, zeta potential gives an indication to determine probable repulsion and attraction between the contaminant

and adsorbent (Youhua Fan et al., 2020). Feedstock materials and pyrolysis heat levels also affect the pH and surface charge of biochar and are linked to its removal performance of organophosphates (P. Liu et al., 2018). Base cations like Ca, Mg, K and Na from raw biomass create an alkaline condition in biochar and can be supportive for the formation of O^{-2}, OH^-, and CO_3^{-2} throughout pyrolysis operation (Gong et al., 2019). An increase in the pyrolysis temperature shows a direct relationship with the increase of ash content and contributes to biochar alkalinity (Leng & Huang, 2018). On the other hand, the surface charges are generated based on the available functional groups on biochar. The significance of the surface charge arises from the generated electrostatic attraction, which enables the adsorption of contaminants by biochar (Y. Yang et al., 2020). Nitrogen loading modification accompanies a more complex electron structure, which attributes to a higher surface charge shift supporting electrochemical action. Main nitrogen precursors are observed to be pyridine and pyrroline type of nitrogen active forms neighboring oxygen, while graphite nitrogen stimulates movement of electrons (Zhonghao Wan et al., 2020b).

2.5.5.4 Surface modification for the enhancement of active sites

Biochar without modification, i.e., pristine biochar, is found to be less efficient for the optimum removal ability of environmental contaminants. Thus, scientists pay appreciable attention to biochar modification methods (W. H. Huang et al., 2021; Y. Yang et al., 2020). There are chemical and physical modification methods as well as the production of biochar-assisted nanomaterials ((Y. Li et al., 2020). While physical activation techniques include steam or gas energizing, chemical additions such as NH_3, HCl, H_2SO_4, H_3PO_4, KOH, and NaOH refer to chemical modification techniques that boost the surface modification of biochar and enhances the active sites and O-containing functional groups on biochar surface (S. jia Liu et al., 2018). Recently, biochar-based nanomaterials have attracted more consideration by scientists as in their stable carbon content, greater specific surface area and porosity

for reducing the concentration of environmental contaminants such as organophosphates (C. Di Dong et al., 2017; Zhe Li et al., 2020). Heteroatom doped biochar has also been utilized for the removal of contaminants *via* Fenton-like systems (R. Z. Wang et al., 2019). There are some well-established and promising modification techniques, such as the production of nanoscale carbonaceous pellets or graphene-like structured complexes; however, they are considered expensive and objectionable due to nanomaterial toxicity. In this regard, nitrogen enrichment becomes a cost-effective and environment-friendly approach to modify biochar material (Zhenhao Li et al., 2020). The research range in the nitrogen-doped carbonaceous material subject is extremely broad and the discussions are mostly agreed upon the improvement in the interface action and removal capacity of biochar for OPPs. Chemical nitrogen modification on biochar can be achieved by the addition of various N-sources such as melamine, urea, ammonium chloride or ammonium nitrate. A study conducted by Kasera et al. (2021) proved that the N-load at the surface of respected biochars has been incremented 8.3%, 3.9%, 2.3%, 2.9% with the doping of melamine, ammonium chloride, ammonium nitrate, urea, respectively. In the previous study, while melamine addition provided the highest portion of pyridinic- and pyrrolic-N (35.2% and 36.8%), modification carried out by urea gave the highest amount to the graphitic-N by 26.6%. Apart from nitrogen addition, B, P, and S are different alternatives to introduce heterogeneity for the biochar modification. The catalytic activity of carbonaceous material can be controlled by systematizing the heterogeneous precursor's type and quantity. However, it was investigated by Ding et al. (2020) that the sulfur enrichment into biochar demonstrates a contradictory property upon the catalytic degradation, and the reason was linked to the deficiency in the O-active forms and shortage of the specific surface area. Another strategy developed to overcome the separation problem of fine-grained biochar from aqueous media is magnetization. Magnetic property on carbonaceous material is created by adding metal atoms such as iron, cobalt, nickel or their combinations with oxygen. It has been demonstrated that the magnetized char can be an outstanding tool in terms of heavy metals and organic

contaminants remediation from an aqueous phase (X. Dong et al., 2018; Yi et al., 2019). Thus, effective contaminant sequestration and immobilization in environmental systems are well-related with the insight of the interaction mechanisms between biochar and contaminants.

2.5.5.5   Hydrophobicity/hydrophilicity

Physical-based alteration methods such as the carbonization temperature rate and duration cause critical changes in the surface characteristics of biochar. Hydrophobicity/hydrophilicity is one of those changes affected by the applied heat treatment conditions (Clurman et al., 2020). A study on the determination of the effect of heat treatment on the biochar's hydrophobicity/hydrophilicity carried out by Mortazavian et al. (2019) indicated that the simple heat treatment process under ambient laboratory conditions lessened the hydrophobicity of biochar for the breakage of its hydrophobic $-C-H$ active forms and supported its hydrophilicity for the activation of hydrophilic $C = O$ active components. The increase in $C = O$ and $C - O$ bands is associated with oxidation of biochar surface and subsequent generation of active adsorption parts, thus promoting the adsorption of pesticides by active functional groups on the biochar's surface (Fahmi et al., 2018). Therefore, the decline in the macro-scale components in biochar and so the decline in polarity formed from the rise in carbonization heat escalate the hydrophilicity of the char interface. However, the biochar and organic contaminant interactions are primarily based on hydrophobicity, which can be further exemplified as π-π complexation, electrical relation, and H-bond formation (Y. Li et al., 2020). Furthermore, supplied gas in the carbonization process is another physical parameter affecting the physicochemical characteristics of the resulting char. It was noted by Zheng et al., 2020 that the modification induced by the CO_2 atmosphere resulted in higher porosity, non-biodegradability, hydrophilicity and polarity compared to nitrogen gas supply and the obtained biochar was an effective agent in the Cr penetration process. For this reason, the physical modification parameters must be well-organized

depending on the specific requirement of the targeted contaminant. Nitrogen addition into biochar can increment the hydrophilicity with the aim of providing interaction with metals and generate metal-ligand complex (Zhonghao Wan et al., 2020a). In the study of Yu et al. (2018), highly adsorptive nitrogen-based biochar managed a surface complexation with its graphitic-N content and hydroxyl groups found at the surface. Ling et al. (2017) used a hydrophyte as a hydrophilic feedstock to remove Pb (II) with an efficiency of 893 mg/g. The components that took role in the adsorption process were described as pyridinic-N, pyrrolic-N and C=O.

CHAPTER 3

MATERIALS AND METHODS

3.1 Sewage sludge feedstock sample

This study used sewage sludge collected from the Tatlar Municipal Wastewater Treatment Plant (WWTP) in Ankara as a feedstock material. In order to keep all the feedstock homogeneous and synchronous, only one collection has been done, which was at the initial stage of the study. The feedstock sample was obtained from the dewatered sludge cake in the WWTP, which is the product from the final sludge dewatering unit in the plant. The collected sludge cake had <25% dry solids.

The sludge sample was spread into large containers under the open ambient atmosphere overnight. Afterward, incompletely dried sludge cake was put in the oven (Dedeoğlu, Turkey) at 80 °C one by one in smaller containers. Each sludge sample was kept in the oven until it was thoroughly dried, which was concluded in 1-2 overnights. After all the sludge sample was dried, it was processed in a grinder. This operation was performed in order to make the particulates homogeneous and finer in terms of their morphology.

At the end of the drying and grinding processes, the feedstock sample preparation has been concluded with the absence of moisture and coarse materials content. From this point on, dried and ground sludge samples will be called as "*Raw sewage sludge* (Raw SS)".

3.2 Phorate as a pesticide studied

In this study, phorate was used as a studied organophosphorus pesticide. The chemical and physical properties of phorate were given in the Section 2.2.3. U.S.

EPA classifies phorate as a highly toxic commercial product (U.S. EPA, 2013). phorate analytical standard (Sigma-Aldrich, U.S.A.) has a molecular formula and molecular weight as $C_7H_{17}O_2PS_3$ and 260.38 g, respectively.

The reason for phorate pesticide choice was its highly preferred commercial use among organophosphorus pesticides (OPPs) which are applied on agricultural products to prevent insects. It has been found as hazardous for mammals, birds, aquatic species and endangered species. It inhibits the secretion of the Acetylcholinesterase enzyme and causes hyperactivity, convulsions, paralysis and death as a result (Birişik et al., 2018).

3.3   Experimental methods

3.3.1   Biochar production experiments

The RAW SS was used as a feedstock in the biochar production. Different operational parameters and modification techniques were applied on the RAW SS and 34 different biochar samples were prepared. The experimental conditions applied in the preparation of the biochar samples and the codes used in the naming of the prepared biochar samples are tabulated in Table 3.1. Most of the modifications and hydrothermal treatment experiments were carried out on biochar samples produced at 700 °C because increase in the pyrolysis temperature decreases the yield of produced biochar (Xiaoxiao Zhang et al., 2020). Therefore, 900 °C biochars were not considered as an effective strategy. On the other hand, incrementing pyrolysis temperature also brings enhanced physicochemical characteristics such as specific surface area, porous structure, mineral content, thermochemical stability, formation of surface functional group (R. Xie et al., 2021). Since the enhanced characteristics encourage the removal of phorate, 700 °C was considered as an efficient temperature.

Table 3.1. Modification and operation details of produced biochar materials

#	BIOCHAR	HT[1]	t (h)[2]	DRY (>24 h)	ACTIVATE[3]	PYROLYSIS[4]	WASH[5] (pH 6-8)	DRY (>24 h)	CODES
0	Raw Sewage Sludge						HCl 0.01 N	95	**RAW SS**
1	N atmosphere					300	HCl 0.01 N	95	**BC300**
2	N atmosphere					500	HCl 0.01 N	95	**BC500**
3	N atmosphere					700	HCl 0.01 N	95	**BC700**
4	N atmosphere					900	HCl 0.01 N	95	**BC900**
5	KOH[6] 0.5:1			80		700	HCl 0.01 N	95	**KOH0.5BC700**
6	KOH 1:1			80		700	HCl 0.01 N	95	**KOH1BC700**
7	KOH 2:1			80		700	HCl 0.01 N	95	**KOH2BC700**
8	Urea 5%			80		700	HCl 0.01 N	95	**U5BC700**
9	Urea 10%			80		700	HCl 0.01 N	95	**U10BC700**
10	Urea 15%			80		700	HCl 0.01 N	95	**U15BC700**
11	KOH1 + Urea 10%			80		700	HCl 0.01 N	95	**KUBC700**
12	Water	210	2	80			HCl 0.01 N	95	**HC210**
13	Water	210	2	80		300	HCl 0.01 N	95	**HC210BC300**
14	Water	210	2	80		500	HCl 0.01 N	95	**HC210BC500**
15	Water	210	2	80		700	HCl 0.01 N	95	**HC210BC700**
16	Water	210	2	80		900	HCl 0.01 N	95	**HC210BC900**
17	Water	210	2	80	KOH 0.5:1	700	HCl 0.01 N	95	**HC210BC700KOH0.5**

[1] Hydrothermal temperature (°C)
[2] Hydrothermal residence time (h)
[3] Applied activation chemical
[4] Pyrolysis temperature (°C)
[5] Washing with 0.01 N Hydrochloric acid
[6] Potassium hydroxide

Table 3.1 (continued)

18	Water	210	2	80	KOH 1:1	700	HCl 0.01 N	95	**HC210BC700KOH1**
19	Water	210	2	80	KOH 1:2	700	HCl 0.01 N	95	**HC210BC700KOH2**
20	Water	210	2	80	Urea 5%	700	HCl 0.01 N	95	**HC210BC700U5**
21	Water	210	2	80	Urea 10%	700	HCl 0.01 N	95	**HC210BC700U10**
22	Water	210	2	80	Urea 15%	700	HCl 0.01 N	95	**HC210BC700U15**
23	Water	210	2	80	KOH1 + Urea 10%	700	HCl 0.01 N	95	**HC210BC700KOH1U10**
24	Urea 10%	210	2	80			HCl 0.01 N	95	**U10HC210**
25	Urea 5%	210	2	80		700	HCl 0.01 N	95	**U5HC210BC700**
26	Urea 10%	210	2	80		700	HCl 0.01 N	95	**U10HC210BC700**
27	Urea 15%	210	2	80		700	HCl 0.01 N	95	**U15HC210BC700**
28	Urea 10%	210	2	80	KOH 1:1	700	HCl 0.01 N	95	**U10HC210BC700KOH1**
29	Water	210	4	80		700	HCl 0.01 N	95	**HC210BC7004h**
30	Water	210	8	80		700	HCl 0.01 N	95	**HC210BC7008h**
31	Water	210	16	80		700	HCl 0.01 N	95	**HC210BC70016h**
32	Water	230	2	80		700	HCl 0.01 N	95	**HC230BC700**
33	Water	190	2	80		700	HCl 0.01 N	95	**HC190BC700**
34	Water	170	2	80		700	HCl 0.01 N	95	**HC170BC700**

3.3.1.1   Pre-modification of biochar samples

Each biochar production experiment was initiated by 30 g of raw sewage sludge. Further treatments were performed on this 30 g of raw sewage sludge. Potassium hydroxide (Merck, Germany), urea (Merck, Germany) and a combination of both (KOH + urea) were applied as pre-modification chemicals. Different doses have been put into use, such as 5%, 10%, 15% of urea and 0.5:1, 1:1, 2:1 of KOH. 10% urea was prepared by solubilizing 5 g urea in 50 mL deionized water (Millipore, U.S.A.).

Therefore, 30 g of raw sewage sludge sample and 50 mL urea-water solution were put in a quartz boat for a 10% urea pre-modified sample. The solution was dried at 80 °C in the oven overnight before pyrolysis. 5% and 15% urea were prepared accordingly with this logic. In the case of KOH, 15 g solid KOH was added in consideration of 30 g raw sewage sludge for a 0.5:1 mass ratio. In order to solubilize and mix KOH with the sludge sample, small drops of UPW were added into the mixture with a Pasteur pipette. All of KOH liquefied with the addition of moisture and it was added onto 30 g of raw sewage sludge sample. The solution was dried at 80 °C in the oven overnight before pyrolysis.

3.3.1.2 Pyrolysis process of biochar samples

Samples to be subjected to pyrolysis (raw sewage sludge without modification, urea pre-modified samples, KOH pre-modified samples and urea + KOH pre-modified samples) were individually taken into quartz boat for biochar production. Pyrolysis experiments were performed in the split-type tube furnace (Protherm ASP 12/100/1500, Turkey) (Figure 3.1) under an oxygen-free environment.
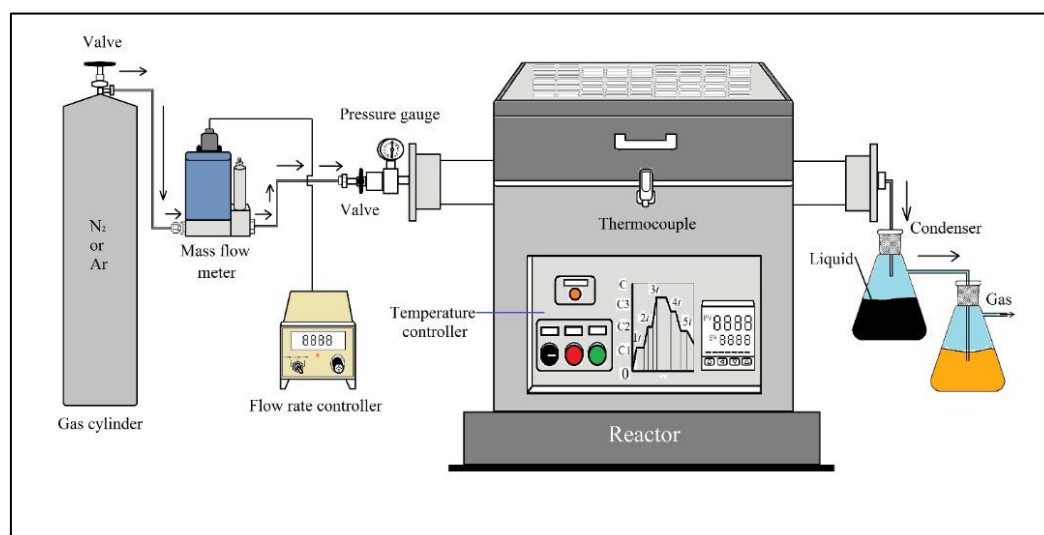
Figure 3.1. Split type tube furnace used in the pyrolysis experiments

All the pyrolysis experiments have been carried out under nitrogen gas in order to provide an inert condition. Loaded quartz boats with biochar materials were taken into the quartz boat inside the tube furnace. Both inlet and outlet gates were locked and the high purity nitrogen gas cylinder was started to give nitrogen gas into the tube furnace. The temperature has been set to 300, 500, 700, 900 °C. The heating rate of 10 °C per minute was adjusted for all experimental runs for biochar production at various temperatures. At the termination of the pyrolysis run, the charred samples were kept in a desiccator overnight filled with silica gel. The comparison between the appearance of the RAW SS sludge and pyrolyzed biochar sample is demonstrated in Figure 3.2. As it can be seen, there is a clear change in the surface texture and appearance between the Raw SS and pyrolyzed biochar sample. The texture of biochar sample is more homogeneous due to grinding with 115 mesh size. Also, the color becomes darker when the sludge was pyrolyzed caused by the destruction of connective and non-structural organic constituents (i.e., hemicellulose), formation of colored degradation products from hemicellulose and extractives, formation of oxidation products (i.e., quinones) and increase in carbon content (Yuxing Fan et al., 2021).
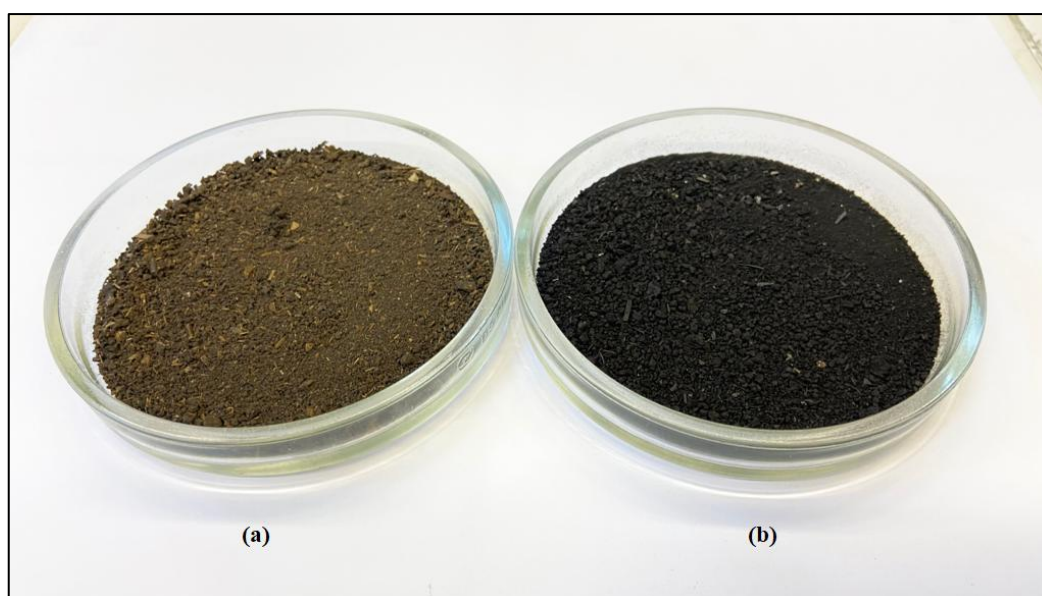
Figure 3.2. The visual difference between (a) RAW SS and (b) pyrolyzed biochar sample

3.3.1.3   Washing and drying of produced biochar samples

The washing process of produced biochar samples were performed by using hydrochloric acid (0.01 N. HCl) (Merck, Germany) in order to remove additional inorganic substances and keep the final pH in the range of neutral. The solution was filtered by a vacuum filtration unit paired with the pump. A five (5) μm filter was used in the filtration process. Residues of each filtration process were dried in the oven at 95 °C overnight.

3.3.2   Hydrothermally treated biochar production experiments

3.3.2.1   Pre-modification of hydrothermally treated biochar samples

Two types of samples were generated; hydrothermally treated biochars prepared with water, and hydrothermally treated biochars prepared with urea solution. The addition of urea solution was accounted as a pre-modification technique and the portions were set to 5%, 10%, 15% as in the pre-modified biochar scenario. Water-based hydrothermally treated biochar samples were prepared by adding 30 g of raw sewage sludge and 50 mL of deionized water, while 10% urea-based hydrothermally treated biochars were prepared by adding 30 g of raw sewage sludge and 5 mg of urea solubilized in 50 mL deionized water. Loaded hydrothermal synthesis autoclave reactors were put in the furnace (Lenton 3826, U.K.). Hydrothermally treated biochars were collected from autoclave reactors after cool down in the water. They were put in an oven at 80 °C to eliminate moisture content and stored in a desiccator overnight.

3.3.2.2   Torrefaction/hydrothermal treatment process

The torrefaction process was carried out at 210 °C for 2 h using a hydrothermal synthesis autoclave reactor (Toption HT-100, China). Different torrefaction

parameters have proceeded in the hydrothermally treated biochar production experiments. In Sample HC210BC7004h, HC210BC7008h, and HC210BC70016h, time was set as a process parameter and the autoclave reactors were kept in the furnace for 4 h, 8 h and 16 h, respectively. In Sample HC230BC700, HC190BC700 and HC170BC700, torrefaction temperature was set as a process parameter and the autoclave reactors were kept in the furnace for 2 h each under 230, 190 and 170 °C, respectively. Autoclave reactors were put in a furnace and produced water-based and urea-based hydrothermally treated biochars were dried in an oven at 80 °C.

3.3.2.3   Post-modification of hydrothermally treated biochar samples

Post-modification techniques were set up with the urea, KOH and combined urea + KOH addition. The same methodology was followed with the post-modification of hydrothermally treated biochar samples. Different doses have been put into use, such as 5%, 10%, 15% of urea and 0.5:1, 1:1, 2:1 of KOH. 10% urea was prepared by solubilizing 5 g urea in 50 mL deionized water. Therefore, 30 g of water-based hydrothermally treated biochar sample, 50 mL urea-water solution were put in quartz boat for 10% urea post-modified sample. The solution was dried at 80°C in the oven overnight before pyrolysis. 5% and 15% urea modification were prepared accordingly with this logic. In the case of KOH, 15 g solid KOH was added in consideration of a 30 g water-based hydrothermally treated biochar sample for 0.5:1 mass ratio. In order to solubilize and mix KOH with a hydrothermally treated biochar sample, small drops were added into the mixture with a Pasteur pipette. All of KOH liquefied with the addition of moisture and it was added onto 30 g of water-based hydrothermally treated biochar sample. The solution was dried at 80°C in the oven overnight before pyrolysis.

In the case of Sample U10HC210BC700KOH1, it was the only post-modified urea-based hydrothermally treated biochar sample which was performed by KOH 1:1 addition. 30 g of solid KOH was taken to moisturize with small droplets of deionized water and added into a 30 g urea-based hydrothermally treated biochar sample. The

solution was dried at 80 °C in the oven overnight before pyrolysis. The comparison between the appearance of the raw sewage sludge, urea modified pyrolyzed biochar sample, and KOH modified pyrolyzed biochar sample is illustrated in Figure 3.3. As it is illustrated, the change in color is clear between the Raw SS, urea modified biochar and KOH modified biochar. While the Raw SS conserves its original color as brown, urea and KOH applied biochar samples were turned into black and grey, respectively. The urea doping on the pyrolyzed biochar material caused no change in the appearance because the simple pyrolyzed biochar samples were also black which can be seen from Figure 3.2 (b). However, it can be easily seen that KOH addition changed the black biochar color into grey. It can be caused by the alkali treatment catalyzes the hydrolysis of lignocellulose and formation of more surface oxygen functional groups (H. Huang et al., 2017).
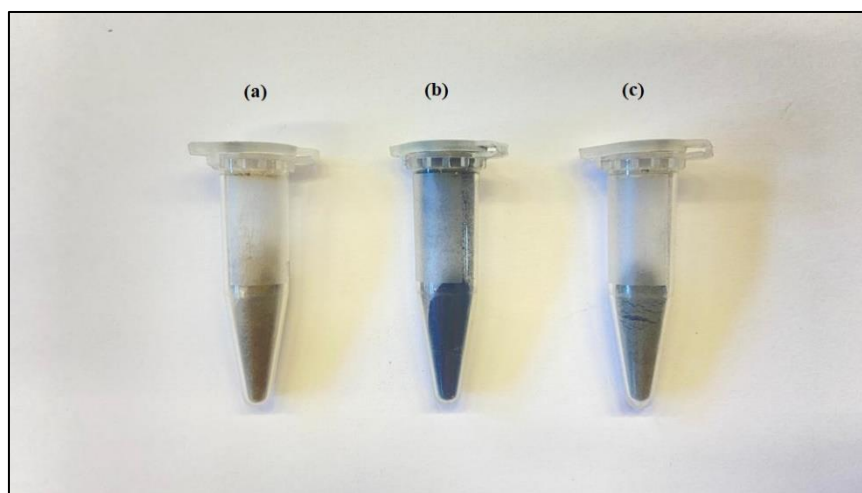
Figure 3.3. The visual difference between (a) Raw SS, (b) urea modified pyrolyzed biochar sample, and (c) KOH modified pyrolyzed biochar sample

3.3.2.4 Pyrolysis process of produced modified hydrothermally treated biochars samples

After all, the water-based and urea-based hydrothermally treated biochars were produced, post-modified and dried, they were taken into pyrolysis process excluding Sample HC210 and U10HC210 as control samples for both types of hydrothermally

treated biochars. Pyrolysis of hydrothermally treated biochars were performed in the split type tube furnace (Protherm ASP 12/100/1500, Turkey) (Figure 3.1) under the oxygen-free environment with the same logic as in the biochar pyrolysis. All the pyrolysis experiments have been carried out under nitrogen gas in order to dope the produced biochars with nitrogen externally. Loaded quartz boats with biochar materials were taken into the silica cylinder inside the tube furnace. Both inlet and outlet gates were locked and the high purity nitrogen gas cylinder was started to give nitrogen gas into the tube furnace. The temperature has been set to 300, 500, 700, 900 °C. Temperature rise was managed as rising 30 minutes to 300°C and keeping stable for 60 min at 300 °C in the 300 °C pyrolysis. The same logic was kept in the 500, 700, 900 °C pyrolysis experiments. When the pyrolysis finished, the charred samples were kept in a desiccator overnight filled with silica gel.

3.3.2.5   Washing and drying of hydrothermally treated samples

The washing process of produced hydrothermally treated biochar samples were performed by using hydrochloric acid (0.01 N. HCl) (Merck, Germany) in order to remove additional inorganic substances and keep the final pH in the range of neutral. The solution was filtered by a vacuum filtration unit paired with the pump. A five (5) μm filter was used in the filtration process. Residues of each filtration process were dried in the oven at 95 °C overnight.

3.4   Analytical procedure and advanced characterization

The use of analytical characterization methods for the detection of physicochemical properties are the important steps of understanding their role in complex environmental medium and biological systems as well as their impacts on organic contaminants removal activity. Therefore, broad ranges of examining techniques have been practiced in order to characterize and quantify the physicochemical properties in produced biochars and hydrothermally treated biochars.

All advanced analytical characterization methods utilized in this study require a solid type of sample except for Electron Paramagnetic Resonance Spectroscopy (EPR). The EPR analysis will be detailly discussed in 3.4.8. For all the other analysis techniques, produced biochar and hydrothermally treated biochar samples were ground in order to obtain homogeneous and fine grain size composition. The grinding process was accomplished with a 115-mesh size. Afterward, ground samples were put in Eppendorf Tubes, which is shown in Figure 3.4. Each tube was filled with approximately one g. of char sample. The Eppendorf Tubes in the blue rack are the samples ready to be utilized in the advanced analytical analyses.
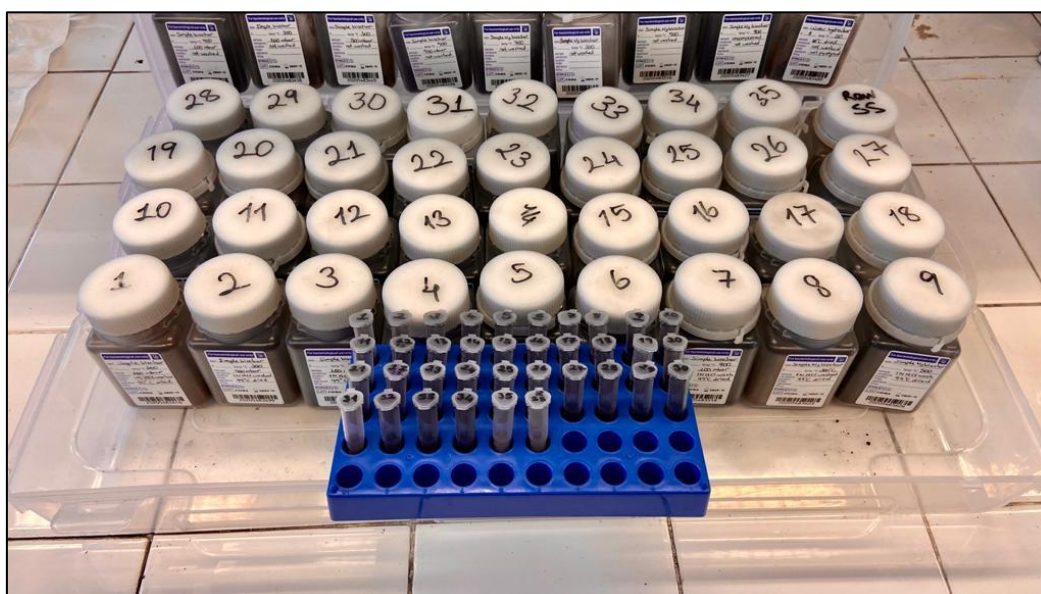
Figure 3.4. Prepared samples for the advanced analytical techniques

3.4.1 Elemental Analysis

The ultimate analysis is a conventional method for the understanding of elemental distribution in biochar and the elemental analyzer is one of the ultimate analyses where the equipment pyrolyzes the sample at >900 °C. The equipment detects C, H, N, S, O concentrations linked with their corresponding gases (i.e., CO_2, SO_2) discharged during the pyrolysis. The study of Nzediegwu et al. (2021) revealed that (N+O):C ratio has a straight correspondence with the polarity index and declines by

the decreasing pyrolysis temperature. Identification of present atoms and their corresponding ratios point out the utilization field of the biochar.

Elemental analysis samples have been examined at the Central Laboratory of METU in order to observe the elemental composition of produced char samples. The samples are in the shape of Figure 3.4. The instrument (LECO, Elemental Analyzer-932) works with a small quantity of sample (~2 mg) for one analysis and analyzes C, H, N, S, O elements synchronously. All the produced samples were sent to the elemental analysis.

3.4.2   Brunauer-Emmett-Teller

Brunauer-Emmett-Teller (BET) is a universal method suggested by the European Biochar Certificate (EBC) for surface area detection as a non-specific pore technique (Maziarka et al., 2021). Biochar with a greater surface area and porosity implies a greater efficiency in sorption from solid and aqueous media. They are changeable with the modification techniques and pyrolysis conditions.

The samples which have a shape as shown in Figure 3.4 have been analyzed at the Central Laboratory of METU. Fifteen samples were sent for analysis from produced biochars. Pre-heating parameters for the BET instrument (AUTOSORB-1C/MS) were determined as 280 °C for 3 h. The desired analysis was based on the micropore size distribution and multiple-point surface area.

3.4.3   Scanning Electron Microscopy

SEM analysis is achieved to find out the organic and inorganic composition of biochar by providing the elemental distribution (Chia et al., 2012). SEM is a common method in materials science since it has particular benefits, such as great resolution ability for a broad range of materials. Physico-chemical properties are contributed by the energy-dispersive X-ray spectroscopy (EDX) and electron backscatter

diffraction (EBDS) methods in SEM. The sample preparation step is a key point in SEM analysis. The interfaces to be analyzed must be high-quality (Busch et al., 2021). Biochar elemental distribution can be characterized by SEM analysis coupled with EDX. Utilization of SEM-EDX after the sorption experiments is sensible in the case of analyzing the surface morphology. However, the inability of organic compounds makes the SEM-EDX disadvantageous in certain applications (Yaashikaa et al., 2020). In some studies, it has been applied and remarked that the SEM-EDX analysis coupled with FTIR imaging shows notable matching results for the spatial classification of organic and inorganic constituents (Chia et al., 2012). In the case of biochar, SEM supports pore size identification because the pore size is what determines the sorption efficiency of pesticides. The surface area and porosity can be altered by the modification techniques or biochar production temperature. In this regard, SEM brings out the applied activation and heat-treatment differences created on the interfacial structure. Micropores and macropores are detectable by SEM analysis as well as the porosity composition of biochar. It is commonly applied that the SEM image before and after the sorption experiments in order to understand the change in interfacial structure (i.e., texture, coarseness, porosity) (Yaashikaa et al., 2020). It is also possible to distinguish the effect of external elemental doping sources on biochar surface morphology. For example, urea, melamine, ammonium chloride or ammonium nitrate are commonly applied nitrogen doping sources and the profile generated from SEM analysis helps to compare the effectiveness added from each source. A highly porous structure serves as a much more powerful interface for the sorption of contaminants (Kasera et al., 2021).

The sample preparation step is a key point in SEM analysis; the interfaces to be analyzed must be high-quality. They were in shape, which is shown in Figure 3.4. 17 samples of produced chars were sent to the Central Laboratory of METU containing one sample as Raw SS in order to compare the before/after results of pyrolysis and torrefaction processes. The analysis was carried out with FEI QUANTA 400F Field Emission SEM equipment with the proper coating under high pressure. The coating is required for samples with no electrical conductivity and it is

made with Au-Pd at a thickness of 3 nm. The magnification ratio was set to 50000, 10000, 5000, 2000X. Only two samples (KUBC700 and HC210BC700KOH1U10) were characterized by SEM coupled with EDX for the examination purpose of specific elements distribution at the surface and the elements expected to be seen are C, O, N, K, Si, Al, Fe, Zn.

3.4.4 X-ray photoelectron spectroscopy

XPS is a quantitative analysis tool to determine surface elemental distribution existing on the surface of biochar by using X-ray to transmit radiation into samples and measuring the photo-electronic energy. In the analysis of nitrogen doping modification, XPS spectra show the increase in nitrogen content, differentiating the bulk content and the surface content. Therefore, it is a beneficial technique to understand the usage impact of different feedstock and doping methods (Leng et al., 2019b). It is performed for the understanding of the binding energy of the C 1s, N 1s, and O 1s photoelectrons of biochar. Specific binding energies are authorized onto various forms of nitrogen functionalities such as amide, pyridine, pyrrole, alkylamine, secondary amide and N-alkylimide. Additionally, XPS approves the binding of tertiary amines onto complex carbonaceous interface resulting from the interaction of pre-oxidized carbons and organic amines (Jansen & van Bekkum, 1995).

Polarity is one of the parameters obtained from the XPS results of surface atomic components indicating the heterogeneous configuration of biochar (Cheng et al., 2020). However, XPS analysis can only provide the correlation within atomic content of various N-containing functional forms such as graphitic, pyrrolic, or pyridinic.

XPS equipment (PHI 5000 VersaProbe) containing Al-monochromatic X-ray anode performed general screening and partial screening of our samples separately. In the

partial screening analysis, the binding energy survey was specifically defined for each desired element: C, O, N, K, Fe. The defined ranges are listed in Table 3.2.

Table 3.2. Selected binding energy ranges of specific elemental compositions for XPS analysis

Element	Binding Energy Range (eV)	References
C1s	279 – 296	(Shchukarev & Korolkov, 2004)
O1s	525 – 538	(Nohira, 2002)
N1s	392 – 410	(Rignanese, 1997)
K2p	290 – 298	(Thermo Fisher Scientific, 2021)
Fe2p3	700 - 740	(Biesinger et al., 2011) (Uhlig et al., 2001)

XPS spectra reveal the surface elemental composition and speciation of corresponding elements on biochar. The speciation of survey spectra of C1s, O1s, N1s, K2p, Fe2p3 is tabulated in Table 3.3. The position changes of peaks found in the XPS spectra of related samples indicate the alteration in the elemental chemical states. The combination of individual speciation peaks forms the spectrum of analyzed elemental composition at the surface of biochar. The XPS analysis was performed for seventeen samples in the Central Laboratory of METU.

Table 3.3. Binding energies of surface elemental functional groups in the XPS spectra

Component	Binding Energies (eV)	References
Carbon containing groups		
Metal carbide	283	(Shchukarev & Korolkov, 2004)
C—C	284.8	
C—O—C	286	
O—C=O	288.5	
Metal carbonate	288 – 290	
Carbon polymers		
C=C	284.5	(Shchukarev & Korolkov, 2004)
C—C	284.8	
C—O	286	
C—N	286	
C=O	288 – 290	
Potassium containing groups		
KCl	292.9	(Thermo Fisher Scientific, 2021)
KO_x	293	
K2p	293	
K2p1/2	296	
Nitrogen containing groups		
Metal nitrides	397	(Rignanese, 1997)
NSi_3 (Si_3N_4)	398	
NSi_2O	399.9	
C—NH_2	400	
$NSiO_2$	402	
Nitrate	>405	
Oxygen containing groups		
Metal oxide	529 – 530	(Nohira, 2002)
Metal carbonate	531.5 – 532	
SiO_2	532.9	
Organic C—O	533	
O—F_x	535	
Iron containing groups		
Fe metal	700.7	(Biesinger et al., 2011) (Uhlig et al., 2001)
FeO	709.6	
$FeCl_2$	710.4	
Fe_2O_3	710.8	

3.4.5 X-ray diffraction spectroscopy

X-ray Diffraction (XRD) Spectroscopy is a way to learn various crystalline compounds' occupancy, which has an impact on the biochar properties and their corresponding utilizations. In the XRD, the principle is based on that each crystal refracts X-rays in a characteristic pattern, depending on the unique atomic arrangement of the phase. These diffraction profiles for each crystal phase identify that crystal, sort of like a fingerprint. XRD analysis method does not destroy the sample during analysis and allows analysis of even very small samples. Qualitative and quantitative investigations of rocks, crystalline materials, thin films and polymers can be performed with XRD. Thus, it is the heart of characterization tools for solid-state materials science. The peaks that occurred in the XRD results graph imply the diversified inorganic constituents in biochar such as halite, quartz, calcite or salts of Ca, Mg, Mn (Sahoo et al., 2021). It is a quick and highly qualified analytical method in order to characterize compounds, while its ease of operation and translation of results serve an uncomplicated template. Powder XRD is one of the common methods used in solid-state materials chemistry and provides qualitative, quantitative information. Peak points display evolutionary symmetry, precisely the size and the shape. Differently, peak intensities indicate the bulk electrons (Thakar et al., 2021). XRD can sometimes be supported by the FTIR and their combined data can be used for comparative purposes (Boukir et al., 2019).

Powder XRD samples have been analyzed in the Central Laboratory of METU (Rigaku MiniFlex) before and after the first stage batch experiments in a screening range of 10-90° for powder XRD. While pre-XRD was done for all samples, post-XRD has only been performed for the following three samples: KUBC700, HC210BC700KOH1U10 and U10HC210BC700KOH1.

3.4.6   Fourier transform infrared spectroscopy

Fourier transform infrared spectroscopy (FTIR) is one of the qualitative characterization techniques in order to detect the nitrogen functionalities in biochar (C. Zhang et al., 2020). It is accepted as a fast and well-developed method in biochar quality assessment (Sajdak & Kotyczka-Morańska, 2018). FTIR utilizes infrared spectroscopy in order to form an adsorption spectrum or sample emission. In this regard, the surface availability of biochar gains importance for the analysis results. Carbon structure and inorganic parts of biochar originate a deviation or an error in the assignation of N-functional groups. Various peak positions of each bond structure and their repulsive bond energies of different functional groups significantly have an impact and drive some deviations on the FTIR analysis (Leng et al., 2019b). The logic behind the FTIR relies on the functional groups' absorbance identified by the vibrational molecular spectroscopy, which differs within the range of 400 and 4000 cm^{-1}. Characteristic absorbance band of lipids, proteins and carbohydrates enable the FTIR to analyze its composition (Meng et al., 2014). It is suggested that when FTIR spectroscopy is combined with multivariate analysis, time becomes an advantage during the preparation of biochar samples. Recently, studies on the quantitative accuracy of infrared spectroscopy peaks have culminated in peak separation operations for the overlapping bands (Sajdak & Kotyczka-Morańska, 2018). On the other hand, if the heat supply in the pyrolysis process is very high (e.g., 800 °C), the FTIR spectrum can have small specific peak positions for biochar functionalities. This mismatching is caused by the destruction of surface functional forms at elevated temperatures (Cheng et al., 2020). FTIR analysis shows the decline in the amount of meso/macro pores and active forms adding to polarity derived from the pyrolysis operation kept at elevated temperatures (800 °C), reducing the penetration and elimination intensities of biochar (J. Li et al., 2020). High heat in the pyrolysis drags the H/N scale to be dropped due to the generation of nitrogen-containing compositions throughout the pyrolysis operation. FTIR results approve this

phenomenon by demonstrating remarkable nitrogenous heterocyclic ring peaks in the C-N spectra (M. Zhang et al., 2014).

Infrared radiation (IR) impacts surfaces through the actions of light absorption, light reflectance from the surface, penetration of light before scattered or a few of those at the same time. Scattered centers can be casually aligned; in this way, the phenomenon becomes isotropic and produces a diffuse reflectance. Collection of scattered light is achieved and transferred into the IR detector, in which the absorption of chemical functional groups is occurred (Accardo et al., 2014).

The surface functional groups and surface chemistry of biochar materials can be characterized by the use of FTIR spectroscopy. FTIR reveals the distribution of main functional groups at the surface of biochar in a defined wavelength range (cm^{-1}) (Yousaf et al., 2021). In Table 3.4, the main interfacial functional groups in the wavelength range of 400 - 4000 cm^{-1} on biochar's surface are given.

Table 3.4. FTIR spectra of main functional groups

Wave numbers (cm^{-1})	Functional groups	Compounds	References
400-750	C─C stretching	Aromatic rings	(Yousaf et al., 2021)
850-900	C─H	Aromatic hydrogen	
1030-1080	C─O stretching and deformation	Ethanol (C─OH)	
1230-1250	C─O─C stretching	Aryl-alkyl ether linkage	
1350-1430	OH bands	Acid	
1373	CH$_3$	Methyl	(Dehghanzad et al., 2016)
1480-1510	C═C stretching	Aromatic rings	(Yousaf et al., 2021)
1550-1700	C═O stretching	Carbonyl and ketone	(Yousaf et al., 2021)
1730-1740	─COOH	Carboxyl acids	
2800-3000	C-Hn stretching	Alkyl/aliphatic	
3000-3750	─OH stretching	Acid, methanol	

Table 3.4 (continued)			
1300-1460	C─N	Alkyl radical	(Dehghanzad et al., 2016)
1550	C═N	Amide	
1568	N─H + C─N (urea)	Amide II	(Ederer et al., 2017)
1616	─C═O (urea)	Amide I	
2265	NCO─	Urethane carbonyl	
3321	N─H	Amines	(Dehghanzad et al., 2016)
3420	NH$_3$	Ammonia	

The FTIR equipment in Environmental Engineering Department (Agilent Cary 630) with the diamond Attenuated Total Reflectance (ATR) technology is very practical in the analysis of both liquid and solid samples. Its portability and ease of operation allowed the analysis of all samples in 1 day. The analysis wavelength was kept in between 400 – 4000 cm^{-1} with 32 times scanning. For each sample, a minimum of 0.5 mg is enough to run the equipment without having a problem. Samples to be analyzed were taken from the Eppendorf tubes in a powder form which is shown in Figure 3.4.

3.4.7 Thermogravimetric analysis

TGA explores the pyrolytic behavior and thermal stability of biochars. Its logic relies on the determination of weight loss over time depending on the temperature rise. The temperature parameter is controllable and it mostly increases with a constant rate. The thermal reaction takes place under various atmospheric conditions such as compressed ambient air, nitrogen, oxygen, corrosive gasses. The analysis shown in a TGA curve consists of the y-axis as mass change and the x-axis as temperature or time. TGA curve is a useful tool for the characterization of biochar samples through the specific decomposition forms (Stylianou et al., 2020). The thermal stability of carbonaceous materials is another parameter that can be assessed by the TGA analysis. The minimized slope in the TGA curve indicates the presence of negligible weight loss and this means the material is thermally stable under applied temperature

and gas atmosphere. Therefore, TGA analysis can be applied for materials characterization, degradation and sorption mechanisms, reaction kinetics, organic and inorganic load in the sample. It is common to combine TGA analysis with IR spectroscopy and gas chromatography techniques if the analyzed matter contains volatile compounds. The combination of infrared spectra into TGA enables the analytical identification of gases resulted from the sample degradation (Peng et al., 2020).

The analyses were done using a PerkinElmer, Pyris 1 model TGA equipment. The TGA program was operated within 50 – 1010 °C with a rate of 20 °C/min. Data monitoring was set as seconds between points with a value of 0.4. In the TGA equipment, the mass holder pan requires a very small quantity of solid-phase mass and this value is the initial mass value in the results. The samples were taken in powder form, which is shown in Figure 3.4.

3.4.8   Electron paramagnetic resonance spectroscopy

EPR allows the samples to be detected in trace amounts of materials by measuring the spins of unpaired electrons. Additionally, deficient sites in the crystals can be detected with EPR analysis. EPR, also called Electron Spin Resonance (ESR), is a branch of spectroscopy concerned with electromagnetic radiation (usually microwave frequency) that causes transitions between magnetic energy levels of electrons with unpaired spins. The ESR spectrometer works in X- and Q-bands with a 10" magnet. Electrochemical and special flat cells are available that can be used in room temperature studies. There are also liquid helium cryostats to be used with the standard X-band cavity so that the measurements can be made from 4 °K to room temperature (Mazur, 2006).

Three biochar samples were characterized in the EPR analysis, which are KUBC700 (Sample No.11), HC210BC700KOH1U10 (Sample No.23) and U10HC210BC700KOH1 (Sample No.28) and their properties are listed in Table 3.5.

Table 3.5. The analysis details of EPR

#	BIOCHAR CODE	REACTION TIME (sec)	TRAPPING AGENT	TIME BEFORE MEASUREMENT (sec)
11	KUBC700	60	DMPO	30
23	HC210BC700KOH1U10	60	DMPO	30
28	U10HC210BC700KOH1	60	DMPO	30

Samples' preparation was initiated by putting 20 mL deionized water into three different 250 mL beakers, one for each sample (11, 23, 28). After 20 mg of related biochar was added to beakers, they were sonicated for 60 sec in order to separate colloids. When the sample was taken to be analyzed, DMPO was added and waited for 30 sec to radiate. The prepared samples are illustrated in Figure 3.5. The spin trap 5,5-dimethyl-1-pyrrolin–N-oxide (DMPO) (Merck, Germany) was used to trap the generated radicals for this study by EPR spectroscopy.
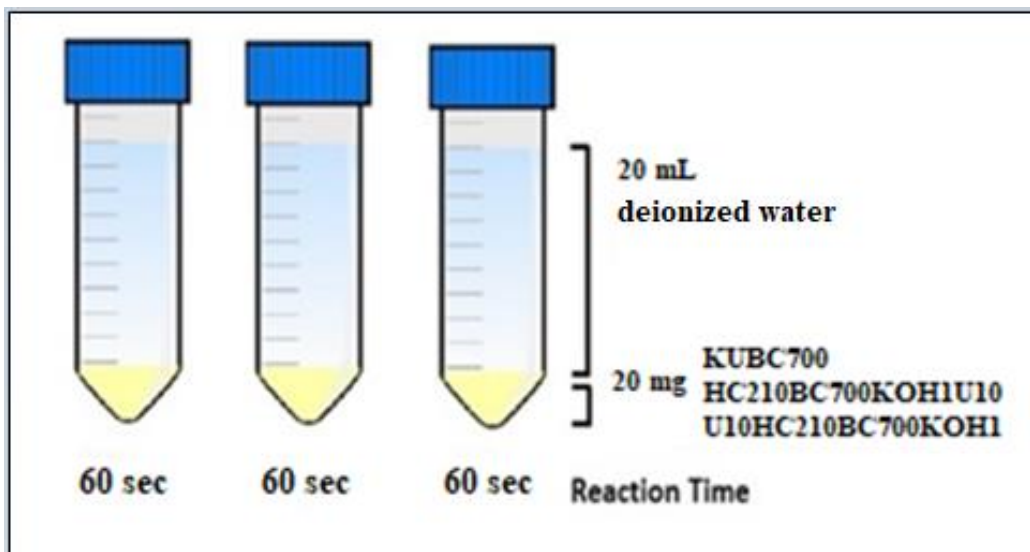
Figure 3.5. The sample preparation of the EPR analysis

3.4.9   Gas chromatography-mass spectroscopy

Gas Chromatography-Mass Spectroscopy (GC-MS) is a unique analysis for the identification of particular organic compositions generated from pyrolysis operation and attached onto the carbonaceous surface (Conti et al., 2014). Degradation products of phorate can be detected by the use of GC-MS. In this study, GC-MS (Agilent 8860 GC, U.S.A.) was utilized for the qualification of degradation products of phorate couple with MS detector (Agilent 5977B Turbo Pump MS, U.S.A.). The operational method parameters are listed in Table 3.6.

Table 3.6. GC-MS method parameters for phorate degradation products analysis

Parameter	Value
Carrier gas	Helium
Volumetric flow rate	2 mL/min
Inlet temperature	250 °C
Mode	Splitless
Pressure	9.954 psi
Injection source	GC ALS
Total Flow	65 mL/min
Thermal aux temperature	281 °C
Injection volume	1 μm
Column	Agilent HP-5ms 350 °C Part number: 19091S-433 30 m x 0.25 mm x 0.25 μm
Average velocity	37.132 cm/sec
Hold-up time	1.3466 min
Flow program	1 mL/min
Oven program	Initial temp, 90 °C for 2 min 6°C/min to 150 °C for 5 min 5°C/min to 220 °C for 5 min 6°C/min to 290 °C for 2 min
Run time	49.667 min
Solvent delay	3 min
EMV mode	Relative
EM voltage	1482
MS source	230 °C
MS quad	155 °C
Actual EMV	1485.35
Gain factor	0.46

In the experiments, reverse phase hydrophobic C18 cartridge (Agilent 12102052, 500 mg/6 mL/40 μm, U.S.A.) have been used in order to eliminate the water-based content and sustain non-polar compounds. Acetonitrile was utilized as a solvent. The samples were prepared in 2 mL screw top GC-MS vials. The experiments were carried out with four different samples which are listed in Table 3.7.

Table 3.7. Samples performed in the GC-MS analysis

Sample No	Description
1	Phorate (1 ppm) solution[7]
2	Phorate (1 ppm) solution + 100 mg KUBC700
3	Phorate (1 ppm) solution. + 100 mg HC210BC700KOH1U10
4	Phorate (1 ppm) ssolution + 100 mg U10HC210BC700KOH1

3.4.10 High-Performance Liquid Chromatography

Produced biochar and hydrothermally treated biochar samples were subjected to batch removal experiments in order to examine their phorate removal efficiencies. The general logic of batch experiments consists of adding a known amount of biochar/ hydrothermally treated biochar sample to a fixed volume of a liquid solution containing an initial concentration of phorate pesticide. The prepared solution was agitated with the use of a shaker (Zhicheng ZHWY-200B, China).

For batch experiments, the phorate stock solution has been prepared to have a 100 ppm concentration. The density of the phorate pesticide solution is 1.16 g/mL. It was calculated that 8.6 μL from the original phorate solution was needed to be taken to prepare 100 mL of 100 ppm phorate solution. The remainder of the solution was filled with Acetonitrile to reach 100 mL in order to form a calibration curve

---

[7] 1 mg/L of phorate solution was prepared with the use of Acetonitrile as a solvent. To prepare 1 ppm phorate solution in a 2 mL screw top GC-MS vial, 0.02 mL from 100 ppm phorate solution and 1.98 mL of Acetonitrile solution were added into the 2 mL vial.

(R^2=0.9999) in High-Performance Liquid Chromatography (HPLC) (Agilent Technologies Inc. 1260 Infinity II, U.S.A.), 1 ppm, 0.75 ppm, 0.5 ppm, 0.25 ppm, 0.1 ppm, 0.05 ppm and 0.02 ppm solutions were run in HPLC vials. The final solutions were filtered through a 0.22 μm nylon syringe filter for the HPLC analysis before putting into vials. The trend of the calibration curve is presented in Figure 3.6. The HPLC method developed for the concentration analysis is listed in Table 3.8
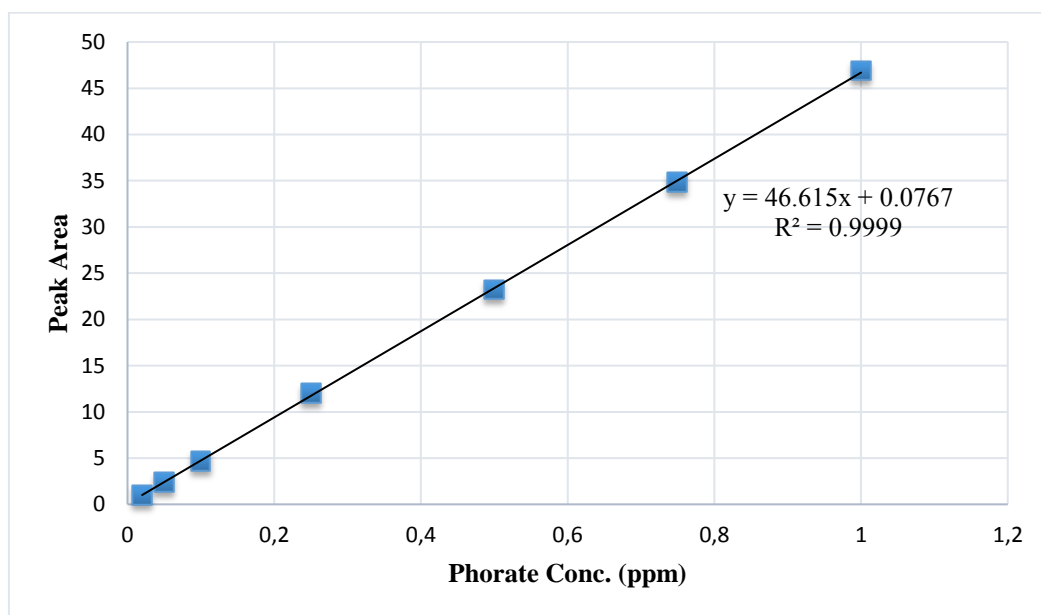
Figure 3.6. Calibration curve for phorate pesticide

Table 3.8. Operational conditions for phorate pesticide in HPLC

Parameter	Details
Mobile Phase	75% Acetonitrile – 25% Deionized Water
Injection Volume and Flow Rate	20 μL and 0.5 mL/min
Retention Time	8 min
Detector	ZORBAX Eclipse Plus C18 LC column
Detection Wavelength	210 nm
Column Temperature	40 °C
Column Type	InertSustain C18 colon (4.6×250 mm, 5-μm), Reverse phase

3.5   Batch removal experiments

The batch removal experiments were carried out in two stages. 1st stage batch removal experiments were conducted on the Raw SS and its derived biochars. 1st stage batch experiments were initiated with the prepared stock solution which was explained in Section 3.4.10. 100 mL batch solutions contain 1 mL of 100 ppm phorate solution which was taken from phorate stock solution and 99 mL of deionized water, resulting in 1 ppm (1 mg/L) phorate solution as a batch experiment standard concentration. 100 mg of each biochar samples were added to its corresponding beaker. All batch experiments were performed in a 250 mL open, glass cylindrical beaker having an internal diameter and height of 0.7 cm and 0.95 cm, respectively. The shaker was set to a speed of 200 rpm to ensure the well-mixed conditions for all the reagents in the solution. The temperature of the shaker was set to 25 °C under mixing conditions. The samples were taken at time intervals of t=0, t=1 min, t=5 min, t=10 min, t=30 min, t=1 h, t=2 h, t=3 h, t=4 h and t=5 h from prepared and mixed solutions. The specific time interval samples were put into the HPLC vials. The final solutions were filtered through a 0.22 μm nylon syringe filter for the HPLC analysis before putting into vials. The phorate concentrations of corresponding samples were determined with the derived calibration curve.

Among Raw SS and its produced 34 biochar samples with different operational parameters and modification techniques, certain biochar materials showed outstanding performances in the 1st batch removal experiments. The results of this selection will be explained in detail in Section 4.3. Therefore, from this point on, the experiments were continued with the specified three samples; Sample No.11 (KUBC700), Sample No.23 (HC210BC700KOH1U10) and Sample No.28 (U10HC210BC700KOH1). These efficient samples were further analyzed under various temperatures, biochar doses, pH values, reusability tests and real wastewater experimentations. The experiments performed with the consideration of these specific parameters will be named as 2nd stage batch experiments.

3.5.1 Effect of temperature

The second stage of batch experiments were performed under different temperatures for the removal of phorate, i.e., 30 °C, 35 °C, and 40 °C. Each of three biochar samples were run in each temperature value and thus, there were nine temperature-dependent batch experiments in total. The temperature was adjusted by the settings of the shaker with a 200-rpm speed.

All the temperature-dependent batch solutions were prepared as 100 mL in 250 mL beakers. 100 mL batch solutions contain 1 mL of 100 ppm phorate solution which was taken from phorate stock solution and 99 mL of deionized water, resulting in 1 ppm phorate solution. 100 mg of each three biochar samples were added to its corresponding beaker. Then, they were operated under 30 °C, 35 °C, and 40 °C. The samples were taken at t=0, t=1 min, t=5 min, t=10 min, t=30 min, t=1 h, t=2 h, t=3 h, t=4 h and t=5 h by filtering them through a 0.22 μm syringe filter and transferring them into HPLC vials.

3.5.2 Effect of biochar dose

Another parameter tested in the second stage of batch experiments was the change in the added biochar dose in a solution, i.e., 20 mg, 500 mg, and 1500 mg. Each of three biochar samples was run in each biochar dose value. Thus, there were nine biochar dosage-dependent batch experiments in total. The temperature was adjusted to 25 °C by the settings of the shaker with a 200-rpm speed.

All the biochar dosage-dependent batch solutions were prepared as 100 mL in 250 mL beakers. 100 mL batch solutions contain 1 mL of 100 ppm phorate solution which was taken from phorate stock solution and 99 mL of deionized water, resulting in 1 ppm phorate solution. 100 mg of each three biochar samples were added to its corresponding beaker. The samples were taken at t=0, t=1 min, t=5 min, t=10 min, t=30 min, t=1 h, t=2 h, t=3 h, t=4 h and t=5 h by filtering them through a 0.22 μm syringe filter and transferring them into HPLC vials.

3.5.3   Effect of pH

Different pH values were performed in the batch experiments for the removal of phorate, i.e., 3, 5, 7, 9, and 11. Each of three biochar samples was run in each pH value and thus, there were fifteen pH-dependent batch experiments in total. In the adjustment of pH, 0.01 M KOH (Merck, Germany) and 0.01 M HCl (Merck, Germany) solutions were used and the temporal pH changes were measured by the portable pH-meter (OAKTON, U.S.A.).

All the pH-dependent batch solutions were prepared as 100 mL in 250 mL beakers. 100 mL batch solutions contain 1 mL of 100 ppm phorate solution which was taken from phorate stock solution and 99 mL of deionized water, resulting in 1 ppm phorate solution. Then, KOH or HCl was added in order to fine-tune the pH. 100 mg of each three biochar samples were added to its corresponding beaker. The pH-dependent batch experiments were carried out under 25°C and 200 rpm speed in the shaker. The samples were taken at t=0, t=1 min, t=5 min, t=10 min, t=30 min, t=1 h, t=2 h, t=3 h, t=4 h and t=5 h by filtering them through a 0.22 μm syringe filter and transferring them into HPLC vials.

3.5.4   Reusability tests

The reuse of produced biochars and hydrothermally treated biochars were studied, performing a series of batch experiments for the removal of phorate. The reusability tests were executed for each of the three selected samples (Samples No. 11-23-28). The residues left from the batch experiment at pH 7 were selected for the reusability tests. Each of the three samples was taken into seven different falcon tubes. The tubes were filled with Acetonitrile (Sigma-Aldrich, U.S.A., ≥99.9%) as a washing liquid until 50 mL indicator line in order to eliminate the phorate residues left on the biochar. The samples were washed for 5 min and 2 times at 5000 rpm speed at 25 °C in a centrifuge (Thermo Fisher Scientific, U.S.A.). The liquid portion of samples was wasted and solid residues were taken into the oven at 50 °C overnight to be reused.

Dried samples were weighed and taken into the Reusability-1 batch experiment. All the reusability batch solutions were prepared as 100 mL in 250 mL beakers. 100 mL batch solutions that contain 1 ppm phorate solution. Then, weighted and dried biochar samples were added to each beaker. The reusability batch experiments were carried out under 25 °C and 200 rpm speed in the shaker. The single sample was taken at t=5 h throughout the experiments from each of the three samples. At the end of the batch experiment, the residue was collected and subjected to washing with Acetonitrile in the centrifuge (Thermo Scientific SR16R, U.S.A.). The residues left at the bottom of falcon tubes were dried in the oven at 50°C overnight to be reused.

The reusability tests were performed four times in the same logic as the aforementioned method and the last data was recorded for the 5th cycle.

3.5.5   Real wastewater experiments

For real wastewater experiments, a wastewater sample was taken from Middle East Technical University (METU) Wastewater Treatment Plant. The METU Wastewater Treatment Plant receives domestic wastewater generated from dormitories, residents and departments and treats it with a membrane bioreactor (MBR) system. MBR-based treatment plants operate the combination of the biological process, i.e., activated sludge and membrane filtration process, rather than a clarifier. The membrane filtration system commonly consists of low-pressure microfiltration or ultrafiltration membranes (AMTA, 2016). In the METU wastewater treatment plant, the MBR system used is of the type vacuum-driven MBR with ultrafiltration membranes. The wastewater sample to be used in phorate removal tests was collected from the effluent of the MBR treatment plant. The initial COD of the sample was 85 mg/L with standard method 5220-D, Hach Method 8000 (Hach, U.S.A.). The pH and electrical conductivity (EC) of wastewater used in this study were measured as 7.91 and 1970 µS/cm, respectively.

Three 1 L bottles of 1 ppm, 2 ppm, and 5 ppm phorate containing wastewater samples were prepared with the addition of phorate from its stock solution. Then, it was shaked under 4 °C and dark overnight. The samples were taken into concentration measurement with HPLC.

The wastewater batch solutions were prepared as 100 mL in 250 mL beakers. 100 mL batch solutions contain 2 ppm of phorate solution, which was taken from 1 Lsolution. Then, 100 mg of each three biochar samples were added to their corresponding beaker. The wastewater batch experiments were carried out under 25 °C and 200 rpm speed in the shaker. The samples were taken at t=0, t=1 min, t=5 min, t=10 min, t=30 min, t=1 h, t=2 h, t=3 h, t=4 h and t=5 h by filtering them through a 0.22 μm nylon syringe filter and transferring them into HPLC vials.

3.5.6 Data arrangement and statistical analysis

Data arrangement is used to optimize and conceptualize the analytical perspectives during the research (Thorne, 2000). In this study, optimization studies are achieved with the arrangement of operational parameters (e.g., surface area, surface-active groups, hydrophilicity, stable nature and pH of biochar) in order to select the most goal-oriented technique.

Regarding the statistical analysis, triplicate samples were carried out in all batch experiments to sustain the recultivity and accuracy under control. The impact of biochar dose, temperature, initial pH of the solution, modification techniques, various carbonization processes and residence time were illustrated in the graphs by using Sigma Plot 11.0 (Systat software Inc., U.S.A.) software.

3.5.7 Laboratory devices and equipment

Laboratory devices and equipment utilized throughout the experimental period are listed in Table 3.9.

Table 3.9. Laboratory devices and equipment

Name	Model / Country	Intention of Utilization
High Performance Liquid Chromatography (HPLC)	Agilent Technologies Inc. 1260 Infinity II/U.S.A.	Pesticide concentration analysis
Deionized water purification system	MilliporeMilli-Q Simplicity 188/U.S.A.	Deionized water supply
Split type tube furnace	Protherm ASP 12/100/1500/Turkey	Pyrolysis process
Autoclave reactor	Toption HT-100, China	Hydrothermal treatment process
Oven	Dedeoğlu/Turkey	Drying
Furnace	Lenton 3826/U.K.	Torrefaction process
Shaker	Zhicheng ZHWY-200B/China	Mixture of batch solutions
Refrigerator	Arçelik/Turkey	Safe storage of the samples and solutions
pH-meter	OAKTON pH 300 Series/U.S.A.	pH and EC measurement
Ultrasonic Stirrer	FALC EN631-1/Italy	Degassing of HPLC mobile phase
Gas Chromatography-Mass Spectroscopy (GC-MS)	Agilent 5977B Turbo Pump MS/U.S.A.	Degradation intermediate products analysis
Thermogravimetric Analyzer (TGA)	PerkinElmer Pyris 1 Model/U.S.A.	Thermochemical stability analysis
Centrifuge	Thermo Scientific SL16R Model/U.S.A.	Washing and separation of liquid and solid portions
Elemental Analyzer	LECO-932/U.S.A.	Elemental analysis
BET Analyzer	Quantachrome Autosorb-1C/MS/U.S.A.	Specific surface area, pore volume and pore size determination
SEM equipment	FEI QUANTA 400F/U.S.A.	Surface morphology identification
XPS equipment	PHI 5000 VersaProbe/Japan	Surface chemistry and speciation
XRD equipment	Rigaku MiniFlex/Japan	Mineral composition determination
FTIR spectroscopy	Agilent Cary 630 with the diamond Attenuated Total Reflectance (ATR) technology/U.S.A.	Surface functional groups identification

CHAPTER 4

RESULTS AND DISCUSSION

4.1 Characterization of the feedstock

The physical and chemical properties of raw sewage sludge (Raw SS) are tabulated in Table 4.1. The listed properties were collected from the advanced characterization techniques achieved in this study. The analyses of fundamental elements (i.e., C, H, N, S, O, O/C, H/C, (O+N)/C, (O+N+S)/C) were assessed by the Elemental Analyzer. The metallic elements were determined with Inductively Coupled Plasma-Mass Spectrometry (ICP-MS). The specific surface area, pore volume and pore size distribution of the feedstock were calculated using BET Surface Analyzer. The methodology of the aforementioned analyses is discussed in Section 3.4.2.

Sewage sludge is a nutrient-rich resource. The feedstock used in this study showed a high amount of nitrogen (3.6%) compared to other researches in the literature. For example, Ren et al. (2018) stated the nitrogen content in the sewage sludge as 1.97%, much lower than our N-content. However, in the study of Zhengjia Li et al. (2018), nitrogen content in the sewage sludge was demonstrated as 4.15%, which is comparable with this study. Jin et al. (2016) also had a similar nitrogen percentage which is 4.08%. Therefore, it can be concluded that sewage sludge is a nitrogen-rich feedstock in producing biochar materials. In terms of specific surface area, the study of Ren et al. (2018) found 22.01 $m^2 \, g^{-1}$ specific surface area, while Chen et al. (2014) revealed a 2.3 $m^2 \, g^{-1}$ surface area by the Barrett-Joyner-Halenda (BJH) desorption surface area. The feedstock used in this study had a lower surface area compared to foundings from the literature. H/C elemental ratio, which is an indication of aromaticity, was determined as 1.60 in this study. In the literature, 1.73 and 2.5 were pronounced as H/C ratio from the study of Zhengjia Li et al. (2018) and Ren et al. (2018), respectively. The H/C ratio is reversely linked with the degree of aromaticity,

so the lower the ratio, becomes higher the aromatic composition. In that sense, the sewage sludge used in this study reveals more aromatic compared to the literature. It can also be taken from Table 4.1 that the raw sewage sludge contains various types of metal content in its composition.

Table 4.1. Physical and chemical properties of raw sewage sludge (Raw SS)

Sample	Unit	RAW SS	Sample	Unit	RAW SS
C	%	30.9	Multiple-point BET	$m^2\,g^{-1}$	1.08E+01
H	%	4.2	BJH Adsorption Surface Area	$m^2\,g^{-1}$	2.35E+01
N	%	3.6	BJH Desorption Surface Area	$m^2\,g^{-1}$	1.22E+01
S	%	0.8	External Surface Area	$m^2\,g^{-1}$	1.08E+01
O	%	27.7	Micro Pore Surface Area	$m^2\,g^{-1}$	2.90E-01
Ash	%	32.9	NLDFT Surface Area	$m^2\,g^{-1}$	1.08E+01
O/C	-	0.67	BJH Adsorption Pore Volume	$cc\,g^{-1}$	2.46E-02
H/C	-	1.60	BJH Desorption Pore Volume	$cc\,g^{-1}$	2.00E-02
(O+N)/C	-	1.83	Micro Pore Volume	$cc\,g^{-1}$	2.35E-04
(O+N+S)/C	-	2.00	HK Pore Volume	$cc\,g^{-1}$	3.94E-03
Mg	$mg\,g^{-1}$	2.9	SF Pore Volume	$cc\,g^{-1}$	4.05E-03
Al	$mg\,g^{-1}$	6.5	NLDFT Pore Volume	$cc\,g^{-1}$	2.00E-02
Ti	$mg\,g^{-1}$	0.665	BJH Adsorption Pore Diameter	(Å)	1.54E+01
V	$mg\,g^{-1}$	0.0165	BJH Desorption Pore Diameter	(Å)	3.76E+01
Mn	$mg\,g^{-1}$	0.24	HK Pore Width	(Å)	6.28E+00
Fe	$mg\,g^{-1}$	7	SF Pore Diameter	(Å)	1.12E+01
Cu	$mg\,g^{-1}$	0.1	NLDFT Pore Diameter	(Å)	1.70E+01
Zn	$mg\,g^{-1}$	10.4			

SEM was another referred technique in this study in order to characterize the surface composition. SEM images of the raw sewage sludge with 50000X, 10000X, 5000X, 2000X magnification are illustrated in Figure 4.1. It can be seen from the image with 5000X that there is an approximately 10 μm sized macropore at the surface of the raw sewage sludge. It becomes much clear at the 10000X magnification. Since SEM images give only the image where it is focused, it is difficult to integrate it to the whole surface. However, if we assume the macropores are abundant at the surface of the feedstock, this explains the lower surface area compared to the literature. The brighter sections mainly indicate the presence of metallic content at that zone and they exist at the surface. It supports the miscellaneous metallic elemental composition listed in Table 4.1. The surface seems smooth rather than having a rough and layered structure. This can be enhanced by the exertion of temperature, which will be debated in Section 4.2.1.
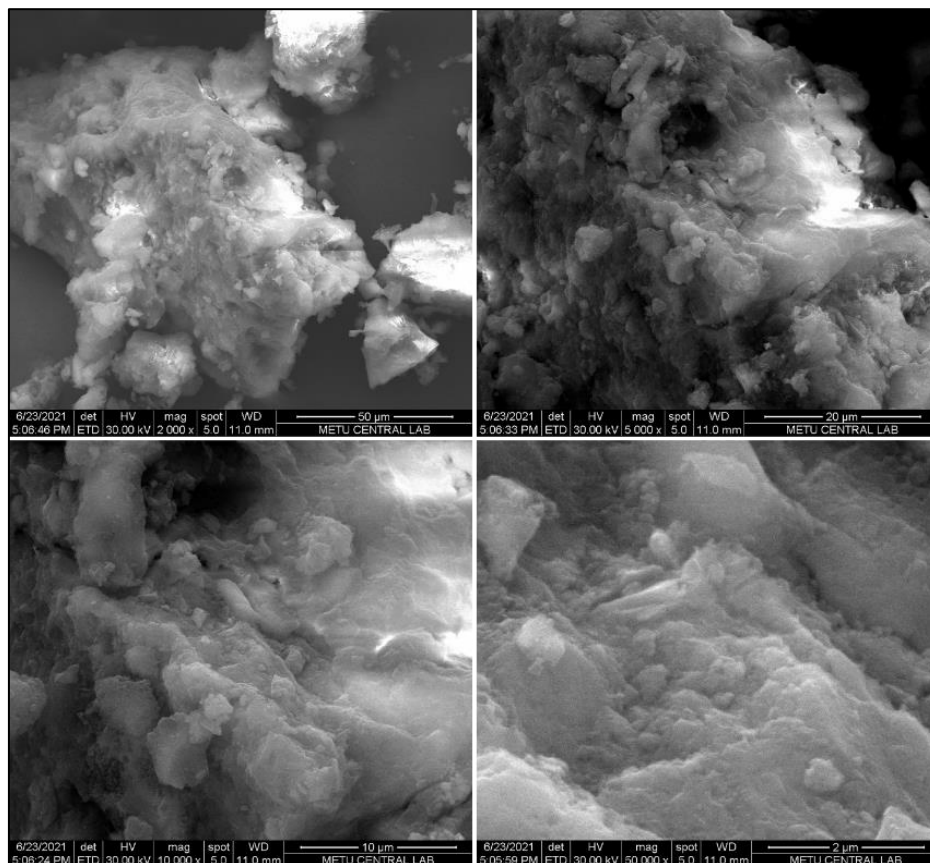
Figure 4.1. SEM image of raw sewage sludge (Raw SS)

4.2   Characterization of the produced samples

4.2.1   Surface morphology and elemental mapping

The surface morphology and elemental mapping analyses of produced biochar materials were performed by using SEM imaging coupled with Energy Dispersive X-ray Analysis (EDX). The SEM images were magnified at 50000X, 10000X, 2000X for all analyzed samples. EDX (2000X magnification) was carried out for two different biochars, which are Sample No. 11 and 23, KUBC700 and HC210BC700KOH1U10, respectively.

Figure 4.2 shows the SEM images of pristine biochar materials pyrolyzed at 300, 500, 700, 900 °C. The raw biomass has a more uniform texture and less porosity compared to pyrolyzed samples (Guizani et al., 2017). In the case of this study, sewage sludge as a raw feedstock have a smoother surface morphology. Moreover, the heating temperature and time of the biochar residues in the furnace are significant parameters of surface morphology (Guizani et al., 2017). With the increasing pyrolysis temperature, the meso and macropores on the carbonaceous surface become visible due to the loss of volatile compounds, especially in the case of 900 °C. In the surface textures of BC300 and BC500, even though the absence of macropores, they showed freshly emerged micropores. BC700 and BC900 represented piecewise cluster-like structures compared to lower temperatures. They demonstrated a clearer modification in the surface morphology with the formation of meso and macropores on the carbonaceous composition. BC900 as a biochar sample produced at the highest temperature exhibited the most significant number of cracks and decline in the micropore structures. In all simple biochar materials, the surface involved interconnections between existing micro, meso and macropores.
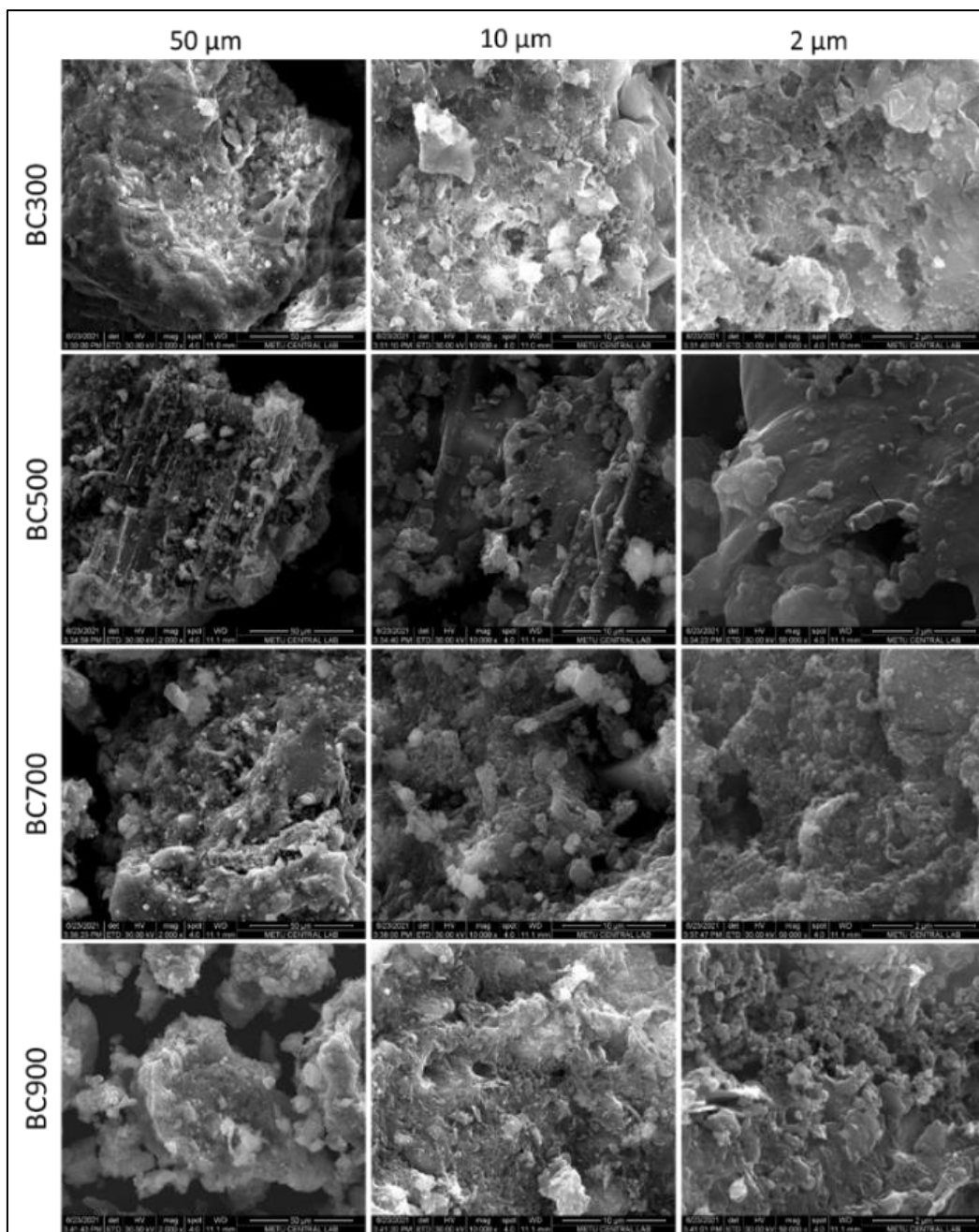
Figure 4.2. SEM images of pristine biochar materials

Figure 4.3 depicts the SEM images of pre-modified biochar materials pyrolyzed at 700 °C. Potassium hydroxide, urea and a combination of two chemicals were applied as a pre-modification technique for corresponding samples. KOH was utilized in

order to activate the biochar and improve the porosity in the carbonaceous material as a commonly referred alkali activating agent. KOH-modified biochars demonstrate an enhanced porous structure enabling advanced adsorption of contaminants (Qu et al., 2021). When the KOH1BC700 sample was compared with the BC700 from Figure 4.2, it was observed that the pores were more prominently and dispersedly spread at the surface of the carbonaceous texture. The impact of urea modification from the SEM images can be observed from the correlation between BC700 and U10BC700 from Figure 4.2 and Figure 4.3, respectively. The pores in U10BC700 were not homogenously dispersed as in the case of KOH1BC700. Doping of nitrogen adds more deficient sites to the carbonaceous structure and it creates a distinguished alteration in the surface morphology (Guo et al., 2020). However, there is a slight increase in the grooves from the nitrogen doping of urea. From the modification blend of KOH and urea, KUBC700 displays a prominently rough surface with small micropores. KUBC700 is rich in porosity due to the heteroatom addition, and the pores are homogeneously spread due to the KOH activation.
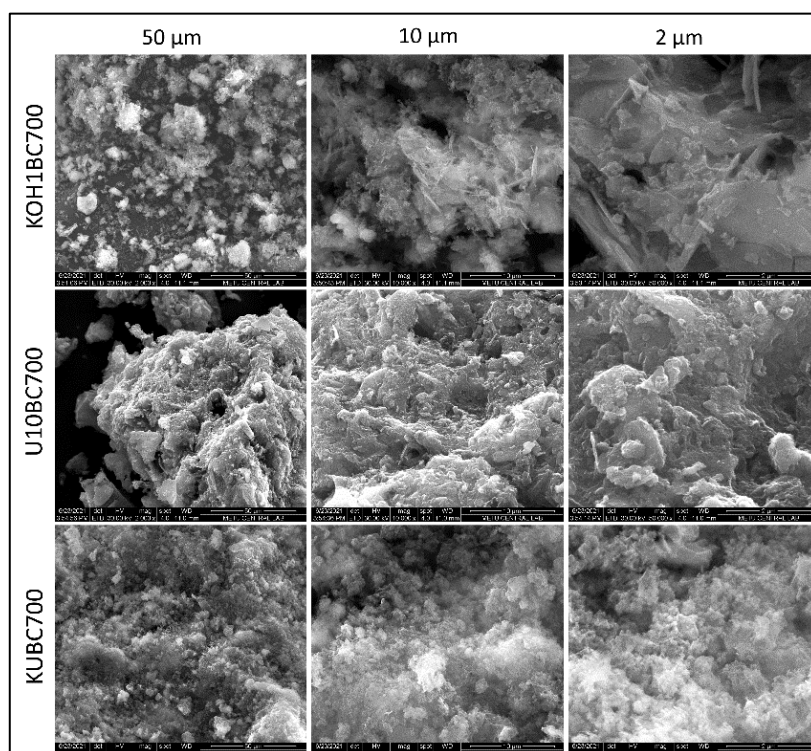
Figure 4.3. SEM images of pre-modified simple biochar materials

80

Figure 4.4 presents the SEM images of hydrothermally treated biochars prior to pyrolysis under temperatures of 300, 500, 700, 900 °C. Hydrothermal treatment and subsequently pyrolysis at increasing temperatures created a difference in the surface morphologies of related biochars. Hydrothermal chars have a greater meso-porosity than biochar materials. Additionally, nitrogen gas provided during the pyrolysis experiment enhances the formation of micropores (Dieguez-Alonso et al., 2018). Supporting this statement, larger pore sizes emerged in the hydrothermally treated biochar samples compared with simple biochars with corresponding pyrolysis temperatures from Figure 4.2. Moreover, as in the case of pristine biochars, hydrothermally treated biochar materials also demonstrated a linear correlation with the increasing pyrolysis temperature with a rising porosity.
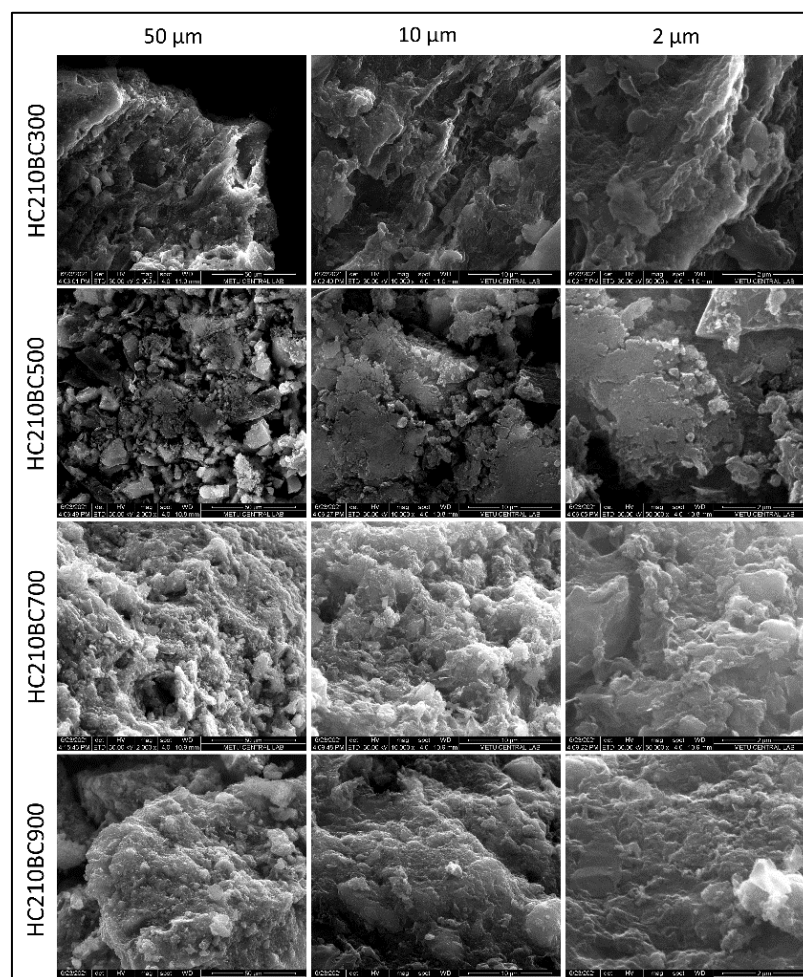
Figure 4.4. SEM images of hydrothermally treated biochars

Figure 4.5 shows the SEM images of hydrothermally treated and post-modified biochar materials pyrolyzed at 700 °C. Since nitrogen doping adds more deficiency to the carbonaceous surface, urea modification as a nitrogen source increased the amorphous texture in the HC210BC700U10. KOH modification, on the other hand, dispersed the pores homogenously through the surface, as was the case in Figure 4.3. When the activation process took place, concurrently, there occurred the forming of pores in the overall structure of the carbon material due to the more intensive release of volatile matters as gases (Pari et al., 2014). Although the KOH modification only itself did not form a significant alteration, concurrent application of urea and KOH resulted in the greatest porous structure in HC210BC700KOH1U10 overall.
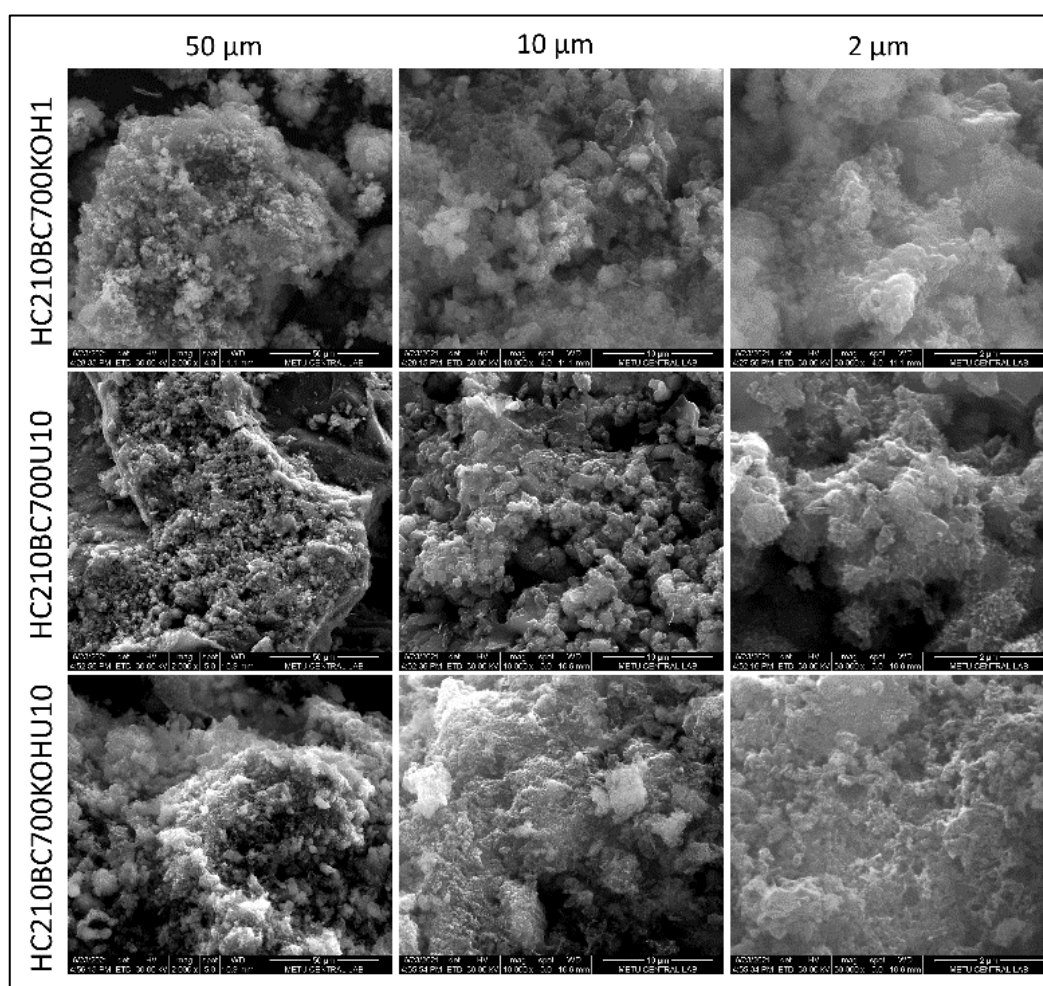
Figure 4.5. SEM images of hydrothermally treated and post-modified biochar materials

Figure 4.6 displays the SEM images of pre- and post-modified hydrothermally treated biochar materials produced at 700 °C. While U10HC210BC700 showed a distinguished porous structure with its vesicles and mesopores, U10HC210BC700KOH1 was imaged as large aggregates. Pre-modification with urea increased the pore sizes and pore amounts. U10HC210BC700KOH1 had a very bright SEM image and this indicates the abundance of organometallic complexes at the surface. Unlike the other small-scale accumulations on a rough surface, here in the U10HC210BC700KOH1, larger and brighter cloud-like structures imply the strong connection between metallic elements and carbonaceous surface. In these types of views, the shiny parts are the result of the presence of metallic elements; however, the carbon is embedded under those coverages.
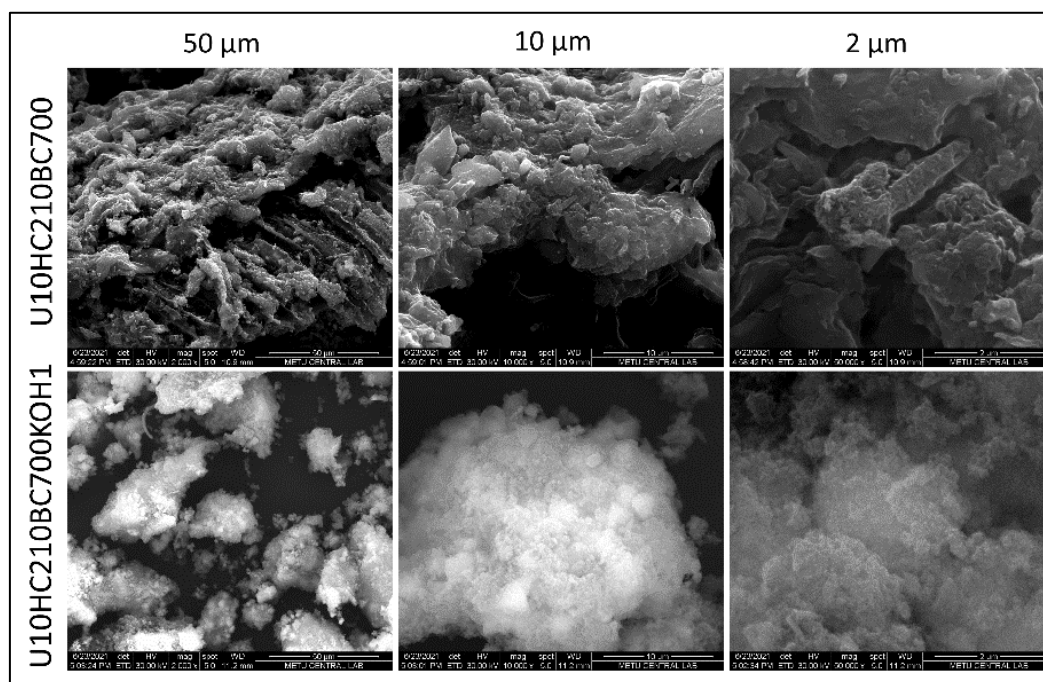
Figure 4.6. SEM images of pre- and post-modified hydrothermally treated biochar materials

Sewage sludge is diversified material and has a varied elemental composition. Especially, Al, K, Si, Zn, Fe elements are incredibly abundant in the environment and the sewage sludge is also rich in these contents. Since the surface of biochar is highly amorphous and carbonaceous, the carbon becomes reactive through different elements and makes carbon-metal composites. Thus, sewage sludge has been chosen as a feedstock in order to have a look at organometallic complexes. In this regard, SEM-EDX analysis gives an idea about the abundance and distribution of these compositions on the analyzed surface (Chia et al., 2012). Although it is difficult to comment on the quantity of elements or organometallic complexes, it gives an outstanding qualification about the distribution and presence of these components. We have chosen the analyzed elements by looking at the Inductively Couple Plasma Mass Spectroscopy (ICP-MS) results and the Al, K, Si, Zn, Fe content were very abundant in the composition.

SEM-EDX images were obtained for two samples, both at a magnification rate of 2000X. Figure 4.7 illustrates the SEM-EDX images of Sample No. 11 (KUBC700) and Sample No. 23 (HC210BC700KOH1U10). Here, the change in the elemental composition can be observed with respect to pre- and post-modification with same amount of the same chemicals. Eight different elements were analyzed in the SEM-EDX analysis of two biochar samples. The homogeneous distribution of these 8 elements can be clearly seen from both two images. However, there are cumulative aggregations at particular points. Brighter the representation indicates more of those specific elements piled up at that point. Notably, in the case of Silicon (Si), it has been stated as an enhancer in the adsorption rate and capacity (J. Liu et al., 2021). In Figure 4.7, the Si content of KUBC700 is comparatively higher than HC210BC700KOH1U10. Moreover, the Si accumulations were observed at the brighter sections of KUBC700 Si imaging, while HC210BC700KOH1U10 had a consistent partition throughout the surface with some absent points.
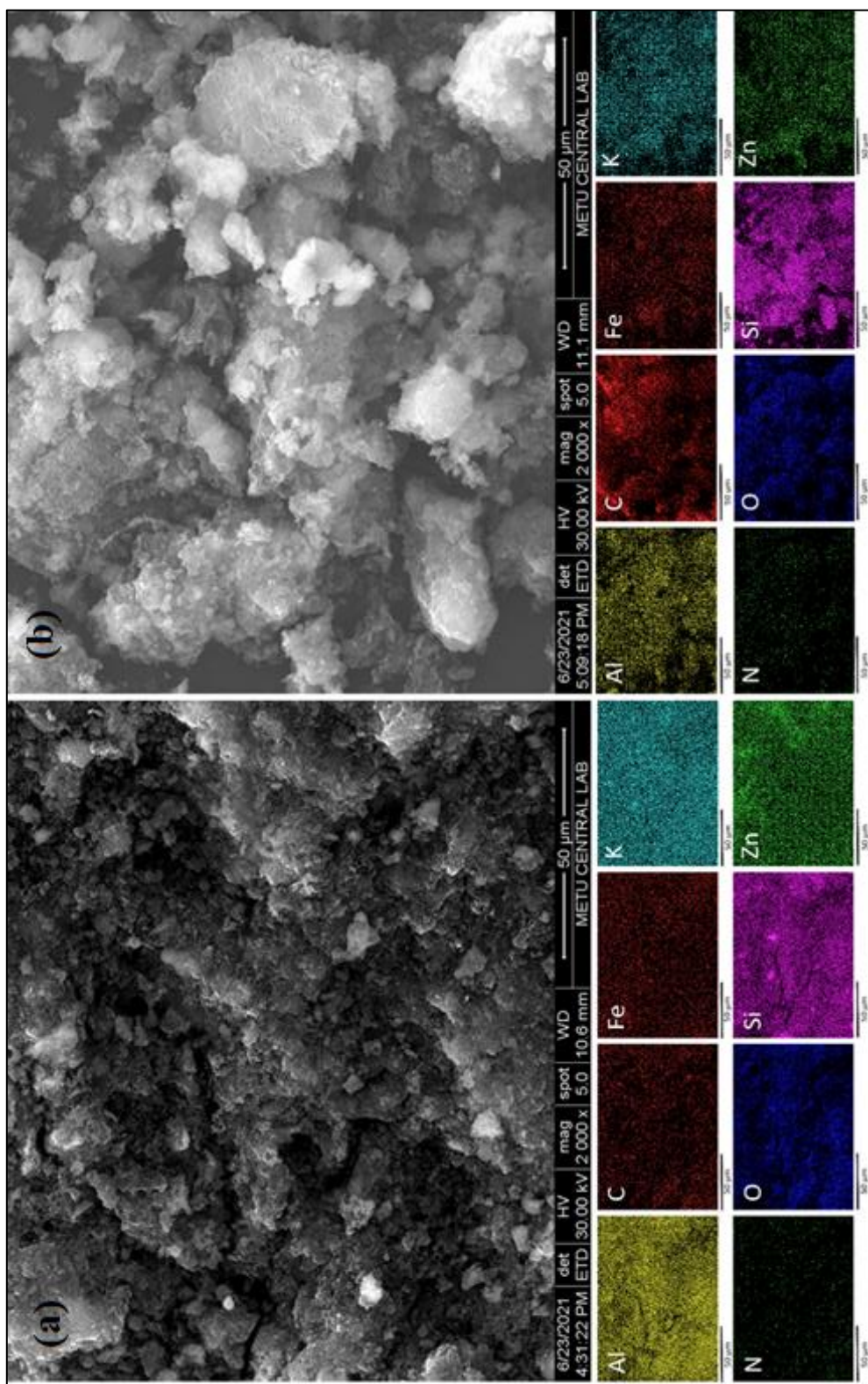
Figure 4.7. (a) SEM-EDX images of Sample No.11 (KUBC700) and (b) Sample No.23 (HC210BC700KOH1U10)

When the elemental distribution was considered in Figure 4.7, the plentiful dispersion of selected elements (Al, C, Fe, K, N, O, Si, Zn) can easily be recognized throughout the SEM images. Therefore, sewage sludge was agreed upon the richness in metallic ingredients. They had a reaction with carbon equally. In the section (a) of Figure 4.7, the darker sites are more plentiful when it is compared with Section (b). This implies the foundation of carbon at that point. On the other hand, Section (b) shows brighter composites on the surface and they are due to the presence of metallic components at that sites. In this regard, organometallic complexes are likely to take place and they are accumulated at larger particle sizes. However, the appearance of brighter metallic sites in the SEM image does not indicate the lack of carbon content. On the contrary, the carbon is embedded inside the organometallic surfaces. Section (a) also includes brighter parts; however, they are smaller in size. Moreover, in the section (a), the structure is rougher and more amorphous, while the section (b) has a smooth form due to the post-modification with KOH. In the case of porosity, almost no pore structure exists in the section (a) with small size micropores. In opposition, Section (b) contains a larger size of pores on the scale of approximately 10-20 μm. Therefore, it can be said that the porosity is enhanced and the surface is lower in the section (b).

4.2.2 Elemental composition of biochar samples

Elemental composition of produced biochar and hydrothermally produced biochar samples were assessed by the Elemental Analyzer. C, H, N, S, O contents of materials are listed in Table 4.2, Table 4.3 and Table 4.4.

Table 4.2 shows the elemental analysis of Raw SS, pristine and modified biochar materials. Studies revealed that the carbon content increases with the increasing pyrolysis temperature, while hydrogen and oxygen content demonstrates a reverse trend by the rise in temperature (Xiao et al., 2018). The results of this study affirmed the mentioned statement and there occurred an upward trend in carbon content from Raw SS to BC900, while the hydrogen and oxygen had a downward trend in the

86

same sample pattern. Xiao et al. (2018) reported that the total nitrogen content in biochars shows a minor increase and subsequent decrease by the rising pyrolysis temperature. Here, the sewage sludge as a feed material is rich in nitrogen functionality. At 300 °C, the produced biochar showed an almost negligible increase, but afterward, a notable decline in N-content has been observed with the increasing temperature up to 900 °C. Furthermore, the KOH application unsurprisingly added oxygen content to a considerable extent compared to the BC700 sample. However, a decrease in the O-content was detected by the increase in exerted KOH dose. Although KOH chemical adds extra oxygen-functionalities to the composition, a fall can happen due to releasing more CO_2 and volatile compounds during the thermochemical process. Moreover, the urea modification performed on the BC700 biochar sample displayed an expected increasing trend with the increase in urea loading dose. The most remarkable jump in the oxygen content was pointed in KUBC700 sample by the combination of KOH and urea application due to miscellaneous chemical interactions.

The atomic ratios of corresponding elemental percentages were calculated with the consideration of their atomic weights. Particular interest was given to O/C, H/C, (O+N)/C and (O+N+S)/C. They collectively refer to the stability of biochar. H/C is a widely used expression of aromaticity. There is an opposite relationship between the H/C ratio and aromaticity, and it increases with decreasing H/C (B. Chen et al., 2008). Higher pyrolysis temperatures result in lower H/C and O/C ratios for biochar (Xiao et al., 2016). In the case of this study, both H/C and O/C atomic ratios were consistent with this methodology. In this regard, the biochar materials produced at higher temperatures become more resistant. The decrease in O/C molarity results in more hydrophobic composition. Therefore, the more the heating temperature forms more hydrophobic structures. On the other hand, O/C implies the degree of aging or undergone oxidization of biochar since the oxygen is promoted into the organic carbonaceous composition in the environmental oxidation processes (Xiao et al., 2018). (O+N)/C ratio is another parameter in the chemical analysis of biochar that expresses the level of polarity. The polarity implication declines with the increasing

pyrolysis temperature due to the weakening of facial polar sections (B. Chen et al., 2008). In this study, the trend in (O+N)/C ratios was downward from 300 °C to 900 °C, which shows the polarity is higher in biochars produced at lower temperatures.

Table 4.2. Elemental analysis data of Raw SS, pristine and modified biochars

Sample	%C	%H	%N	%S	O%	O/C	H/C	(O+N)/C	(O+N+S)/C
RAW SS	30.9	4.2	3.6	0.8	27.7	0.67	1.60	1.83	2.00
BC300	33.4	3.5	3.7	0.8	18.6	0.42	1.23	1.26	1.44
BC500	37.7	1.4	2.8	1.0	15.6	0.31	0.45	1.04	1.18
BC700	43.4	0.8	1.7	1.2	8.2	0.14	0.22	0.55	0.64
BC900	47.4	0.6	0.8	1.4	3.2	0.05	0.14	0.22	0.27
KOH0.5BC700	25.4	1.3	1.3	0.8	19.5	0.58	0.62	1.26	1.32
KOH1BC700	20.6	1.0	1.3	1.6	18.2	0.67	0.55	1.19	1.26
KOH2BC700	18.8	1.1	0.4	0.7	17.8	0.71	0.70	1.13	1.15
U5BC700	43.2	0.8	1.8	1.1	8.7	0.15	0.23	0.58	0.68
U10BC700	45.9	0.8	2.1	1.2	6.0	0.10	0.20	0.41	0.53
U15BC700	46.5	0.8	2.2	1.1	5.5	0.09	0.21	0.39	0.51
KUBC700	19.5	1.3	1.3	0.8	34.2	1.32	0.79	2.19	2.25

Table 4.3 represents the elemental analysis data of pristine and post-modified hydrothermally treated biochars. When the elemental composition of hydrothermally produced chars was compared to those in the feedstock, their carbon contents were increased and the oxygen contents were decreased. It can be linked to the dehydration and decarboxylation processes in which the hydrogen and oxygen contents are significantly diminished from carbonaceous composite and released as water (H_2O) and carbon dioxide (CO_2) (Fang et al., 2018). The oxygen content was observed to be lower in hydrothermally produced materials than the pyrolyzed biochars since the oxygen-active forms at the surface are more plentiful in the biochars (Nzediegwu et al., 2021). The impact of temperature on the hydrothermally treated applications was the same as those in biochar materials. Carbon increased, whereas hydrogen and oxygen decreased with the rise in temperature from 300 °C to 900 °C. Contrarily to Table 4.2, O-content escalated with the KOH loading ratio. This can occur from the

fact that the organic content can increase with the degradation of carbon. However, the oxygen addition was lower compared to KOH-modified biochars. Urea loading created similar results in the nitrogen atomic content, while the combination of both KOH and urea again displayed a notable rise in the oxygen content.

The comparison between H/C ratio of biochars and hydrothermal biochars signifies the variation in carbon stability and aromaticity (Nzediegwu et al., 2021). Here, Table 4.2 and Table 4.3 show a slight divergence in the H/C ratio with slightly lower H/C atomic ratios in hydrothermally treated biochars. Since the oxygen content is lower in hydrothermally treated biochars, the O/C ratios were slightly lower compared to biochars. The polarity index demonstrated the same logic with increasing temperature.

Table 4.3. Elemental analysis data of post-modified hydrothermally treated biochars

Sample	%C	%H	%N	%S	O%	O/C	H/C	(O+N)/C	(O+N+S)/C
HC210	33.8	4.7	5.0	0.9	25.0	0.55	1.66	1.69	1.93
HC210BC300	38.4	3.3	3.8	0.7	14.9	0.29	1.01	1.02	1.21
HC210BC500	39.9	1.6	3.3	1.5	14.2	0.27	0.47	0.96	1.14
HC210BC700	45.7	1.6	2.3	1.3	7.3	0.12	0.41	0.50	0.63
HC210BC900	48.8	0.5	0.8	0.9	5.8	0.09	0.13	0.38	0.42
HC210BC700KOH0.5	25.6	0.8	2.0	1.7	11.2	0.33	0.38	0.77	0.86
HC210BC700KOH1	23.1	1.0	0.4	0.5	13.7	0.45	0.53	0.87	0.90
HC210BC700KOH2	21.4	1.3	0.3	0.4	14.7	0.52	0.70	0.93	0.95
HC210BC700U5	46.1	1.0	3.5	1.3	5.6	0.09	0.25	0.41	0.61
HC210BC700U10	46.7	1.1	3.5	1.6	4.1	0.07	0.27	0.32	0.52
HC210BC700U15	44.9	0.8	3.9	1.2	5.3	0.09	0.21	0.41	0.63
HC210BC700KOH1U10	24.4	1.5	1.6	0.5	30.9	0.95	0.71	1.99	2.05

Table 4.4 lists the elemental analysis data of pre-modified and other hydrothermally treated biochars. The residence time and heating temperature operational parameters of the hydrothermal process affected the elemental composition. The hydrothermal process was operated under 170 °C, 190 °C and 230 °C. When the hydrothermal temperature was increased, it was observed that the carbon content raised and the oxygen content dropped in a similar logic with pyrolysis temperature. Supportive to

the study of Krysanova et al. (2019), the maximum carbon percentage and minimum oxygen percentage were recognized with the hydrothermal treatment under 230 °C. The residence time, on the other hand, was performed under 4, 8, and 16 h. Differently than the literature, the carbon content decreased by the higher residence time, while the oxygen content showed an increase (Wilk & Magdziarz, 2017). This can be happened because of the difference in the feed material. Since the various feedstocks contain a diversified range of organic and inorganic fractions, the carbon and oxygen content fluctuate from one study to another.

Table 4.4. Elemental analysis data of pre-modified and other hydrothermally treated biochars

Sample	%C	%H	%N	%S	O%	O/C	H/C	(O+N)/C	(O+N+S)/C
U10HC210	31.1	4.1	4.4	0.9	28.9	0.70	1.57	1.92	2.13
U5HC210BC700	41.4	0.9	1.9	1.2	14.5	0.26	0.24	0.95	1.06
U10HC210BC700	42.1	0.9	2.8	1.3	14.3	0.26	0.26	0.95	1.10
U15HC210BC700	42.9	0.9	2.9	1.3	14.0	0.24	0.24	0.93	1.10
U10HC210BC700KOH1	13.5	0.9	0.7	1.3	12.4	0.69	0.83	0.81	0.85
HC210BC7004h	45.2	0.8	2.8	1.5	8.8	0.15	0.21	0.60	0.76
HC210BC7008h	42.7	0.8	2.5	1.7	12.7	0.22	0.22	0.84	0.99
HC210BC70016h	41.4	1.6	2.2	1.1	15.8	0.29	0.47	1.03	1.15
HC230BC700	46.1	0.9	2.4	1.6	8.3	0.14	0.22	0.57	0.71
HC190BC700	43.8	0.8	2.4	1.5	9.2	0.16	0.22	0.62	0.76
HC170BC700	43.3	0.7	2.3	1.3	9.4	0.16	0.20	0.63	0.76

4.2.3   Porosity and surface area influenced by pre- and post- modification

Specific surface area and porosity of biochars and hydrothermally treated biochars were analyzed with Brunauer–Emmett–Teller (BET) surface area analyzer and the equipment works by considering the material's nitrogen adsorption and desorption capacity. BET surface area, pore volume and pore size data of analyzed samples are tabulated in Table 4.5, Table 4.6 and Table 4.7 , respectively.

Various examination methods (i.e., Multiple point BET, BJH method cumulative adsorption surface area, BJH method cumulative desorption surface area, t-method

external surface area, t-method micropore surface area, non-local density functional theory (NLDFT) method cumulative surface area have been used in the BET specific surface area analysis and the specific surface areas determined by each method are given in the columns of Table 4.5. It is clear that the raw sewage sludge, which is the feedstock in this study, had a lower specific surface area compared to pyrolyzed samples in each analysis method. This supports the trend investigated in the literature (Chatterjee et al., 2020). Since the heat releases volatile contents from the composition of biochars, increasing pyrolysis temperature increases the surface area by removing more volatiles (Tag et al., 2016). In this study, the pyrolysis temperature was carried out under 300, 500, 700 and 900 °C. It was observed that the specific surface area rose by the pyrolysis temperature. So, the highest surface area was encountered in BC900 sample among simple biochars. KOH activation created a significant difference in the specific surface area of KOH1BC700 and KUBC700 samples, while the urea doping generated a relatively lower increase. KOH addition enhanced the external surface area by 47% and 70%, respectively; urea generated 26% in the t-method when the BC700 samples were taken into consideration. The values support the idea that KOH modification enhances the surface area and microporosity. Greater surface area reinforcing with the improved porous composition enables the material having a rich active sites (Zeng et al., 2021).

In the case of hydrothermally treated biochars, an increase in the specific surface area can be recognized when they are compared with the pristine biochars produced at the same temperatures (S. Tong et al., 2021). When the hydrothermal operation was applied on biochars, the increase was observed in both multiple-point method, BJH adsorption/desorption method, external and micro pore surface area, and NLDFT method. By the comparison of NLDFT cumulative surface area values; BC300 sample showed a decline by 42%, BC500, BC700, BC900 risen by 37.5%, 27%, 37%, respectively. The greatest specific surface area has been observed in the HC210BC700KOH1U10 sample, even outrunning the only modification with KOH. Therefore, the greatest change was seen in the combined modification of KOH and urea on hydrothermal treatment conditions. The comparison between KOH + urea

modified biochar (KUBC700) and hydrothermal char (HC210BC700KOH1U10) demonstrated a 42% and 52% increment in BJH adsorption and desorption surface areas, respectively.

Table 4.5. BET surface area of the produced biochar samples

Sample	Multiple-point BET (m^2/g)	BJH Method Cumulative Adsorption Surface Area (m^2/g)	BJH Method Cumulative Desorption Surface Area (m^2/g)	t-Method External Surface Area (m^2/g)	t-Method Micro Pore Surface Area (m^2/g)	NLDFT Method Cumulative Surface Area (m^2/g)
RAW SS	1.08E+01	2.35E+01	1.22E+01	1.08E+01	2.90E-01	1.08E+01
BC300	1.60E+01	3.47E+01	1.77E+01	1.50E+01	2.18E+00	1.29E+01
BC500	5.05E+01	1.95E+02	3.08E+01	3.40E+01	1.64E+01	5.00E+01
BC700	5.72E+01	1.87E+02	4.25E+01	4.22E+01	1.49E+01	5.73E+01
BC900	8.91E+01	3.38E+02	6.09E+01	6.07E+01	2.83E+01	9.15E+01
KOH1BC700	2.27E+02	7.48E+02	8.26E+01	7.90E+01	1.48E+02	2.34E+02
U10BC700	6.94E+01	2.55E+02	5.43E+01	5.72E+01	1.21E+01	7.04E+01
KUBC700	3.80E+02	1.08E+03	1.48E+02	1.42E+02	2.38E+02	3.71E+02
HC210BC300	7.23E+00	1.83E+01	5.47E+00	6.67E+00	5.64E-01	7.36E+00
HC210BC500	8.38E+01	2.75E+02	5.39E+01	5.50E+01	2.58E+01	8.02E+01
HC210BC700	7.76E+01	3.03E+02	5.30E+01	5.46E+01	2.30E+01	7.76E+01
HC210BC900	1.43E+02	5.13E+02	8.67E+01	8.65E+01	5.64E+01	1.47E+02
HC210BC700KOH1	1.69E+02	4.59E+02	7.62E+01	6.80E+01	1.01E+02	1.68E+02
HC210BC700U10	5.97E+01	2.07E+02	5.39E+01	5.34E+01	6.32E+00	5.84E+01
HC210BC700KOH1U10	4.48E+02	1.30E+03	1.72E+02	1.66E+02	2.83E+02	4.36E+02

Various examination methods (i.e., BJH method cumulative adsorption pore volume, BJH method cumulative desorption pore volume, t-method micropore volume, HK method cumulative pore volume, SF method cumulative pore volume, NLDFT method cumulative pore volume) have been used in the BET analysis and the pore volumes determined by each method are given in the columns of Table 4.6. It is clear that the raw sewage sludge, which is the feedstock in this study, had a lower pore volume compared to pyrolyzed samples in each analysis method. Even at some analysis methods (i.e., t-method, HK method, SF method), the pore volume was

nearly zero. The elevating temperature in the pyrolysis process encouraged the small-sized surface area and pore volume due to the deterioration of organic components and the development of cracks at the carbonaceous surface (Chatterjee et al., 2020). In this study, increasing pyrolysis heat from 300 °C to 900 °C brought along the increase in pore volume in each analysis method.

In the case of modified samples (KOH1BC700 and KUBC700), KOH similarly enhanced the pore volume when applied alone or coupled with urea. KOH created a notable increase of 68% (KOH1BC700) and 79% (KUBC700) in the BJH cumulative adsorption method, while urea increased the pore volume by 27% U10BC700. Without any exception, an increase has been seen in each analysis when the KOH or urea doped alone, and combined doping generated an even further increase in the pore volumes. It was simply explained by Dehkhoda et al. (2016) which the insertion of potassium elements coming from KOH expands the pores, and the additional roughness is added by the gasifying of carbon. The pore volumes of hydrothermally treated biochars were higher than the pristine biochars at corresponding temperatures. As it was the case in the surface area in Table 4.5, hydrothermal application initiated a decrease in both surface area and pore volume at 300 °C. However, there was a clear increment in the pore volume of BC500, BC700, BC900 in each analysis method. It was argued in the literature that the hydrothermal pre-modification creates a significant improvement in porous structure due to the enrichment of oxygen-functional groups by the hydrolysis and dehydration mechanisms (Jain et al., 2014; S. Tong et al., 2021). To support that, SF method cumulative pore volume demonstrated an increase by 50%, 33% 33% in HC210BC500, HC210BC700, HC210BC900, respectively. Modification performed on hydrothermally treated biochars showed a similar trend with surface area in Table 4.5. The largest pore volume has been observed in the HC210BC700KOH1U10 sample with the combination of modification chemicals in each analysis method.

Table 4.6. BET pore volume data of produced biochar samples

Sample	BJH Method Cumulative Adsorption Pore Volume (cc/g)	BJH Method Cumulative Desorption Pore Volume (cc/g)	t-Method Micro Pore Volume (cc/g)	HK Method Cumulative Pore Volume (cc/g)	SF Method Cumulative Pore Volume (cc/g)	NLDFT Method Cumulative Pore Volume (cc/g)
RAW SS	2.46E-02	2.00E-02	2.35E-04	3.94E-03	4.05E-03	2.00E-02
BC300	4.20E-02	2.50E-02	4.10E-02	2.40E-02	1.18E-02	4.02E-02
BC500	7.70E-02	4.09E-02	7.06E-03	2.08E-02	2.11E-02	5.23E-02
BC700	8.45E-02	5.37E-02	6.48E-03	2.36E-02	2.40E-02	6.21E-02
BC900	1.26E-01	7.19E-02	1.22E-02	3.69E-02	3.75E-02	8.66E-02
KOH1BC700	2.46E-01	1.13E-01	6.15E-02	9.25E-02	9.36E-02	1.71E-01
U10BC700	1.08E-01	6.50E-02	5.09E-03	2.83E-02	2.88E-02	7.62E-02
KUBC700	3.88E-01	1.86E-01	9.97E-02	1.55E-01	1.57E-01	2.80E-01
HC210BC300	1.61E-02	1.12E-02	1.48E-04	2.88E-03	2.95E-03	1.26E-02
HC210BC500	1.17E-01	6.61E-02	1.14E-02	3.46E-02	3.52E-02	8.29E-02
HC210BC700	1.15E-01	6.27E-02	9.97E-03	3.21E-02	3.26E-02	7.72E-02
HC210BC900	1.89E-01	1.05E-01	2.42E-02	5.91E-02	6.00E-02	1.31E-01
HC210BC700KOH1	1.94E-01	1.12E-01	4.35E-02	6.93E-02	7.03E-02	1.49E-01
HC210BC700U10	9.96E-02	6.76E-02	3.12E-03	2.48E-02	2.53E-02	7.28E-02
HC210BC700KOH1U10	4.54E-01	2.11E-01	1.18E-01	1.83E-01	1.85E-01	3.22E-01

Various examination methods (i.e., BJH method adsorption diameter, BJH method desorption pore diameter, HK method pore width, SF method pore diameter, NLDFT method pore diameter) have been used in the BET analysis and the pore sizes determined by each method are given in the columns of Table 4.7. Increasing the combustion temperature brings along the decomposition of organic structures and generating more microporous arrangements (Chatterjee et al., 2020). Although the differences in the pore size date were not obvious, which creates an obstacle to comment on the results, comparatively clear impacts were observed on the KOH modified samples. It has been revealed that the KOH addition dramatically enhanced the specific surface areas and pore volumes in Table 4.5 and Table 4.6, respectively. Here, in Table 4.7, KOH drove the formation of micropores compared to unmodified

samples and so that this situation caused a decrease in the pore size data. In more detail, when KOH1BC700 and KUBC700 were compared with their default sample (BC700), the pore size in the NLDFT method decreased by 76% and 75%, respectively. In terms of urea modification, pore size in the NLDFT method decreased by 69% in U10BC700.

Table 4.7. BET pore size data of produced samples

Sample	BJH Method Adsorption Pore Diameter (Mode) (Å)	BJH Method Desorption Pore Diameter (Mode) (Å)	HK Method Pore Width (Mode) (Å)	SF Method Pore Diameter (Mode) (Å)	NLDFT method Pore Diameter (Mode) (Å)
RAW SS	1.54E+01	3.76E+01	6.28E+00	1.12E+01	1.70E+01
BC300	6.25E+00	3.80E+01	6.27E+00	1.12E+01	1.79E+01
BC500	6.54E+00	3.79E+01	6.28E+00	1.11E+01	1.56E+01
BC700	6.04E+00	3.81E+01	6.33E+00	1.10E+01	5.30E+01
BC900	6.19E+00	3.80E+01	6.33E+00	1.11E+01	5.30E+01
KOH1BC700	5.91E+00	3.81E+01	6.23E+00	1.08E+01	1.27E+01
U10BC700	6.97E+00	3.78E+01	6.33E+00	1.12E+01	1.56E+01
KUBC700	6.08E+00	3.83E+01	6.33E+00	1.11E+01	1.26E+01
HC210BC300	6.99E+00	2.41E+01	6.38E+00	1.12E+01	1.56E+01
HC210BC500	6.08E+00	3.79E+01	6.33E+00	1.11E+01	1.56E+01
HC210BC700	6.21E+00	3.78E+01	6.33E+00	1.12E+01	1.56E+01
HC210BC900	6.67E+00	3.83E+01	6.28E+00	1.11E+01	5.30E+01
HC210BC700KOH1	6.10E+00	1.92E+01	6.23E+00	1.09E+01	1.27E+01
HC210BC700U10	6.89E+00	3.81E+01	6.33E+00	1.12E+01	5.30E+01
HC210BC700KOH1U10	6.08E+00	3.80E+01	1.05E+01	1.93E+01	1.22E+01

4.2.4   Change in mineral composition of produced biochar samples

The change in the mineral composition of produced biochar samples was characterized by XRD. XRD diffraction patterns of analyzed samples are given in Figure 4.8, Figure 4.9, Figure 4.10, Figure 4.11, Figure 4.12, Figure 4.13 and Figure 4.14.

Figure 4.8 demonstrates the XRD diffraction pattern of the Raw SS and pristine biochars. XRD patterns revealed that various kinds of crystalline structures are present in both raw feed material and produced biochars. Concerned biochars and the feedstock showed a typical broad pattern between $2\theta=18-34°$. However, the hump got narrower through BC900. While the most apparent peak was seen at $2\theta=29°$ as Calcite in Raw SS and BC300; Quartz peak became prominent at $2\theta=26°$ in higher temperatures where the Calcite intensity decreased gradually with increasing temperature and showed its lowest tension in BC900. Quartz peaks correspond to $2\theta=20, 26, 36, 56, 68, 73$ and $81°$ in the pattern. Graphite occurred at $2\theta=28°$ and has the lowest intensity in Raw SS and highest intensity in BC900. This means the rise in pyrolysis temperature favored the formation of Graphite in the amorphous structure. Another crystal structure that appeared in the XRD diffraction pattern is the Sylvite (KCl). It took place at $2\theta=35°$ and showed denser presence in Raw SS compared to pyrolyzed samples. The reason is explained by Xu Yang & Wang, 2021 as the biochar materials that are not pre-treated prior to the combustion process maintain the chloride and water-soluble potassium salts from the feed source. Hereby, the raw material supports the aforementioned idea by having a higher density of Sylvite in this study. K_2O can be the second indication of not pre-treated feedstock since its tension increased by the decrease in pyrolysis temperature and appealed as highest in Raw SS. K_2O was affirmed by the peak at $2\theta=39°$. Kalicinite ($KHCO_3$) occurred at lower range degrees, whereas the Aluminum oxide showed its presence at higher theta degrees.
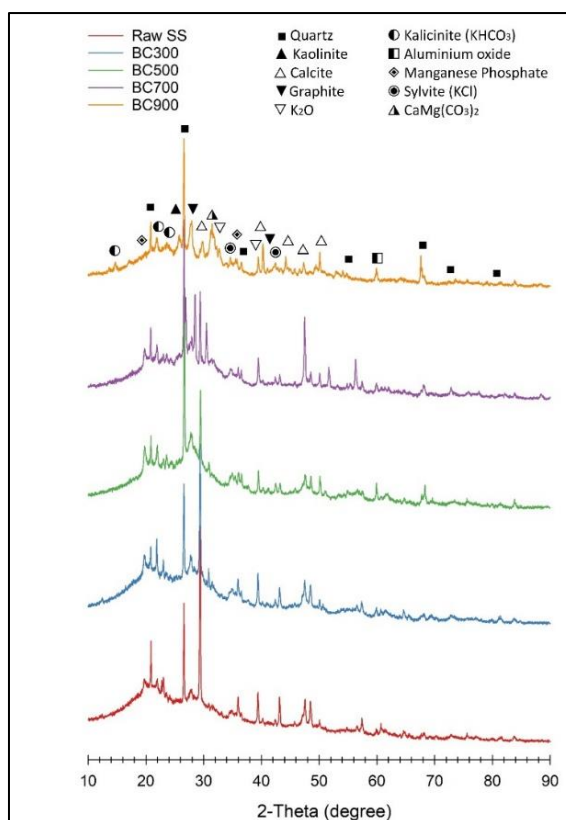
Figure 4.8. XRD diffraction pattern of the Raw SS and pristine biochars

Figure 4.9 illustrates the XRD diffraction pattern of pre-modified biochars. XRD patterns revealed that a diversified number of inorganic structures reside in modified biochar samples. The pattern demonstrated that the Calcite ($2\theta=29°$) was the most prominent among other crystalline structures in KOH modified samples, whereas the Quartz ($2\theta=26°$) was dominant in urea modified samples. The intensity of Calcite increased with the increase in applied KOH dose. A similar trend was noticed in the formation of Quartz by the increase in urea dose. In the case of KOH doping, the structure became rich in K_2O and Kalicinite ($KHCO_3$). Besides, Quartz crystalline structure showed more presence in the urea doped biochars. Calcite at $2\theta=47°$ surprisingly came up more intensified in the urea-modified samples. The combined modification of KOH and urea, on the other hand, did not show particular peaks except the broad hump region at $2\theta=18-34°$. The recognizable peaks of Calcite and

97

Quartz became weaker when the chemicals were applied combined. However, it can be deduced that KUBC700 carries the characteristics of both modification chemicals.
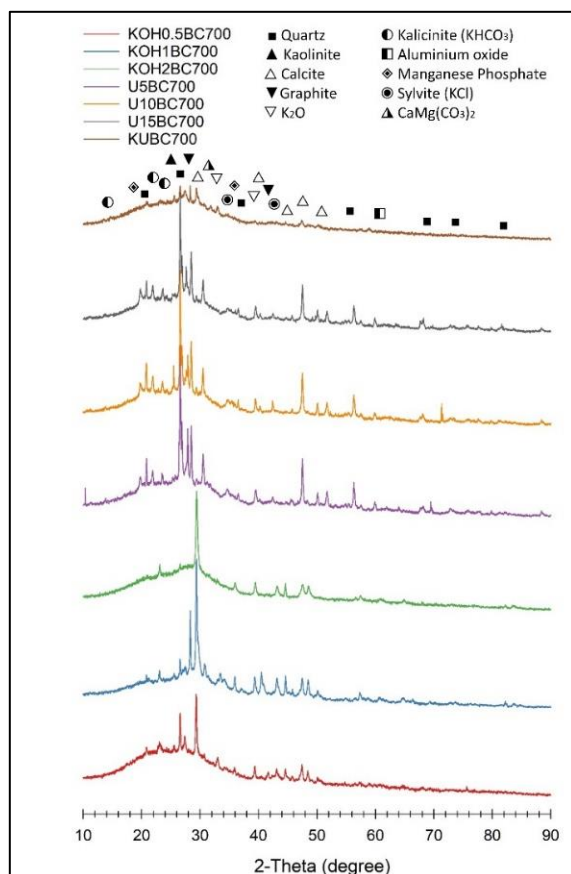
Figure 4.9. XRD diffraction pattern of pre-modified biochars

Figure 4.10 depicts the XRD diffraction pattern of hydrothermally treated biochars. Pyrolyzed and not pyrolyzed hydrothermal biochars displayed a recognizable Quartz peak at $2\theta=26°$ and the most intensified peaks HC210BC900 due to the increased applied temperature (Pariyar et al., 2020). Moreover, Calcite also became prominent at $2\theta=50°$ in the XRD pattern and its tension escalated by the rise in the pyrolysis heat. However, what has been revealed in Figure 4.8 as the steep peaks of Calcite at $2\theta=29°$ did not occur in the hydrothermal case; they were very small compared to peaks in biochars. Another difference between Figure 4.8 and Figure 4.10, the noticeable crystallographic composition of Graphite has been observed at $2\theta=28°$ in

hydrothermal chars and the peak got upright by the increase in pyrolysis temperature. Throughout the XRD diffraction spectra, the patterns of hydrothermally treated biochars and pyrolyzed biochars were very similar; however, the samples presented a more diversified range of K_2O, Aluminum oxide, $CaMg\,(CO_3)_2$ in Figure 4.10.
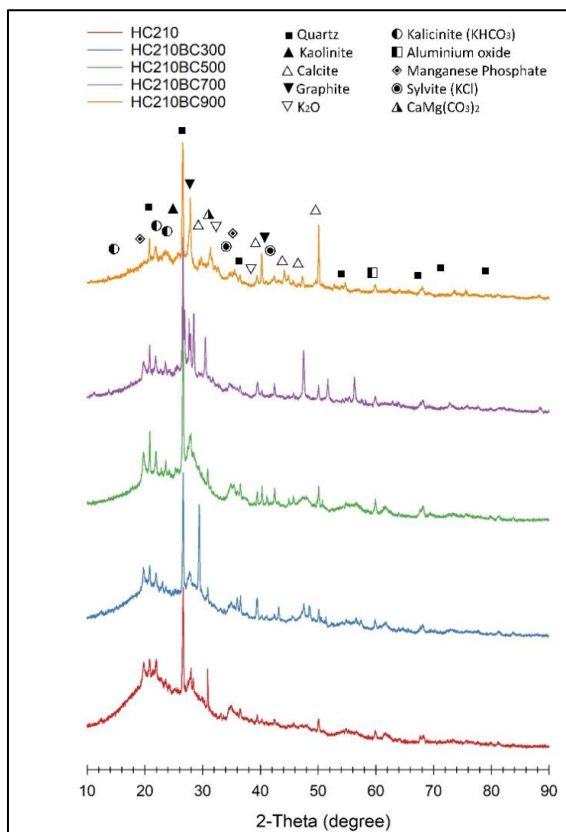
Figure 4.10. XRD diffraction pattern of hydrothermally treated biochars

Figure 4.11 establishes the XRD diffraction pattern of post-modified hydrothermally treated biochars. The related samples showed a similar pattern with pre-modified biochars in Figure 4.9. The pattern demonstrated that the Calcite ($2\theta=29°$) was the most prominent among other crystalline structures in KOH modified samples, whereas the Quartz ($2\theta=26°$) was dominant in urea modified samples. The intensity of Calcite increased with the increase in applied KOH dose. A similar trend was noticed in the formation of Quartz by the increase in urea dose. Differently, the trend

had an exception in HC210BC700KOH0.5 because it showed a recognizable peak of Quartz and Graphite at 2θ=26° and 28°, respectively. This can be due to the reason of low dosage of applied KOH. Similarly, the recognizable peaks of Calcite and especially Quartz became weaker when the chemicals were applied combined. However, it can be deduced that HC210BC700KOH1U10 carries the characteristics of both modification chemicals.
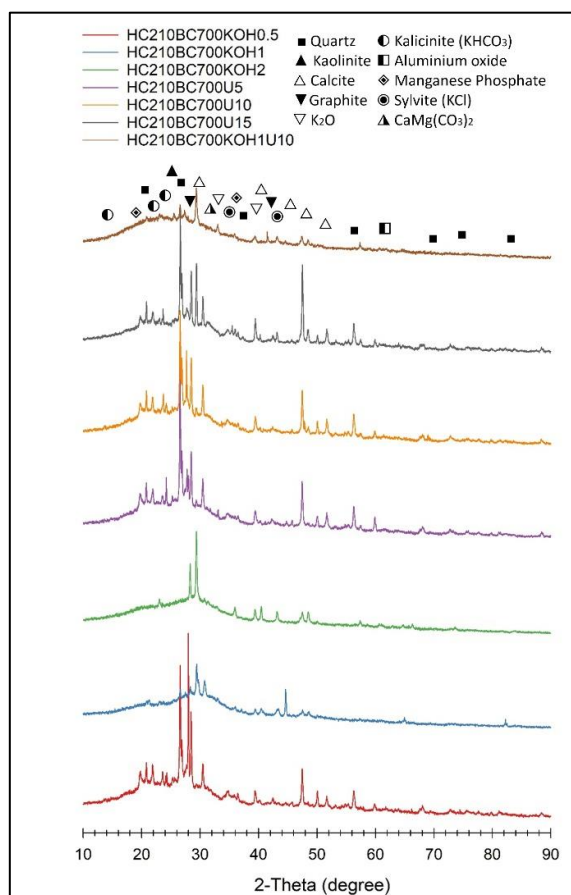
Figure 4.11. XRD diffraction pattern of post-modified hydrothermally treated biochars

Figure 4.12 interprets the XRD diffraction pattern of urea pre-modified hydrothermally treated biochars. As it was seen from Figure 4.9 and Figure 4.11, urea application encouraged the formation of Quartz crystalline structure. While the clearest peaks in U10HC210 were Quartz and Calcite, Graphite composition rose by

increasing the urea dose. Exclusively, the Graphite peak intensity in the U10HC210BC700KOH1 sample surpassed the tension of Quartz and Calcite. Although the combined application of KOH and urea was achieved both in HC210BC700KOH1U10 and U10HC210BC700KOH1 samples at the same dosage level, the difference between XRD diffraction patterns can be clearly seen from the comparison of Figure 4.11 and Figure 4.12. In U10HC210BC700KOH1, both Quartz, Graphite and Calcite levels were increased when the urea was applied prior to the hydrothermal process. Further, it can also be deducted from Figure 4.12 that the intensity of Kalicinite ($KHCO_3$) is lower than in HC210BC700KOH1U10 (Figure 4.12). This affirms that the potassium-containing groups were not likely dominant in the sample.
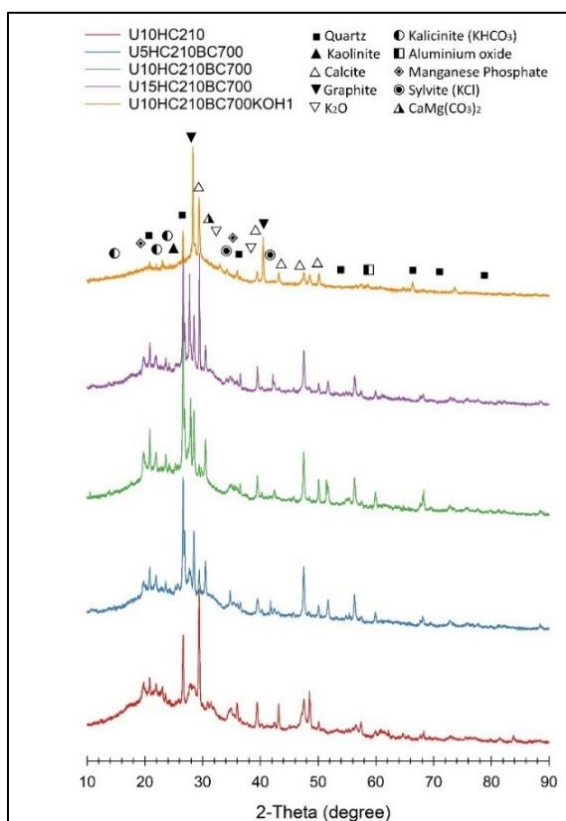
Figure 4.12. XRD diffraction pattern of urea pre-modified hydrothermally treated biochars

Figure 4.13 exhibits the XRD diffraction pattern of hydrothermally treated biochars with various residence times. The spectacular peak appeared in the patterns which belong to Quartz at $2\theta=26°$. Moreover, the intensity of the Quartz structure gradually expanded and reached the greatest in the HC210BC70016h sample. This explains the crystal structure gets intensified with time (J. Yang et al., 2021). The hump became progressively broader in the degree range of $2\theta=18-34°$. On the other hand, the peak demonstrated a decrease by the increase in time.
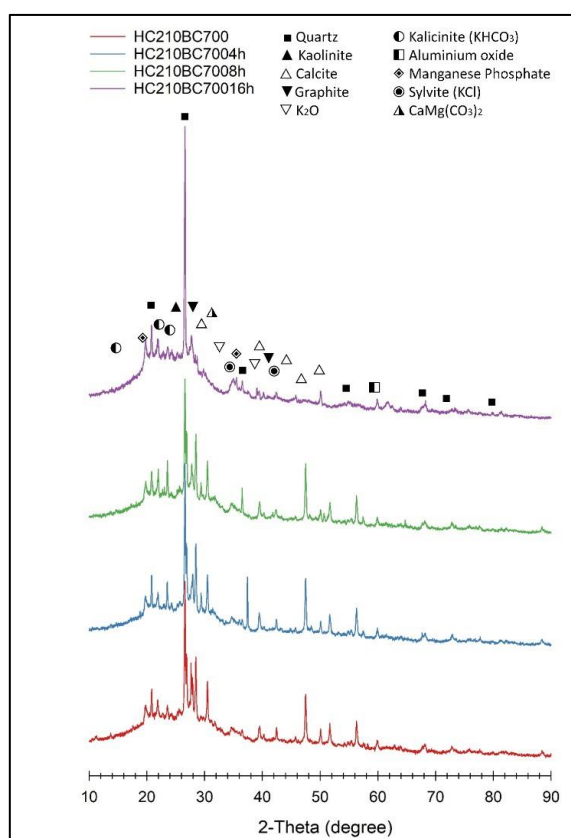
Figure 4.13. XRD diffraction pattern of hydrothermally treated biochars with various residence times

Figure 4.14 reveals the XRD diffraction pattern of hydrothermally treated biochars with various temperatures. The recognizable peaks appeared in compliance with the Quartz, Graphite and Calcite. There occurred a jump in the intensity of Quartz and Graphite in HC230BC700 as the highest hydrothermal temperature. It can be said

that most crystalline structures in the XRD diffraction pattern seemed not affected by the increase or decrease in hydrothermal treatment temperature. Only, Quartz and Graphite held an outrageous rise in the HC230BC700 sample.
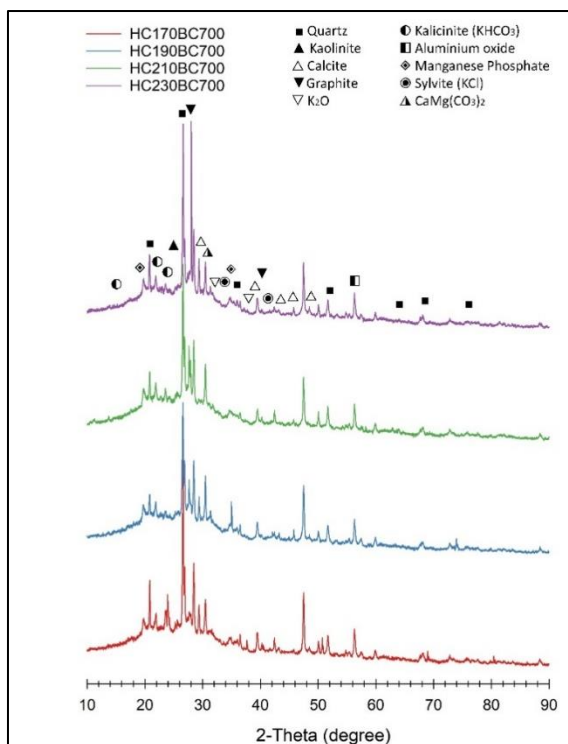
Figure 4.14. XRD diffraction pattern of hydrothermally treated biochars with various temperatures

4.2.5 Change in surface functional groups

In this study, the surface functional groups on produced biochar samples were characterized with FTIR in the range between 400 - 4000 cm^{-1}. The analyzed infrared spectrum of all biochar samples showed an enrichment of functional groups. The infrared absorbance spectrum was filled with main surface-active groups as C─H, C─O, C─O─C, C─N, ─C≡N, ─C═O, NCO─, C─Hn, N─H and NH_3 at the intensity 850, 985, 1200, 1387, 1588, 1610, 2300, 2860, 3263 and 3465 cm^{-1}, respectively. The spectrum demonstrated a very similar trend with the literature listed in Table 3.4.

Figure 4.15 illustrates the FTIR spectra of pristine and modified biochars. From the infrared absorbance spectrum, the alteration in the spectral intensity along pyrolysis temperature in all aforementioned bondages was relatively decreasing and N─H and C─Hn bonds apparently disappeared in BC500, BC700 and BC900. It is the case because, at lower temperatures, the active functional groups can be easily distinguished, whereas, at higher temperatures, most of the groups are diminished (Janu et al., 2021). Therefore, the loss of studied functional groups was observed by the rising pyrolysis temperature. On the other hand, the modified biochar samples with potassium hydroxide (KOH) and urea behaved similarly with BC700 except for few points. In the case of KOH doping, the absorbance intensity of C─O, C─O─C and ─C═O bonds representing the oxygen-containing functional groups gradually increased with the increase in KOH loading dose. Moreover, the absorbance intensity of C─N at 1387 cm^{-1} demonstrated an unexpected peak in KOH modification spectrums. Urea modification resulted in a decline in the carbon-oxygen bondages due to the introduction of amino groups (Lu et al., 2021). A peak at 1387 cm^{-1} belongs to C─N did not show a prominent alteration in urea application, but C─O peak at 985 cm^{-1} thinned out. NCO─, C─Hn, N─H and NH_3 almost had no change in the single KOH or urea-based modified biochar samples' spectrums. Exceptionally, the greatest KOH application dose which was in KOH2BC700, formed a slight intensification in N─H and NH_3 absorbances. However, the combined modification technique created a notable rise in C─O bond intensity and a relative increase in N─H and NH_3 absorbances. It can be due to the interaction of various kinds of elemental compositions introduced.
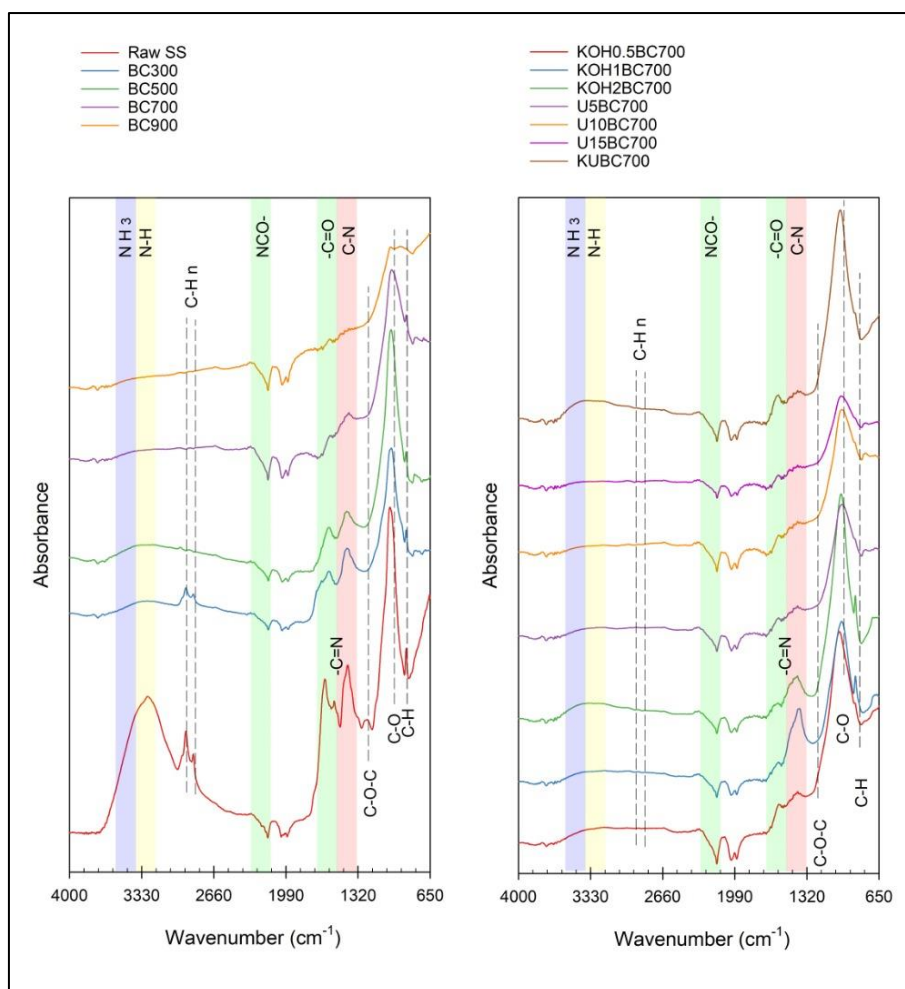
Figure 4.15. FTIR spectra of pristine and modified biochars

Figure 4.16 highlights the FTIR spectra of pristine and modified hydrothermally treated biochars. The trend in the infrared absorbance spectra of hydrothermally treated biochars displayed a very similar pattern with pyrolyzed biochars in Figure 4.15. Other than HC210 and slightly HC210BC300, almost no peaks occurred for C─Hn, N─H and NH$_3$ groups. While NCO─ did not show any difference, C─H, C─O, C─O─C, C─N, ─C≡N, ─C═O surface-active functionalities lost their absorbance intensity compared to pristine biochars in Figure 4.15. In the case of single KOH loading, the impact occurred as same as in the pyrolyzed biochars. It prominently enhanced the absorbance peaks of C─O, C─O─C and ─C═O

105

functionalities, while the spectra of N─H and NH$_3$ have increased at a minor level. Urea dosage barricaded the intensified peaks of ─O, C─O─C and ─C═O; however, it did not create a clear difference in any other spectra. Application of KOH and urea together in HC210BC700KOH1U10 developed the highest peaks of C─O, N─H and NH$_3$ absorbance levels.
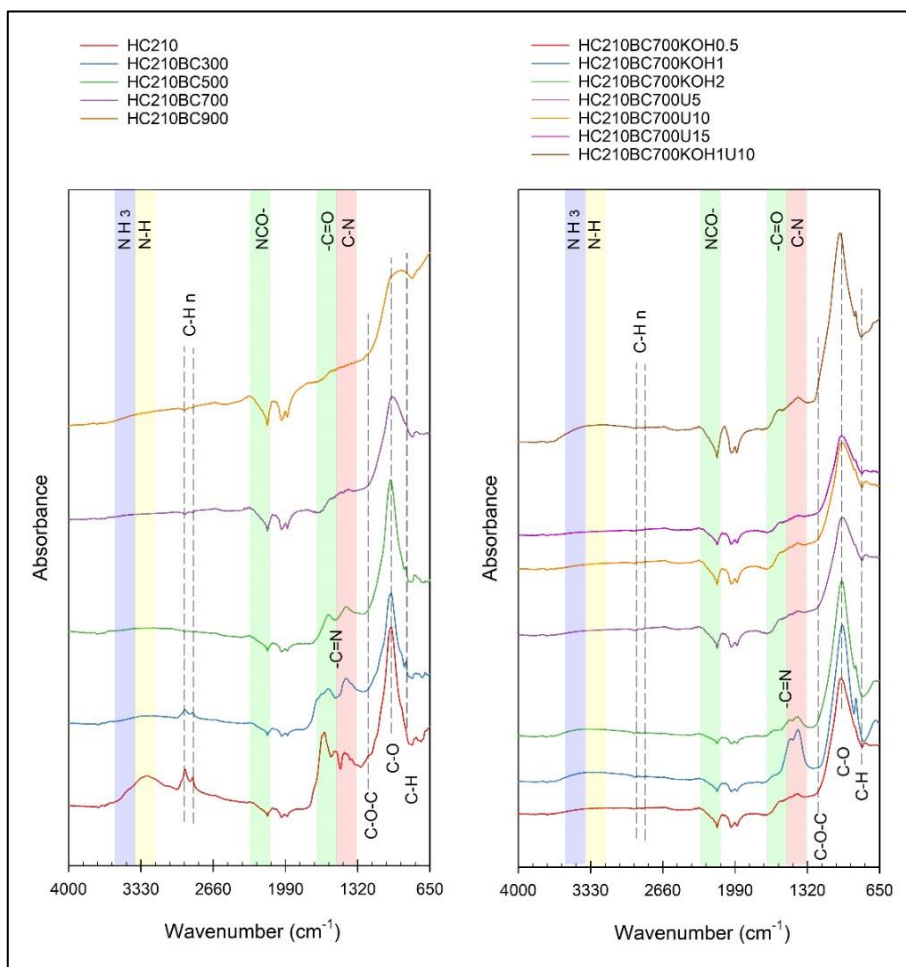
Figure 4.16. FTIR spectra of pristine and modified hydrothermally treated biochars

Figure 4.17 exemplifies the FTIR spectra of time- and temperature-varied hydrothermal biochars and urea pre-modified hydrothermal biochars. The increase in the hydrothermal temperature lessened the absorbance intensity of NCO─, C─N, and C─O functional groups. The changes were a minor scale and this can be due to

106

the increase in hydrothermal temperature. In the case of the hydrothermal operation time, longer residence time encouraged the infrared tension of C—H, C—O and —C=O groups, while NCO— was reversely affected by the longer residence time. Urea pre-modification applied onto HC210 sample (U10HC210) formed a prominent C—N peak at 1387 cm^{-1} which was much weaker in HC210 in Figure 4.16. In U10HC210, the spectra of C—H, C—O, C—O—C absorbance values were also intensified. Hydrothermally treated biochar samples with increasing urea pre-dosed reduced the intensities of surface functional groups as a result of the exertion of pyrolysis at 700 °C (Janu et al., 2021). For instance, the apparent C—N peak dissipated in pyrolyzed samples (U5HC210BC700) and slightly increased by the urea dose. Moreover, it can also be deducted from Figure 4.17 that the peaks of N—H and NH_3 faded away from the spectrum of urea pre-modified and hydrothermally treated biochar materials. KOH addition in U10HC210BC700KOH1 added a modest intensity of N—H, NH_3, —C=N, C—N, C—O—C, C—O and C—H, which has also been observed in Figure 4.15 and Figure 4.17.
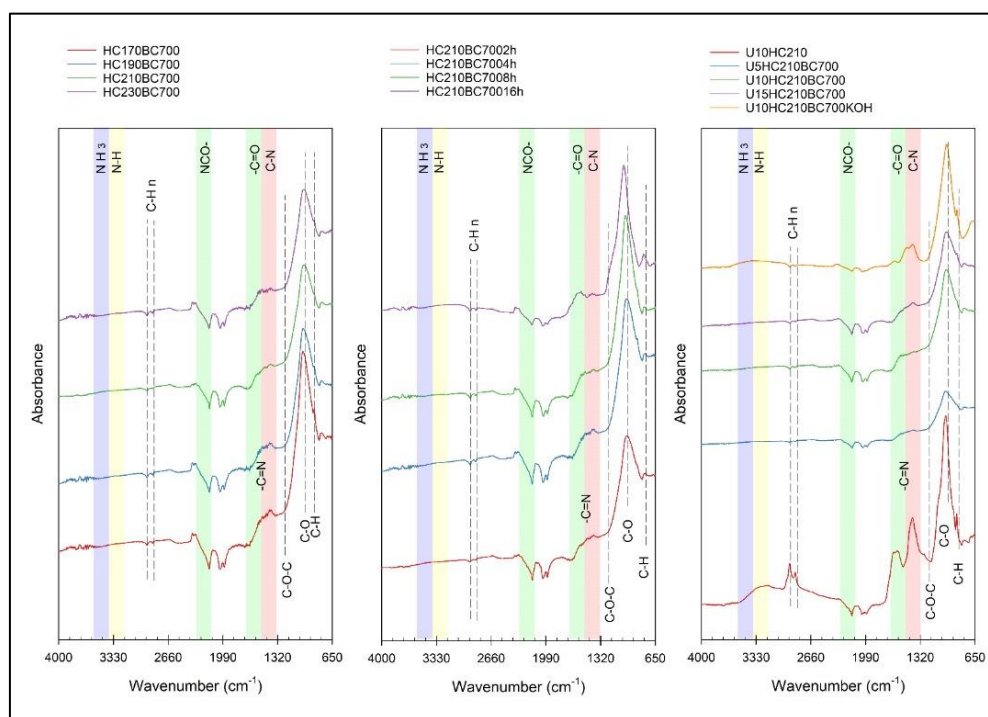
Figure 4.17. FTIR spectra of time- and temperature-varied hydrothermal biochars and urea pre-modified hydrothermal biochars

107

4.2.6   Thermochemical stability of produced biochar samples

The thermochemical stability of produced biochar samples was characterized by the use of Thermogravimetric Analyzer (TGA). In this study, samples were categorized into seven parts, illustrating their thermochemical differences in weight loss (%) and derivative weight (mg/min).

Figure 4.18 depicts the thermochemical properties of the feedstock and related pristine biochar samples pyrolyzed under 300, 500, 700 and 900 °C. Particular weight loss points were observed at different temperature intervals. This can be explained by the presence of various carbonaceous fractions such as volatile organic-C (30–200 °C), labile organic-C (200–380 °C, including aliphatic-C and carbohydrates, predominantly cellulose), recalcitrant organic-C (380–475 °C, including aromatic-C, predominantly lignin and recalcitrant-C), refractory organic-C (475–600 °C; including poly-condensed forms of lipids and aromatic-C) and inorganic-C (600–1000 °C; including carbonates) (Zornoza et al., 2016). In the case of Figure 4.18, low-temperature pyrolyzed biochars (BC300 and BC500) have a higher number of peaks compared to raw sewage sludge. The reason for this is the occupancy of diversified recalcitrant components. However, BC700 and BC900 displayed fewer peaks due to enhanced homogenous structure and were more stable by nature. In a clearer explanation, the sharp peaks of the Raw SS were observed at 350 °C, 460 °C and 540 °C. BC300 did not dissociate from the Raw SS apparently since it also had peaks at 330 °C, 440 °C and 820 °C. BC500 showed a very steep peak at 430°C with the disappearance of peaks at higher temperatures. BC700 and BC900 were observed to have peaks at 500 °C and 560 °C, respectively. These configurations approved the fact that the number of peaks decreases with an increase in pyrolysis temperature and the value of peaks shifts towards higher combustion temperatures due to the remaining resistant components after pyrolysis (Zornoza et al., 2016). While the Raw SS lost its 15% of weight at 340 °C; BC300, BC500, BC700 and BC900 achieved the same weight loss percentage (85%) at 340 °C, 440 °C, 510 °C and 580 °C, respectively.
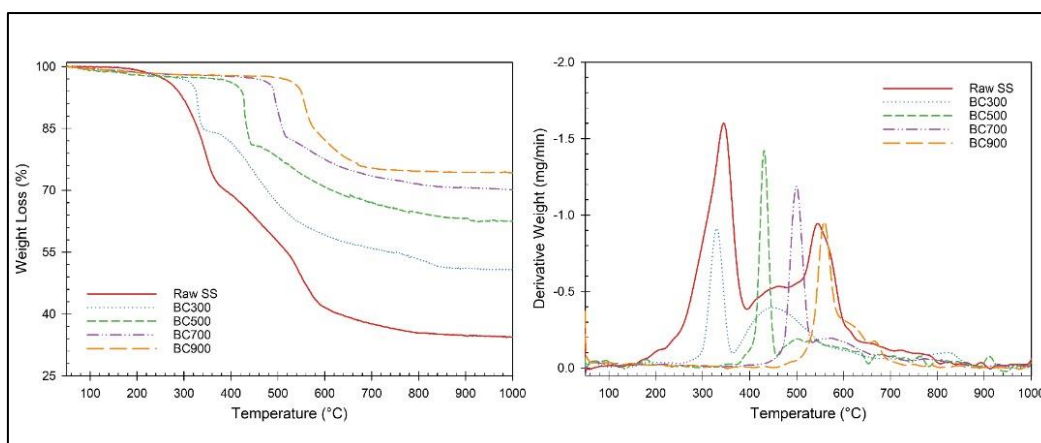
Figure 4.18. Thermochemical properties of Raw SS and pristine biochars

Figure 4.19 interprets the thermochemical properties of pre-modified biochar samples with urea and KOH chemicals in different doses. Since the pyrolysis temperature is 700 °C in all samples, particular weight loss points were analyzed with respect to applied modification techniques. Almost all the peaks in Figure 4.19 occurred at the same temperature interval between 450 – 550 °C due to the equal pyrolysis temperature. However, the peaks of U5BC700, U10BC700, U15BC700, and KUBC700 were considerably sharp, while KOH0.5BC700, KOH1BC700 KOH2BC700 showed broader peaks. In terms of weight loss, the biochar samples with urea modification showed a more recalcitrant nature because their significant weight losses appeared at higher temperatures than the other modified biochars. To illustrate, the weight loss percentage of corresponding samples at 350 °C in Figure 4.19 are as follows: KOH0.5BC700 (93%), KOH1BC700 (93%), KOH2BC700 (92%), U5BC700 (98%), U10BC700 (97%), U15BC700 (97%), KUBC700 (90%).
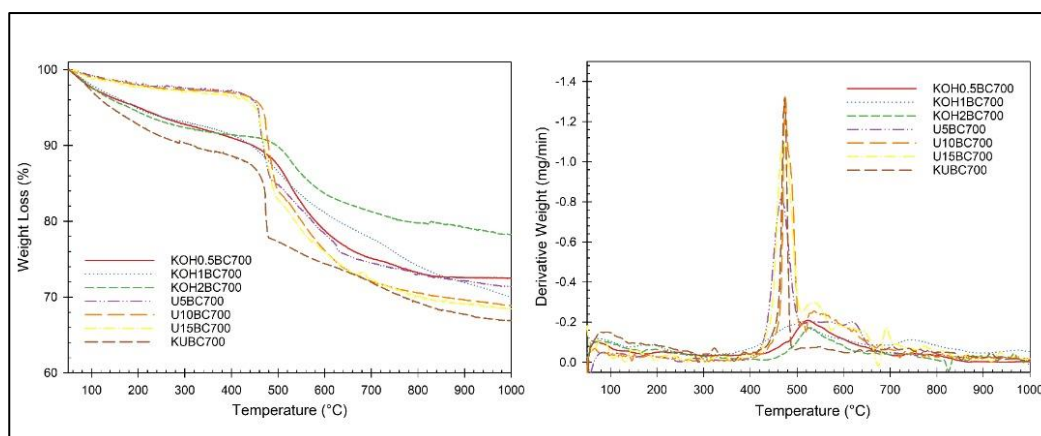
Figure 4.19. Thermochemical properties of pre-modified biochars

Figure 4.20 clarifies the thermochemical properties of hydrothermally treated biochars under the same temperature intervals (i.e., 300, 500, 700 and 900 °C). In a similar manner with pristine biochars, the weight loss periods were distinctive from each other due to the variation in pyrolysis temperatures. The number of peaks can be ordered asHC210>HC210BC300>HC210BC500>HC210BC700>HC210BC900. The peaks shifted towards higher combustion temperatures in the same logic with pristine biochar materials. The sudden decrease in BC900 at the very initial stages of combustion implies the presence of volatile matter in the sample (S. Zhou et al., 2019). Almost no change is observed in HC210 when it is compared to Raw SS. Therefore, it can be said that there is a very slight change when the hydrothermal treatment is applied preliminarily. While the Raw SS lost its 85% of weight at 340 °C; HC210, HC210BC300, HC210BC500, HC210BC700 and HC210BC900 achieved the same weight loss percentage (85%) at 320 °C, 340 °C, 420 °C, 520 °C and 560 °C, respectively.
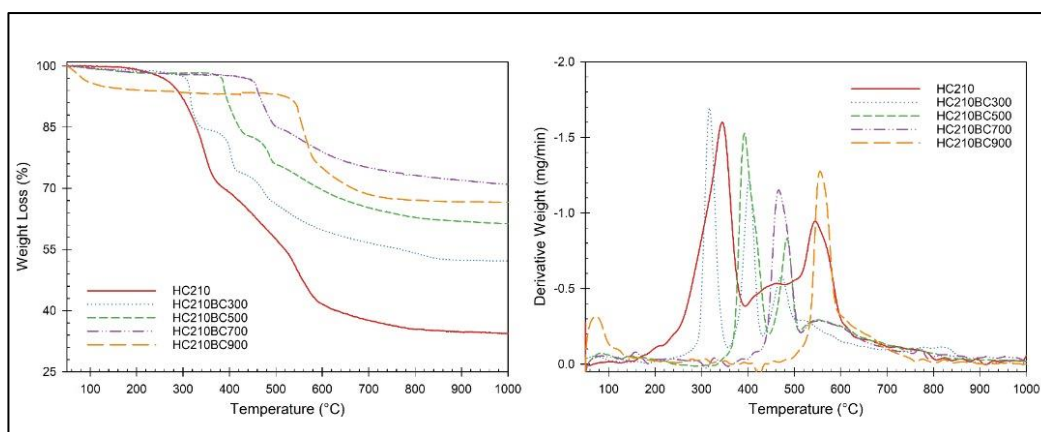
Figure 4.20. Thermochemical properties of hydrothermally treated biochars

Figure 4.21 shows the thermochemical properties of post-modified hydrothermally treated biochars with urea and KOH chemicals in different doses. Since the pyrolysis temperature is 700 °C in all samples, particular weight loss points were analyzed concerning applied modification techniques. Almost all the peaks in Figure 4.21 are shaped at the same temperature interval between 440 – 520 °C due to the equal pyrolysis temperature. However, the peaks of HC210BC700KOH0.5, HC210BC700U5, HC210BC700U10, HC210BC700U15 were considerably sharp, while HC210BC700KOH1, HC210BC700KOH2, HC210BC700KOH1U10 showed broader peaks. In terms of weight loss, the biochar samples with urea modification showed a more recalcitrant nature because their significant weight losses appeared at higher temperatures than the other modified biochars. Surprisingly, HC210BC700KOH0.5 also got involved in this trend and displayed resistance compared to other KOH-modified samples. To illustrate, the weight loss percentage of corresponding samples at 350 °C in Figure 4.21 are as follows: HC210BC700KOH0.5 (97%), HC210BC700KOH1 (93%), HC210BC700KOH2 (91%), HC210BC700U5 (99%), HC210BC700U10 (98%), HC210BC700U15 (98%), HC210BC700KOH1U10 (90%).
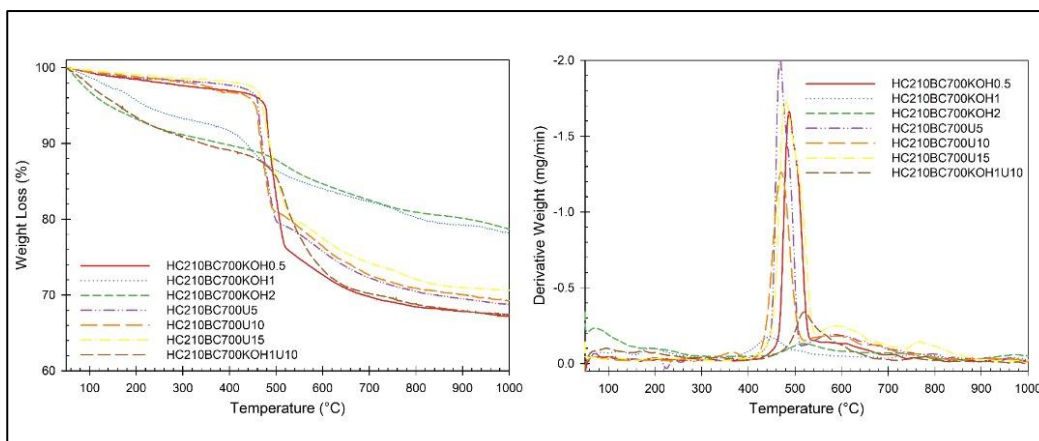
Figure 4.21. Thermochemical properties of post-modified hydrothermally treated biochars

Figure 4.22 illustrates the thermochemical properties of urea pre-modified hydrothermally treated biochars with urea in different doses. Additionally, there is a KOH post-treatment in U10HC210BC700KOH1. Although there are minor differences between applied urea doses, the samples displayed outstanding thermochemical stability by the increased combustion temperature. Three different dosed urea modified samples showed peaks at approximately the same temperature (≈570 °C) and the peaks slightly shifted towards higher temperature values. On the other hand, U10HC210BC700KOH1 did not particularly form a sharp peak except a very small peak at 500 °C. While most of the components were removed in urea modified samples, U10HC210BC700KOH1 held up to 84% of its mass which is due to the presence of hardly degradable inorganic components.

112
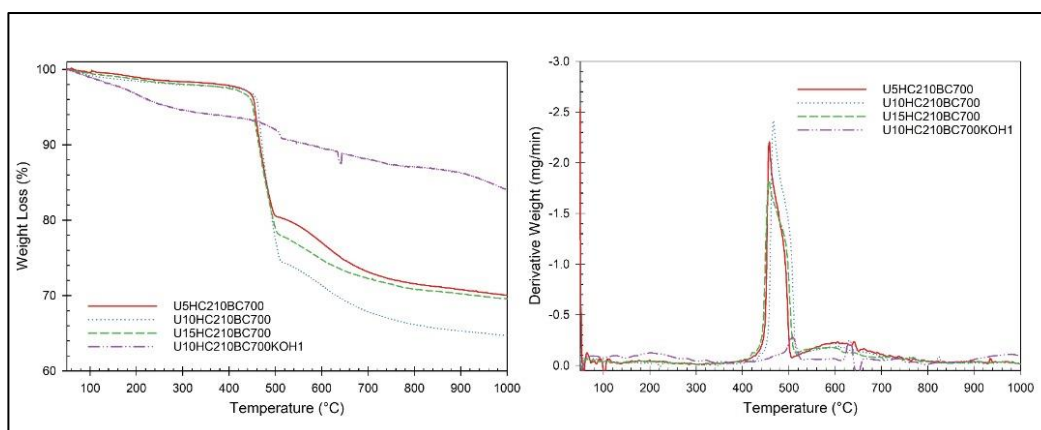
Figure 4.22. Thermochemical properties of urea pre-modified hydrothermally treated biochars

Figure 4.23 interprets the thermochemical properties of hydrothermally treated biochars with various residence times. The default hydrothermal treatment lasts for 2 h at 210 °C. Besides, different hydrothermal residence times were performed (i.e., 4, 8 and 16 h). The peaks of 2, 4, 8 and 16 h biochars were occurred at 460, 480, 470 and 440 °C, respectively. The residence times created a prominent change in the weight losses. While the particular weight loss points of 2, 4, 8 h samples were decreased 13%, 22%, 20%, respectively; the sample hydrolyzed for 16 h showed a steep loss with 28% by weight and most significant loss (≈46%) among other urea modified hydrothermal biochar samples.
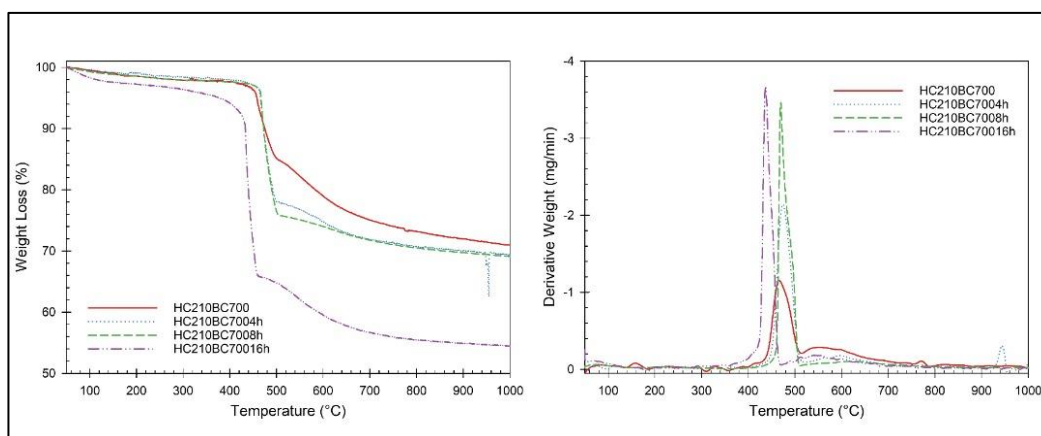
Figure 4.23. Thermochemical properties of hydrothermally treated biochars with various residence times

113

Figure 4.24 represents the thermochemical properties of hydrothermally treated biochars at various temperatures. The default hydrothermal treatment was carried out under 210 °C. Besides, different hydrothermal temperatures were performed (i.e., 170, 190 and 230 °C). The peaks were shaped around 480 °C and they showed a similar trend in weight loss curves. The respective losses for HC170BC700, HC190BC700, HC210BC700, HC230BC700 were 18%, 16%, 12%, 23%, respectively. Therefore, it can be said that there occurred no regular trend by the hydrothermal temperature increase in this study.
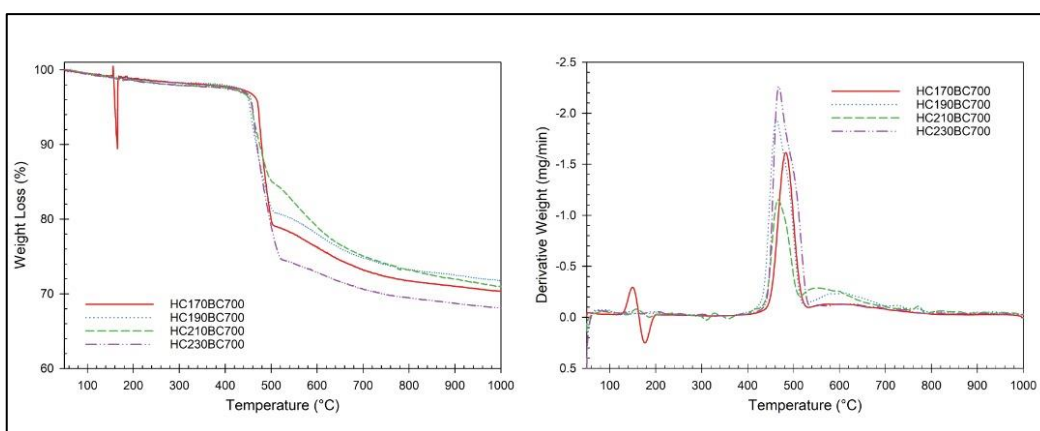
Figure 4.24. Thermochemical properties of hydrothermally treated biochars with various temperatures

4.2.7 Change in surface chemistry and speciation

The change in the surface chemistry and speciation of produced biochar samples were characterized the X-ray Photoelectron Spectroscopy (XPS). XPS-derived surface elemental configuration of analyzed samples is tabulated in Table 4.8. Samples were studied in terms of C, O, N, Fe and K atomic contents.

The surface elemental composition of sewage sludge as the feedstock was characterized in terms of its abundant carbon (71.8%) and nitrogen (4.4%) contents. A gradual decline was observed in the interfacial C- and N-content of biochars with increased pyrolysis temperature while the O-content increased in corresponding samples. It can be due to the fact that the oxidation process adds more oxygen

114

functional groups to the biochar's surface (Abdoul Magid et al., 2021). Since the XPS analysis shows only the interfacial elemental composition of analyzed samples, the decline in the carbon as a result of XPS analysis is not a good indication of the total sample carbon trend. For instance, the elemental analysis results in Table 4.2 and Table 4.3 stated the carbon content of BC900 and HC210BC900 were 47.4% and 48.8%, respectively. They were one of the highest carbon contents in all analyzed biochar samples. However, the XPS results contravened this logic and presented the reverse idea. In order to support XPS analysis, SEM images can be referred because the images show the surface of samples from a microscopic scale. In general, darker parts show the dominant carbon regions where the brighter parts correspond to metallic species presence.

Iron showed its highest level in BC900 and K kept steady its amount in pristine biochars. The addition of KOH increased the iron content by 98% (KOH1BC700) compared to Raw SS. On the other side, urea doping (U10BC700) supported the external nitrogen addition by an increase of 55% than BC700. However, the combined application of KOH and urea kept the K and N content in the mid-range and did not create a substantial difference in the elemental composition. In the case of hydrothermally treated biochars, temperature created the same logic in the elemental results by decreasing the C- and N-content, increasing the O- and Fe-content, and keeping the K-content stable. The post-KOH-modification on hydrothermally treated biochar (HC210BC700KOH1) caused a rise by 99% when it was compared with BC700. Moreover, the oxygen content in HC210BC700KOH1 became the second-highest oxygen concentrated biochar surface after U10HC210BC700KOH1 (O=75.7%). As stated in pyrolyzed biochars, urea doping created a noticeable increase in hydrothermally treated biochars by 41% (HC210BC700U10). The elemental composition of pre- and post-urea-modified samples was at the minor level in HC210BC700U10 and U10HC210BC700. The lowest carbon and oxygen content were observed in the U10HC210BC700KOH1 sample. When we investigated Figure 4.6 in the SEM analysis, U10HC210BC700KOH1 showed a metallic composition at the surface and

organometallic interactions occurred between carbon elements and metallic content. Therefore, the results of XPS supported the SEM images and the carbon can be embedded inside the organometallic compositions.

Table 4.8. XPS derived surface elemental configuration of analyzed biochar and hydrothermally produced biochar materials

Sample	Surface elemental distribution (%)				
	C1s	O1s	N1s	Fe2p3	K2p
Raw SS	71.8	23.4	4.4	0.3	0.1
BC300	69.2	26.0	4.3	0.4	0.1
BC500	51.1	44.0	4.1	0.7	0.1
BC700	50.6	46.1	1.9	1.3	0.1
BC900	38.5	57.9	1.3	2.2	0.1
KOH1BC700	35.2	57.9	0.1	0.5	6.3
U10BC700	55.8	39.1	4.2	0.8	0.1
KUBC700	36.6	59.2	1.9	0.9	1.4
HC210BC300	68.9	26.1	4.7	0.2	0.1
HC210BC500	67.8	27.3	4.7	0.1	0.1
HC210BC700	56.5	39.5	2.2	1.7	0.1
HC210BC900	55.4	40.4	2.2	1.9	0.1
HC210BC700KOH1	19.2	71.8	0.7	1.0	7.3
HC210BC700U10	59.8	36.3	3.2	0.6	0.1
HC210BC700KOH1U10	42.6	54.1	1.2	1.0	1.1
U10HC210BC700	63.2	31.9	3.9	0.9	0.1
U10HC210BC700KOH1	16.2	75.7	0.1	1.0	7.0

The XPS spectra of analyzed samples separated by specific categories are showed in Figure 4.25, Figure 4.26, Figure 4.27, Figure 4.28 and Figure 4.29. The spectra were divided into five different sections (i.e., C1s, K2p, N1s, O1s, Fe2p3) for each figure in order to narrow down the surface elemental configurations. The specific binding energies of surface elemental configurations were taken from Table 3.3 and matched with the results in this study. One key point is to consider that the surface elemental configurations do not have to fully match with the XPS spectra of corresponding samples because while XPS spectra give individual peaks for individual elemental configurations. In contrast, surface elemental distributions indicate the percentages

of defined elements (C, O, N, Fe, K). However, there are miscellaneous types of elements found at the surface of the biochar and the percentages of C, O, N, Fe, K change when they are excluded. Therefore, the surface elemental distribution is not a good indicator of individual peaks in XPS spectra.

Figure 4.25 illustrates the XPS spectra of Raw SS and pristine biochars. The intensity of the C1s peak decreased from raw sewage sludge to BC500, but it showed an increase in BC700 and BC900. The position of peak shifted to the right-hand side in BC500, BC700 and BC900. While the C1s binding energies of Raw SS and BC300 were determined as 283 eV, which corresponds to metal carbide, the shifted peak positions of BC500, BC700 and BC900 can be attributed to C─C at 284.8 eV. In terms of potassium, no distinguishable signals appeared in samples. The feed material used in this study was a nitrogen-rich material. The intensity of N1s is seen as the highest in the Raw SS, then it continuously decreased by the pyrolysis temperature. The binding energies of nitrogen-containing groups increased and created a shift in their position. The nitrogen component was determined as NSi_3 (Si_3N_4) with 398 eV for Raw SS, BC300 and BC500, while BC700 and BC900 with their positional deviation were assigned to NSi_2O (399.8 eV) and C─NH_2 (400 eV), respectively. Oxygen and iron demonstrated the reverse trend so that they intensified towards 900 °C. The XPS signals of Raw SS, BC300, BC700 and BC900 were located at 530 eV (metal oxide), while it was slightly shifted towards the right-hand side in BC500, which corresponds to 532 eV (metal carbonate). Two noticeable peaks of Fe2p3 deconvolution have been observed as Fe2p 3/2 and Fe2p 1/2. The iron elemental configuration increase by the rise in pyrolysis temperature. While Raw SS and BC300 intensities showed up at around 710 eV, they were associated with $FeCl_2$. The positional deviation in the XPS iron spectra of BC500, BC700 and BC900 moved to slightly higher binding energy, approximately 711 eV (Fe_2O_3).
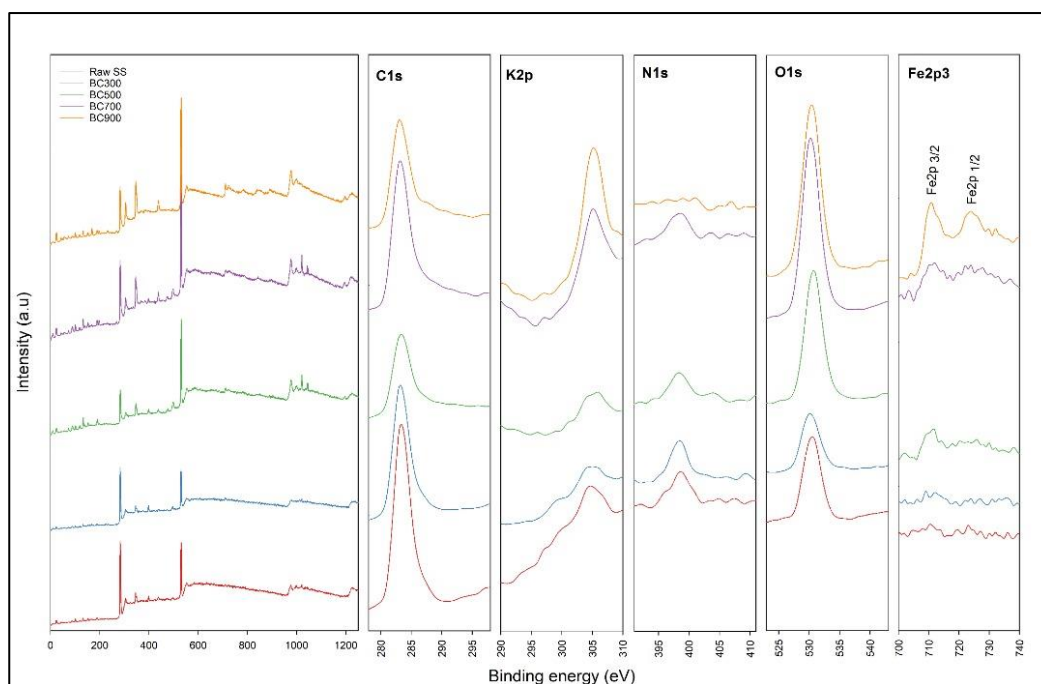
Figure 4.25. XPS spectra of Raw SS and pristine biochars

Figure 4.26 represents the XPS spectra of modified biochar with potassium hydroxide (KOH) and urea chemicals. The C1s spectrum of urea-modified biochar showed the highest peak, while the single KOH application and combined application created the same intensity levels but at a lower level than the urea application. The carbon-containing component is raised as metal carbide with 283 ev in the KOH1BC700 sample XPS spectrum. However, the peak signals deviated towards the right-hand side to ~285 eV (C—C) in U10BC700 and KUBC700 biochars. This shift also occurred in the C-spectra of Figure 4.25. K2p configuration has its most intensified peak in KOH1BC700 and it was followed by KUBC700. It was expected by the addition of K element onto the surface of biochar because U10BC700 biochar did not demonstrate any signal. In KOH-applied samples, the K elemental signal was observed at 293 eV, which can be linked with KO_x from Table 3.3. U10BC700 did not show any difference compared to its pristine version in BC700. Urea addition showed its prominent alteration in U10BC700 and its intensity in N1s configuration was the greatest among the others. While KOH1BC700 and

118

KUBC700 emerged their nitrogen signals at 297 eV (metal nitrides), urea modified sample U10BC700 intensified in between 400 – 401 eV (C─NH$_2$). The intensity of oxygen deconvolution had the most featured peaks in all modified biochars. Although the tension in U10BC700 was also high, KOH1BC700 and KUBC700 showed the greatest levels. The oxygen signals shifted towards the right-hand side in order of KOH1BC700, U10BC700, KUBC700 at 532 eV (metal carbonate). The Fe2p3 spectra peaks of analyzed samples in Figure 4.26 were lower compared to BC700 in the modified biochars. Iron signals did not create a significant difference in positional means, so they both formed at ~711 eV (Fe$_2$O$_3$).
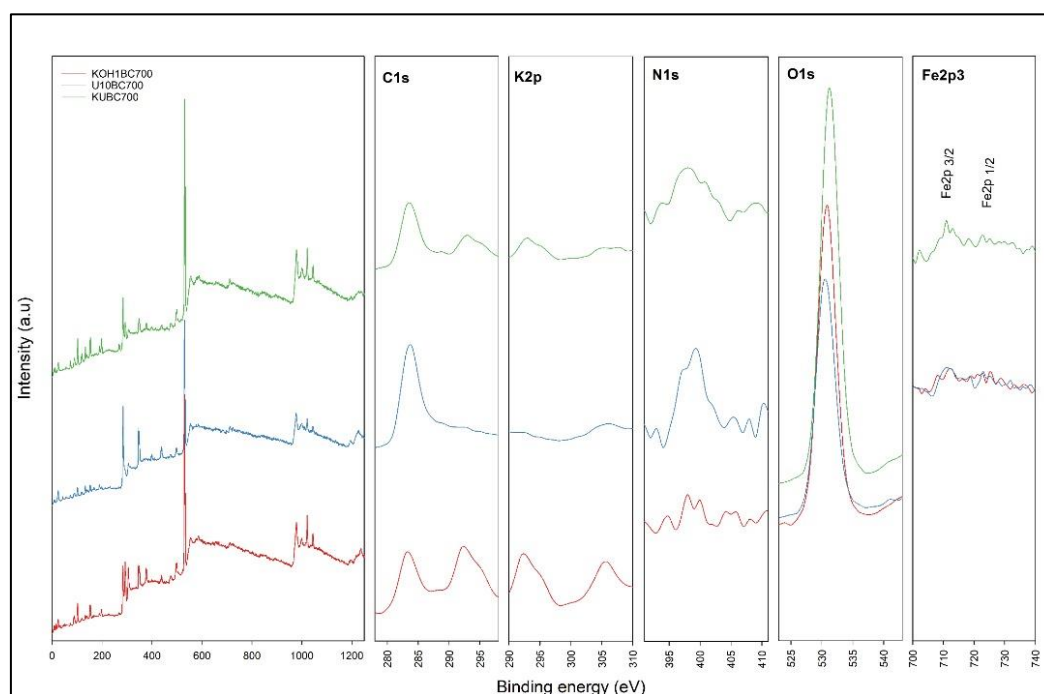
Figure 4.26. XPS spectra of modified biochars

Figure 4.27 reveals the XPS spectra of hydrothermally produced biochars. C1s spectra affirmed a higher level of configurational peaks compared to those in the pristine biochars. The decreasing C1s order was followed in the hydrothermal biochar samples from 300 °C to 900 °C. There were no obvious shifts that occurred and C1s signals of hydrothermal biochars were around 284 – 285 eV. The jump was

119

observed in K2p composition belongs to HC210BC700. In terms of potassium, no distinguishable signals appeared in samples. Nitrogen spectra had higher tension in HC210BC300 and HC210BC500 since the higher temperatures affect the nitrogen content reversely (S. Xu et al., 2021). The N-signals of HC210BC300, HC210BC500 and HC210BC700, can be assigned to NSi_3 (Si_3N_4) with 398 eV, however, a very small right-handed shift was formed in HC210BC900 and its peak corresponded to 400 eV (C─NH$_2$). The trend in O-content showed similar characteristics with the pristine biochars and the intensities increased by the pyrolysis temperature, but their levels were low compared to pristine biochars produced at the same temperatures. O1s signals of HC210BC300 and HC210BC700 samples located at ~530 eV (metal oxide), while the positions of HC210BC500 and HC210BC900 appeared at 532 eV (metal carbonate). Iron spectrum displayed relatively larger peaks in the samples produced at elevated temperatures (HC210BC700 and HC210BC900), while lower temperature biochars were almost the same with each other. HC210BC300 sample showed its iron peak at ~709 eV (FeO), while the other hydrothermal temperatures appeared at 710 – 711 eV (Fe_2O_3).
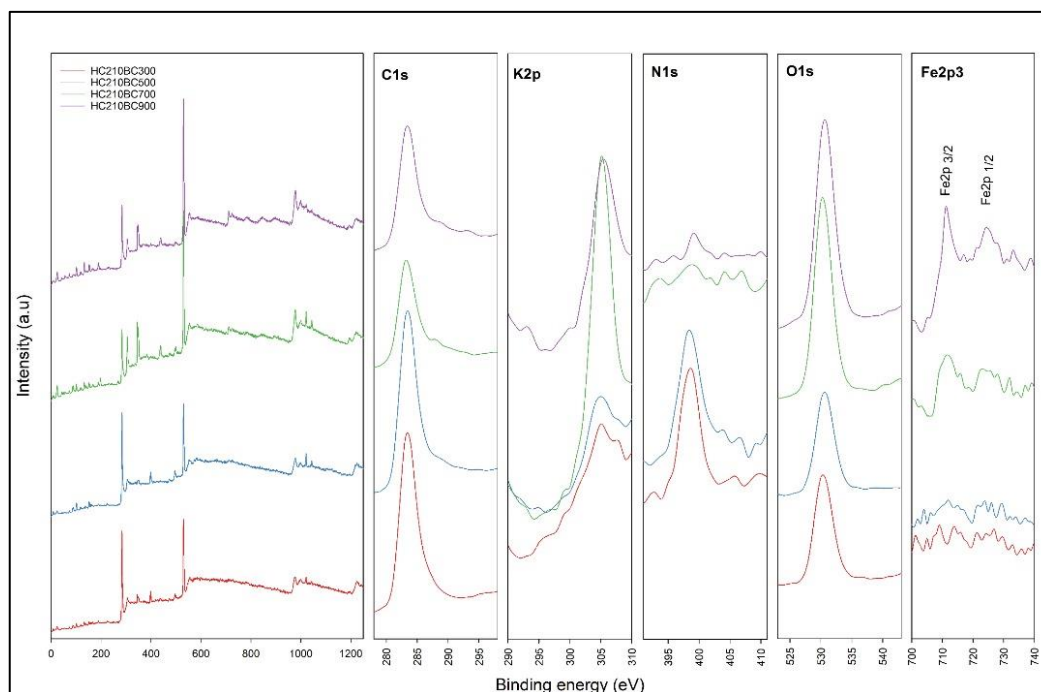
Figure 4.27. XPS spectra of hydrothermally produced biochars

Figure 4.28 exhibits the XPS spectra of post-modified hydrothermally treated biochars. The greatest C1s configurational peak seen in HC210BC700U10 and the other two samples had lower C1s peak levels compared to HC210BC700. Specifically, the C1s peak of HC210BC700KOH1 was very low compared to other biochars. No noticeable shift in C1s developed in the related biochar and the peaks were located at 283 – 284 eV. In contrast, single KOH modification had the highest K2p level of intensity while combined application formed a lower but appreciable peak and single urea stayed far behind that level. That was an expectable result because in the single KOH application, the formation would result in a K-densified composition and the combined application of KOH and urea would create a comparatively lower potassium ratio. About positions of potassium signals, the peaks of HC210BC700KOH1 and HC210BC700KOH1U10 are located at 293 eV (K2p). The N1s spectrum order from highest to lowest was as follows: HC210BC700U10>HC210BC700KOH1U10>HC210BC700KOH1. Thus, the combined chemical modification did not create that much impact as it was in a single urea application. The shift appeared in the N signal of HC210BC700U10 biochar at 398 eV (NSi$_3$ (Si$_3$N$_4$)), while the KOH containing samples showed up at 396 – 397 eV (metal nitrides). One of the greatest oxygen intensity level among all analyzed samples belonged to HC210BC700KOH1 as a result of a single KOH modification. KOH application also affected the O1s peak of the combined modified sample (HC210BC700KOH1U10) compared to its unmodified version (HC210BC700), but the impact was not as high as in the single KOH doping. The oxygen signal of HC210BC700KOH1U10 shifted to the right-hand side and had ~532 eV (metal carbonate) compared to other samples in Figure 4.28. In terms of iron, there were not prominent differences between samples. All three post-modified hydrothermally produced biochar iron tension were lower than in HC210BC700. The positional deviation was formed towards increasing binding energy from HC210BC700KOH1 (709.6 eV) <HC210BC700U10 (710.4 eV) < HC210BC700KOH1U10 (711 eV).

121
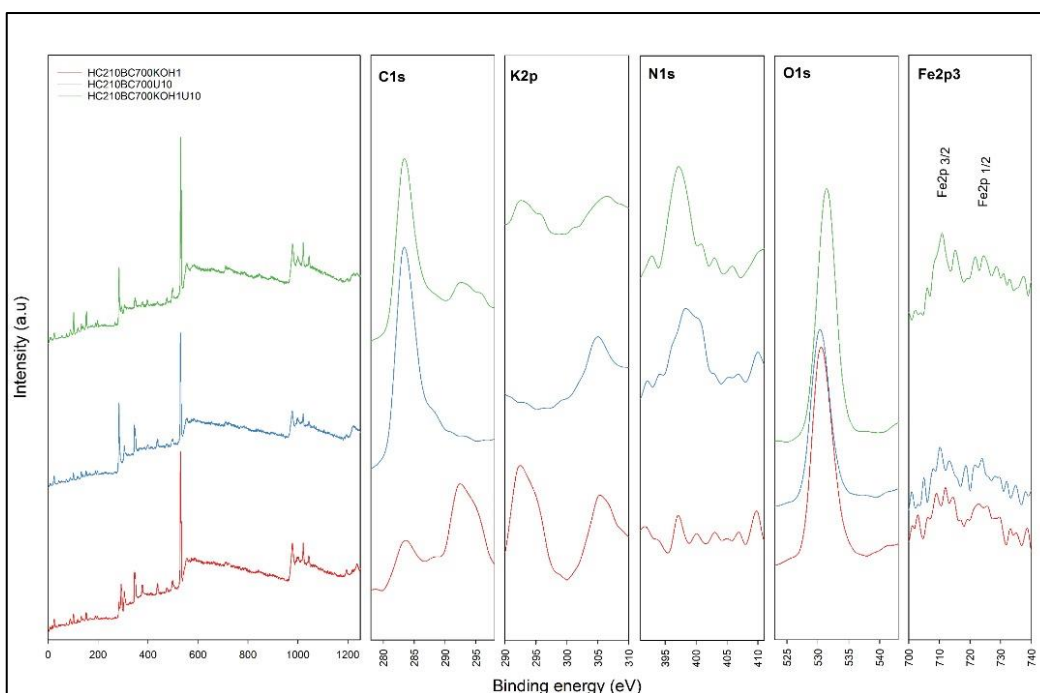
Figure 4.28. XPS spectra of post-modified hydrothermally treated biochars

Figure 4.29 shows the XPS spectra of pre- and post-modified hydrothermally produced biochars. In terms of C1s spectrum, the highest intensity seen in urea pre-modified biochar (U10HC210BC700), while KOH added hydrothermal biochars showed a lower level of tensions compared to HC210BC700. The peak was located at 284 eV (C─C), while modified samples' signals appeared at 286 eV (C─O─C). K2p spectra of analyzed samples were demonstrated expected results and KOH modified samples acquired a high level of intensities. As it was expected, the KOH modified biochars (HC210BC700KOH1 and U10HC210BC700KOH1) demonstrated higher intensity levels and their peaks positioned at 292 – 293 eV (KO$_x$) (Table 3.3). Since any peaks could be observed in the other two samples, no positions could be detected as well. N1s configuration increased the intensity of U10HC210BC700 compared to its unmodified version, whereas the pre-urea-modified sample (U10HC210BC700KOH1) surprisingly had the lowest peak of N1s spectra. While HC210BC700 and HC210BC700KOH1 biochars had their peaks at

397 eV, urea-modified biochars shifted slightly and were located at 399 – 400 eV. The highest oxygen level was observed in combined modified samples (U10HC210BC700KOH1). Although HC210BC700 and U10HC210BC700 showed a moderate level of peaks, they were compared lower than KOH modified samples. Oxygen peaks of all samples were positioned at 530 – 531 eV (metal oxide). In the iron case, other than HC210BC700KOH1 biochar material, other modified and unmodified samples showed moderate iron intensities which were located at 710 – 711 eV (FeCl$_2$) or Fe$_2$O$_3$.
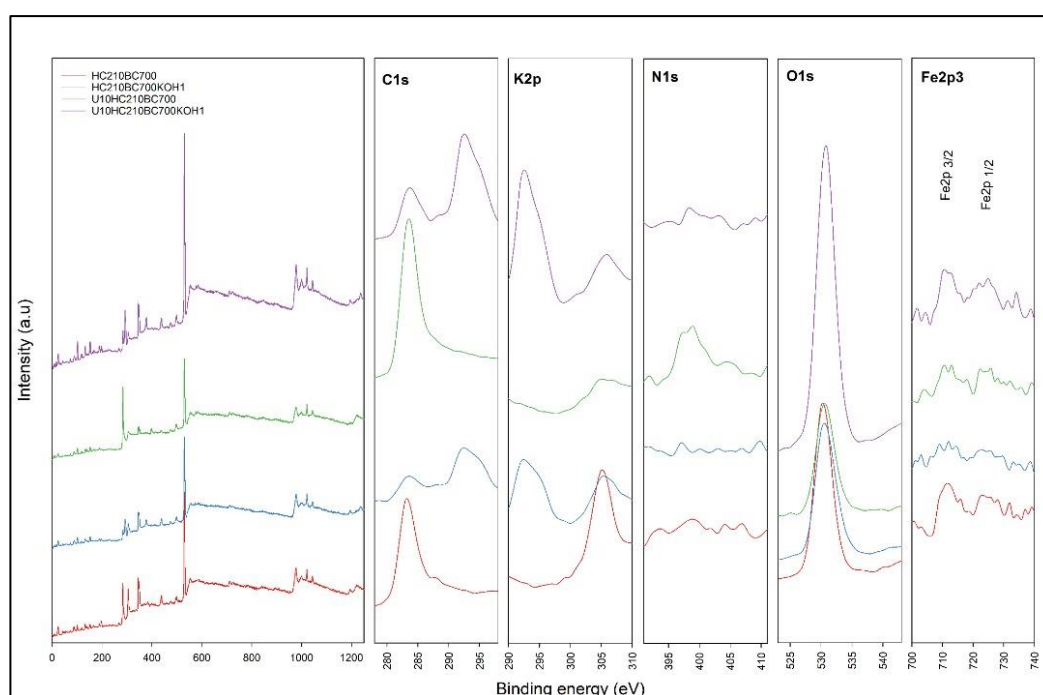
Figure 4.29. XPS spectra of pre- and post-modified hydrothermally produced biochars

4.2.8   Identification of biochar based free-radicals generated for phorate degradation

Detection of biochar-based free-radical generation was investigated by the Electron Paramagnetic Resonance (EPR) Spectroscopy. The methodology used in the EPR analysis was given in Section 3.4.8. In this study, oxygen-centered reactive species

were examined in KUBC700, HC210BC700KOH1U10 and U10HC210BC700KOH1 biochar samples. The spin trap 5,5-dimethyl-1-pyrrolin–N-oxide (DMPO) (Merck, Germany) was used to trap the generated oxygen-centered radicals by EPR spectroscopy.

Liao et al. (2014) suggested that the rising pyrolysis temperature positively influences the EPR peak intensities. However, the pyrolysis temperature of the selected three biochar samples was the same as 700 °C. Therefore, although it has been considered that 700 °C is an elevated temperature, change in pyrolysis temperature is not a valid parameter in this EPR study. Moreover, •OH radicals are strongly attracted by the free radicals in biochar (Liao et al., 2014). •OH and •SO$_4$ radicals take part in the degradation of organic pollutants as a removal mechanism. However, they show dissimilarities within their reaction techniques. As such, •OH engages in the hydrogen-atom abstraction reactions along with electron-transfers, while •SO$_4$ only undergoes the electron-transfer mechanisms (Ashraf et al., 2021). In this study, DMPO trapped the hydroxyl and sulfate radicals from aqueous solutions. As a result, the EPR spectra contained DMPO-OH and DMPO-SO$_4$ signals in three different biochar samples. The magnetic field (G) of the spectrum in which the radical signals are investigated were defined as 320 − 329. Distinguished EPR peaks were observed for all three biochar samples in Figure 4.30. The intensity of the peaks in the EPR spectra indicates the production amount of oxygen focused free-radicals for phorate degradation (Abbas et al., 2020). The clear EPR signals were attributed to •OH and •SO$_4$ as oxygen-centered free radicals, while the noisy peaks were stated as transition metals in the literature (Liao et al., 2014). In this study, since the intensities of the transition metals were very low and presented as mg/kg amounts, they were ignored. Related oxygen-centered free reactive radicals were produced during the pyrolysis and their concentrations were enhanced by the hydrothermal treatment. Enhanced free radical concentration indicates the reactivity of the sample (Mujtaba Munir et al., 2020). 4 signals for •OH and 4 signals for •SO$_4$ in each sample spectrum emerged and their intensities decreased with the order of U10HC210BC700KOH1, HC210BC700KOH1U10 and KUBC700 biochars. The

augmentation in the free radicals is explained by the cleavage of weak bonds in the biochar after hydrothermal treatment and these weak bonds are further separated from each other in the pyrolysis process (D. Zhang et al., 2016). This explains the reason why KUBC700 showed the lowest signal intensities for $\cdot$OH and $\cdot$SO$_4$ free-radicals because no hydrothermal treatment was operated for this sample. In terms of HC210BC700KOH1U10 and U10HC210BC700KOH1 samples, the carbonization treatments exerted on the feedstock and the chemical modification techniques are the same except for the application order. Urea modification was applied prior to the carbonization operation in U10HC210BC700KOH1, while HC210BC700KOH1U10 was formed from the combined post-application of KOH and urea chemicals. The reason why the U10HC210BC700KOH1 sample demonstrated higher intensities could be due to the increased amorphous structure by the urea-based hydrothermal treatment. It can be seen from the SEM image of U10HC210BC700KOH1 (Figure 4.6) that the sample is in the form of larger aggregates and pore sizes are prominently higher. Since U10HC210BC700KOH1 is the pyrolysis of urea-based hydrothermally treated char, the pre-application of urea enhanced porous structure breaks the bonds and follows that pyrolysis further splitted up the remaining weaker bonds. Subsequent to pyrolysis, KOH modification dispersed the pores homogenously and this blend created the greatest EPR signal intensity for $\cdot$OH and $\cdot$SO$_4$ free-radicals.
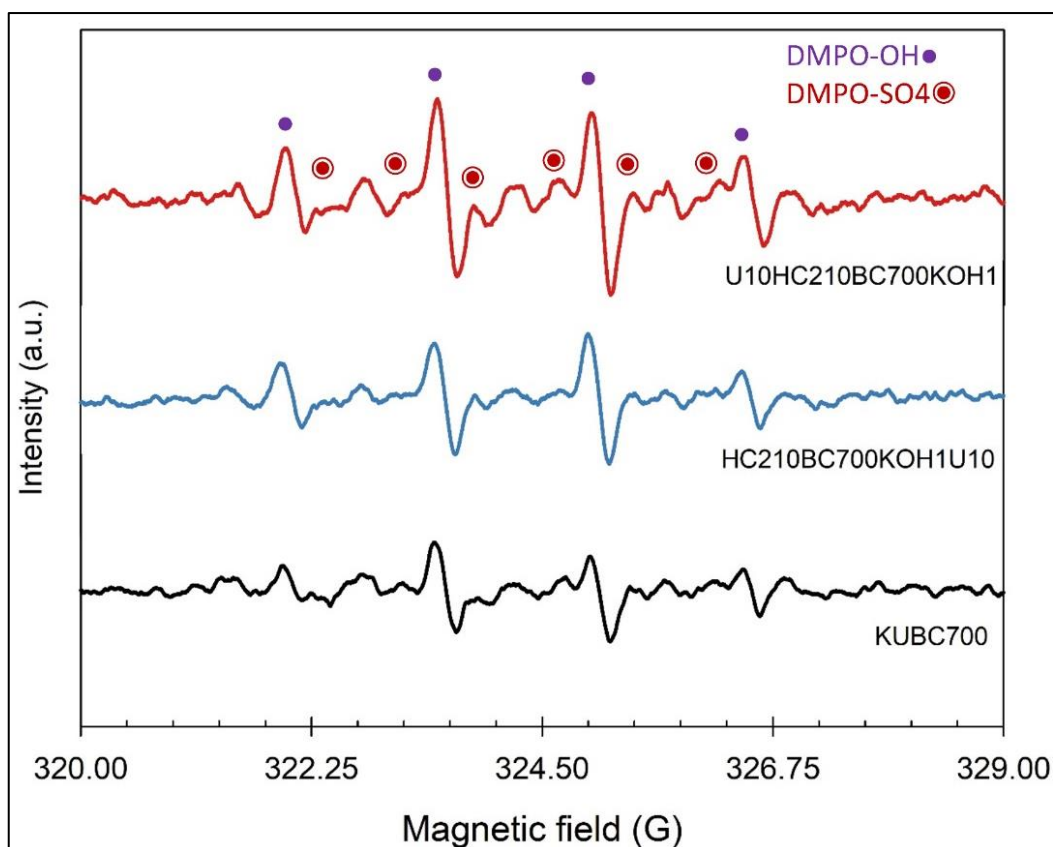
Figure 4.30. EPR spectra of generated oxygen focused free-radicals for three selected biochar samples

4.3 First stage batch removal experiments

Results of the 1st stage batch phorate removal experiments were discussed in this section. The results were presented as phorate removal ratios (C/C_0) and phorate removal efficiencies (%) for each biochar sample. The phorate removal with respect to its initial and final concentrations were given in Table A.1 in the Appendix.

Phorate removal ratios of 1 g/L pristine biochars at 25 °C are shown in Figure 4.31. The increase in the pyrolysis temperature enhanced the removal ability of biochar since BC900 obtained the lowest final concentration. The final phorate removal ratios (C/C_0) at t=5 h of BC900, BC700, BC500, BC300 were 0.15, 0.22, 0.30, 0.40, respectively. Although the sudden drop happened in the first 30 min, the removal gradually continued throughout the experimental time interval.
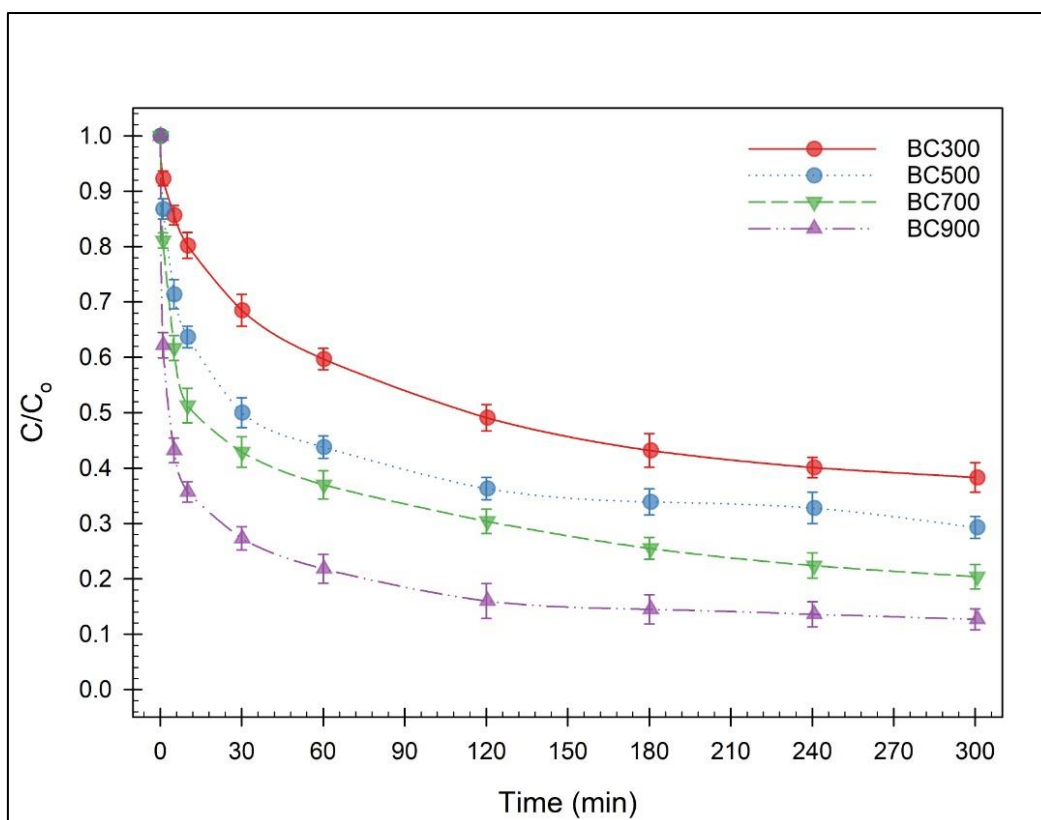
Figure 4.31. Phorate removal ratios of 1 g/L pristine biochars at 25 °C

Corresponding phorate removal efficiencies of 1 g/L pristine biochars at 25 °C are listed in Table 4.9. It can be clearly seen that the removal efficiency showed higher levels at the initial stages of batch sorption experiments, but they continued to proceed up the phorate removal. Since the biochar does and batch temperature were constant in the 1st stage experiments, here the variation between pyrolysis temperature can be examined in Table 4.9. The removals at 1 min demonstrated the increasing phorate removal ability of related biochars with the increase in pyrolysis temperature. As such, 7.7%, 13.2%, 18.9% and 37.8% removal percentages were observed for BC300, BC500, BC700 and BC900, respectively. At the end of the batch experiment, BC300 removed the total phorate 61.7%, while BC500, BC700, BC900 extracted 70.7%, 79.6% and 87.3% of the initial phorate concentration, respectively. These results apparently showed that the increasing carbonization temperature encourages the removal mechanism of phorate in the batch experiments.

127

Table 4.9. Phorate removal efficiencies (%) of 1 g/L pristine biochars at 25 °C

Time	BC300	BC500	BC700	BC900
0	0.00	0.00	0.00	0.00
1	7.66	13.18	18.91	37.77
5	14.28	28.62	38.32	56.85
10	19.79	36.34	48.69	64.35
30	31.48	50.01	57.07	72.73
60	40.31	56.19	63.02	78.15
120	50.89	63.68	69.64	83.98
180	56.85	66.11	74.49	85.52
240	59.93	67.21	77.58	86.40
300	61.70	70.74	79.56	87.28

Figure 4.32 demonstrates phorate removal ratios of 1 g/L KOH and urea modified biochars at 25 °C. Three doses of KOH application, impacts of three doses of urea application and combined modification techniques exerted on related biochars were investigated on the phorate removal ratios in batch experiments. In the case of KOH, increasing KOH: biochar dose from 0.5:1 to 2:1. At the final stage (t=5 h), 0.18%, 0.13% and 0.04% removal ratios (C/C_0) were obtained with an increasing KOH dosage order (0.5, 1, 2), respectively. On the other side, Urea modification was applied as 5%, 10%, and 15%. The efficiency of urea-modified biochar samples was increased with the increasing urea dose. Thus, removal ratios (C/C_0) at the 5th h were accounted as 0.24%, 0.18% and 0.12% for U5, U10, U15 samples, respectively. To make a comparison between individual KOH and urea applications on phorate removal efficiencies, the most promising results were seen in the highest application dose of referred chemicals and the efficiencies were comparable with each other. Most prominently, the combined application of 1:1 dosed KOH and 10% dosed urea (KUBC700) generated an outstanding efficiency showing 100% phorate removal in 2 h.
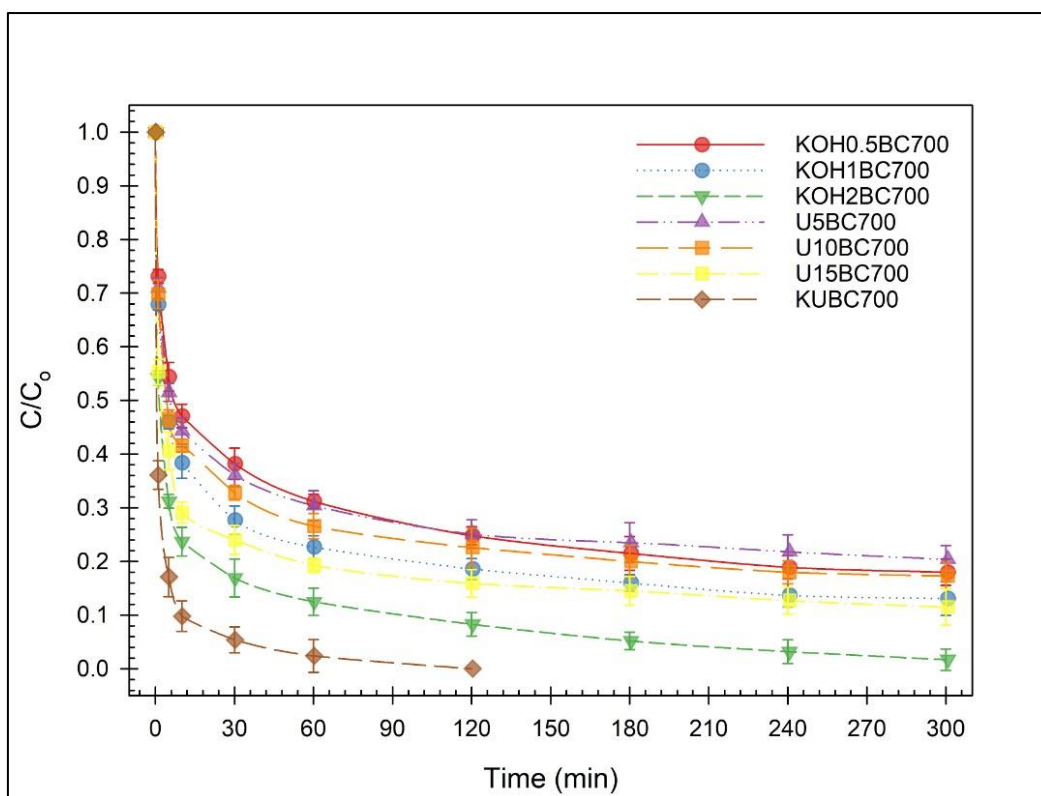
Figure 4.32. Phorate removal ratios of 1 g/L KOH and urea modified biochars at 25 °C

The aforementioned removal ratios of 1 g/L KOH and urea-modified biochars at 25 °C are further described in Table 4.10 concerning their removal efficiencies. It was evident that the increasing chemical dose increased the percentage of phorate removal. This was valid both in the case of KOH and urea modifications. To illustrate, the phorate pesticide removal efficiencies at t=2 h of KOH modified samples 0.5, 1, 2) were determined as 75.1%, 81.4%, 91.7% and urea modified samples (U5, U10, U15) were assessed as 74.9%, 77.3%, 84.1%. The illustration implies the fact that encouraging impact of escalating chemical doses on phorate removal in the batch experiments. The percentage increments in the initial intervals were more remarkable, which was due almost for all batch experiments. Particularly, the KUBC700 sample demonstrated great phorate removal during the experimental period. It created a 64% removal at the first minute and removed 100% of initially

129

added phorate at the 2nd h. Therefore, this revealed that the combination of KOH and urea modifications encouraged the removal mechanism compared to single applications. Above all, the modification techniques by single or coupled chemical application generated more significant differences in the phorate concentration compared to the unmodified sample (BC700).

Table 4.10. Phorate removal efficiencies (%) of 1 g/L KOH and urea modified biochars at 25 °C

Time	KOH0.5BC700	KOH1BC700	KOH2BC700	U5BC700	U10BC700	U15BC700	KUBC700
0	0.00	0.00	0.00	0.00	0.00	0.00	0.00
1	26.85	32.14	45.82	29.06	30.16	44.72	63.90
5	45.60	53.98	68.76	48.47	53.43	59.38	82.87
10	52.88	61.57	76.26	55.74	58.39	70.87	90.15
30	61.81	72.33	83.09	63.90	67.21	76.04	94.56
60	68.76	77.27	87.50	69.64	73.39	80.67	97.61
120	75.15	81.37	91.67	74.93	77.36	84.06	100.00
180	78.46	83.98	94.80	76.48	80.01	85.54	
240	81.11	86.31	96.83	78.24	81.99	87.26	
300	82.01	86.93	98.31	79.56	82.67	88.45	

Phorate removal ratios of 1 g/L hydrothermally treated biochars at 25 °C are presented in Figure 4.33. The pyrolysis temperature increases in the hydrothermally treated biochars enhanced the rate of the phorate removal process. Although the final concentration ratios (C/C_0) were observed as relatively close to each other, the rate between t=1 min to t=4 h dissociated from each other. For example, phorate removal ratio (C/C_0) 0.2 was obtained for HC210BC300, HC210BC500, HC210BC700, HC210BC900 at 102 min, 45 min, 24 min and 5 min, respectively. This indicates that hydrothermally treated biochar pyrolyzed at higher temperatures (i.e., 700 °C, 900 °C) achieved the same level of phorate removal much earlier and faster than low temperature pyrolyzed samples.

130
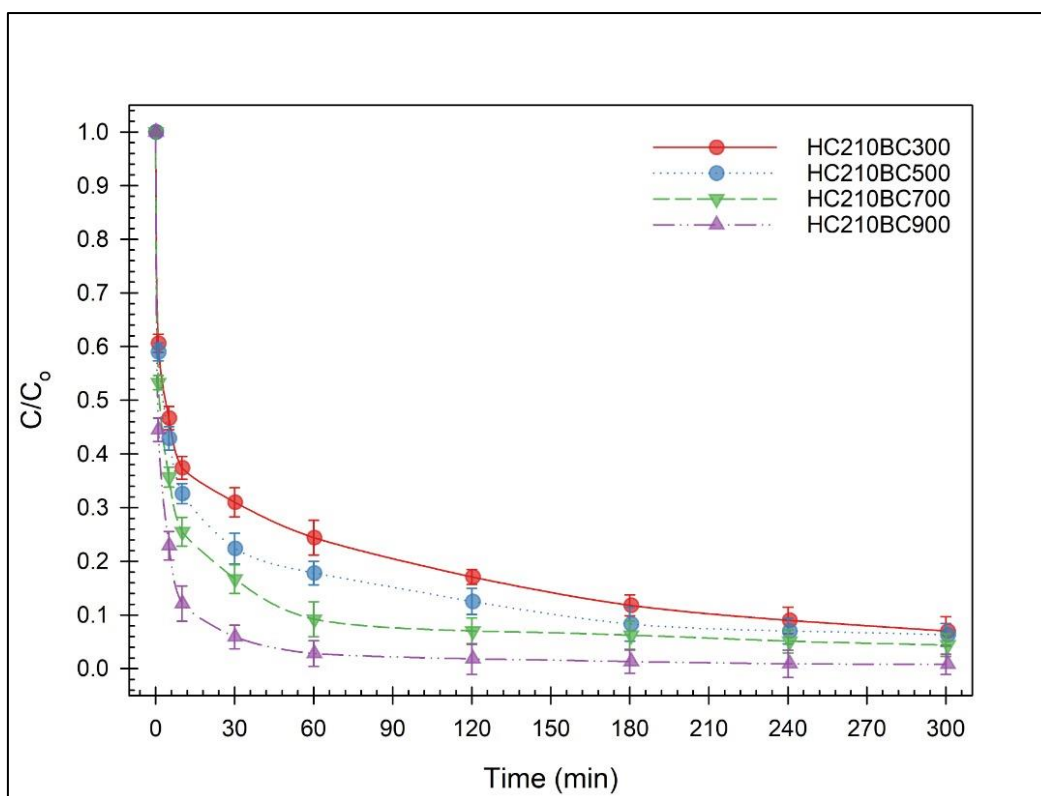
Figure 4.33. Phorate removal ratios of 1 g/L hydrothermally treated biochars at 25 °C

Table 4.11 tabulates phorate removal efficiencies of 1 g/L hydrothermally treated biochars at 25 °C. The results showed that the removal efficiencies of hydrothermally treated biochars were shown greater levels than pristine biochar at the same pyrolysis temperatures. To exemplify, the phorate removal efficiency of BC300 at t=1 min was assessed as 7.7%, while the HC210BC300 at t=1 min had 39.4% removal. The difference in all four samples with various pyrolysis temperatures followed the same manner throughout the batch period. Even though slight differences in the temperature, at the end of the batch experiments, more than 90% removal was obtained in all hydrothermal biochars.

Table 4.11. Phorate removal efficiencies (%) of 1 g/L hydrothermally treated biochars at 25 °C

Time	HC210BC300	HC210BC500	HC210BC700	HC210BC900
0	0.00	0.00	0.00	0.00
1	39.42	40.97	46.70	55.52
5	53.32	57.07	64.35	77.14
10	62.58	67.43	74.49	87.95
30	68.98	77.58	83.31	94.12
60	75.59	82.21	90.81	97.21
120	82.87	87.50	93.04	98.16
180	88.17	91.69	93.81	98.69
240	91.03	93.02	94.94	99.08
300	93.02	93.68	95.64	99.19

Figure 4.34 illustrates phorate removal ratios of 1 g/L KOH and urea modified hydrothermally treated biochars at 25 °C. The scheme explains the impact of varied doses of KOH, urea, and their coupled application as a post-modification technique on hydrothermally treated biochars. Similar results were obtained with the outcomes from Figure 4.32. Escalating doses of single KOH and urea modification generated lower phorate concentrations during the batch experiment. Applied KOH dosages on HC210BC700KOH0.5, HC210BC700KOH1, HC210BC700KOH2 created removal ratios (C/C_0) as almost 0.1, 0.02 and 0.01 at the 5th h, respectively. Likewise, urea doping with an increasing dose (U5, U10, U15) resulted in (C/C_0) = 0.2, 0.1, 0.04 at the 5th h, respectively. The observation between KOH and urea modification showed relatively similar results, but KOH gave more powerful results at a minor scale. While the highest chemical doped biochar samples demonstrated the lowest phorate concentration at the end of the batch experiment, the lowest dosed biochar samples stayed far behind them. Most prominently, the combined application of 1:1 dosed KOH and 10% dosed urea (KUBC700) generated an outstanding efficiency showing 100% phorate removal in 30 min. This time interval was 2 h in Figure 4.32 with post-modified biochars. Therefore, it can be concluded that hydrothermal treatment encourages the phorate removal and modification techniques added more onto that efficiency.

132
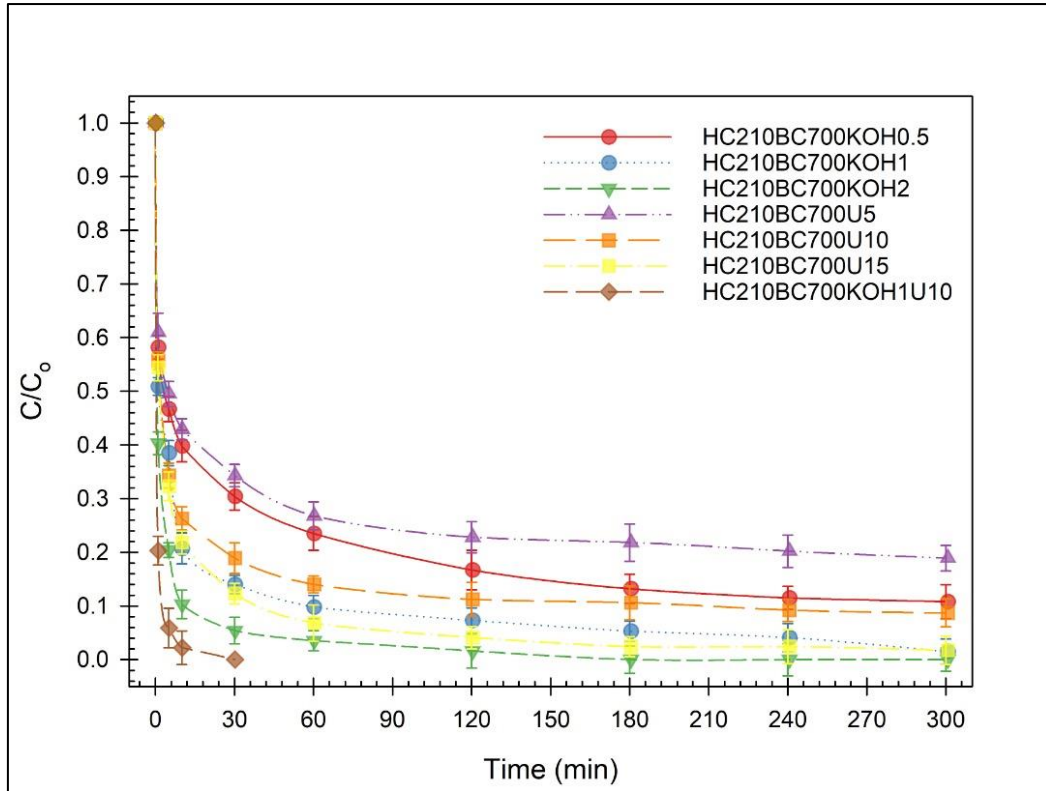
Figure 4.34. Phorate removal ratios of 1 g/L KOH and urea modified hydrothermally treated biochars at 25 °C

Table 4.12 classifies phorate removal efficiencies of 1 g/L KOH and urea modified hydrothermally treated biochars at 25 °C. It can be deducted that more than 50% removal efficiency in every sample was achieved in 5 min. Therefore, the biochar samples performed their highest phorate removal rates at the initial points of the batch experiments. Phorate removal efficiencies of related biochars revealed that the single chemical dose (KOH or urea) positively influenced the removal capacities, but KOH modified samples displayed slightly better results than urea modified samples. When the comparison was made by considering the results in Table 4.10, it was seen that the phorate removal efficiency of simple biochar with the same modification technique showed lower percentages compared to hydrothermally treated biochars in Table 4.12. To exemplify, while the KOH1BC700 sample achieved 84% removal efficiency at the 3rd hour, HC210BC700KOH1 had 94.7% at

t=3 h. Although a minor impact can be added by the difference of pre- and post-treatment order in the methodology, the reason clearly occurred from the exertion of hydrothermal treatment. Extraordinary results were performed by HC210BC700KOH2 and HC210BC700KOH1U10 samples by removing the initially added phorate concentration 100% in 3 h and 30 min, respectively. 100% phorate removal performance was also obtained from KUBC700 in 2 h (Table 4.10).

Table 4.12. Phorate removal efficiencies (%) of 1 g/L KOH and urea modified hydrothermally treated biochars at 25 °C

Time	HC210BC700 KOH0.5	HC210BC700 KOH1	HC210BC700 KOH2	HC210BC700 U5	HC210BC700 U10	HC210BC700 U15	HC210BC700 KOH1U10
0	0.00	0.00	0.00	0.00	0.00	0.00	0.00
1	41.85	49.15	59.71	38.98	44.28	45.60	79.65
5	53.32	61.48	79.56	50.52	65.67	67.65	94.12
10	60.16	79.34	89.71	57.07	73.72	78.24	97.78
30	69.64	85.96	94.56	65.67	81.11	87.72	100.00
60	76.45	90.15	96.55	73.17	85.96	93.24	
120	83.31	92.69	98.42	77.16	88.83	95.89	
180	86.78	94.69	100.00	78.24	89.45	97.65	
240	88.50	95.89		79.78	90.83	97.65	
300	89.16	98.53		81.06	91.32	98.31	

Phorate removal ratios of 1 g/L urea pre-modified hydrothermally treated biochars at 25 °C are detailed in Figure 4.35. Various urea dosages exerted on different materials were studied in detail. It is depicted that the lowest phorate decrease from the initial concentration was achieved in the U10HC210 sample. The removal patterns of urea pre-modified hydrothermally treated biochars with various urea doses (U5, U10, U15) were almost identical throughout the batch experiment and they showed much greater performance than U10HC210. While U10HC210 ended up with 0.4 C/C_0, other three urea pre-modified materials (U5HC210BC700, U10HC210BC700, U15HC210BC700) finalized the batch experiment $C/C_0=0.04$ at the 5th h. Notably, the greatest performance was carried out by U10HC210BC700KOH1 as 100% phorate removal in 30 min, which was similar to

HC210BC700KOH1U10. Therefore, it was deduced that the combined modification with KOH and urea generates 100% removals among other biochar materials.

Figure 4.35. Phorate removal ratios of 1 g/L urea pre-modified hydrothermally treated biochars at 25 °C

Phorate removal efficiencies of 1 g/L KOH and urea pre-modified hydrothermally treated biochars at 25 °C are specified in Table 4.13. The results have shown that the pyrolysis operation catalyzes the removal performance of biochars. Therefore, urea-modified and hydrothermally produced hydrothermally treated biochar at 210 °C (U10HC210) showed the lowest performance sharing the role with BC300 among other samples in this study. In between urea pre-modified hydrothermal biochars, there were comparable outcomes and all three displayed more than 95% phorate removal at the end of the batch experiments. The greatest efficiency was also generated by the combined modification technique (U10HC210BC700KOH1) by

having 100% removal in 30 min. The results were very similar to the HC210BC700KOH1U10 (Table 4.12) sample, which unsurprisingly have almost the same characteristics. In order to compare the effect of pre- and post-modification on phorate removal efficiency, Table 4.12 and Table 4.13 were referred and t=30 min was taken as a parameter. At t=30 min in Table 4.12, the phorate removal percentages of U5, U10, U15 samples were listed as 65.7%, 81.1%, 87.7%; while at t=30 min in Table 4.13, the phorate removal percentages of U5, U10, U15 samples were determined as 85.1%, 87.5%, 91.3%, respectively. There can be observed a slight increase when the pre-treatment was performed instead of post-treatment.

Table 4.13. Phorate removal efficiencies (%) of 1 g/L KOH and urea pre-modified hydrothermally treated biochars at 25 °C

Time	U10HC210	U5HC210BC700	U10HC210BC700	U15HC210BC700	U10HC210BC700KOH1
0	0.00	0.00	0.00	0.00	0.00
1	18.47	51.11	55.52	57.84	79.83
5	35.67	67.65	69.64	73.17	95.26
10	48.02	77.58	78.46	81.55	98.58
30	54.86	85.08	87.50	91.25	100.00
60	58.39	92.64	93.24	94.87	
120	59.71	94.96	95.29	96.48	
180	60.60	95.27	95.81	97.41	
240	61.26	95.78	96.14	97.98	
300	61.48	96.70	97.07	98.18	

Figure 4.36 displays phorate removal ratios of 1 g/L residence time varied hydrothermally treated biochars at 25 °C. Almost identical phorate removal patterns have been achieved by residence time varied hydrothermally treated biochars. The characteristics of the usual hydrothermal biochar are the production under 210 °C for 2 h. It can be deducted that the longer residence times generated more effective phorate removal ratios (C/C_0) but on a very minor scale. At the end of the batch experiments, while usual hydrothermal biochar (210°C, 2 h) had 0.06 C/C_0, the samples stayed longer residence time achieved 0.02 C/C_0 at the 5th h.
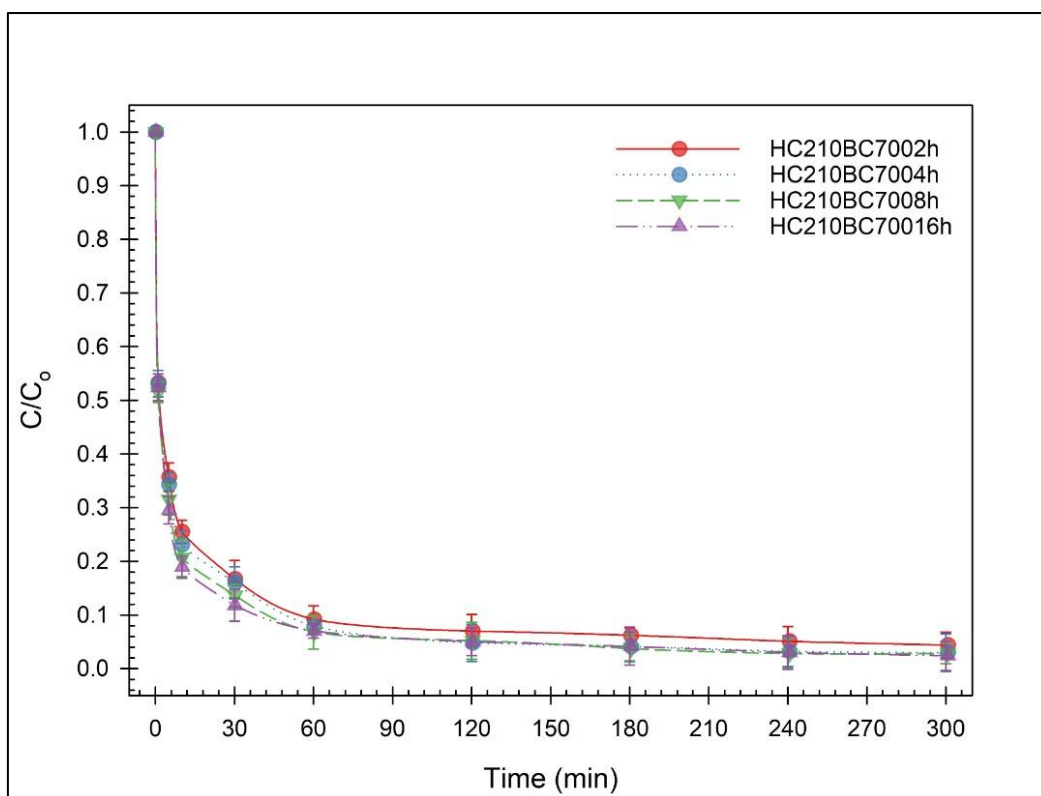
Figure 4.36. Phorate removal ratios of 1 g/L residence time varied hydrothermally treated biochars at 25 °C

Phorate removal efficiencies of 1 g/L residence time varied hydrothermally treated biochars at 25 °C are recorded in Table 4.14. The numerical phorate efficiency percentages were evaluated very close to each other and upgraded in the same manner. They all removed more than 95% of initially added phorate at the end of the batch experiments. Even though the negligible difference, the sample stayed for 16 h in the furnace resulted in a more efficient concentration decrease.

Table 4.14. Phorate removal efficiencies (%) of 1 g/L residence time varied hydrothermally treated biochars at 25 °C

Time	HC210BC7002h	HC210BC7004h	HC210BC7008h	HC210BC70016h
0	0.00	0.00	0.00	0.00
1	46.70	46.92	48.47	47.58
5	64.35	65.67	68.54	70.52
10	74.49	76.92	79.34	81.11
30	83.31	83.98	86.40	88.17
60	90.81	92.14	93.24	93.02
120	93.04	95.22	94.78	95.00
180	93.81	95.89	96.33	95.89
240	94.94	96.77	97.21	96.99
300	95.64	96.99	97.21	97.65

Figure 4.37 shows phorate removal ratios of 1 g/L temperature varied hydrothermally treated biochars at 25 °C. The characteristics of the usual hydrothermal biochar are the production under 210°C for 2 h. The lowest hydrothermal temperature (170 °C) demonstrated the lowest phorate removal performed compared to higher temperatures. The phorate removal ratios (C/C_0) of HC230BC700, HC210BC700, HC190BC700, HC170BC700 samples were recorded as 0.03, 0.05, 0.07, 0.26. As a result, biochars produced temperatures higher than 210 °C displayed similar trends with slight differences, while the biochar produced at 170 °C hydrothermal temperature created a bigger difference and ranked as the lowest among them.
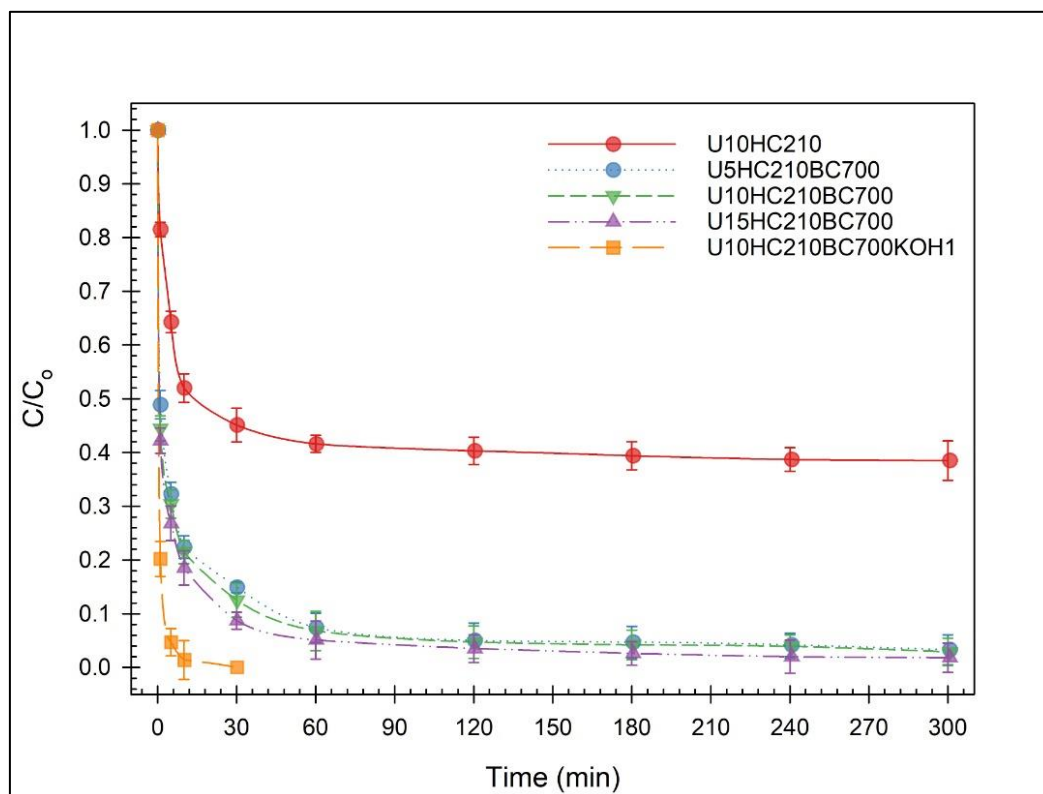
138
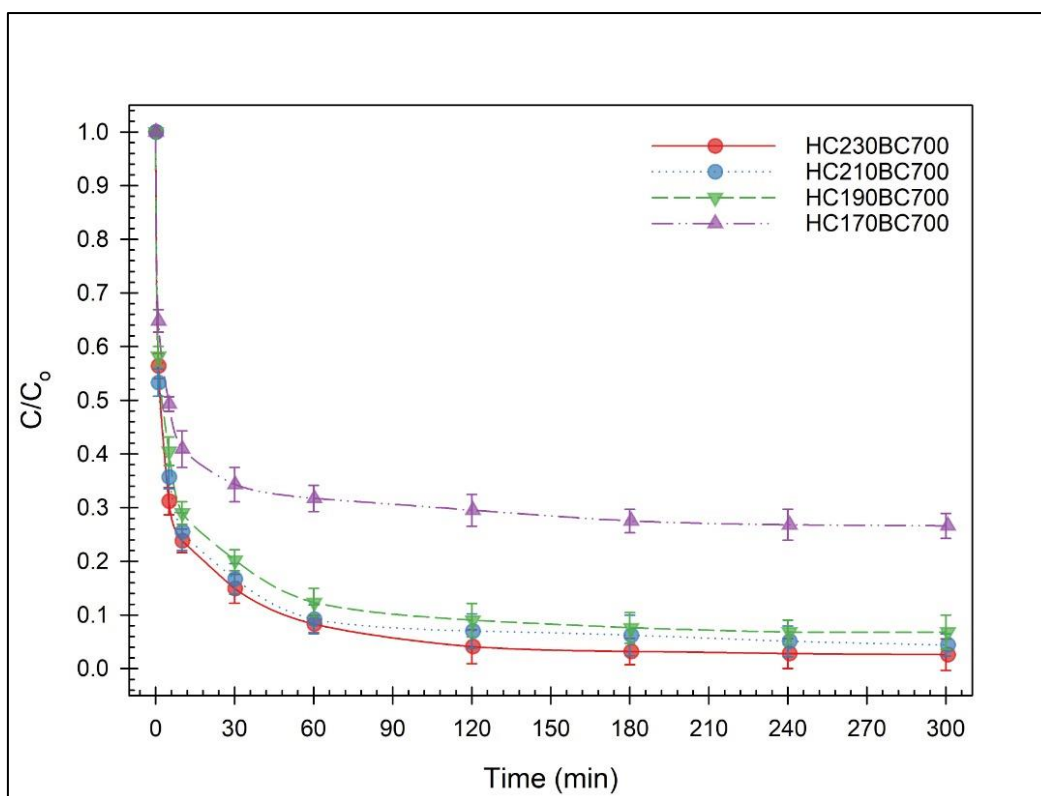
Figure 4.37. Phorate removal ratios of 1 g/L temperature varied hydrothermally treated biochars at 25 °C

Phorate removal efficiencies of 1 g/L temperature varied hydrothermally treated biochars at 25 °C are listed in Table 4.15. At the initial stages, all-temperature varied hydrothermal biochars showed more than 50% removal and the final phorate removal percentages were more than 90% in HC230BC700, HC210BC700 and HC190BC700. The temperature rise (230 °C) added more skill to the usual hydrothermal treated biochar's removal efficiency, while the lower temperature (190 °C) created a small negative impact. However, HC170BC700 achieved poor phorate removal performance and ranked as the fourth-lowest performance biochar after BC300, BC500 and U10HC210 in this study.

Table 4.15. Phorate removal efficiencies (%) of 1 g/L temperature varied hydrothermally treated biochars at 25 °C

Time	HC230BC700	HC210BC700	HC190BC700	HC170BC700
0	0.00	0.00	0.00	0.00
1	43.61	46.70	41.85	35.23
5	68.76	64.35	59.49	50.67
10	76.16	74.49	70.96	59.05
30	85.08	83.31	79.78	65.67
60	91.65	90.81	87.72	68.32
120	95.89	93.04	91.03	70.52
180	96.77	93.81	92.36	72.51
240	97.21	94.94	93.24	73.17
300	97.43	95.64	93.24	73.39

As a result of the 1st stage batch removal experiments, KUBC700, HC210BC700KOH1U10, U10HC210BC700KOH1 biochar samples demonstrated the greatest phorate removal efficiencies overall. HC210BC700KOH1U10 and U10HC210BC700KOH1 removed 100% of initially applied phorate concentration at t=30 min, KUBC700 showed the same removal capability at t=2 h. Phorate removal efficiencies of other samples displayed results likewise and they ended up the batch experiments with more than 80% removal from the initially exerted phorate concentration. Only the samples, which are BC300, BC500, U10HC210 and HC170BC700, were able to remove the phorate by less than 70% and the operational parameters and modification techniques were explained as reasons for the corresponding efficiencies. The conclusion from the 1st batch removal results was the competence of combined application of KOH and urea chemicals on the biochar activation to remove phorate from the solution. The 2nd batch removal experiments were continued with these three promising biochar materials.

4.4 Second stage batch removal experiments influenced by the reaction parameters

Results of the 2nd stage batch phorate removal experiments were discussed in this section with varied temperature, applied biochar dose as well as the reusability and real wastewater tests. The results were presented as phorate removal ratios (C/C_0) and phorate removal efficiencies (%) for each of three biochar samples. The phorate removal with respect to its initial and final concentrations were given in Table A.2, Table A.3, Table A.4 in the Appendix.

4.4.1 Effect of temperature on OPPs removal

The temperature was headed as one of the operational parameters in the 2nd stage batch removal experiments achieved with KUBC700, HC210BC700KOH1U10 and U10HC210BC700KOH1 samples. The usual batch removal was operated under 25 °C in the 1st stage experiments. The shaker where the batch experiments were being carried out was set to the temperatures of 30 °C, 35 °C and 40 °C and their impacts on phorate removal were examined in this section.

Figure 4.38 demonstrates the effect of 1 g/L KUBC700 on the phorate removal under varying temperatures. KUBC700 totally eliminated the samples in 2 hours and 4 h under 25 °C and 30 °C, respectively. However, 0.09 and 0.12 phorate removal ratios (C/C_0) were achieved for the experiments carried under 35°C and 40°C, respectively. Therefore, the conclusion that can be taken from here is the negative impact of temperature increase on the phorate removal. At higher temperatures, there is a chance of low removal since some materials work effectively at the lower temperatures. So, KUBC700 showed enhanced performance at 25 °C, which means the chemical activity to remove phorate for KUBC700 samples were escalated around 25 – 30 °C.
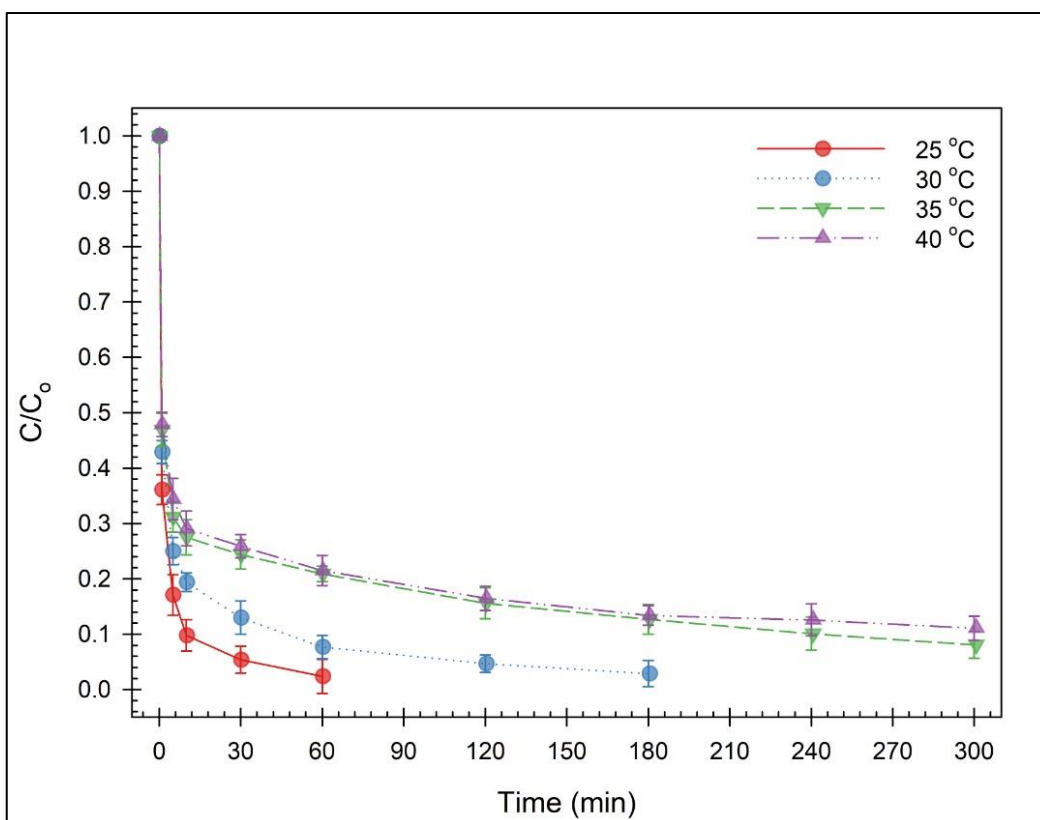
Figure 4.38. Effect of 1 g/L KUBC700 on the phorate removal under varied
temperatures

Phorate removal efficiencies (%) of 1 g/L KUBC700 sample at temperatures 25 °C,
30 °C, 35 °C and 40 °C were tabulated in Table 4.16. The results have shown that
the rise in the batch experimental temperature created a disadvantage for the phorate
removal. While the experiments carried under lower temperatures could achieve the
total phorate removal, the phorate removal efficiency was dropped up to 91.9% and
88.9% at 35 °C and 40 °C at the end of the batch experiment (t=5 h), respectively.
The rate of the removal operation gradually decreased with the increasing
temperature since the chemical activity of KUBC700 decreased.

Table 4.16. Phorate removal efficiencies (%) of 1 g/L KUBC700 under varied temperatures

Time (min)	Temperature (°C)			
	25	30	35	40
1	63.90	57.07	53.10	52.11
5	82.87	74.98	68.76	65.56
10	90.15	80.65	72.51	70.85
30	94.56	86.95	75.59	74.07
60	97.61	92.29	79.12	78.46
120	100.00	95.31	84.42	83.51
180		97.12	87.33	86.58
240		100.00	89.93	87.44
300			91.89	88.89

In the case of the HC210BC700KOH1U10 sample, the conclusions became identical with the case in Figure 4.38 and the increase in the batch operational temperature lessened the decrease in the performance. The sample performance has already been known from the results of 1st stage batch experiments (Figure 4.34) and it had 100% pesticide removal in 10 min. With the increase in the batch temperature from 25 °C to 40 °C, the remaining phorate concentration in the solution became higher in Figure 4.39. HC210BC700KOH1U10 had the total pesticide removal in 30 min and 4 h under 25 °C and 30 °C, respectively. The phorate removal ratios (C/C_0) of biochars performed under 35 °C and 40 °C were determined as 0.06 and 0.19, which were comparable with KUBC700 at the same temperatures.
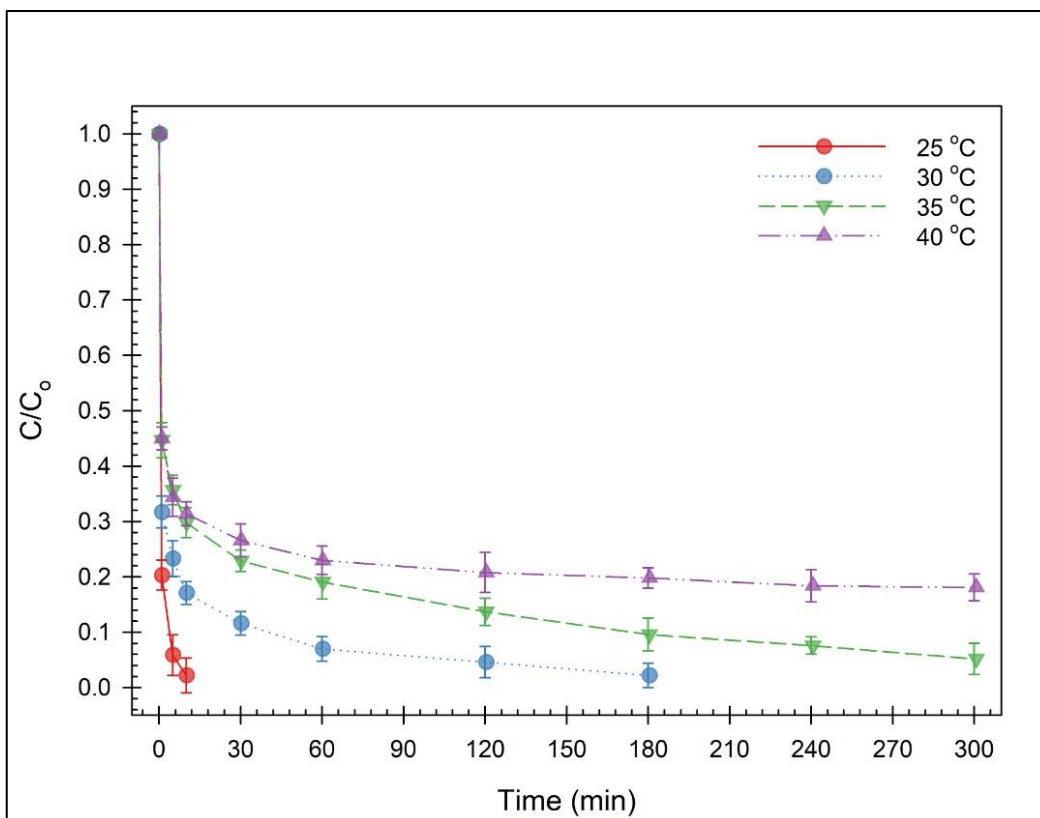
Figure 4.39. Effect of 1 g/L HC210BC700KOH1U10 on the phorate removal under varied temperatures

Table 4.17 gives the details of phorate removal efficiencies (%) of 1 g/L HC210BC700KOH1U10 sample under 25 °C, 30 °C, 35 °C and 40 °C. The impact of incrementing batch temperature was unfavorable for the phorate removal rate. Therefore, the lowest value was observed as 81.9% removal at 40 °C. This supports the idea of having the best chemical performance at lower temperatures.

144

Table 4.17. Phorate removal efficiencies (%) of 1 g/L HC210BC700KOH1U10 under varied temperatures

Time (min)	Temperature (°C)			
	25	30	35	40
1	79.65	68.32	55.30	54.97
5	94.12	76.70	64.35	65.55
10	97.78	82.87	70.21	68.61
30	100.00	88.39	77.09	73.43
60		93.02	80.92	77.02
120		95.40	86.27	79.21
180		97.78	90.38	80.24
240		100.00	92.39	81.60
300			94.80	81.87

U10HC210BC700KOH1 showed the same and highest performance with HC210BC700KOH1U10 in the 1st stage batch removal experiments. The impact of the operational batch temperature gave different results in Figure 4.40 and there occurred desorption at 35 °C and 40 °C. In some cases, the rising temperature increases the chance of desorption phenomena. When the dissolution happens, the contaminant tries to interact with biochar's surface in a short time of period. In that sense, the concentration of contaminant can increase where the dissolution occurred. In this study, U10BC210BC700KOH1 dissolved at 35 °C and 40 °C, and the phorate removal ratios (C/C$_0$) raised to 0.07 and 0.55, respectively. The dissolution of phorate started from t=4 h and t=2 h for 35 °C and 40 °C, respectively. After these points, phorate concentration in the solution increased until the end of the batch experiment.
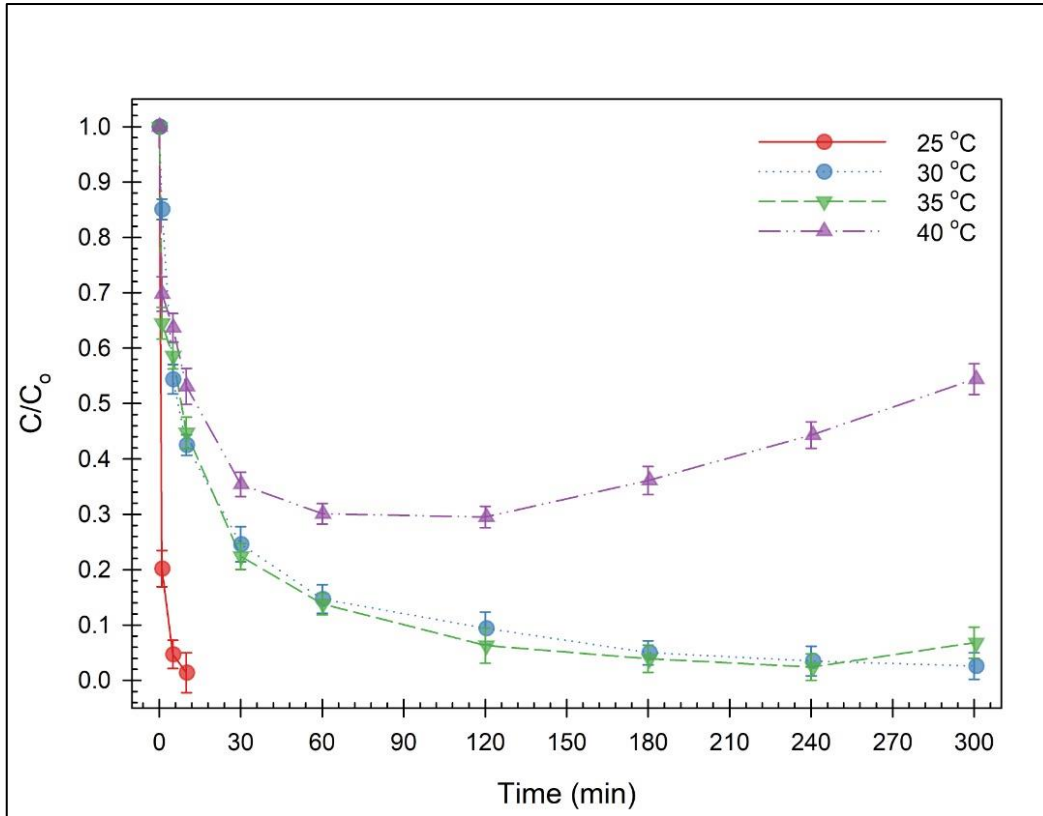
Figure 4.40. Effect of 1 g/L U10BC210BC700KOH1 on the phorate removal under varied temperatures

Table 4.18 represents the timewise phorate removal efficiencies (%) of 1 g/L U10HC210BC700KOH1 under varied temperatures. U10HC210BC700KOH1 totally removed phorate from the solution under 25 °C in 30 min, the same as in HC210BC700KOH1U10. However, at 30 °C, 35 °C, 40 °C, the efficiency considerably decreased compared to results in Table 4.17. Unlike KUBC700 and HC210BC700KOH1U10, there occurred desorption in U10HC210BC700KOH1 at 35 °C and 40 °C. The highest removal (97.7%) was observed at t=4 h under 35 °C, while it was 70.5% under 40 °C at t=2 h. After these removal percentages were obtained, the phorate concentration in the solution started to increase as a result of desorption phenomena and they reached up to 93.2% and 45.6% at the end of the batch experiments. This shows that the increasing batch operational temperatures

146

derived the dissolution chance in U10HC210BC700KOH1 and its chemical activity decreased.

Table 4.18. Phorate removal efficiencies (%) of 1 g/L U10HC210BC700KOH1 under varied temperatures

Time (min)	Temperature (°C)			
	25	30	35	40
1	79.83	14.94	35.45	30.16
5	95.26	45.60	41.41	36.34
10	98.58	57.51	55.30	46.92
30	100.00	75.37	77.58	64.57
60		85.30	86.18	69.86
120		90.59	93.68	70.52
180		95.00	96.11	63.90
240		96.55	97.65	55.74
300		97.43	93.24	45.60

At the end of the 2nd stage batch removal experiments under mixed batch operational temperatures, it can be concluded that the batch temperature has a reverse impact on the phorate removal. All three biochar materials achieved 100% phorate removal at 25 °C; however, the removal performance decreased by the increasing temperature from 25 °C to 40 °C. As an exception, the U10HC210BC700KOH1 sample showed dissolution at 35 °C and 40 °C and the phorate removal efficiency at 40 °C lessened up to 45% at the end of the batch experiment. This suggests that these biochars modified with the combination of KOH and urea have the most significant chemical activity at lower temperatures.

4.4.2 Effect of biochar dosage on OPPs removal

Biochars with different doses were performed in the second stage of batch experiments. The experiments were achieved with three samples: KUBC700, HC210BC700KOH1U10 and U10HC210BC700KOH1. The exerted biochar dosages were 0.2 g/L, 1 g/L, 5 g/L and 15 g/L. The usual dose in the 1st batch analysis

was performed as 1 g/L. Therefore, lower and higher doses compared to 1 g/L usual biochar dose were tried in order to see the influence of applied biochar dose on the phorate removal efficiency. The effects of various KUBC700, HC210BC700KOH1U10 and U10HC210BC700KOH1 biochar doses on the phorate removal at 25 °C are demonstrated in Figure 4.41, Figure 4.42 and Figure 4.43, respectively.

The removal of phorate with KUBC700 sample affected by the exerted dose. From Figure 4.41, the low loading amount (0.02 g/100 mL = 0.2 g/L) caused to remain higher final phorate concentration in the solution and achieved 80% removal at the end of the batch experiment, while higher dosages (1 g/L, 5 g/L, 15 g/L) removed 100% phorate in 60 min. It can be easily deduced that the increasing biochar doses applied in the phorate removal batch experiments had an encouraging effect on the performance. As such, 0.2 g/L dose biochar created the lowest performance and it ended up the batch removal experiment with phorate removal ratio (C/C_0) as 0.2, while 15 g/L dosage demonstrated the highest phorate removal rate.
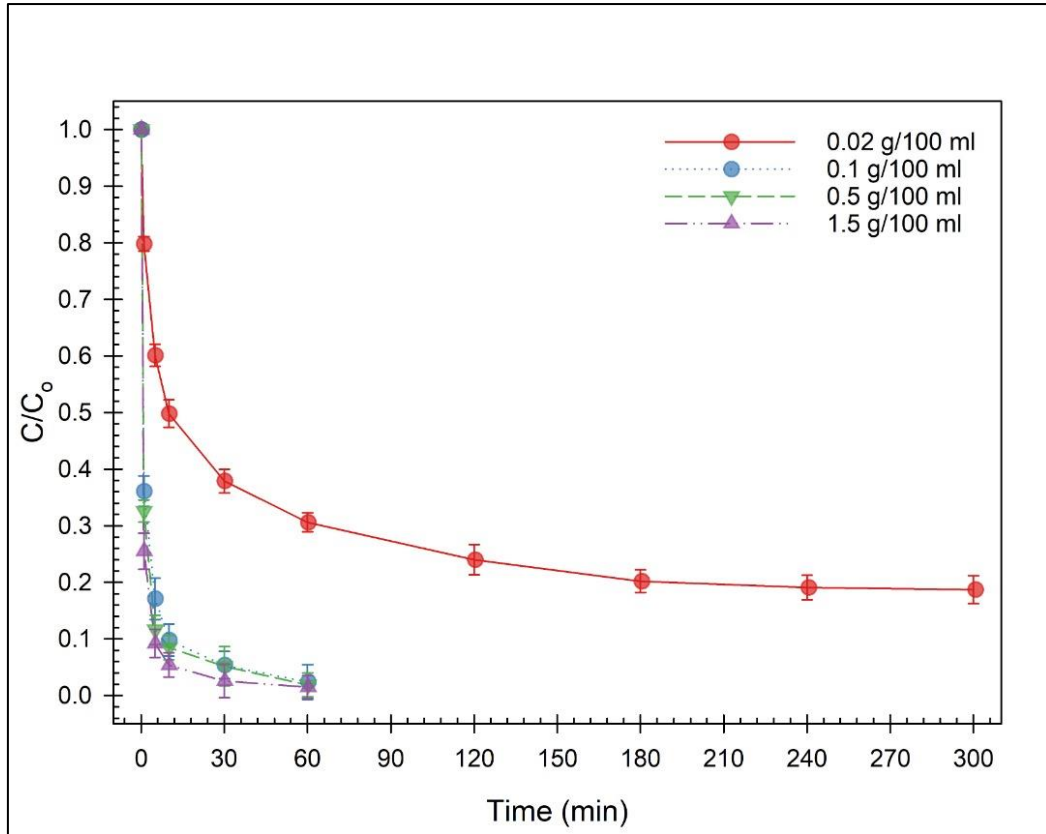
Figure 4.41. Effect of various KUBC700 biochar dose on the phorate removal at 25 °C

Phorate removal efficiencies generated by the addition of dose-varied KUBC700 at 25 °C are tabulated in Table 4.19. Applied doses of 1 g/L, 5 g/L and 15 g/L performed 100% phorate removal at t=2 h with similar trends, while the 0.2 g/L removed 81.3% of initially added phorate at the end of the batch experiment.

Table 4.19. Phorate removal efficiencies (%) of various KUBC700 biochar dose at 25 °C

Time (min)	Biochar Dose (g/L)			
	0.2	1	5	15
1	20.23	63.90	67.43	74.49
5	39.86	82.87	88.39	90.81
10	50.23	90.15	91.47	94.56
30	62.14	94.56	94.78	97.43
60	69.42	97.61	98.09	98.53
120	76.04	100.00	100.00	100.00
180	79.76			
240	80.89			
300	81.33			

In the case of the HC210BC700KOH1U10 sample, the removal pattern showed a similar trend with KUBC700 and the performance was enhanced by the developing dose loaded. However, in Figure 4.42, higher efficiencies were observed for 1 g/L, 5 g/L and 15 g/L compared to KUBC700. HC210BC700KOH1U10 with mentioned doses achieved 100% removal in 10 min. The low dose, which is 0.2 g/L, also showed promising performance and the remaining phorate concentration was 4% of the initial phorate concentration at the final stage. Therefore, 0.2 g/L of HC210BC700KOH1U10 sample became more efficient than 0.2 g/L of KUBC700.
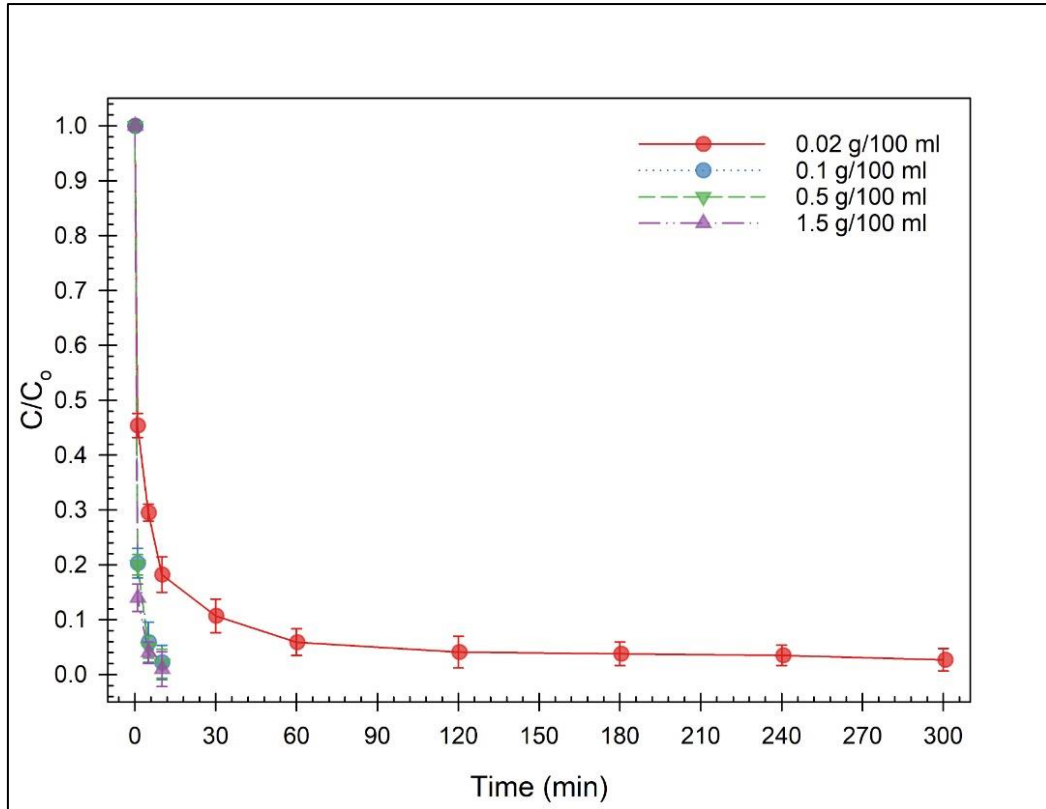
Figure 4.42. Effect of various HC210BC700KOH1U10 biochar dose on the phorate removal at 25 °C

Phorate removal efficiencies generated by the addition of dose-varied HC210BC700KOH1U10 at 25 °C are tabulated in Table 4.20. Applied doses of 1 g/L, 5 g/L and 15 g/L performed 100% phorate removal at t=30 min with similar trends, while the 0.2 g/L removed 97.3% of initially added phorate at the end of the batch experiment. The removal efficiency of 0.2 g/L HC210BC700KOH1U10 showed better results when it is compared to 0.2 g/L KUBC700 in Table 4.19.

Table 4.20. Phorate removal efficiencies (%) of various HC210BC700KOH1U10 biochar dose at 25 °C

Time (min)	Biochar Dose (g/L)			
	0.2	1	5	15
1	54.64	79.65	80.01	85.96
5	70.52	94.12	95.00	95.97
10	81.77	97.78	98.02	99.02
30	89.27	100.00	100.00	100.00
60	94.12			
120	95.91			
180	96.19			
240	96.55			
300	97.34			

U10HC210BC700KOH1, on the other hand, followed the similar flow in the phorate removal efficiency and it improved by the increasing dose. The dosages as 1 g/L, 5 g/L and 15 g/L totally removed the initially applied phorate concentration in 10 min, the same value as HC210BC700KOH1U10. 0.2 g/L applied biochar dose in Figure 4.43 finalized the batch experiment with 90% phorate removal, which was comparatively lower than HC210BC700KOH1U10 in Figure 4.42. However, it was still favorable performance when it is compared with KUBC700. The slight increase in biochar elimination performance was observed by the increasing amount of biochar applied.
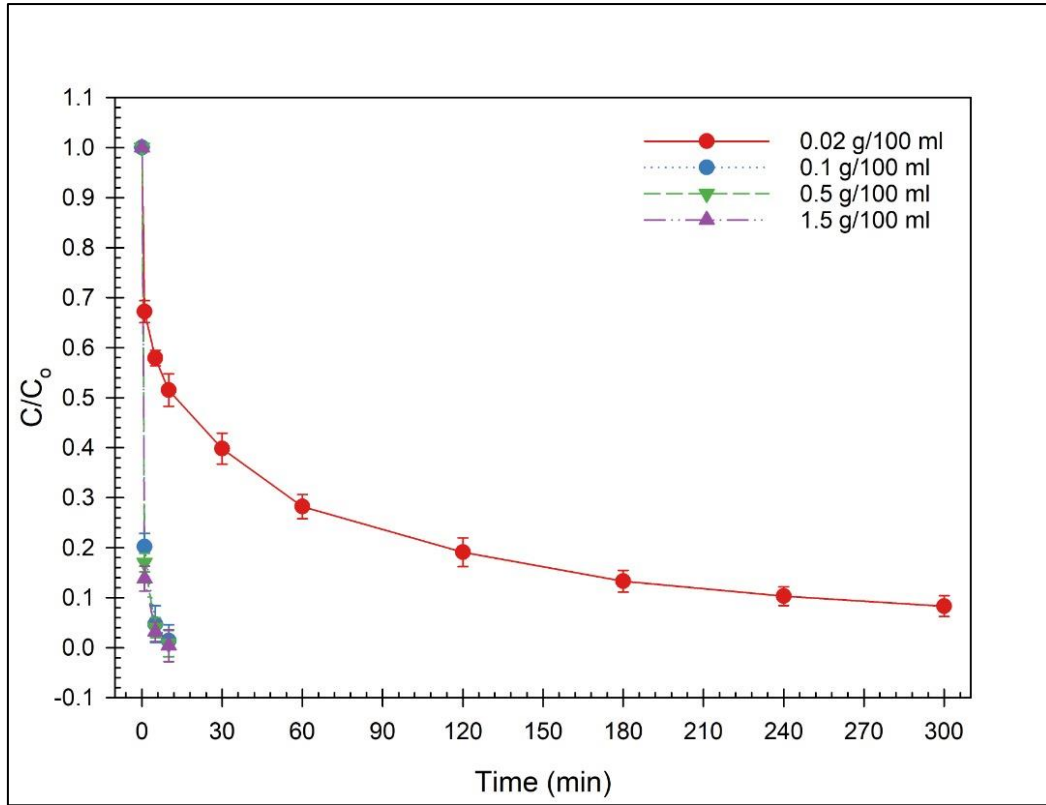
Figure 4.43. Effect of various U10HC210BC700KOH1 biochar dose on the phorate removal at 25 °C

Phorate removal efficiencies generated by the addition of dose-varied U10HC210BC700KOH1 at 25 °C are tabulated inTable 4.21. Applied doses of 1 g/L, 5 g/L and 15 g/L performed 100% phorate removal at t=30 min with similar trends, while the 0.2 g/L removed 91.7% of initially added phorate at the end of the batch experiment. U10HC210BC700KOH1 showed similar phorate removal efficiencies at higher biochar doses with HC210BC700KOH1U10 (Table 4.20); however, 0.2 g/L of U10HC210BC700KOH1 eliminated slightly less amount of phorate from water.

Table 4.21. Phorate removal efficiencies (%) of various U10HC210BC700KOH1 biochar dose at 25 °C

Time (min)	Biochar Dose (g/L)			
	0.2	1	5	15
1	32.81	79.83	83.01	86.18
5	42.07	95.26	96.03	96.77
10	48.47	98.58	99.20	99.61
30	60.16	100.00	100.00	100.00
60	71.84			
120	80.89			
180	86.67			
240	89.71			
300	91.69			

All in all, it can be said that these three biochar samples applied as 1 g/L, 5 g/L and 15 g/L showed comparable results. However, KUBC700 removed the total applied phorate in 60 min, HC210BC700KOH1U10 and U10HC210BC700KOH1 achieved 100% removal in 10 mins. Therefore, it is clear that hydrothermally treated biochars' performance was higher than KUBC700, which was simply pyrolyzed. In the case of lower dose (0.2 g/L), although all the biochars performed more than 80% removal, HC210BC700KOH1U10 and U10HC210BC700KOH1 eliminated 96% and 90% of initial phorate concentration, respectively.

4.4.3   Effect of initial pH on OPPs removal

The pH was placed as one of the operational parameters in the 2nd stage batch removal experiments achieved with KUBC700, HC210BC700KOH1U10 and U10HC210BC700KOH1 samples. The usual batch removal in the 1st stage experiments was operated using deionized water, which has a pH between 6 – 6.5. The solution will be used in the 2nd stage pH-dependent batch removal experiments were adjusted as pH 3, pH 5, Ph 7, pH 9 and pH 11 by adding proper amounts of 0.01 M KOH and 0.01 M HCl into the deionized water solution. The impact of

various pH values on phorate removal was examined in this section. The expression of '*no pH adjustment*' indicates the direct use of deionized water from the water supply (Milli-Q Simplicity 188/U.S.A.) without any pH adjustment.

Figure 4.44 illustrates the impact of different pH values on phorate removal efficiencies with 1 g/L KUBC700 sample at 25 °C. As a result of the pH experiments, no regular trend was determined. The higher phorate remaining in the solution at the end of the batch experiments was observed in pH 11, then it was followed by pH 9, pH 3, pH 7, pH 5. The total phorate removal ($C/C_0=0$) happened in the no pH adjusted deionized water in 2 hours. Desorption occurred in the solution with pH 7 and after t=2 hours, phorate started to de-attach from KUBC700. Even though the lack of regular trends, the results reveal that KUBC700 samples have their best performance in between 5 – 6.5 pH solution since it performed greater efficiencies in the no pH adjusted solution and pH 5 solution.
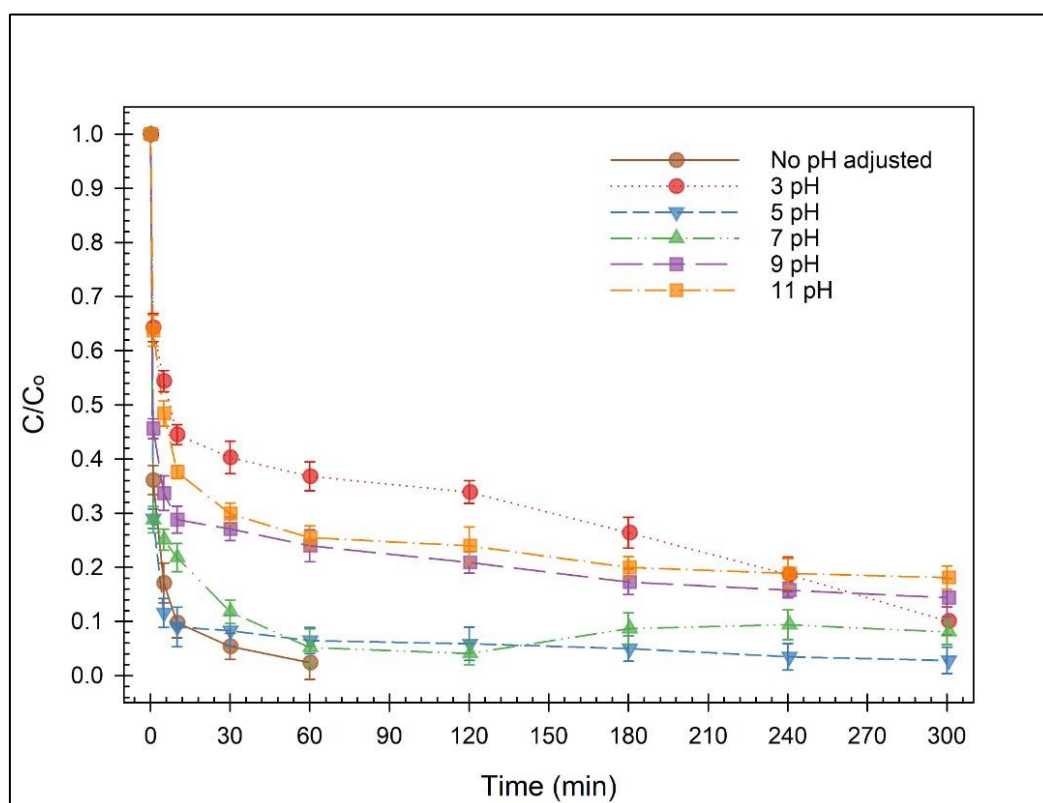
Figure 4.44. Effect of 1 g/L KUBC700 on the phorate removal in pH varied solutions at 25 °C

The results illustrated in Figure 4.44 are detailed concerning phorate removal efficiency percentages in Table 4.22. The only 100% phorate removal happened in the no pH adjusted solution which is in between pH 6 – 6.5. The removal efficiencies at the end of the batch experiments were ordered as 89.9%, 97.2%, 91.9%, 85.6%, 81.9% for pH 3, pH 5, pH 7, pH 9 and pH 11, respectively. In pH 7 solution, desorption occurred at t=2 hours and after that, removed concentration lessened by 4% at t=5 hours as a result of phorate de-attachment.

Table 4.22. Phorate removal efficiencies (%) of 1 g/L KUBC700 in pH varied solutions at 25 °C

Time	pH					
	No pH adjusted	3	5	7	9	11
0	0.00	0.00	0.00	0.00	0.00	0.00
1	63.90	35.67	70.96	71.18	54.42	36.34
5	82.87	45.60	88.39	74.93	66.33	51.55
10	90.15	55.52	91.03	78.24	71.18	62.36
30	94.56	59.71	91.69	88.17	72.95	70.08
60	97.61	63.24	93.46	94.78	76.04	74.49
120	100.00	66.11	94.12	95.89	79.12	76.04
180		73.61	95.00	91.25	82.65	80.01
240		81.33	96.55	90.59	84.20	81.11
300		89.93	97.23	91.92	85.61	81.91

Figure 4.45 demonstrates the effect of 1 g/L HC210BC700KOH1U10 on the phorate removal in various pH solutions at 25 °C. The higher removals were also seen in the no pH adjusted solution and pH 5 solution. They removed 100% of the initial phorate in 30 mins and 1 hour, respectively. Phorate removal ratios (C/C_0) were relatively lower than KUBC700 in Figure 4.44. They were determined as 0.14, 0.04, 0.03, 0.02 in pH 11, pH 9, pH 7, pH 3, respectively. The lower C/C_0 indicates less phorate remaining in the solution at the end of the batch experiment. Therefore, it can be obtained that the HC210BC700KOH1U10 sample showed higher performances than KUBC700 in all pH ranges.
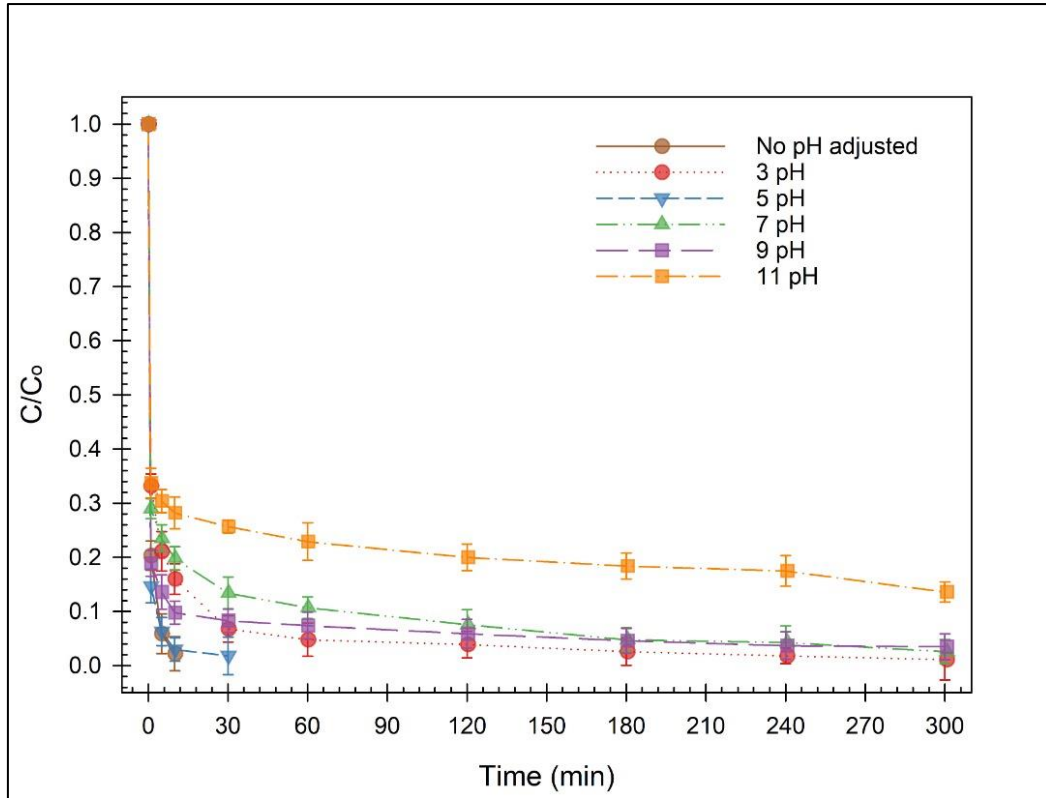
Figure 4.45. Effect of 1 g/L HC210BC700KOH1U10 on the phorate removal in pH varied solutions at 25 °C

Table 4.23 lists phorate removal efficiencies (%) of 1 g/L HC210BC700KOH1U10 in various pH solutions at 25 °C. 100% removal efficiencies were obtained in the no pH adjusted solution and pH 5 solution in 30 mins and 1 hour, respectively. The highest percentage obtained at the end of the batch experiments were recorded as 98.9%, 97.4%, 96.6%, 86.4% for pH 3, pH 7, pH 9, pH 11, respectively. This shows that the increasing pH value lessened the performance of the HC210BC700KOH1U10 sample and the sample demonstrated its best performance in the pH range of 5 – 6.5. It formed a similar range with KUBC700 in Table 4.22 because they both work efficiently in the pH range between 5 – 6.5.

Table 4.23. Phorate removal efficiencies (%) of 1 g/L HC210BC700KOH1U10 in pH varied solutions at 25 °C

Time	pH					
	No pH adjusted	3	5	7	9	11
0	0.00	0.00	0.00	0.00	0.00	0.00
1	79.65	66.77	85.30	70.96	81.11	66.33
5	94.12	78.90	93.68	76.48	86.40	69.64
10	97.78	83.98	96.99	80.23	90.15	71.84
30	100.00	93.24	98.20	86.62	91.69	74.27
60		95.22	100.00	89.27	92.58	77.14
120		96.11		92.36	94.12	80.01
180		97.43		95.22	95.44	81.58
240		98.18		95.66	96.33	82.54
300		98.86		97.43	96.55	86.40

In the case of the U10HC210BC700KOH1 sample, the working performance in various pH ranges is shown in Figure 4.46. Differently than KUBC700 and HC210BC700KOH1U10 biochar materials, the performance was upgraded in the no pH adjusted solution, pH 7 and pH 11 for U10HC210BC700KOH1 biochar. 100% phorate removal was performed in 30 mins, 4 hours and 5 hours for no pH adjusted, pH 7 and pH 11 solution, respectively. However, phorate remaining in the solution at the end of the batch experiments in pH 3, pH 5 and pH 9 samples was higher than HC210BC700KOH1U10 material in Figure 4.45 and lower compared to KUBC700 material in Figure 4.44 by looking at phorate removal ratios (C/C_0).
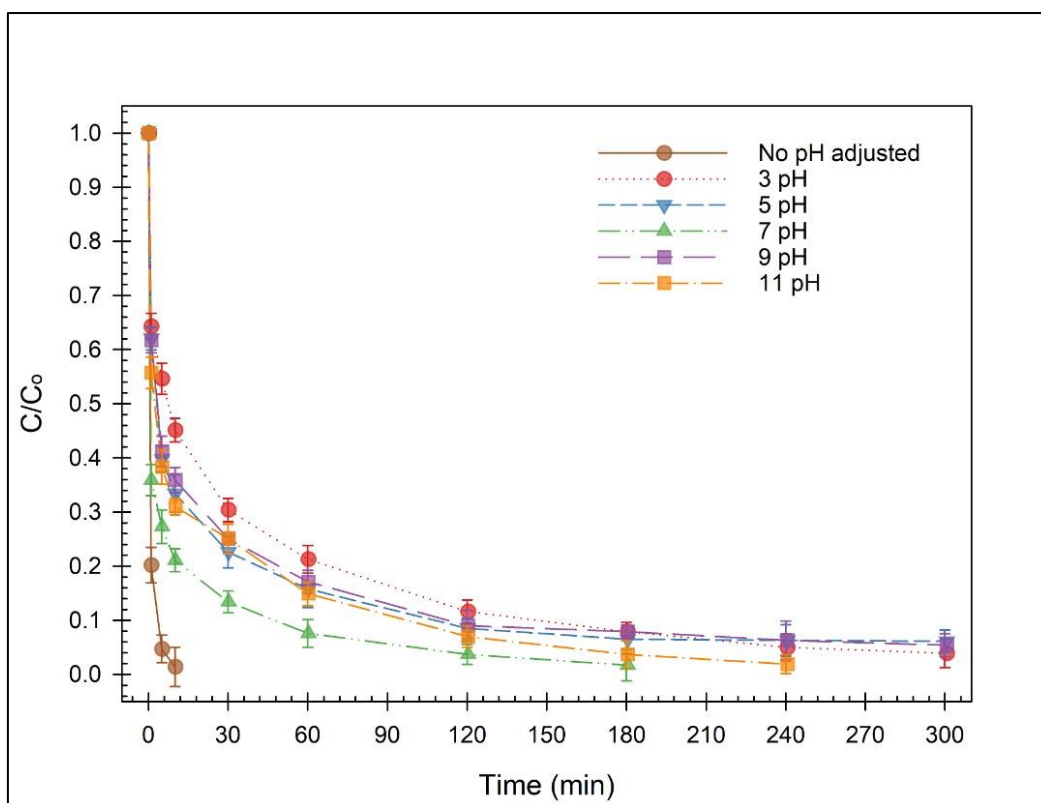
Figure 4.46. Effect of 1 g/L U10HC210BC700KOH1 on the phorate removal in pH
varied solutions at 25 °C

The numerical values of phorate removal efficiencies are described in Table 4.24. 1
g/L U10HC210BC700KOH1 at 25 °C achieved 100% removal from the initial
phorate concentration in the no pH adjusted, pH 7 and pH 11 solutions. This gives a
broader range to work efficiently for the U10HC210BC700KOH1 sample. However,
other pH values, which are pH 3, pH 5 and pH 9, also created a favorable
environment for phorate removal and U10HC210BC700KOH1 accomplished
96.1%, 93.9% and 94.6% removal in related solutions, respectively.

Table 4.24. Phorate removal efficiencies (%) of 1 g/L U10HC210BC700KOH1 in pH varied solutions at 25 °C

Time	pH					
	No pH adjusted	3	5	7	9	11
0	0.00	0.00	0.00	0.00	0.00	0.00
1	79.83	35.67	37.88	64.13	38.32	44.28
5	95.26	45.38	60.16	72.73	58.83	61.70
10	98.58	54.86	66.55	78.95	64.13	68.98
30	100.00	69.64	77.36	86.62	74.93	74.93
60		78.68	84.20	92.36	82.87	85.08
120		88.39	91.47	96.33	91.03	93.02
180		92.14	93.46	98.31	92.14	96.33
240		95.00	93.68	100.00	93.68	98.09
300		96.11	93.90		94.56	100.00

The conclusion that can be made from pH varied batch experiments of three biochar materials is that different pH ranges exerted on different biochar materials have a diversified impact on the phorate removal efficiencies. Therefore, it is difficult to determine a regular trend in the pH experiments. As such, KUBC700 and HC210BC700KOH1U10 samples performed better in the pH range between 6 – 7, while U10HC210BC700KOH1 work efficiently in a broader pH range. On the other hand, the pH range where all three samples showed their best performances in the no pH adjusted range, which was pure deionized water (pH 6 – 6.5). The reason can be due to the lack of ions or ionic constituents in the deionized water and this situation eliminated the chance of competitive atmosphere for the removal of pesticide by the use of biochar material. However, since the KOH and HCl was added in the pH adjustment, the atmosphere has been changed with the increase/decrease of H^+ and OH^- ions. For example, it can be observed similar removal ration between the no pH adjusted solutions and pH 7, but the efficiency was always best in the no pH adjusted solution. In the pH 7 solution, there were more OH^- ions compared to the deionized water. Since the nitrogen functional groups are positively charged, this OH^- ions could be attracted by the nitrogen functionalities and after the attraction between them, the role of nitrogen active groups in the phorate removal might be lessened.

Therefore, the pH adjustment caused a decrease in the phorate removal reaction rate. Phorate removal efficiencies of 1 g/L three selective biochars in pH varied solutions at 300 min under 25 °C are tabulated in Table 4.25.

Table 4.25. Phorate removal efficiencies (%) of 1 g/L from three selective biochars in pH varied solutions at 300 min under 25 °C

Biochar	pH					
	No pH adjusted	3	5	7	9	11
KUBC700	100	89.93	97.23	91.92	85.61	81.91
HC210BC700KOH1U10	100	98.86	100	97.43	96.55	86.40
U10HC210BC700KOH1	100	96.11	93.90	100	94.56	100.00

4.4.4 Removal efficiency of reused biochars

Biochar is a promising material with its reusability characteristic (El-Naggar et al., 2021). Reusability also indicates related material's stable nature, which is critical in the field operation (Mian et al., 2019). Three produced biochar samples (KUBC700, HC210BC700KOH1U10, U10HC210BC700KOH1) were reused 5 times to characterize its reusability and material stability. These three samples were further analyzed by XRD Spectroscopy (Figure 4.48) for the change in mineral composition and FTIR Spectroscopy (Figure 4.49) for the change in surface functional groups. These analyses were performed in the before and after stages of batch experiments.

The phorate removal efficiencies of three 1 g/L biochars for each 5-reusability experiment at 25 °C were illustrated in Figure 4.47. All reusability cycles were carried out with the same volume of solution and the same concentration of phorate pesticide. Since these three samples were performed the best efficiencies in the 1st stage of the batch experiments and showed a 100% phorate removal, their percentages in the 1st cycle were all 100%. The biochar remaining after washing with Acetonitrile was taken into the 2nd reusability cycle. KUBC700, HC210BC700KOH1U10, U10HC210BC700KOH1 displayed 94%, 97%, 98% removal from the initial phorate concentration, respectively. The 3rd cycle followed with a slight decrease, accounting for 92%, 96%, and 97%. KUBC700,

HC210BC700KOH1U10 and U10HC210BC700KOH1 materials in the 4th reusability batch experiment demonstrated 89%, 93%, and 96% phorate removal efficiencies, respectively. 5th and the final cycle ended up with 86%, 91%, and 93% performances, which were highly promising and showed the material's stable nature.

When the performances of these three biochar samples were compared with the similar materials' activities in the literature, it was observed that the results presented in Figure 4.47 revealed the outstanding performances of related biochar materials. For example, in the study of Mian et al. (2019), the role of N-doped metal-biochar composites has been investigated in the mineralization of Methylene Blue (MB), which is an organic chloride salt. In the study, they performed 5-reusability experiments similarly. The MB removal efficiencies at t=5 h in the reusability tests were evaluated as 100%, 99%, 95%, 92% and 85% in each cycle order, respectively. In the reusability experiments of this study, two of the biochar samples, which are HC210BC700KOH1U10 and U10HC210BC700KOH1, displayed higher percentages in all cycles, while all were left behind in the 5th cycle.
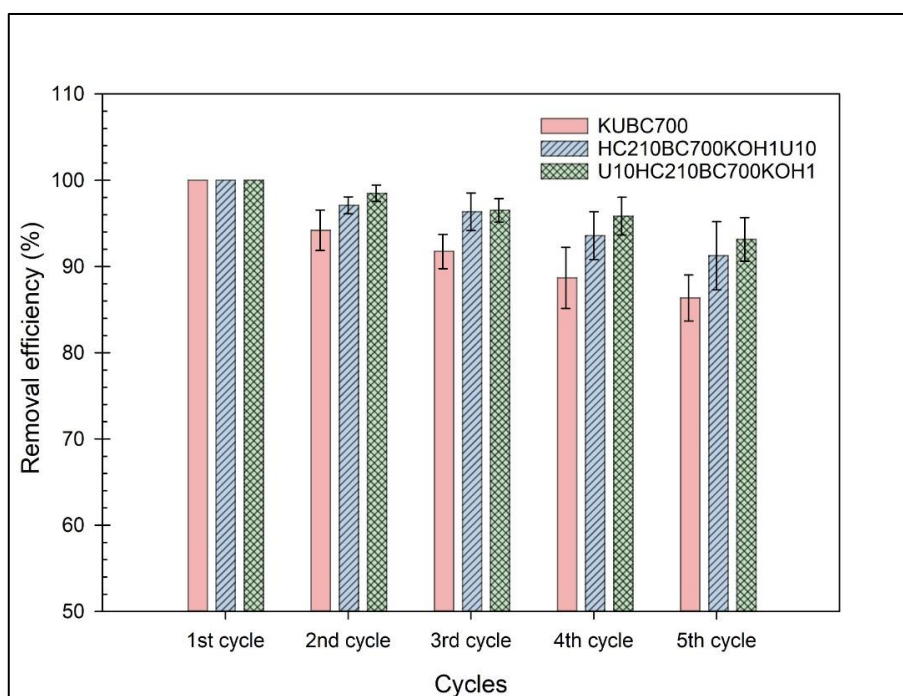
Figure 4.47. Phorate removal efficiencies of 1 g/L biochars for each reusability experiment at 25 °C

Figure 4.48 shows the XRD diffraction pattern of used and unused modified biochars. This analysis was performed to have an information about the impact of the removal mechanism of phorate on the biochar mineral composition. The analysis was carried on the modified samples, which were KUBC700, HC210BC700KOH1U10 and U10HC210BC700KOH1. All the present crystalline structures in U10HC210BC700KOH1 except Graphite were increased in the used version. However, Graphite displayed a particular increase in the pattern. In the case of HC210BC700KOH1U10 and KUBC700 samples, all the inorganic compositions showed a rise in intensity without any exception. Besides, the gap between used and unused sample XRD diffraction patterns is minor and almost equal in low and very high theta degree ranges, the medium section relatively opened the gap in the inorganic densities.
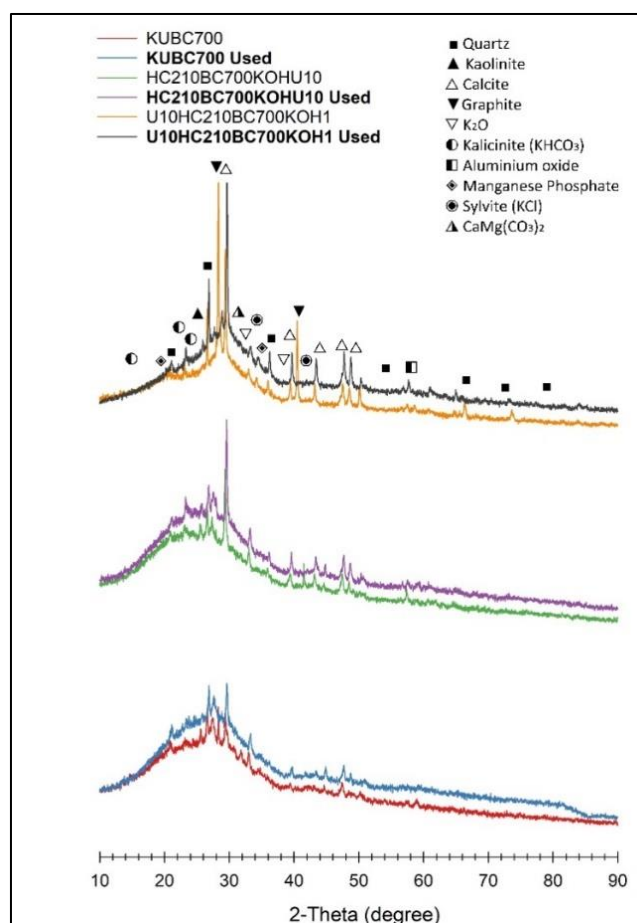
Figure 4.48. XRD diffraction pattern of used and unused modified biochars

163

Figure 4.49 illustrates the FTIR spectra of used and unused modified biochars. The analysis was achieved to observe the impact of the removal mechanism of phorate on the biochar surface functional groups. The analysis was carried on the modified samples, which were KUBC700, HC210BC700KOH1U10 and U10HC210BC700KOH1. For all three samples, the noise has been noticed in the used stage of samples. In KUBC700, there was an apparent occurrence in N—H and NH₃ peaks and the absorbance level intensified after it has been used. NCO— and C—Hn groups almost had no change in the spectra regardless of biochar usage. The increase in oxygen-containing functional groups (i.e., C—O, C—O—C and —C=O) has been recognized with the usage of the KUBC700 sample, where there was a decrease in the C—N functionality. In terms of HC210BC700KOH1U10, the spectrums of both used and unused samples were almost the same, considering all the present surface-active components. No apparent change was observed. For the U10HC210BC700KOH sample, a slight upturn in N—H and NH₃ was marked when the related biochar was used to remove the phorate pesticide. The other active groups followed a similar pattern with the original biochar sample.
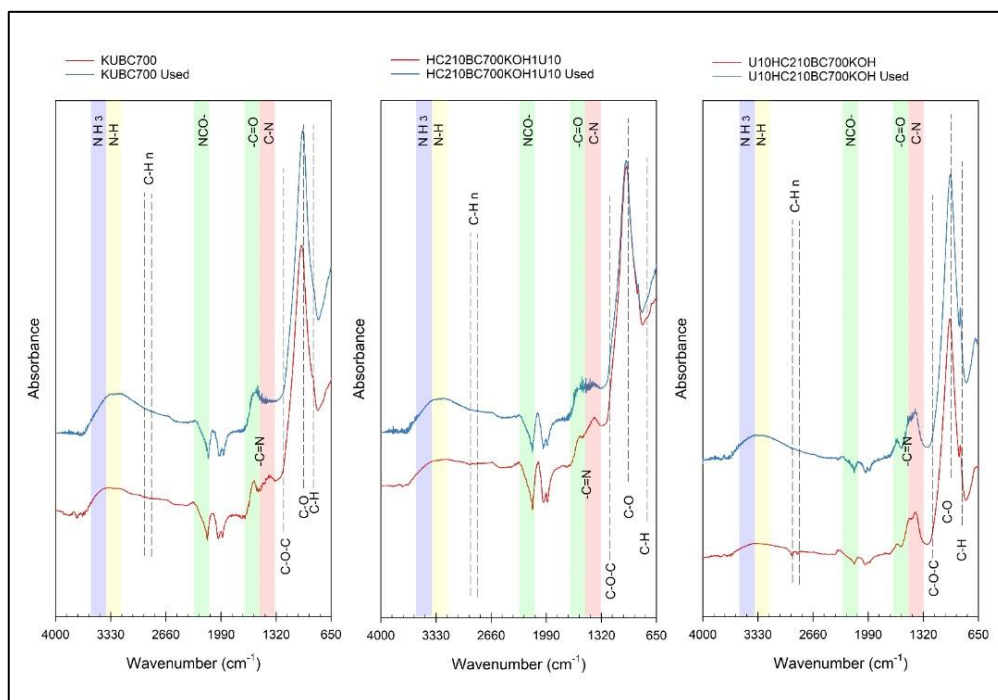
Figure 4.49. FTIR spectra of used and unused modified biochars

4.4.5   Biochar removal efficiency in the real wastewater for phorate

The phorate removal efficiency of biochar was also checked in the real wastewater sample collected from the Membrane Bioreactor (MBR) system from the METU wastewater treatment plant in the purpose of simulation of the ambient environmental scenario. 1 L bottles of 1 ppm, 2 ppm, and 5 ppm wastewater solutions were prepared with the addition of phorate from its stock solution. Then, it was incubated under 4 °C and dark overnight. Incubated samples were taken into concentration measurement with HPLC. HPLC results showed that most of the phorate in the solutions was adsorbed or degraded during the incubation period. Therefore, the concentration of corresponding samples was reduced. Since in the batch experiments, 1 ppm was the standard concentration value, 2 ppm was selected with the consideration of a decrease in concentration. 1 ppm phorate solution was prepared with the dilution of wastewater and three (KUBC700, HC210BC700KOH1U10, U10HC210BC700KOH1) biochars were applied into these solutions for the batch experiments. The dose of experimental biochar was 1 g/L and the batch experiments were carried out under 25 °C. Figure 4.50 illustrates the comparison between the usual batch experiments deionized water and tests with wastewater. KUBC700, HC210BC700KOH1U10 and U10HC210BC700KOH1 achieved the total phorate removal from the solution prepared with deionized water (DI) in 2 hours, 1 hour and 30 mins, respectively. However, the difference between the two types of water was very broad and at the end of the batch experiments, only the U10HC210BC700KOH1 sample was able to remove 100% of the initial phorate concentration in 3 hours. KUBC700 and HC210BC700KOH1U10 samples could decrease the phorate concentration by 86% and 90% at the end of the batch experiments. The reason for that is the abundance of various ambitious ions or organic compounds in the wastewater. These ions or organic compounds can compete and result in a low phorate removal in the wastewater.
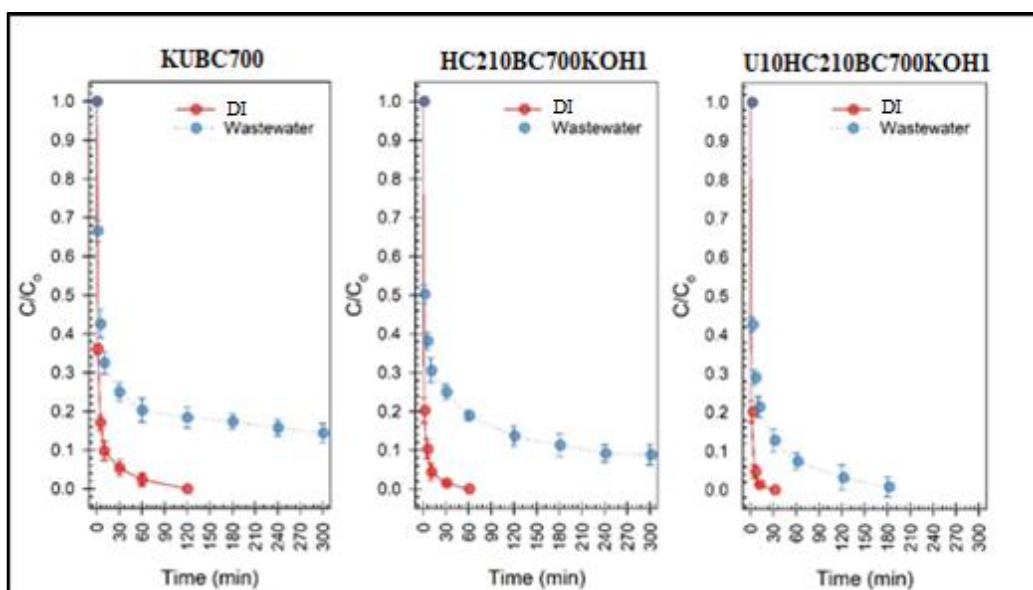
Figure 4.50. Phorate removal ratios of 1 g/L biochars in DI and wastewater at 25 °C

4.5   Mechanism and pathway of phorate degradation

This study employed Gas Chromatography-Mass Spectroscopy (GC-MS) analysis to characterize the mechanism and pathway of phorate degradation. To illustrate the fundamental mechanism involved in biochar based free-radical-assisted degradation of phorate pesticide, the reaction pathway was depicted in Figure 4.51. It demonstrates the hydroxyl radical (•OH) assisted degradation of phorate present on the surface of biochar. The hydroxyl radical is highly reactive with a great oxidation capacity (Bano et al., 2021). In this study, GC-MS analyses were carried out with four different samples as follows: phorate, KUBC700, HC210BC700KOH1U10 and U10HC210BC700KOH1. The details of used samples were given in Table 3.7. As a result of degradation, CO_2, H_2O and phorate intermediate products were generated and generated phorate degradation intermediates from corresponding samples were listed in Table 4.26.

166
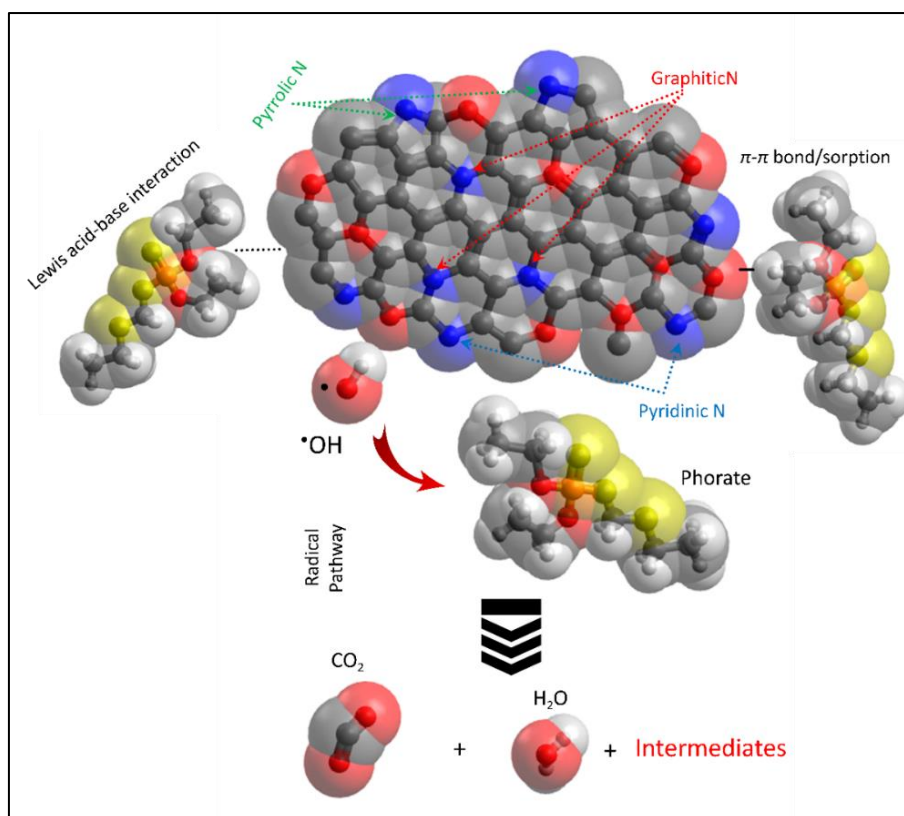
Figure 4.51. Biochar based free-radical-assisted degradation mechanism of phorate into intermediate degradation products

Table 4.26 tabulates the corresponding biochar-based degradation intermediate products of phorate pesticide as a result of the advanced oxidation process, which was free radical-assisted degradation in this study. Retention time was measured when the mass spectrometer detected each compound. Mass spectrometry is a destructive method that uses the compound's molecular weight and converts it into molecular structure data. It becomes differentiative from other spectrometers since the MS ionizes the compound. Ionized molecules become excited and activate the fragmentation. Detection of these fragmentations indicates the structure of molecules. The fragments are identified by the mass-to-charge ratio (m/z) and MS detectors can characterize these ions. In Table 4.26, mass spectra peaks of identified degradation intermediates were given with respect to the analyzed sample.

Table 4.26. Intermediates of the degradation of phorate identified by GC-MS

Reaction system	Retention time (min)	Mass spectra peaks (m/z)	Degradation intermediates
Phorate	3.698	283, 282, 281, 265, 249, 207, 193, 191, 133, 73	Cyclotetrasiloxane, octamethyl-
	6.543	358, 357, 356, 355, 269, 268, 267, 251, 74, 73	Cyclotetrasiloxane, decamethyl-
	10.188	431, 430, 429, 343, 342, 341, 325, 147, 74, 73	Cyclotetrasiloxane, dodecamethyl-
	14.465	206, 192, 191, 163, 91, 74, 57, 41, 39, 29	2, 4-Di-tert-butylphenol
	15.382	242, 240, 227, 226, 225, 197, 115, 57, 55, 41	Phenol, 4-chloro-2, 6-bis(1,1-dimethylethyl)-
	20.351	212, 198, 197, 165, 155, 154, 153, 141, 91	2,6-Diisopropylnapthtalene
	20.779	260, 231, 129, 125, 121, 97, 93, 75, 65, 47	Phorate
	21.498	212, 198, 197, 165, 155, 153, 152, 141, 43, 27	2,6-Diisopropylnapthtalene
	40.154	239, 134, 112, 98, 84, 74, 69, 57, 55, 43	Hexadecanoic acid, 2-hydroxy-1-(hydroxymethyl)ethyl ester
	43.833	134, 98, 84, 74, 71, 69, 57, 55, 43, 41	Octadecanoic acid, 2,3-dihydroxypropyl ester
KUBC700	3.637	129, 69, 59, 56, 55, 43, 41, 31, 29, 27	2-Octanol, 2-methyl-
	4.499	108, 107, 91, 80, 79, 78, 77, 51, 50, 39	Benzyl alcohol
	7.371	97, 83, 71, 69, 58, 57, 55, 43, 41, 29	Oxirane, [(hexadecyloxy)methyl]-
	7.805	83, 71, 69, 59, 57, 56, 55, 43, 42, 41	1-Decanol, 5,9-dimethyl-
	10.188	99, 85, 71, 70, 69, 57, 56, 55, 43, 41	Heptadecane, 2,6,10,15-tetramethyl-
	10.989	111, 95, 75, 70, 69, 59, 58, 55, 43, 41	2,5-dimethylhexane-2,5-dihydroperoxide
	14.492	206, 192, 191, 163, 91, 74, 57, 41, 39, 29	2,4-Di-tert-butylphenol
	20.752	260, 121, 97, 93, 75, 65, 47, 45, 29, 27	Phorate
	36.970	410, 395, 354, 339, 283, 227, 207, 190, 57, 29	[1,1'-Biphenyl]-2,3'-diol, 3,4',5,6'-tetrakis(1,1-dimethylethyl)-
HC210BC700KOH1U10	3.698	129, 69, 59, 56, 55, 43, 41, 31, 29, 27	2-Octanol, 2-methyl-
	4.560	108, 107, 91, 80, 79, 78, 77, 51, 50, 39	Benzyl alcohol
	7.398	113, 95, 93, 85, 71, 69, 59, 55, 43, 41	α-Methyl-α-[4-methylpenty] oxiranmethanol
	7.832	83, 71, 69, 59, 57, 56, 55, 43, 42, 41	1-Decanol, 5,9-dimethyl-
	10.989	111, 95, 75, 70, 69, 59, 58, 55, 43, 41	2,5-dimethylhexane-2,5-dihydroperoxide
	14.492	206, 192, 191, 163, 91, 74, 57, 41, 39, 29	2, 4-Di-tert-butylphenol
	20.752	260, 121, 97, 93, 75, 65, 47, 45, 29, 27	Phorate
	36.970	410, 395, 354, 339, 283, 227, 207, 190, 57, 29	[1,1'-Biphenyl]-2,3'-diol, 3,4',5,6'-tetrakis(1,1-dimethylethyl)-
U10HC210BC700KOH1	3.671	123, 83, 71, 70, 69, 59, 56, 55, 43, 41	1,7-Octanediol, 3,7-dimethyl-
	4.526	108, 107, 91, 80, 79, 78, 77, 51, 50, 39	Benzyl alcohol

Table 4.26 (continued)

5.015	111, 70, 55, 53, 43, 41, 39, 29, 28, 27	Bicyclo [2.2.2] octan-1-ol, 4-methyl-	
7.371	69, 57, 56, 55, 44, 43, 42, 41, 39, 36	4-Cyclopropylcarbonyloxytridecane	
7.805	97, 83, 69, 59, 57, 55, 43, 41, 31, 29	3-Heptadecanol	
10.188	99, 85, 71, 70, 69, 57, 56, 55, 43, 41	Heptadecane, 2,6,10,11-tetramethyl-	
10.989	111, 95, 75, 70, 69, 59, 58, 55, 43, 41	2,5-dimethylhexane-2,5-dihydroperoxide	
14.492	206, 192, 191, 163, 91, 74, 57, 41, 39, 29	2, 4-Di-tert-butylphenol	
15.409	242, 240, 227, 226, 225, 197, 115, 57, 55, 41	Phenol, 4-chloro-2, 6-bis(1,1-dimethylethyl)-	
20.752	260, 121, 97, 93, 75, 65, 47, 45, 29, 27	Phorate	
36.970	410, 395, 354, 339, 283, 227, 207, 190, 57, 29	[1,1'-Biphenyl]-2,3'-diol, 3,4',5,6'-tetrakis(1,1-dimethylethyl)-	

Figure 4.52 represents chromatograms recorded in 49.667 min run time of GC-MS analysis. GC-MS chromatogram of only phorate pesticide solution was illustrated in the first section. It was measured to easily and clearly comprehend the difference created by biochar samples. The peak measured at 20.752 min indicates the peak of individual phorate pesticide and its absorbance was recorded as 2e+6. The corresponding relative absorbance value of phorate was decreased when the biochar samples were added to the solution due to the degradation activity. It decreased to 1e+6 by KUBC700 sample, 0.7e+6 by HC210BC700KOH1U10 sample, and almost reached zero (0) by U10HC210BC700KOH1 sample. Other peaks distinguishably appeared in the GC-MS chromatogram indicates the generated phorate degradation intermediates listed in Table 4.26. For example, the peak observed at 14.492 min, which was detected as 2, 4-Di-tert-butylphenol was not visible in the gas chromatogram of a single phorate solution. Whereas the corresponding peak's relative absorbance value gradually increased by order of KUBC700, HC210BC700KOH1U10 and U10HC210BC700KOH1. This indicates that 2, 4-Di-tert-butylphenol compound is one of the phorate degradation intermediates and it increases with the degradation of phorate in the solution.
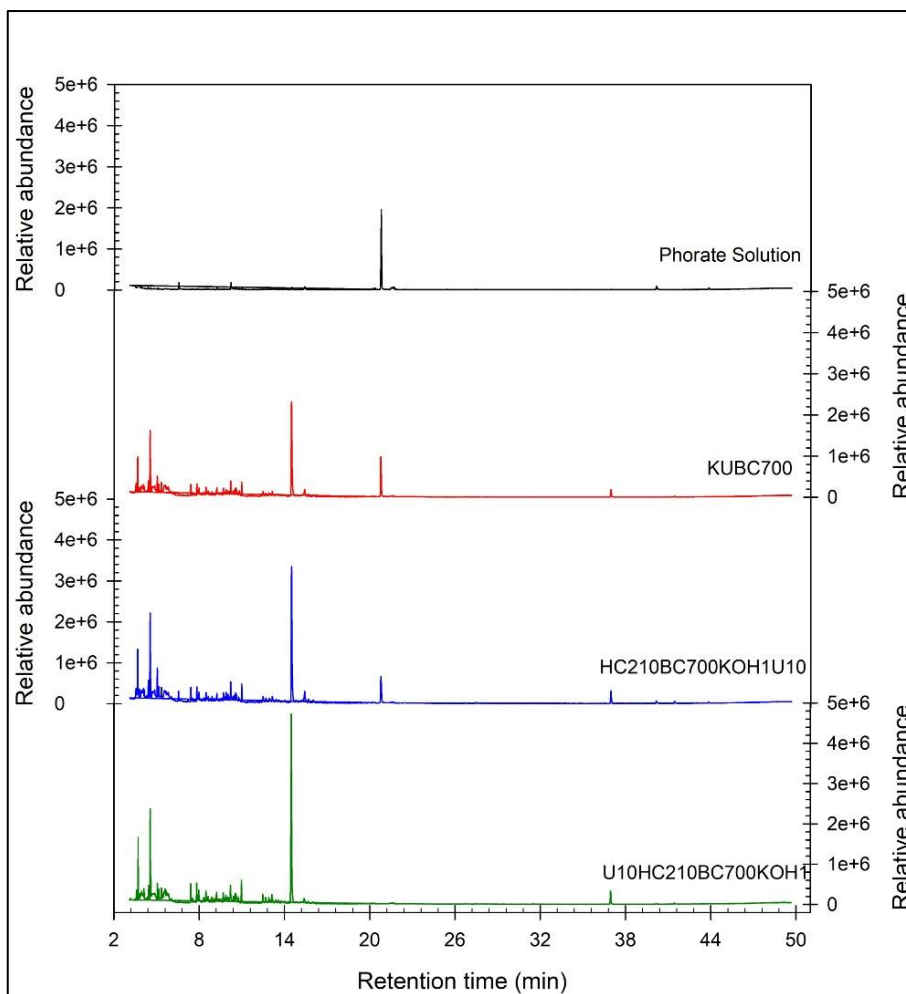
Figure 4.52. GS-MS chromatogram obtained for a phorate solution and phorate degradation by different biochar samples

CHAPTER 5

CONCLUSIONS

Phorate is a commonly used agricultural OPP classified under 'restricted use' and its leftovers create acute dermal and oral toxicity on living creatures and the environment. A novel way to remove phorate from water by utilizing sewage sludge-derived biochar material is the main target of this study. In a comparison to other sewage sludge management scenarios, the sewage sludge-derived biochar production becomes feasible in areas where low-cost sewage sludge biomass waste is available abundantly such as in wastewater treatment plants.

The present study consists of two objectives: i) use of potassium hydroxide (KOH) and urea on production characteristics of produced biochars and interfacial chemical behavior towards the organic contaminant (i.e. phorate), ii) effect of reaction parameters on enhanced phorate removal from water using produced sewage sludge biochar-based catalyst. In line with the first objective, various operational parameters (i.e., pyrolysis temperature, hydrothermal treatment) and specific modification techniques (dose varied KOH and urea application) were performed during the production of biochar samples. KOH have been selected as an activating agent to enhance the adsorption capacity and urea has been applied to add surface active nitrogen functionalities to produced biochars. Multiple advanced analytical techniques (i.e., Elemental Analysis, BET analysis, SEM analysis, XPS, XRD spectroscopy, FTIR spectroscopy, TGA, EPR spectroscopy) were used in order to provide an essential basis for the knowledge of the surface functionalities and physicochemical properties of produced biochars. Elemental and XPS Analyses showed the richness of biochar elemental content and their chemical behaviors towards different applied techniques. Diversified range of elemental composition supported the results of FTIR spectroscopy by showing varied surface functional groups. While the KOH application increased the specific surface area, urea

171

modification enhanced the formation of nitrogen functional groups. Increase in the specific surface area is exposed to the formation of more surface-active functional groups. N-functionalities, on the other hand, strengthened the removal efficiency of phorate. In the organic contaminant removal, nitrogen functionalities are more efficient as compared to hydroxyl or carboxyl groups because organic contaminants have negatively charged and nitrogen active groups have positively charged. This creates a good attraction between them. The surface morphology and porosity were explored by the BET and SEM analyses, respectively. Porosity and specific surface area were enhanced with the increase in the pyrolysis temperature. Urea added micropores and KOH dispersed the them equally at the surface. Therefore, their combined modification provokes more capacity for the contaminant adsorption. XRD Spectroscopy showed the diversified range of mineral composition found in the biochars. XRD analyzed structural characteristics of carbon minerals in biochar and the metal phases added by KOH (i.e. Sylvite, Kalicinite). Nitrogen doping increased the intensities of the amorphous carbon planes (i.e., Quartz, Kaolinite, Calcite) which indicates the degree of graphitization. TGA gave three main information: which treatment increases the inorganic content in the biochar, stability and degradation behavior under thermal condition. In terms of modified samples, the biochar samples with KOH modification showed a more recalcitrant nature. While urea was degraded quickly, KOH containing samples took their time until elevated temperatures. Among all, urea based hydrothermally treated and KOH modified biochar showed the most stable nature with the slowest degradation.

In line with the second objective, two stages of batch experiments have been carried out throughout the experimental framework. 1st stage batch removal experiments were based on the standard conditions (i.e., 1 g/L biochar dose in 1 ppm phorate solution under 25 °C) with the use of the raw sewage sludge (Raw SS) and 34 biochars. 2nd stage batch removal experiments were continued with the selective biochars having 100% phorate removal efficiencies in the 1st stage batch experiments. 1st stage batch experiments were performed to screen the best efficient samples among all produced biochars and at the end, three biochars achieved 100%

172

phorate removal: KUBC700, HC210BC700KOH1U10 and U10HC210BC700KOH1. Selection of these three biochars were also supported by the analysis of advanced analytical techniques. They were further performed in the 2nd stage batch experiments. In the 2nd stage, phorate removal performances were conducted by various temperatures (25, 30, 35 and 40 °C), pH (3, 5, 7, 9 and 11) and biochar doses (0.2, 1, 5 and 15 g/L). In addition to these two stages, reusability experiments were conducted in order to test the stability of the material. Moreover, real wastewater has been utilized in the batch experiment to compare the phorate removal efficiency of biochars with the deionized water. 2nd stage experiments revealed that their best efficiencies were appeared at lower temperature, higher applied biochar dose and pH between 6 – 6.5. These three selective biochar samples were reused four times and they showed higher than 85% removal at the 5th experiment, showing the material's stable nature. Although the phorate removal performances were lower than in the deionized water, KUBC700 and HC210BC700KOH1U10 achieved 86% and 90% removal while U10HC210BC700KOH1 showed 100% efficiency from the collected wastewater sample. •OH and •SO$_4$ free radicals took part in the degradation of phorate and their intensities have been analyzed by the EPR method for each three biochars by having the highest intensity in U10HC210BC700KOH1 biochar. Free radical assisted biochar-based degradation of phorate was investigated by the GC-MS analysis and degradation intermediates were determined with respect to their residence times. The most efficient degradation was observed in U10HC210BC700KOH1 biochar which exhibits the highest oxygen centered free radical intensities.

To conclude, this study shows that phorate can be removed from water by the use of carbonaceous biochar material. As a result of several modification techniques and various operational parameters, water can be 100% purified from phorate by the combined KOH- and urea-modification of hydrothermally treated biochars.

CHAPTER 6

RECOMMENDATIONS AND FUTURE PERSPECTIVES

According to the results obtained from this study, the use of three selected biochar modifications (KUBC700, HC210BC700KOH1U10, U10HC210BC700KOH1) is recommended in the efficient removal of phorate under broad pH and temperature range. The results showed that these three biochar materials are suitable for the reuse option with efficient results in each cycle. Real wastewater tests revealed its applicability in the wastewater treatment under natural conditions and it can be used in wastewater treatment plants before discharging of wastewater into a water body for the removal of pesticide residues. For future studies, it is recommended that the identified degradation intermediates can be subjected to toxicity tests. Cost-benefit analysis report on the economic suitability of our products is another future perspective of this study by keeping the sustainability in mind. The raw sewage sludge can be performed and valorized in different technologies and life cycle assessment on the comparison of biochar application with these technologies becomes necessary in future studies. Lastly, various application fields of our product such as photocatalytic activities or electrochemically performing catalysts can be further explored.

REFERENCES

Abbas, Q., Liu, G., Yousaf, B., Ali, M. U., Ullah, H., Munir, M. A. M., & Liu, R. (2018). Contrasting effects of operating conditions and biomass particle size on bulk characteristics and surface chemistry of rice husk derived-biochars. *Journal of Analytical and Applied Pyrolysis*, *134*(June), 281–292. https://doi.org/10.1016/j.jaap.2018.06.018

Abbas, Q., Yousaf, B., Ullah, H., Ali, M. U., Zia-ur-Rehman, M., Rizwan, M., & Rinklebe, J. (2020). Biochar-induced immobilization and transformation of silver-nanoparticles affect growth, intracellular-radicles generation and nutrients assimilation by reducing oxidative stress in maize. *Journal of Hazardous Materials*, *390*(March 2019), 121976. https://doi.org/10.1016/j.jhazmat.2019.121976

Abdoul Magid, A. S. I., Islam, M. S., Chen, Y., Weng, L., Li, J., Ma, J., & Li, Y. (2021). Enhanced adsorption of polystyrene nanoplastics (PSNPs) onto oxidized corncob biochar with high pyrolysis temperature. *Science of the Total Environment*, *784*. https://doi.org/10.1016/j.scitotenv.2021.147115

Abraham, J., Silambarasan, S., & Logeswari, P. (2014). Simultaneous degradation of organophosphorus and organochlorine pesticides by bacterial consortium. *Journal of the Taiwan Institute of Chemical Engineers*, *45*(5), 2590–2596. https://doi.org/10.1016/j.jtice.2014.06.014

Accardo, G., Cioffi, R., Colangelo, F., d'Angelo, R., De Stefano, L., & Paglietti, F. (2014). Diffuse reflectance infrared fourier transform spectroscopy for the determination of asbestos species in bulk building aterials. *Materials*, *7*(1), 457–470. https://doi.org/10.3390/ma7010457

AMTA. (2016). *Membrane Bioreactors for Wastewater Treatment*. American Membrane Technology Association. http://www.amtaorg.com/Membrane_Bioreactors_for_Wastewater_Treatment.html

Ashraf, A., Liu, G., Yousaf, B., Arif, M., Ahmed, R., Irshad, S., Cheema, A. I., Rashid, A., & Gulzaman, H. (2021). Recent trends in advanced oxidation process-based degradation of erythromycin: Pollution status, eco-toxicity and degradation mechanism in aquatic ecosystems. *Science of the Total Environment*, *772*, 145389. https://doi.org/10.1016/j.scitotenv.2021.145389

Baharum, N. A., Nasir, H. M., Ishak, M. Y., Isa, N. M., Hassan, M. A., & Aris, A. Z. (2020). Highly efficient removal of diazinon pesticide from aqueous solutions by using coconut shell-modified biochar. *Arabian Journal of Chemistry*, *13*(7), 6106–6121. https://doi.org/10.1016/j.arabjc.2020.05.011

Banerjee, G., & Kumar, B. (2002). Pesticide (acephate) removal by GAC: a case study. *Indian Journal of Environmental Health*, *44*(2), 92–101. https://europepmc.org/article/med/14503380

Bano, K., Kaushal, S., & Singh, P. P. (2021). A review on photocatalytic degradation of hazardous pesticides using heterojunctions. *Polyhedron*, 115465. https://doi.org/10.1016/j.poly.2021.115465

Başer, B., Yousaf, B., Yetis, U., Abbas, Q., Kwon, E. E., Wang, S., Bolan, N. S., & Rinklebe, J. (2021). Formation of nitrogen functionalities in biochar materials and their role in the mitigation of hazardous emerging organic pollutants from wastewater. *Journal of Hazardous Materials*, *416*(March). https://doi.org/10.1016/j.jhazmat.2021.126131

Beckinghausen, A., Reynders, J., Merckel, R., Wu, Y. W., Marais, H., & Schwede, S. (2020). Post-pyrolysis treatments of biochars from sewage sludge and A. mearnsii for ammonia (NH4-n) recovery. *Applied Energy*, *271*(May), 115212. https://doi.org/10.1016/j.apenergy.2020.115212

Biesinger, M. C., Payne, B. P., Grosvenor, A. P., Lau, L. W. M., Gerson, A. R., & Smart, R. S. C. (2011). Resolving surface chemical states in XPS analysis of first row transition metals, oxides and hydroxides: Cr, Mn, Fe, Co and Ni. *Applied Surface Science*, *257*(7), 2717–2730.

https://doi.org/10.1016/j.apsusc.2010.10.051

Birişik, N., Özdem, A., Karahan, A., Sezgen, M., Ertürk, S., Alkan, M., Çakır, E., Elibüyük, E. A., Koca, E., & Aksu, P. (n.d.). *Teoriden Pratiğe Kimyasal Mücadele* (N. Birişik (ed.)).

Boukir, A., Fellak, S., & Doumenq, P. (2019). Structural characterization of Argania spinosa Moroccan wooden artifacts during natural degradation progress using infrared spectroscopy (ATR-FTIR) and X-Ray diffraction (XRD). *Heliyon*, *5*(9), e02477. https://doi.org/10.1016/j.heliyon.2019.e02477

Busch, R., Tielemann, C., Reinsch, S., Müller, R., Patzig, C., Krause, M., & Höche, T. (2021). Sample preparation for analytical scanning electron microscopy using initial notch sectioning. *Micron*, 103090. https://doi.org/10.1016/j.micron.2021.103090

Cebrián, A. N. (2010). *Emerging Organic Contaminants in Sewage Sludge* (Issue May).

Chacón, F. J., Sánchez-Monedero, M. A., Lezama, L., & Cayuela, M. L. (2020). Enhancing biochar redox properties through feedstock selection, metal preloading and post-pyrolysis treatments. *Chemical Engineering Journal*, *395*(March), 125100. https://doi.org/10.1016/j.cej.2020.125100

Chatterjee, R., Sajjadi, B., Chen, W. Y., Mattern, D. L., Hammer, N., Raman, V., & Dorris, A. (2020). *Effect of Pyrolysis Temperature on PhysicoChemical Properties and Acoustic-Based Amination of Biochar for Efficient CO2 Adsorption*. Frontiers in Energy Research. https://doi.org/10.3389/fenrg.2020.00085

Chellappan, S., Nair, V., Sajith, V., & Aparna, K. (2018). Synthesis, optimization and characterization of biochar based catalyst from sawdust for simultaneous esterification and transesterification. *Chinese Journal of Chemical Engineering*, *26*(12), 2654–2663. https://doi.org/10.1016/j.cjche.2018.02.034

Chen, B., Zhou, D., & Zhu, L. (2008). Transitional adsorption and partition of nonpolar and polar aromatic contaminants by biochars of pine needles with different pyrolytic temperatures. *Environmental Science and Technology*, *42*(14), 5137–5143. https://doi.org/10.1021/es8002684

Chen, J. P., Pehkonen, S. O., & Lau, C. C. (2004). Phorate and Terbufos adsorption onto four tropical soils. *Colloids and Surfaces A: Physicochemical and Engineering Aspects*, *240*(1–3), 55–61. https://doi.org/10.1016/j.colsurfa.2004.03.008

Chen, Q., Sun, Y., Liu, S., Zhang, J., Zhang, C., Jiang, H., Han, X., He, L., Wang, S., & Zhang, K. (2021). Colorimetric and fluorescent sensors for detection of nerve agents and organophosphorus pesticides. *Sensors and Actuators, B: Chemical*, *344*(June), 130278. https://doi.org/10.1016/j.snb.2021.130278

Chen, T., Zhang, Y., Wang, H., Lu, W., Zhou, Z., Zhang, Y., & Ren, L. (2014). Influence of pyrolysis temperature on characteristics and heavy metal adsorptive performance of biochar derived from municipal sewage sludge. *Bioresource Technology*, *164*, 47–54. https://doi.org/10.1016/j.biortech.2014.04.048

Chen, W. H., Du, J. T., Lee, K. T., Ong, H. C., Park, Y. K., & Huang, C. C. (2021). Pore volume upgrade of biochar from spent coffee grounds by sodium bicarbonate during torrefaction. *Chemosphere*, *275*, 129999. https://doi.org/10.1016/j.chemosphere.2021.129999

Chen, W., Yang, H., Chen, Y., Chen, X., Fang, Y., & Chen, H. (2016). Biomass pyrolysis for nitrogen-containing liquid chemicals and nitrogen-doped carbon materials. *Journal of Analytical and Applied Pyrolysis*, *120*, 186–193. https://doi.org/10.1016/j.jaap.2016.05.004

Chen, W., Yang, H., Chen, Y., Xia, M., Chen, X., & Chen, H. (2017). Transformation of Nitrogen and Evolution of N-Containing Species during Algae Pyrolysis. *Environmental Science and Technology*, *51*(11), 6570–6579.

https://doi.org/10.1021/acs.est.7b00434

Chen, X., Duan, X., Oh, W. Da, Zhang, P. H., Guan, C. T., Zhu, Y. A., & Lim, T. T. (2019). Insights into nitrogen and boron-co-doped graphene toward high-performance peroxymonosulfate activation: Maneuverable N-B bonding configurations and oxidation pathways. *Applied Catalysis B: Environmental*, *253*(January), 419–432. https://doi.org/10.1016/j.apcatb.2019.04.018

Cheng, H., Ji, R., Bian, Y., Jiang, X., & Song, Y. (2020). From macroalgae to porous graphitized nitrogen-doped biochars – Using aquatic biota to treat polycyclic aromatic hydrocarbons-contaminated water. *Bioresource Technology*, *303*(71), 122947. https://doi.org/10.1016/j.biortech.2020.122947

Chia, C. H., Gong, B., Joseph, S. D., Marjo, C. E., Munroe, P., & Rich, A. M. (2012). Imaging of mineral-enriched biochar by FTIR, Raman and SEM-EDX. *Vibrational Spectroscopy*, *62*, 248–257. https://doi.org/10.1016/j.vibspec.2012.06.006

Clurman, A. M., Rodríguez-narvaez, O. M., Jayarathne, A., Silva, G. De, Ranasinghe, M. I., Goonetilleke, A., & Bandala, E. R. (2020). of emerging contaminants. *Chemical Engineering Journal*, 126277. https://doi.org/10.1016/j.cej.2020.126277

Commission, E. (2020). *Pesticides*. https://ec.europa.eu/food/plant/pesticides_en

Conti, R., Rombolà, A. G., Modelli, A., Torri, C., & Fabbri, D. (2014). Evaluation of the thermal and environmental stability of switchgrass biochars by Py-GC-MS. *Journal of Analytical and Applied Pyrolysis*, *110*(1), 239–247. https://doi.org/10.1016/j.jaap.2014.09.010

Dai, L., Fan, L., Liu, Y., Ruan, R., Wang, Y., Zhou, Y., Zhao, Y., & Yu, Z. (2017). Production of bio-oil and biochar from soapstock via microwave-assisted co-catalytic fast pyrolysis. *Bioresource Technology*, *225*, 1–8. https://doi.org/10.1016/j.biortech.2016.11.017

Dehghanzad, B., Razavi Aghjeh, M. K., Rafeie, O., Tavakoli, A., & Jameie Oskooie, A. (2016). Synthesis and characterization of graphene and functionalized graphene via chemical and thermal treatment methods. *RSC Advances*, *6*(5), 3578–3585. https://doi.org/10.1039/c5ra19954a

Dehkhoda, A. M., Gyenge, E., & Ellis, N. (2016). A novel method to tailor the porous structure of KOH-activated biochar and its application in capacitive deionization and energy storage. *Biomass and Bioenergy*, *87*, 107–121. https://doi.org/10.1016/j.biombioe.2016.02.023

Dhangar, K., & Kumar, M. (2020). Tricks and tracks in removal of emerging contaminants from the wastewater through hybrid treatment systems: A review. *Science of The Total Environment*, *738*(336), 140320. https://doi.org/10.1016/j.scitotenv.2020.140320

Dieguez-Alonso, A., Funke, A., Anca-Couce, A., Rombolà, A. G., Ojeda, G., Bachmann, J., & Behrendt, F. (2018). Towards biochar and hydrochar engineering-influence of process conditions on surface physical and chemical properties, thermal stability, nutrient availability, toxicity and wettability. *Energies*, *11*(3). https://doi.org/10.3390/en11030496

Ding, D., Yang, S., Qian, X., Chen, L., & Cai, T. (2020). Nitrogen-doping positively whilst sulfur-doping negatively affect the catalytic activity of biochar for the degradation of organic contaminant. *Applied Catalysis B: Environmental*, *263*(1), 118348. https://doi.org/10.1016/j.apcatb.2019.118348

Dong, C. Di, Chen, C. W., & Hung, C. M. (2017). Synthesis of magnetic biochar from bamboo biomass to activate persulfate for the removal of polycyclic aromatic hydrocarbons in marine sediments. *Bioresource Technology*, *245*(August), 188–195. https://doi.org/10.1016/j.biortech.2017.08.204

Dong, X., He, L., Hu, H., Liu, N., Gao, S., & Piao, Y. (2018). Removal of 17B-estradiol by using highly adsorptive magnetic biochar nanoparticles from aqueous solution. *Chemical Engineering Journal*, *352*(March), 371–379.

https://doi.org/10.1016/j.cej.2018.07.025

Duan, X., Indrawirawan, S., Sun, H., & Wang, S. (2015). Effects of nitrogen-, boron-, and phosphorus-doping or codoping on metal-free graphene catalysis. *Catalysis Today*, *249*, 184–191. https://doi.org/10.1016/j.cattod.2014.10.005

Duan, X., Sun, H., & Wang, S. (2018). Metal-Free Carbocatalysis in Advanced Oxidation Reactions. *Accounts of Chemical Research*, *51*(3), 678–687. https://doi.org/10.1021/acs.accounts.7b00535

Dunnigan, L., Morton, B. J., Ashman, P. J., Zhang, X., & Kwong, C. W. (2018). Emission characteristics of a pyrolysis-combustion system for the co-production of biochar and bioenergy from agricultural wastes. *Waste Management*, *77*, 59–66. https://doi.org/10.1016/j.wasman.2018.05.004

Ederer, J., Janoš, P., Ecorchard, P., Tolasz, J., Štengl, V., Beneš, H., Perchacz, M., & Pop-Georgievski, O. (2017). Determination of amino groups on functionalized graphene oxide for polyurethane nanomaterials: XPS quantitation vs. functional speciation. *RSC Advances*, *7*(21), 12464–12473. https://doi.org/10.1039/c6ra28745j

El-Naggar, A., Ahmed, N., Mosa, A., Niazi, N. K., Yousaf, B., Sharma, A., Sarkar, B., Cai, Y., & Chang, S. X. (2021). Nickel in soil and water: Sources, biogeochemistry, and remediation using biochar. *Journal of Hazardous Materials*, *419*(May), 126421. https://doi.org/10.1016/j.jhazmat.2021.126421

EPA, E. P. A. (2001). Phorate IRED Facts. *US EPA Pesticides Registration*.

European Commission. (2000). Water Framework Directive (WFD) (2000/60/EC). *Official Journal of the European Communities*, *L 269*(September 2000), 1–15.

European Parliament. (2019). Chemicals and Pesticides. *Fact Sheets on the European Union*.

Fahmi, A. H., Samsuri, A. W., Jol, H., & Singh, D. (2018). Bioavailability and leaching of Cd and Pb from contaminated soil amended with different sizes of

biochar. *Royal Society Open Science*, *5*(11). https://doi.org/10.1098/rsos.181328

Fan, Youhua, Wang, H., Deng, L., Wang, Y., Kang, D., Li, C., & Chen, H. (2020). Enhanced adsorption of Pb(II) by nitrogen and phosphorus co-doped biochar derived from Camellia oleifera shells. *Environmental Research*, *191*(August), 110030. https://doi.org/10.1016/j.envres.2020.110030

Fan, Yuxing, Xiong, Y., Zhang, Y., Jiang, Z., Tang, H., Wu, L., Li, M., Xiao, X., Hu, C., & Zou, X. (2021). Method to characterize color of biochar and its prediction with biochar yield as model property. *Biochar*, *0123456789*. https://doi.org/10.1007/s42773-021-00119-w

Fang, J., Zhan, L., Ok, Y. S., & Gao, B. (2018). Minireview of potential applications of hydrochar derived from hydrothermal carbonization of biomass. *Journal of Industrial and Engineering Chemistry*, *57*, 15–21. https://doi.org/10.1016/j.jiec.2017.08.026

Flach, B., Lieberz, S., & Bolla, S. (2019). GAIN Report - EU Biofuels Annual 2019. In *Global Agricultural Information Network*. https://apps.fas.usda.gov/newgainapi/api/report/downloadreportbyfilename?filename=Biofuels Annual_The Hague_EU-28_7-15-2019.pdf

Gandhi, K., Lari, S., Tripathi, D., & Kanade, G. (2016). Advanced oxidation processes for the treatment of chlorpyrifos, dimethoate and phorate in aqueous solution. *Journal of Water Reuse and Desalination*, *6*(1), 195–203. https://doi.org/10.2166/wrd.2015.062

Gao, J. R., & Zhu, K. Y. (2000). Comparative toxicity of selected organophosphate insecticides against resistant and susceptible clones of the greenbug, Schizaphis graminum (Homoptera: Aphididae). *Journal of Agricultural and Food Chemistry*, *48*(10), 4717–4722. https://doi.org/10.1021/jf000548p

García, J., García-Galán, M. J., Day, J. W., Boopathy, R., White, J. R., Wallace, S., & Hunter, R. G. (2020). A review of emerging organic contaminants (EOCs),

antibiotic resistant bacteria (ARB), and antibiotic resistance genes (ARGs) in the environment: Increasing removal with wetlands and reducing environmental impacts. *Bioresource Technology*, *307*(February), 123228. https://doi.org/10.1016/j.biortech.2020.123228

Ghodake, G. S., Shinde, S. K., Kadam, A. A., Saratale, R. G., Saratale, G. D., Kumar, M., Palem, R. R., AL-Shwaiman, H. A., Elgorban, A. M., Syed, A., & Kim, D. Y. (2021). Review on biomass feedstocks, pyrolysis mechanism and physicochemical properties of biochar: State-of-the-art framework to speed up vision of circular bioeconomy. *Journal of Cleaner Production*, *297*, 126645. https://doi.org/10.1016/j.jclepro.2021.126645

Gong, X., Huang, D., Liu, Y., Zeng, G., Chen, S., Wang, R., Xu, P., Cheng, M., Zhang, C., & Xue, W. (2019). Biochar facilitated the phytoremediation of cadmium contaminated sediments: Metal behavior, plant toxity, and microbial activity. *Science of the Total Environment*, *666*, 1126–1133. https://doi.org/10.1016/j.scitotenv.2019.02.215

Guizani, C., Jeguirim, M., Valin, S., Limousy, L., & Salvador, S. (2017). Biomass chars: The effects of pyrolysis conditions on their morphology, structure, chemical properties and reactivity. *Energies*, *10*(6). https://doi.org/10.3390/en10060796

Guo, R., Yan, L., Rao, P., Wang, R., & Guo, X. (2020). Nitrogen and sulfur co-doped biochar derived from peanut shell with enhanced adsorption capacity for diethyl phthalate *. *Environmental Pollution*, *258*, 113674. https://doi.org/10.1016/j.envpol.2019.113674

Güzel, F., Sayğılı, H., Akkaya Sayğılı, G., Koyuncu, F., & Yılmaz, C. (2017). Optimal oxidation with nitric acid of biochar derived from pyrolysis of weeds and its application in removal of hazardous dye methylene blue from aqueous solution. *Journal of Cleaner Production*, *144*, 260–265. https://doi.org/10.1016/j.jclepro.2017.01.029

Hassan, M., Liu, Y., Naidu, R., Parikh, S. J., Du, J., Qi, F., & Willett, I. R. (2020). Influences of feedstock sources and pyrolysis temperature on the properties of biochar and functionality as adsorbents: A meta-analysis. *Science of the Total Environment, 744*, 140714. https://doi.org/10.1016/j.scitotenv.2020.140714

Henderson, M. C., Krueger, S. K., Siddens, L. K., Stevens, J. F., & Williams, D. E. (2004). S-oxygenation of the thioether organophosphate insecticides phorate and disulfoton by human lung flavin-containing monooxygenase 2. *Biochemical Pharmacology, 68*(5), 959–967. https://doi.org/10.1016/j.bcp.2004.05.051

Ho, S. H., Chen, Y. di, Li, R., Zhang, C., Ge, Y., Cao, G., Ma, M., Duan, X., Wang, S., & Ren, N. qi. (2019). N-doped graphitic biochars from C-phycocyanin extracted Spirulina residue for catalytic persulfate activation toward nonradical disinfection and organic oxidation. *Water Research, 159*, 77–86. https://doi.org/10.1016/j.watres.2019.05.008

Huang, H., Tang, J., Gao, K., He, R., Zhao, H., & Werner, D. (2017). Characterization of KOH modified biochars from different pyrolysis temperatures and enhanced adsorption of antibiotics. *RSC Advances, 7*(24), 14640–14648. https://doi.org/10.1039/c6ra27881g

Huang, W. H., Lee, D. J., & Huang, C. (2021). Modification on biochars for applications: A research update. *Bioresource Technology, 319*(September 2020). https://doi.org/10.1016/j.biortech.2020.124100

Isakovski, M. K., Maletić, S., Tamindžija, D., Apostolović, T., Petrović, J., Tričković, J., & Agbaba, J. (2020). Impact of hydrochar and biochar amendments on sorption and biodegradation of organophosphorus pesticides during transport through Danube alluvial sediment. *Journal of Environmental Management, 274*(April). https://doi.org/10.1016/j.jenvman.2020.111156

Jain, A., Jayaraman, S., Balasubramanian, R., & Srinivasan, M. P. (2014). Hydrothermal pre-treatment for mesoporous carbon synthesis: Enhancement of

chemical activation. *Journal of Materials Chemistry A*, *2*(2), 520–528. https://doi.org/10.1039/c3ta12648j

Jaipieam, S., Visuthismajarn, P., Sutheravut, P., Siriwong, W., Thoumsang, S., Borjan, M., & Robson, M. (2009). Organophosphate pesticide residues in drinking water from artesian wells and health risk assessment of agricultural communities, Thailand. *Human and Ecological Risk Assessment*, *15*(6), 1304–1316. https://doi.org/10.1080/10807030903306984

Janos, P., Kuran, P., Kormunda, M., Stengl, V., Grygar, T. M., Dosek, M., Stastny, M., Ederer, J., Pilarova, V., & Vrtoch, L. (2014). Cerium dioxide as a new reactive sorbent for fast degradation of parathion methyl and some other organophosphates. *Journal of Rare Earths*, *32*(4), 360–370. https://doi.org/10.1016/S1002-0721(14)60079-X

Jansen, R. J. J., & van Bekkum, H. (1995). XPS of nitrogen-containing functional groups on activated carbon. *Carbon*, *33*(8), 1021–1027. https://doi.org/10.1016/0008-6223(95)00030-H

Janu, R., Mrlik, V., Ribitsch, D., Hofman, J., Sedláček, P., Bielská, L., & Soja, G. (2021). Biochar surface functional groups as affected by biomass feedstock, biochar composition and pyrolysis temperature. *Carbon Resources Conversion*, *4*(November 2020), 36–46. https://doi.org/10.1016/j.crcon.2021.01.003

Jariyal, M., Jindal, V., Mandal, K., Gupta, V. K., & Singh, B. (2018). Bioremediation of organophosphorus pesticide phorate in soil by microbial consortia. *Ecotoxicology and Environmental Safety*, *159*(December 2017), 310–316. https://doi.org/10.1016/j.ecoenv.2018.04.063

Jin, J., Li, Y., Zhang, J., Wu, S., Cao, Y., Liang, P., Zhang, J., Wong, M. H., Wang, M., Shan, S., & Christie, P. (2016). Influence of pyrolysis temperature on properties and environmental safety of heavy metals in biochars derived from municipal sewage sludge. *Journal of Hazardous Materials*, *320*, 417–426. https://doi.org/10.1016/j.jhazmat.2016.08.050

Kasera, N., Hall, S., & Kolar, P. (2021). Effect of surface modification by nitrogen-containing chemicals on morphology and surface characteristics of N-doped pine bark biochars. *Journal of Environmental Chemical Engineering*, *9*(2), 105161. https://doi.org/10.1016/j.jece.2021.105161

Kaushal, J., Khatri, M., & Arya, S. K. (2021). A treatise on Organophosphate pesticide pollution: Current strategies and advancements in their environmental degradation and elimination. *Ecotoxicology and Environmental Safety*, *207*, 111483. https://doi.org/10.1016/j.ecoenv.2020.111483

Khalid, S., Shahid, M., Murtaza, B., Bibi, I., Natasha, Asif Naeem, M., & Niazi, N. K. (2020). A critical review of different factors governing the fate of pesticides in soil under biochar application. *Science of the Total Environment*, *711*, 134645. https://doi.org/10.1016/j.scitotenv.2019.134645

Khedr, T., Hammad, A. A., Elmarsafy, A. M., Halawa, E., & Soliman, M. (2019). Degradation of some organophosphorus pesticides in aqueous solution by gamma irradiation. *Journal of Hazardous Materials*, *373*(August 2018), 23–28. https://doi.org/10.1016/j.jhazmat.2019.03.011

Krysanova, K., Krylova, A., & Zaichenko, V. (2019). Properties of biochar obtained by hydrothermal carbonization and torrefaction of peat. *Fuel*, *256*(July), 115929. https://doi.org/10.1016/j.fuel.2019.115929

Ku, Y., Lin, H. S., Wang, W., & Ma, C. M. (2007). Decomposition of phorate in aqueous solution by ozonation. *Journal of Environmental Science and Health - Part B Pesticides, Food Contaminants, and Agricultural Wastes*, *42*(2), 143–149. https://doi.org/10.1080/03601230601123268

Lapworth, D. J., Baran, N., Stuart, M. E., & Ward, R. S. (2012). Emerging organic contaminants in groundwater: A review of sources, fate and occurrence. *Environmental Pollution*, *163*, 287–303. https://doi.org/10.1016/j.envpol.2011.12.034

Lee, J., Lee, K., Sohn, D., Kim, Y. M., & Park, K. Y. (2018). Hydrothermal

carbonization of lipid extracted algae for hydrochar production and feasibility of using hydrochar as a solid fuel. *Energy*, *153*, 913–920. https://doi.org/10.1016/j.energy.2018.04.112

Lee, X. J., Lee, L. Y., Gan, S., Thangalazhy-Gopakumar, S., & Ng, H. K. (2017). Biochar potential evaluation of palm oil wastes through slow pyrolysis: Thermochemical characterization and pyrolytic kinetic studies. *Bioresource Technology*, *236*, 155–163. https://doi.org/10.1016/j.biortech.2017.03.105

Leng, L., & Huang, H. (2018). An overview of the effect of pyrolysis process parameters on biochar stability. *Bioresource Technology*, *270*(August), 627–642. https://doi.org/10.1016/j.biortech.2018.09.030

Leng, L., Xu, S., Liu, R., Yu, T., Zhuo, X., Leng, S., Xiong, Q., & Huang, H. (2019a). Nitrogen containing functional groups of biochar: An overview. *Bioresource Technology*, *298*(October 2019), 122286. https://doi.org/10.1016/j.biortech.2019.122286

Leng, L., Xu, S., Liu, R., Yu, T., Zhuo, X., Leng, S., Xiong, Q., & Huang, H. (2019b). Nitrogen containing functional groups of biochar: An overview. *Bioresource Technology*, *298*(August 2019), 122286. https://doi.org/10.1016/j.biortech.2019.122286

Li, Changkun, Ma, Y., Mi, Z., Huo, R., Zhou, T., Hai, H., Kwok, L. yu, Sun, Z., Chen, Y., & Zhang, H. (2018). Screening for Lactobacillus plantarum strains that possess organophosphorus pesticide-degrading activity and metabolomic analysis of phorate degradation. *Frontiers in Microbiology*, *9*(SEP), 1–13. https://doi.org/10.3389/fmicb.2018.02048

Li, Chenglong, He, D., Huang, Z.-H., & Wang, M.-X. (2018). Hierarchical Micro-/Mesoporous Carbon Derived from Rice Husk by Hydrothermal Pre-Treatment for High Performance Supercapacitor. *Journal of The Electrochemical Society*, *165*(14), A3334–A3341. https://doi.org/10.1149/2.0121814jes

Li, J., He, F., Shen, X., Hu, D., & Huang, Q. (2020). Pyrolyzed fabrication of N/P

co-doped biochars from (NH4)3PO4-pretreated coffee shells and appraisement for remedying aqueous Cr(VI) contaminants. *Bioresource Technology*, *315*(June), 123840. https://doi.org/10.1016/j.biortech.2020.123840

Li, S., Barreto, V., Li, R., Chen, G., & Hsieh, Y. P. (2018). Nitrogen retention of biochar derived from different feedstocks at variable pyrolysis temperatures. *Journal of Analytical and Applied Pyrolysis*, *133*(April), 136–146. https://doi.org/10.1016/j.jaap.2018.04.010

Li, Y., Xing, B., Ding, Y., Han, X., & Wang, S. (2020). A critical review of the production and advanced utilization of biochar via selective pyrolysis of lignocellulosic biomass. *Bioresource Technology*, *312*(June), 123614. https://doi.org/10.1016/j.biortech.2020.123614

Li, Zhe, Sun, Y., Yang, Y., Han, Y., Wang, T., Chen, J., & Tsang, D. C. W. (2020). Biochar-supported nanoscale zero-valent iron as an efficient catalyst for organic degradation in groundwater. *Journal of Hazardous Materials*, *383*(September 2019), 121240. https://doi.org/10.1016/j.jhazmat.2019.121240

Li, Zhengjia, Deng, H., Yang, L., Zhang, G., Li, Y., & Ren, Y. (2018). Influence of potassium hydroxide activation on characteristics and environmental risk of heavy metals in chars derived from municipal sewage sludge. *Bioresource Technology*, *256*(January), 216–223. https://doi.org/10.1016/j.biortech.2018.02.013

Li, Zhenhao, Xing, B., Ding, Y., Li, Y., & Wang, S. (2020). A high-performance biochar produced from bamboo pyrolysis with in-situ nitrogen doping and activation for adsorption of phenol and methylene blue. *Chinese Journal of Chemical Engineering*, *xxxx*. https://doi.org/10.1016/j.cjche.2020.03.031

Lian, F., Cui, G., Liu, Z., Duo, L., Zhang, G., & Xing, B. (2016). One-step synthesis of a novel N-doped microporous biochar derived from crop straws with high dye adsorption capacity. *Journal of Environmental Management*, *176*, 61–68. https://doi.org/10.1016/j.jenvman.2016.03.043

Liao, S., Pan, B., Li, H., Zhang, D., & Xing, B. (2014). Detecting free radicals in biochars and determining their ability to inhibit the germination and growth of corn, wheat and rice seedlings. *Environmental Science and Technology*, *48*(15), 8581–8587. https://doi.org/10.1021/es404250a

Lin, X., Yu, Q., Yang, W., He, C., Zhou, Y., Duan, N., & Wu, S. (2021). Double-enzymes-mediated fluorescent assay for sensitive determination of organophosphorus pesticides based on the quenching of upconversion nanoparticles by Fe3+. *Food Chemistry*, *345*(September 2020), 128809. https://doi.org/10.1016/j.foodchem.2020.128809

Lin, Y., Ma, X., Peng, X., Yu, Z., Fang, S., Lin, Y., & Fan, Y. (2016). Combustion, pyrolysis and char CO2-gasification characteristics of hydrothermal carbonization solid fuel from municipal solid wastes. *Fuel*, *181*, 905–915. https://doi.org/10.1016/j.fuel.2016.05.031

Lin, Z., Waller, G., Liu, Y., Liu, M., & Wong, C. P. (2012). Facile synthesis of nitrogen-doped graphene via pyrolysis of graphene oxide and urea, and its electrocatalytic activity toward the oxygen-reduction reaction. *Advanced Energy Materials*, *2*(7), 884–888. https://doi.org/10.1002/aenm.201200038

Ling, L. L., Liu, W. J., Zhang, S., & Jiang, H. (2017). Magnesium Oxide Embedded Nitrogen Self-Doped Biochar Composites: Fast and High-Efficiency Adsorption of Heavy Metals in an Aqueous Solution. *Environmental Science and Technology*, *51*(17), 10081–10089. https://doi.org/10.1021/acs.est.7b02382

Ling, W., Qiang, Z., Shi, Y., Zhang, T., & Dong, B. (2011). Fe(III)-loaded activated carbon as catalyst to improve omethoate degradation by ozone in water. *Journal of Molecular Catalysis A: Chemical*, *342–343*, 23–29. https://doi.org/10.1016/j.molcata.2011.04.005

Liu, J., Liu, H., Yang, X., Jia, X., Cai, M., & Bao, Y. (2021). Preparation of Si–Mn/biochar composite and discussions about characterizations, advances in

application and adsorption mechanisms. *Chemosphere*, *281*(May), 130946. https://doi.org/10.1016/j.chemosphere.2021.130946

Liu, L., Tan, Z., & Ye, Z. (2018). Transformation and Transport Mechanism of Nitrogenous Compounds in a Biochar "preparation-Returning to the Field" Process Studied by Employing an Isotope Tracer Method. *ACS Sustainable Chemistry and Engineering*, *6*(2), 1780–1791. https://doi.org/10.1021/acssuschemeng.7b03172

Liu, P., Ptacek, C. J., Blowes, D. W., & Gould, W. D. (2018). Control of mercury and methylmercury in contaminated sediments using biochars: A long-term microcosm study. *Applied Geochemistry*, *92*(September 2017), 30–44. https://doi.org/10.1016/j.apgeochem.2018.02.004

Liu, S. jia, Liu, Y. guo, Tan, X. fei, Zeng, G. ming, Zhou, Y. hui, Liu, S. bo, Yin, Z. hong, Jiang, L. hua, Li, M. fang, & Wen, J. (2018). The effect of several activated biochars on Cd immobilization and microbial community composition during in-situ remediation of heavy metal contaminated sediment. *Chemosphere*, *208*, 655–664. https://doi.org/10.1016/j.chemosphere.2018.06.023

Lu, Z., Zhang, H., Shahab, A., Zhang, K., Zeng, H., Bacha, A. U. R., Nabi, I., & Ullah, H. (2021). Comparative study on characterization and adsorption properties of phosphoric acid activated biochar and nitrogen-containing modified biochar employing Eucalyptus as a precursor. *Journal of Cleaner Production*, *303*. https://doi.org/10.1016/j.jclepro.2021.127046

Ma, W., Wang, N., Du, Y., Xu, P., Sun, B., Zhang, L., & Lin, K. Y. A. (2019). Human-Hair-Derived N, S-Doped Porous Carbon: An Enrichment and Degradation System for Wastewater Remediation in the Presence of Peroxymonosulfate. *ACS Sustainable Chemistry and Engineering*, *7*(2), 2718–2727. https://doi.org/10.1021/acssuschemeng.8b05801

Ma, X. K., Lee, N. H., Oh, H. J., Jung, S. C., Lee, W. J., & Kim, S. J. (2011).

Morphology control of hexagonal boron nitride by a silane coupling agent. *Journal of Crystal Growth*, *316*(1), 185–190. https://doi.org/10.1016/j.jcrysgro.2010.12.066

MAF, M. of A. and F. (2019). 2018 Yılı Faaliyet Raporu. *Tarım ve Orman Bakanlığı, Gıda ve Kontrol Genel Müdürlüğü*.

Malakootian, M., Shahesmaeili, A., Faraji, M., Amiri, H., & Silva Martinez, S. (2020). Advanced oxidation processes for the removal of organophosphorus pesticides in aqueous matrices: A systematic review and meta-analysis. *Process Safety and Environmental Protection*, *134*, 292–307. https://doi.org/10.1016/j.psep.2019.12.004

Maliutina, K., Tahmasebi, A., & Yu, J. (2018a). Pressurized entrained-flow pyrolysis of microalgae: Enhanced production of hydrogen and nitrogen-containing compounds. *Bioresource Technology*, *256*(December 2017), 160–169. https://doi.org/10.1016/j.biortech.2018.02.016

Maliutina, K., Tahmasebi, A., & Yu, J. (2018b). The transformation of nitrogen during pressurized entrained-flow pyrolysis of Chlorella vulgaris. *Bioresource Technology*, *262*(April), 90–97. https://doi.org/10.1016/j.biortech.2018.04.073

Manyà, J. J. (2012). Pyrolysis for biochar purposes: A review to establish current knowledge gaps and research needs. *Environmental Science and Technology*, *46*(15), 7939–7954. https://doi.org/10.1021/es301029g

Maziarka, P., Wurzer, C., Arauzo, P. J., Dieguez-Alonso, A., Mašek, O., & Ronsse, F. (2021). Do you BET on routine? The reliability of N2 physisorption for the quantitative assessment of biochar's surface area. *Chemical Engineering Journal*, *418*(February). https://doi.org/10.1016/j.cej.2021.129234

Mazur, M. (2006). A dozen useful tips on how to minimise the influence of sources of error in quantitative electron paramagnetic resonance (EPR) spectroscopy - A review. *Analytica Chimica Acta*, *561*(1–2), 1–15. https://doi.org/10.1016/j.aca.2006.01.006

193

Meng, Y., Yao, C., Xue, S., & Yang, H. (2014). Application of fourier transform infrared (FT-IR) spectroscopy in determination of microalgal compositions. *Bioresource Technology*, *151*, 347–354. https://doi.org/10.1016/j.biortech.2013.10.064

Mian, M. M., Liu, G., Yousaf, B., Fu, B., Ahmed, R., Abbas, Q., Munir, M. A. M., & Ruijia, L. (2019). One-step synthesis of N-doped metal/biochar composite using NH 3 -ambiance pyrolysis for efficient degradation and mineralization of Methylene Blue. *Journal of Environmental Sciences (China)*, *78*, 29–41. https://doi.org/10.1016/j.jes.2018.06.014

Mian, M. M., Liu, G., & Zhou, H. (2020). Preparation of N-doped biochar from sewage sludge and melamine for peroxymonosulfate activation: N-functionality and catalytic mechanisms. *Science of The Total Environment*, *744*, 140862. https://doi.org/10.1016/j.scitotenv.2020.140862

Mohan, D., Sarswat, A., Ok, Y. S., & Pittman, C. U. (2014). Organic and inorganic contaminants removal from water with biochar, a renewable, low cost and sustainable adsorbent - A critical review. *Bioresource Technology*, *160*, 191–202. https://doi.org/10.1016/j.biortech.2014.01.120

Mortazavian, S., Jones-Lepp, T., Bae, J. H., Chun, D., Bandala, E. R., & Moon, J. (2019). Heat-treated biochar impregnated with zero-valent iron nanoparticles for organic contaminants removal from aqueous phase: Material characterizations and kinetic studies. *Journal of Industrial and Engineering Chemistry*, *76*, 197–214. https://doi.org/10.1016/j.jiec.2019.03.041

Mujtaba Munir, M. A., Liu, G., Yousaf, B., Ali, M. U., Cheema, A. I., Rashid, M. S., & Rehman, A. (2020). Bamboo-biochar and hydrothermally treated-coal mediated geochemical speciation, transformation and uptake of Cd, Cr, and Pb in a polymetal(iod)s-contaminated mine soil. *Environmental Pollution*, *265*, 114816. https://doi.org/10.1016/j.envpol.2020.114816

Nidheesh, P. V., Gopinath, A., Ranjith, N., Praveen Akre, A., Sreedharan, V., &

Suresh Kumar, M. (2021). Potential role of biochar in advanced oxidation processes: A sustainable approach. *Chemical Engineering Journal*, *405*(May 2020), 126582. https://doi.org/10.1016/j.cej.2020.126582

Nohira, H. (2002). Characterization of ALCVD-Al2O3 and ZrO2 layer using X-ray photoelectron spectroscopy. *Journal of Non-Crystalline Solids*, *303*, 83–87.

Nzediegwu, C., Naeth, M. A., & Chang, S. X. (2021). Lead(II) adsorption on microwave-pyrolyzed biochars and hydrochars depends on feedstock type and production temperature. *Journal of Hazardous Materials*, *412*(January), 125255. https://doi.org/10.1016/j.jhazmat.2021.125255

Oh, W. Da, Lisak, G., Webster, R. D., Liang, Y. N., Veksha, A., Giannis, A., Moo, J. G. S., Lim, J. W., & Lim, T. T. (2018). Insights into the thermolytic transformation of lignocellulosic biomass waste to redox-active carbocatalyst: Durability of surface active sites. *Applied Catalysis B: Environmental*, *233*(February), 120–129. https://doi.org/10.1016/j.apcatb.2018.03.106

Ortiz-Medina, J., Wang, Z., Cruz-Silva, R., Morelos-Gomez, A., Wang, F., Yao, X., Terrones, M., & Endo, M. (2019). Defect Engineering and Surface Functionalization of Nanocarbons for Metal-Free Catalysis. *Advanced Materials*, *31*(13), 1–16. https://doi.org/10.1002/adma.201805717

Pailan, S., Gupta, D., Apte, S., Krishnamurthi, S., & Saha, P. (2015). Degradation of organophosphate insecticide by a novel Bacillus aryabhattai strain SanPS1, isolated from soil of agricultural field in Burdwan, West Bengal, India. *International Biodeterioration and Biodegradation*, *103*, 191–195. https://doi.org/10.1016/j.ibiod.2015.05.006

Pari, G., Darmawan, S., & Prihandoko, B. (2014). Porous Carbon Spheres from Hydrothermal Carbonization and KOH Activation on Cassava and Tapioca Flour Raw Material. *Procedia Environmental Sciences*, *20*, 342–351. https://doi.org/10.1016/j.proenv.2014.03.043

Pariyar, P., Kumari, K., Jain, M. K., & Jadhao, P. S. (2020). Evaluation of change in

biochar properties derived from different feedstock and pyrolysis temperature for environmental and agricultural application. *Science of the Total Environment, 713*, 136433. https://doi.org/10.1016/j.scitotenv.2019.136433

Peng, Y.-Y., Dussan, D. D., & Narain, R. (2020). Chapter 9 - Thermal, mechanical, and electrical properties. In R. Narain (Ed.), *Polymer Science and Nanotechnology* (pp. 179–201). Elsevier. https://doi.org/https://doi.org/10.1016/B978-0-12-816806-6.00009-1

Prabakar, D., Manimudi, V. T., Suvetha K, S., Sampath, S., Mahapatra, D. M., Rajendran, K., & Pugazhendhi, A. (2018). Advanced biohydrogen production using pretreated industrial waste: Outlook and prospects. *Renewable and Sustainable Energy Reviews*, *96*(August 2017), 306–324. https://doi.org/10.1016/j.rser.2018.08.006

Qu, J., Wang, Y., Tian, X., Jiang, Z., Deng, F., Tao, Y., Jiang, Q., Wang, L., & Zhang, Y. (2021). KOH-activated porous biochar with high specific surface area for adsorptive removal of chromium (VI) and naphthalene from water: Affecting factors, mechanisms and reusability exploration. *Journal of Hazardous Materials*, *401*(May 2020), 123292. https://doi.org/10.1016/j.jhazmat.2020.123292

Raaij, J. van, Raat, W. de, & Krüse, J. (2003). Phorate; Health-based Reassessment of Administrative Occupational Exposure Limits. In *The Hague: Health Council of the Netherlands* (Issue 2000). https://doi.org/10.1016/b978-081551401-5.50287-2

Ren, N., Tang, Y., & Li, M. (2018). Mineral additive enhanced carbon retention and stabilization in sewage sludge-derived biochar. *Process Safety and Environmental Protection*, *115*, 70–78. https://doi.org/10.1016/j.psep.2017.11.006

Rignanese, G. (1997). Nitrogen Incorporation at Si (001) − SiO 2 Interfaces: Relation between N 1 s Core-Level Shifts and Microscopic Structure. *Physical*

Review Letters, *79*, 5174.

Safaei Khorram, M., Zhang, Q., Lin, D., Zheng, Y., Fang, H., & Yu, Y. (2016). Biochar: A review of its impact on pesticide behavior in soil environments and its potential applications. *Journal of Environmental Sciences (China)*, *44*, 269–279. https://doi.org/10.1016/j.jes.2015.12.027

Saha, D., & Kienbaum, M. J. (2019). Role of oxygen, nitrogen and sulfur functionalities on the surface of nanoporous carbons in CO2 adsorption: A critical review. *Microporous and Mesoporous Materials*, *287*(March), 29–55. https://doi.org/10.1016/j.micromeso.2019.05.051

Sahoo, S. S., Vijay, V. K., Chandra, R., & Kumar, H. (2021). Production and characterization of biochar produced from slow pyrolysis of pigeon pea stalk and bamboo. *Cleaner Engineering and Technology*, *3*, 100101. https://doi.org/10.1016/j.clet.2021.100101

Sajdak, M., & Kotyczka-Morańska, M. (2018). Development and validation of a fast method based on infrared spectroscopy for biochar quality assessment. *Biomass and Bioenergy*, *112*(February 2017), 99–109. https://doi.org/10.1016/j.biombioe.2018.02.019

Sajjadi, B., Chen, W. Y., & Egiebor, N. O. (2019). A comprehensive review on physical activation of biochar for energy and environmental applications. *Reviews in Chemical Engineering*, *35*(6), 735–776. https://doi.org/10.1515/revce-2017-0113

Sarlak, Z., Khosravi-Darani, K., Rouhi, M., Garavand, F., Mohammadi, R., & Sobhiyeh, M. R. (2021). Bioremediation of organophosphorus pesticides in contaminated foodstuffs using probiotics. *Food Control*, *126*(November 2020), 108006. https://doi.org/10.1016/j.foodcont.2021.108006

Shareef, T. M. E., & Zhao, B. (2017). Review Paper: The Fundamentals of Biochar as a Soil Amendment Tool and Management in Agriculture Scope: An Overview for Farmers and Gardeners. *Journal of Agricultural Chemistry and*

Environment, *06*(01), 38–61. https://doi.org/10.4236/jacen.2017.61003

Sharma, A., Kumar, V., Shahzad, B., Tanveer, M., Sidhu, G. P. S., Handa, N., Kohli, S. K., Yadav, P., Bali, A. S., Parihar, R. D., Dar, O. I., Singh, K., Jasrotia, S., Bakshi, P., Ramakrishnan, M., Kumar, S., Bhardwaj, R., & Thukral, A. K. (2019). Worldwide pesticide usage and its impacts on ecosystem. *SN Applied Sciences*, *1*(11), 1–16. https://doi.org/10.1007/s42452-019-1485-1

Shchukarev, A., & Korolkov, D. (2004). XPS Study of Group IA Carbonates. *Central European Journal of Communication*, *2*(2), 347–362.

Shen, W., & Fan, W. (2013). Nitrogen-containing porous carbons: Synthesis and application. *Journal of Materials Chemistry A*, *1*(4), 999–1013. https://doi.org/10.1039/c2ta00028h

Singh, S., Kumar, V., Dhanjal, D. S., Datta, S., Bhatia, D., Dhiman, J., Samuel, J., Prasad, R., & Singh, J. (2020). A sustainable paradigm of sewage sludge biochar: Valorization, opportunities, challenges and future prospects. *Journal of Cleaner Production*, *269*, 122259. https://doi.org/10.1016/j.jclepro.2020.122259

Sizmur, T., Fresno, T., Akgül, G., Frost, H., & Moreno-Jiménez, E. (2017). Biochar modification to enhance sorption of inorganics from water. *Bioresource Technology*, *246*, 34–47. https://doi.org/10.1016/j.biortech.2017.07.082

States, U., & Ache, D. R. B. C. (n.d.). *Organophosphate Insecticides*. 43–55.

Stylianou, M., Christou, A., Dalias, P., Polycarpou, P., Michael, C., Agapiou, A., Papanastasiou, P., & Fatta-Kassinos, D. (2020). Physicochemical and structural characterization of biochar derived from the pyrolysis of biosolids, cattle manure and spent coffee grounds. *Journal of the Energy Institute*, *93*(5), 2063–2073. https://doi.org/10.1016/j.joei.2020.05.002

Suliman, W., Harsh, J. B., Abu-Lail, N. I., Fortuna, A. M., Dallmeyer, I., & Garcia-Perez, M. (2016). Influence of feedstock source and pyrolysis temperature on

biochar bulk and surface properties. *Biomass and Bioenergy*, *84*, 37–48. https://doi.org/10.1016/j.biombioe.2015.11.010

Szeto, S. Y., Price, P. M., Mackenzie, J. R., & Vernon, R. S. (1990). Persistence and Uptake of Phorate in Mineral and Organic Soils. *Journal of Agricultural and Food Chemistry*, *38*(2), 501–504. https://doi.org/10.1021/jf00092a037

Tag, A. T., Duman, G., Ucar, S., & Yanik, J. (2016). Effects of feedstock type and pyrolysis temperature on potential applications of biochar. *Journal of Analytical and Applied Pyrolysis*, *120*, 200–206. https://doi.org/10.1016/j.jaap.2016.05.006

Tan, X. F., Zhu, S. S., Wang, R. P., Chen, Y. Di, Show, P. L., Zhang, F. F., & Ho, S. H. (2021). Role of biochar surface characteristics in the adsorption of aromatic compounds: Pore structure and functional groups. *Chinese Chemical Letters*, *xxxx*. https://doi.org/10.1016/j.cclet.2021.04.059

Tan, X. fei, Liu, Y. guo, Gu, Y. ling, Xu, Y., Zeng, G. ming, Hu, X. jiang, Liu, S. bo, Wang, X., Liu, S. mian, & Li, J. (2016). Biochar-based nano-composites for the decontamination of wastewater: A review. *Bioresource Technology*, *212*, 318–333. https://doi.org/10.1016/j.biortech.2016.04.093

Tankiewicz, M., Fenik, J., & Biziuk, M. (2010). Determination of organophosphorus and organonitrogen pesticides in water samples. *TrAC - Trends in Analytical Chemistry*, *29*(9), 1050–1063. https://doi.org/10.1016/j.trac.2010.05.008

Teutscherova, N., Vazquez, E., Masaguer, A., Navas, M., Scow, K. M., Schmidt, R., & Benito, M. (2017). Comparison of lime- and biochar-mediated pH changes in nitrification and ammonia oxidizers in degraded acid soil. *Biology and Fertility of Soils*, *53*(7), 811–821. https://doi.org/10.1007/s00374-017-1222-0

Thakar, M. A., Saurabh Jha, S., Phasinam, K., Manne, R., Qureshi, Y., & Hari Babu, V. V. (2021). X ray diffraction (XRD) analysis and evaluation of antioxidant activity of copper oxide nanoparticles synthesized from leaf extract of Cissus vitiginea. *Materials Today: Proceedings*, *xxxx*.

https://doi.org/10.1016/j.matpr.2021.05.410

Thermo Fisher Scientific. (2021). *Potassium X-ray photoelectron spectra, potassium electron configuration, and other elemental information.* https://www.thermofisher.com/tr/en/home/materials-science/learning-center/periodic-table/alkali-metal/potassium.html

Thorne, S. (2000). EBN notebook Data analysis in qualitative research. *EBN Notebook, 3*, 68–70.

Tong, S., Zhang, S., Yin, H., Wang, J., & Chen, M. (2021). Study on co-hydrothermal treatment combined with pyrolysis of rice straw/sewage sludge: Biochar properties and heavy metals behavior. *Journal of Analytical and Applied Pyrolysis, 155*(January), 105074. https://doi.org/10.1016/j.jaap.2021.105074

Tong, X., You, L., Zhang, J., Chen, H., Nguyen, V. T., He, Y., & Gin, K. Y.-H. (2021). A comprehensive modelling approach to understanding the fate, transport and potential risks of emerging contaminants in a tropical reservoir. *Water Research, 200*, 117298. https://doi.org/10.1016/j.watres.2021.117298

Uhlig, I., Szargan, R., Nesbitt, H. W., & Laajalehto, K. (2001). Surface states and reactivity of pyrite and marcasite. *Applied Surface Science, 179*(1–4), 222–229. https://doi.org/10.1016/S0169-4332(01)00283-5

US EPA. (2006). Interim Reregistration Eligibility Decision for Phorate. In *United States, Environmental Protection Agency (US EPA)*.

Van Vinh, N., Zafar, M., Behera, S. K., & Park, H. S. (2015). Arsenic(III) removal from aqueous solution by raw and zinc-loaded pine cone biochar: equilibrium, kinetics, and thermodynamics studies. *International Journal of Environmental Science and Technology, 12*(4), 1283–1294. https://doi.org/10.1007/s13762-014-0507-1

Varjani, S., Kumar, G., & Rene, E. R. (2019). Developments in biochar application

for pesticide remediation: Current knowledge and future research directions. *Journal of Environmental Management*, *232*(August 2018), 505–513. https://doi.org/10.1016/j.jenvman.2018.11.043

Venkatachalapathy, R., Packirisamy, A. S. B., Indira Ramachandran, A. C., Udhyasooriyan, L. P., Peter, M. J., Senthilnathan, K., Basheer, V. A., & Muthusamy, S. (2020). Assessing the effect of chitosan on pesticide removal in grape juice during clarification by gas chromatography with tandem mass spectrometry. *Process Biochemistry*, *94*(April), 305–312. https://doi.org/10.1016/j.procbio.2020.04.035

Vicent, T., Caminal, G., & Eljarrat, E. (2013). *Emerging Organic Contaminants in Sludges - Analysis, Fate and Biological Treatment* (D. Bacelo (ed.)).

Vlyssides, A., Barampouti, E. M., Mai, S., Arapoglou, D., & Kotronarou, A. (2004). Degradation of methylparathion in aqueous solution by electrochemical oxidation. *Environmental Science and Technology*, *38*(22), 6125–6131. https://doi.org/10.1021/es049726b

Wan, Zeqing, & Li, K. (2018). Effect of pre-pyrolysis mode on simultaneous introduction of nitrogen/oxygen-containing functional groups into the structure of bagasse-based mesoporous carbon and its influence on Cu(II) adsorption. *Chemosphere*, *194*, 370–380. https://doi.org/10.1016/j.chemosphere.2017.11.181

Wan, Zhonghao, Sun, Y., Tsang, D. C. W., Khan, E., Yip, A. C. K., Ng, Y. H., Rinklebe, J., & Ok, Y. S. (2020a). Customised fabrication of nitrogen-doped biochar for environmental and energy applications. *Chemical Engineering Journal*, *401*(May), 126136. https://doi.org/10.1016/j.cej.2020.126136

Wan, Zhonghao, Sun, Y., Tsang, D. C. W., Khan, E., Yip, A. C. K., Ng, Y. H., Rinklebe, J., & Ok, Y. S. (2020b). Customised fabrication of nitrogen-doped biochar for environmental and energy applications. *Chemical Engineering Journal*, *401*(July), 126136. https://doi.org/10.1016/j.cej.2020.126136

Wang, L., Yan, W., He, C., Wen, H., Cai, Z., Wang, Z., Chen, Z., & Liu, W. (2018). Microwave-assisted preparation of nitrogen-doped biochars by ammonium acetate activation for adsorption of acid red 18. *Applied Surface Science*, *433*, 222–231. https://doi.org/10.1016/j.apsusc.2017.10.031

Wang, R. Z., Huang, D. L., Liu, Y. G., Zhang, C., Lai, C., Wang, X., Zeng, G. M., Gong, X. M., Duan, A., Zhang, Q., & Xu, P. (2019). Recent advances in biochar-based catalysts: Properties, applications and mechanisms for pollution remediation. *Chemical Engineering Journal*, *371*(December 2018), 380–403. https://doi.org/10.1016/j.cej.2019.04.071

Wang, Y., Chen, L., Chen, C., Xi, J., Cao, H., Duan, X., Xie, Y., Song, W., & Wang, S. (2019). Occurrence of both hydroxyl radical and surface oxidation pathways in N-doped layered nanocarbons for aqueous catalytic ozonation. *Applied Catalysis B: Environmental*, *254*(January), 283–291. https://doi.org/10.1016/j.apcatb.2019.05.008

Weber, K., & Quicker, P. (2018). Properties of biochar. *Fuel*, *217*(December 2017), 240–261. https://doi.org/10.1016/j.fuel.2017.12.054

Wei, J., Tu, C., Yuan, G., Liu, Y., Bi, D., Xiao, L., Lu, J., Theng, B. K. G., Wang, H., Zhang, L., & Zhang, X. (2019). Assessing the effect of pyrolysis temperature on the molecular properties and copper sorption capacity of a halophyte biochar. *Environmental Pollution*, *251*, 56–65. https://doi.org/10.1016/j.envpol.2019.04.128

WHO. (2008). *Pesticides*.

Wilk, M., & Magdziarz, A. (2017). Hydrothermal carbonization, torrefaction and slow pyrolysis of Miscanthus giganteus. *Energy*, *140*, 1292–1304. https://doi.org/10.1016/j.energy.2017.03.031

Wu, D., Senbayram, M., Zang, H., Ugurlar, F., Aydemir, S., Brüggemann, N., Kuzyakov, Y., Bol, R., & Blagodatskaya, E. (2018). Effect of biochar origin and soil pH on greenhouse gas emissions from sandy and clay soils. *Applied*

Soil Ecology, *129*(April), 121–127. https://doi.org/10.1016/j.apsoil.2018.05.009

Wu, D., Song, W., Chen, L., Duan, X., Xia, Q., Fan, X., Li, Y., Zhang, F., Peng, W., & Wang, S. (2020). High-performance porous graphene from synergetic nitrogen doping and physical activation for advanced nonradical oxidation. *Journal of Hazardous Materials*, *381*(May 2019), 1–10. https://doi.org/10.1016/j.jhazmat.2019.121010

Wu, R. J., Chen, C. C., Lu, C. S., Hsu, P. Y., & Chen, M. H. (2010). Phorate degradation by TiO2 photocatalysis: Parameter and reaction pathway investigations. *Desalination*, *250*(3), 869–875. https://doi.org/10.1016/j.desal.2009.03.026

Xiang, W., Zhang, X., Chen, J., Zou, W., He, F., Hu, X., Tsang, D. C. W., Ok, Y. S., & Gao, B. (2020). Biochar technology in wastewater treatment: A critical review. *Chemosphere*, *252*, 126539. https://doi.org/10.1016/j.chemosphere.2020.126539

Xiao, X., Chen, B., Chen, Z., Zhu, L., & Schnoor, J. L. (2018). Insight into Multiple and Multilevel Structures of Biochars and Their Potential Environmental Applications: A Critical Review. *Environmental Science and Technology*, *52*(9), 5027–5047. https://doi.org/10.1021/acs.est.7b06487

Xiao, X., Chen, Z., & Chen, B. (2016). H/C atomic ratio as a smart linkage between pyrolytic temperatures, aromatic clusters and sorption properties of biochars derived from diverse precursory materials. *Scientific Reports*, *6*(March), 1–13. https://doi.org/10.1038/srep22644

Xie, R., Zhu, Y., Zhang, H., Zhang, P., & Han, L. (2021). Effects and mechanism of pyrolysis temperature on physicochemical properties of corn stalk pellet biochar based on combined characterization approach of microcomputed tomography and chemical analysis. *Bioresource Technology*, *329*(January), 124907. https://doi.org/10.1016/j.biortech.2021.124907

Xie, Y., Hu, W., Wang, X., Tong, W., Li, P., Zhou, H., Wang, Y., & Zhang, Y. (2020). Molten salt induced nitrogen-doped biochar nanosheets as highly efficient peroxymonosulfate catalyst for organic pollutant degradation. *Environmental Pollution*, *260*, 114053. https://doi.org/10.1016/j.envpol.2020.114053

Xu, C., Tan, X., Zhao, J., Cao, J., Ren, M., Xiao, Y., & Lin, A. (2021). Optimization of biochar production based on environmental risk and remediation performance: Take kitchen waste for example. *Journal of Hazardous Materials*, *416*(April), 125785. https://doi.org/10.1016/j.jhazmat.2021.125785

Xu, S., Chen, J., Peng, H., Leng, S., Li, H., Qu, W., Hu, Y., Li, H., Jiang, S., Zhou, W., & Leng, L. (2021). Effect of biomass type and pyrolysis temperature on nitrogen in biochar, and the comparison with hydrochar. *Fuel*, *291*(October 2020), 120128. https://doi.org/10.1016/j.fuel.2021.120128

Yaashikaa, P. R., Kumar, P. S., Varjani, S., & Saravanan, A. (2020). A critical review on the biochar production techniques, characterization, stability and applications for circular bioeconomy. *Biotechnology Reports*, *28*, e00570. https://doi.org/10.1016/j.btre.2020.e00570

Yan, Y., Ma, X., Cao, W., Zhang, X., Zhou, J., Liu, Q., & Qian, G. (2018). Identifying the reducing capacity of biomass derived hydrochar with different post-treatment methods. *Science of the Total Environment*, *643*, 486–495. https://doi.org/10.1016/j.scitotenv.2018.06.232

Yang, C., Liu, J., & Lu, S. (2021). Pyrolysis temperature affects pore characteristics of rice straw and canola stalk biochars and biochar-amended soils. *Geoderma*, *397*(October 2020), 115097. https://doi.org/10.1016/j.geoderma.2021.115097

Yang, F., Sun, L., Xie, W., Jiang, Q., Gao, Y., Zhang, W., & Zhang, Y. (2017). Nitrogen-functionalization biochars derived from wheat straws via molten salt synthesis: An efficient adsorbent for atrazine removal. *Science of the Total Environment*, *607–608*, 1391–1399.

https://doi.org/10.1016/j.scitotenv.2017.07.020

Yang, J., Zhang, M., Wang, H., Xue, J., Lv, Q., & Pang, G. (2021). Efficient recovery of phosphate from aqueous solution using biochar derived from co-pyrolysis of sewage sludge with eggshell. *Journal of Environmental Chemical Engineering*, *9*(5). https://doi.org/10.1016/j.jece.2021.105354

Yang, Xiao, Igalavithana, A. D., Oh, S. E., Nam, H., Zhang, M., Wang, C. H., Kwon, E. E., Tsang, D. C. W., & Ok, Y. S. (2018). Characterization of bioenergy biochar and its utilization for metal/metalloid immobilization in contaminated soil. *Science of the Total Environment*, *640–641*, 704–713. https://doi.org/10.1016/j.scitotenv.2018.05.298

Yang, Xu, & Wang, X.-Y. (2021). Hydration-strength-durability-workability of biochar-cement binary blends. *Journal of Building Engineering*, *42*(May), 103064. https://doi.org/10.1016/j.jobe.2021.103064

Yang, Xuanmin, Kang, K., Qiu, L., Zhao, L., & Sun, R. (2020). Effects of carbonization conditions on the yield and fixed carbon content of biochar from pruned apple tree branches. *Renewable Energy*, *146*, 1691–1699. https://doi.org/10.1016/j.renene.2019.07.148

Yang, Xue, Zhang, S., Ju, M., & Liu, L. (2019). Preparation and modification of biochar materials and their application in soil remediation. *Applied Sciences (Switzerland)*, *9*(7). https://doi.org/10.3390/app9071365

Yang, Y., Ye, S., Zhang, C., Zeng, G., Tan, X., Song, B., Zhang, P., Yang, H., Li, M., & Chen, Q. (2020). Application of biochar for the remediation of polluted sediments. *Journal of Hazardous Materials*, *404*(PA), 124052. https://doi.org/10.1016/j.jhazmat.2020.124052

Yi, Y., Huang, Z., Lu, B., Xian, J., Tsang, E. P., Cheng, W., Fang, J., & Fang, Z. (2019). Magnetic biochar for environmental remediation: A review. *Bioresource Technology*, *298*(September 2019). https://doi.org/10.1016/j.biortech.2019.122468

Yousaf, B., Liu, G., Ubaid Ali, M., Abbas, Q., Liu, Y., Ullah, H., & Imtiyaz Cheema, A. (2021). Decisive role of vacuum-assisted carbonization in valorization of lignin-enriched (Juglans regia-shell) biowaste. *Bioresource Technology*, *323*(December 2020), 124541. https://doi.org/10.1016/j.biortech.2020.124541

Yu, J., Maliutina, K., & Tahmasebi, A. (2018). A review on the production of nitrogen-containing compounds from microalgal biomass via pyrolysis. *Bioresource Technology*, *270*(August), 689–701. https://doi.org/10.1016/j.biortech.2018.08.127

Yu, W., Lian, F., Cui, G., & Liu, Z. (2018). N-doping effectively enhances the adsorption capacity of biochar for heavy metal ions from aqueous solution. *Chemosphere*, *193*, 8–16. https://doi.org/10.1016/j.chemosphere.2017.10.134

Yuan, S., Tan, Z., & Huang, Q. (2018). Migration and transformation mechanism of nitrogen in the biomass–biochar–plant transport process. *Renewable and Sustainable Energy Reviews*, *85*(January), 1–13. https://doi.org/10.1016/j.rser.2018.01.008

Zaeni, J. R. J., Lim, J. W., Wang, Z., Ding, D., Chua, Y. S., Ng, S. L., & Oh, W. Da. (2020). In situ nitrogen functionalization of biochar via one-pot synthesis for catalytic peroxymonosulfate activation: Characteristics and performance studies. *Separation and Purification Technology*, *241*(January), 116702. https://doi.org/10.1016/j.seppur.2020.116702

Zeng, B., Xu, W., Khan, S. B., Wang, Y., Zhang, J., Yang, J., Su, X., & Lin, Z. (2021). Preparation of sludge biochar rich in carboxyl/hydroxyl groups by quenching process and its excellent adsorption performance for Cr(VI). *Chemosphere*, *285*(March), 131439. https://doi.org/10.1016/j.chemosphere.2021.131439

Zhang, C., Zhang, L., Gao, J., Zhang, S., Liu, Q., Duan, P., & Hu, X. (2020). Evolution of the functional groups/structures of biochar and heteroatoms during the pyrolysis of seaweed. *Algal Research*, *48*(March), 101900.

https://doi.org/10.1016/j.algal.2020.101900

Zhang, D., Liu, P., Lu, X., Wang, L., & Pan, T. (2016). Upgrading of low rank coal by hydrothermal treatment: Coal tar yield during pyrolysis. *Fuel Processing Technology*, *141*, 117–122. https://doi.org/10.1016/j.fuproc.2015.06.037

Zhang, M., Shu, L., Shen, X., Guo, X., Tao, S., Xing, B., & Wang, X. (2014). Characterization of nitrogen-rich biomaterial-derived biochars and their sorption for aromatic compounds. *Environmental Pollution*, *195*, 84–90. https://doi.org/10.1016/j.envpol.2014.08.018

Zhang, P., Song, D., XuejingXu, Hao, Y., Shang, X., Wang, C., Tang, J., & Sun, H. (2021). Sulfidated zero valent iron as a persulfate activator for oxidizing organophosphorus pesticides (OPPs) in aqueous solution and aged contaminated soil columns. *Chemosphere*, *281*(April), 130760. https://doi.org/10.1016/j.chemosphere.2021.130760

Zhang, W. (2018). Global pesticide use: Profile, trend, cost / benefit and more. *Proceedings of the International Academy of Ecology and Environmental Sciences*, *8*(1), 1–27. www.iaees.org

Zhang, Xiaoxiao, Zhang, P., Yuan, X., Li, Y., & Han, L. (2020). Effect of pyrolysis temperature and correlation analysis on the yield and physicochemical properties of crop residue biochar. *Bioresource Technology*, *296*(September 2019), 122318. https://doi.org/10.1016/j.biortech.2019.122318

Zhang, Xiong, Zhang, S., Yang, H., Feng, Y., Chen, Y., Wang, X., & Chen, H. (2014). Nitrogen enriched biochar modified by high temperature CO2-ammonia treatment: Characterization and adsorption of CO2. *Chemical Engineering Journal*, *257*, 20–27. https://doi.org/10.1016/j.cej.2014.07.024

Zhang, Xueyang, Gao, B., Fang, J., Zou, W., Dong, L., Cao, C., Zhang, J., Li, Y., & Wang, H. (2019). Chemically activated hydrochar as an effective adsorbent for volatile organic compounds (VOCs). *Chemosphere*, *218*, 680–686. https://doi.org/10.1016/j.chemosphere.2018.11.144

Zhao, X., Wang, J., Li, T., & Zhang, Y. (2012). Degradation behaviors of seven organophosphorus pesticides in skimmed milk inoculated with Streptococcus thermophilus or Lactobacillus helveticus. *Milchwissenschaft*, *67*(4), 399–401.

Zhen, M., Song, B., Liu, X., Chandankere, R., & Tang, J. (2018). Biochar-mediated regulation of greenhouse gas emission and toxicity reduction in bioremediation of organophosphorus pesticide-contaminated soils. *Chinese Journal of Chemical Engineering*, *26*(12), 2592–2600. https://doi.org/10.1016/j.cjche.2018.01.028

Zheng, C., Yang, Z., Si, M., Zhu, F., Yang, W., Zhao, F., & Shi, Y. (2020). Application of biochars in the remediation of chromium contamination: Fabrication, mechanisms, and interfering species. *Journal of Hazardous Materials*, *July*, 124376. https://doi.org/10.1016/j.jhazmat.2020.124376

Zhou, S., Liang, H., Han, L., Huang, G., & Yang, Z. (2019). The influence of manure feedstock, slow pyrolysis, and hydrothermal temperature on manure thermochemical and combustion properties. *Waste Management*, *88*, 85–95. https://doi.org/10.1016/j.wasman.2019.03.025

Zhou, X., Zhu, Y., Niu, Q., Zeng, G., Lai, C., Liu, S., Huang, D., Qin, L., Liu, X., Li, B., Yi, H., Fu, Y., Li, L., Zhang, M., Zhou, C., & Liu, J. (2021). New notion of biochar: A review on the mechanism of biochar applications in advannced oxidation processes. *Chemical Engineering Journal*, *416*(December 2020), 129027. https://doi.org/10.1016/j.cej.2021.129027

Zhou, Y., Qin, S., Verma, S., Sar, T., Sarsaiya, S., Ravindran, B., Liu, T., Sindhu, R., Patel, A. K., Binod, P., Varjani, S., Rani Singhnia, R., Zhang, Z., & Awasthi, M. K. (2021). Production and beneficial impact of biochar for environmental application: A comprehensive review. *Bioresource Technology*, *337*(May), 125451. https://doi.org/10.1016/j.biortech.2021.125451

Zhu, S., Huang, X., Ma, F., Wang, L., Duan, X., & Wang, S. (2018). Catalytic Removal of Aqueous Contaminants on N-Doped Graphitic Biochars: Inherent

Roles of Adsorption and Nonradical Mechanisms. *Environmental Science and Technology*, *52*(15), 8649–8658. https://doi.org/10.1021/acs.est.8b01817

Zhuang, Z., Wang, L., & Tang, J. (2021). Efficient removal of volatile organic compound by ball-milled biochars from different preparing conditions. *Journal of Hazardous Materials*, *406*(September 2020), 124676. https://doi.org/10.1016/j.jhazmat.2020.124676

Zornoza, R., Moreno-Barriga, F., Acosta, J. A., Muñoz, M. A., & Faz, A. (2016). Stability, nutrient availability and hydrophobicity of biochars derived from manure, crop residues, and municipal solid waste for their use as soil amendments. *Chemosphere*, *144*, 122–130. https://doi.org/10.1016/j.chemosphere.2015.08.046

APPENDICES

A. First and second stage batch phorate removal results

Table A.1. Initial and final phorate concentration (µg/L) in the batch removal experiments and overall removal efficiencies (%) of 1 g/L biochar samples at 25 °C

Biochar Sample	Conc. (t=0) (µg/L)	Conc. (t=5 h) (µg/L)	Removal Eff. (t=5 h) (%)
BC300	1000	383	61.70
BC500	1000	293	70.74
BC700	1000	204	79.65
BC900	1000	127	87.28
KOH0.5BC700	1000	180	82.01
KOH1BC700	1000	131	86.93
KOH2BC700	1000	17	98.31
U5BC700	1000	204	79.56
U10BC700	1000	173	82.67
U15BC700	1000	115	88.45
KUBC700	1000	0	100
HC210BC300	1000	70	93.02
HC210BC500	1000	63	93.68
HC210BC700	1000	44	95.64
HC210BC900	1000	8	99.19
HC210BC700KOH0.5	1000	108	89.16
HC210BC700KOH1	1000	15	98.53
HC210BC700KOH2	1000	0	100
HC210BC700U5	1000	189	81.06
HC210BC700U10	1000	87	91.32
HC210BC700U15	1000	17	98.31
HC210BC700KOH1U10	1000	0	100
U10HC210	1000	385	61.48
U5HC210BC700	1000	33	96.7
U10HC210BC700	1000	29	97.07
U15HC210BC700	1000	18	98.18
U10HC210BC700KOH1	1000	0	100
HC210BC7004h	1000	30	96.99
HC210BC7008h	1000	28	97.21
HC210BC70016h	1000	23	97.65
HC230BC700	1000	26	97.43
HC190BC700	1000	68	93.24
HC170BC700	1000	266	73.39

Table A.2. Initial and final phorate concentration (µg/L) in the batch removal experiments and overall removal efficiencies (%) of 1 g/L biochar samples under varied temperatures

Temp.	Biochar Sample	KUBC700	HC210BC700KOH1U10	U10HC210BC700KOH1
25 °C	Initial conc. (t=0) (µg/L)	1000	1000	1000
	Final Conc. (t=5 h) (µg/L)	0	0	0
	Removal Efficiency (t=5 h) (%)	100	100	100
30 °C	Initial conc. (t=0) (µg/L)	1000	1000	1000
	Final Conc. (t=5 h) (µg/L)	0	0	26
	Removal Efficiency (t=5 h) (%)	100	100	97.43
35 °C	Initial conc. (t=0) (µg/L)	1000	1000	1000
	Final Conc. (t=5 h) (µg/L)	81	52	68
	Removal Efficiency (t=5 h) (%)	91.89	94.8	93.24
40 °C	Initial conc. (t=0) (µg/L)	1000	1000	1000
	Final Conc. (t=5 h) (µg/L)	111	181	544
	Removal Efficiency (t=5 h) (%)	88.89	81.87	45.6

Table A.3. Initial and final phorate concentration (µg/L) in the batch removal experiments and overall removal efficiencies (%) of dosage varied biochar samples at 25 °C

Biochar Dose (g/L)	Biochar Sample	KUBC700	HC210BC700KOH1U10	U10HC210BC700KOH1
0.2	Initial conc. (t=0) (µg/L)	1000	1000	1000
	Final Conc. (t=5 h) (µg/L)	187	27	83
	Removal Efficiency (t=5 h) (%)	81.33	97.34	91.69
1	Initial conc. (t=0) (µg/L)	1000	1000	1000
	Final Conc. (t=5 h) (µg/L)	0	0	0
	Removal Efficiency (t=5 h) (%)	100	100	100
5	Initial conc. (t=0) (µg/L)	1000	1000	1000
	Final Conc. (t=5 h) (µg/L)	0	0	0
	Removal Efficiency (t=5 h) (%)	100	100	100
15	Initial conc. (t=0) (µg/L)	1000	1000	1000
	Final Conc. (t=5 h) (µg/L)	0	0	0
	Removal Efficiency (t=5 h) (%)	100	100	100

Table A.4. Initial and final phorate concentration (μg/L) in the batch removal experiments and overall removal efficiencies (%) of 1 g/L biochar samples in pH varied solution at 25 °C

pH	Biochar Sample	KUBC700	HC210BC700KOH1U10	U10HC210BC700KOH1
No pH adjusted (6 - 6.5)	Initial conc. (t=0) (μg/L)	1000	1000	1000
	Final Conc. (t=5 h) (μg/L)	0	0	0
	Removal Eff. (t=5 h) (%)	100	100	100
3	Initial conc. (t=0) (μg/L)	1000	1000	1000
	Final Conc. (t=5 h) (μg/L)	101	11	39
	Removal Eff. (t=5 h) (%)	89.93	98.86	96.11
5	Initial conc. (t=0) (μg/L)	1000	1000	1000
	Final Conc. (t=5 h) (μg/L)	28	0	61
	Removal Eff. (t=5 h) (%)	97.23	100	93.90
7	Initial conc. (t=0) (μg/L)	1000	1000	1000
	Final Conc. (t=5 h) (μg/L)	81	26	0
	Removal Eff. (t=5 h) (%)	91.92	97.43	100
9	Initial conc. (t=0) (μg/L)	1000	1000	1000
	Final Conc. (t=5 h) (μg/L)	144	34	54
	Removal Eff. (t=5 h) (%)	85.61	96.55	94.56
11	Initial conc. (t=0) (μg/L)	1000	1000	1000
	Final Conc. (t=5 h) (μg/L)	181	136	0
	Removal Eff. (t=5 h) (%)	81.91	86.4	100